



HAL
open science

Study of baryonic resonances in the channel $pp \rightarrow pp\pi^+\pi$ at 3.5 GeV beam energy with the HADES detector

Amel Belounnas

► **To cite this version:**

Amel Belounnas. Study of baryonic resonances in the channel $pp \rightarrow pp\pi^+\pi$ at 3.5 GeV beam energy with the HADES detector. Nuclear Experiment [nucl-ex]. Université Paris-Saclay, 2019. English. NNT : 2019SACLS243 . tel-02614181

HAL Id: tel-02614181

<https://theses.hal.science/tel-02614181>

Submitted on 20 May 2020

HAL is a multi-disciplinary open access archive for the deposit and dissemination of scientific research documents, whether they are published or not. The documents may come from teaching and research institutions in France or abroad, or from public or private research centers.

L'archive ouverte pluridisciplinaire **HAL**, est destinée au dépôt et à la diffusion de documents scientifiques de niveau recherche, publiés ou non, émanant des établissements d'enseignement et de recherche français ou étrangers, des laboratoires publics ou privés.

Study of baryonic resonances in the channel $pp \rightarrow pp\pi^+\pi^-$ at 3.5 GeV beam energy with the HADES detector

Thèse de doctorat de l'Université Paris-Saclay
Préparée à l'Université de Paris-Sud
à l'Institut de Physique Nucléaire d'Orsay

ED n°576 : particules hadrons énergie et noyau : instrumentation, imagerie, cosmos et simulation (PHENIX)
Spécialité de doctorat : Physique hadronique

Thèse présentée et soutenue à Orsay, le 18/09/2019, par

Amel Belounnas

Composition du Jury :

Mikhail Bashkanov

Senior scientist, Department of Physics University of York

Rapporteur

Hannah Elfner

Professor, Goethe University Frankfurt

Rapporteur

Silvia Niccolai

Directeur de recherche, Institut de Physique Nucléaire d'Orsay

Président

Jean-Christophe David

Directeur de recherche, CEA-Saclay IRFU-DPhN

Examineur

Miklos Zetenyi

Senior scientist, Wigner Research Centre for Physics, Budapest

Examineur

Béatrice Ramstein

Directeur de recherche, Institut de Physique Nucléaire d'Orsay

Directeur de thèse

Study of baryonic resonances in the channel $pp \rightarrow pp\pi^+\pi^-$
at 3.5 GeV beam energy with the HADES detector

Amel Belounnas

18 September 2019

“Sometimes the public says, ‘What’s in it for Numero Uno? Am I going to get better television reception? Am I going to get better Internet reception?’ Well, in some sense, yeah. ... All the wonders of quantum physics were learned basically from looking at atom-smasher technology. ... But let me let you in on a secret : We physicists are not driven to do this because of better color television. ... That’s a spin-off. We do this because we want to understand our role and our place in the universe.”

Michio Kaku

Table des matières

1	Introduction	1
1.1	Properties of strong interactions	3
1.2	Baryon resonances and vector mesons	5
1.2.1	Quark Model predictions	5
1.2.2	Baryon spectroscopy	6
1.2.3	Exotic Baryons	9
1.2.4	Baryon resonances in the early universe	10
1.2.5	”Resonance” matter	11
1.2.6	Dileptons and vector meson spectral functions	12
1.2.7	Baryon resonance Dalitz decay and Vector Meson Dominance Model	14
1.3	HADES experiments	15
1.3.1	Main motivations	15
1.3.2	Dilepton spectroscopy in medium	16
1.3.3	Dilepton spectroscopy in elementary reactions	17
1.4	One pion production in NN reactions with HADES	17
1.4.1	pp collisions at $T = 1.25$ GeV	18
1.4.2	pp collisions at $T = 2.2$ GeV	19
1.4.3	pp collisions at $T = 3.5$ GeV	20
1.5	Double pion production in nucleon-nucleon reactions	23
1.5.1	Motivations	23
1.5.2	Existing measurements	24
1.5.3	Theoretical developments for $NN \rightarrow NN\pi\pi$	24
1.5.4	HADES results in the $np \rightarrow np\pi^+\pi^-$ reaction at 1.25 GeV	25
1.5.5	WASA results for the $pp \rightarrow pp\pi^+\pi^-$ reaction	25
2	HADES detector	28
2.1	Target	30
2.2	The Ring Imaging Cherenkov detector	30
2.3	The Multi-wire Drift Chambers	32
2.4	The Superconducting Magnet	33
2.5	The Multiplicity Electron Trigger Array	34
2.5.1	Time-Of-Flight Detectors : TOF and TOFino	34
2.5.2	Pre-Shower detector	36
2.6	The trigger system	37
3	Experimental Data Analysis	39
3.1	Introduction	39
3.2	Particle reconstruction and identification	41
3.2.1	Momentum reconstruction	41

3.2.2	Time of flight calculation	42
3.2.3	Time and momentum correlation	43
3.3	Event selection	44
3.4	Background Subtraction	46
3.5	Efficiency and Acceptance Considerations	48
3.5.1	Acceptance Matrices	49
3.5.2	Efficiency Matrices	50
3.6	Efficiency cuts	52
3.7	Data Normalization	54
3.8	Systematic errors estimation	55
4	Simulations	58
4.1	The PLUTO event generator	58
4.2	PLUTO Resonance Cocktail	59
4.3	Inputs from the one pion production analysis	60
4.4	Accounting for the detector geometrical effects	64
4.4.1	Acceptance filtering	64
4.4.2	Simulation efficiency cuts	65
4.4.3	Momentum Smearing	66
4.5	Angular distribution parametrization	67
4.6	Kinematics variables	69
5	Extraction of the baryon resonance contributions	71
5.1	Evidence for single and double baryon excitation	71
5.1.1	Correlations between invariant masses	71
5.1.2	Comparing data to phase space distributions	74
5.2	Comparing Data with PLUTO simulation	76
5.2.1	Comparing with one resonance production model	76
5.2.2	Implementation of the double resonance contribution	77
5.2.3	Sensitivity of the data to the cocktail parameters	78
5.3	Extraction of the Cross Sections	81
5.3.1	Manually adjusted cross sections	81
5.3.2	Automatic fitting procedure	82
5.3.3	Impact of the results for dielectron production	88
5.4	Dibaryon investigation	89
6	Extraction of the light meson contributions	92
6.1	Introduction	92
6.2	ρ meson	93
6.2.1	ρ meson signal extraction	93
6.2.2	ρ spectral function	95
6.2.3	ρ meson angular distribution	98
6.2.4	Total cross sections	105
6.2.5	Comparing ρ result with theoretical models	107
6.3	$f_0(500)$ meson or σ	113
6.4	$f_0(980)$ meson	114

7	Theoretical development of a Lagrangian model	116
7.1	General expression of the differential cross section	116
7.2	Model Formalism	117
7.2.1	Choice of Feynman graphs	117
7.2.2	Lagrangians	118
7.2.3	Form factors	119
7.2.4	Propagators	120
7.3	Amplitude Calculation	122
7.3.1	Double Δ production	122
7.3.2	N(1520) production followed by decay to $\Delta\pi$	124
7.3.3	N(1520) production followed by decay to $p\rho$	127
7.4	Numerical calculation result and discussion	129
7.4.1	Building an event generator	129
7.4.2	Differences with the resonance cocktail model	130
7.4.3	Results of the Lagrangian model	131
7.5	Interference effect	133
8	Comparison to theoretical models	136
8.1	OPER model	136
8.2	Cao Lagrangian Model	140
8.3	GiBUU model	145
8.4	UrQMD model	146
8.5	SMASH model	148
8.6	Conclusion on data/model comparison	151
9	Conclusion	152
A	Four-body final state	156
	Bibliographie	159

1

Introduction

In 2007, the HADES collaboration measured proton proton collisions at GSI with a kinetic energy of the projectile equal to 3.5 GeV. The main purpose of this experiment was the measurement of electron-positron pairs (the so-called di-electrons). However, with HADES, it is also possible to measure charged hadrons such as protons and pions, which gives the possibility of complementary measurements which are important for the production of e^+e^- pairs. The main purpose of the "hadron" analysis is to study reaction mechanisms and determine cross sections, which are important sources of e^+e^- pairs. One important aspect at GSI energies is the baryon resonance excitation.

In the framework of this dissertation the analysis of the exclusive $pp \rightarrow pp\pi^+\pi^-$ channel at 3.5 GeV kinetic energy is presented, aiming to study baryonic resonance excitations and ρ meson production. In this chapter, I start with a general introduction of hadron physics and baryon resonances, then I present the general physics motivations of HADES experiments. HADES results in NN reactions are briefly discussed. Finally I clarify the motivation for double pion production experiments.

In Chapter 2 the description of the HADES spectrometer will be given with emphasis on the MDC (Multiwire Drift Chamber) sub-detector.

In Chapter 3 I explain the steps of the experimental data analysis : particle reconstruction, event selection, background subtraction, efficiency correction and normalization.

In Chapter 4 the simulation framework is described together with the ingredients used for the interpretation of the data.

In Chapter 5 the results of exclusive double-pion production channel in pp reaction are discussed. The measured spectra, such as invariant mass and angular distributions, are compared to the simulation and resonance contributions cross sections are extracted.

In Chapter 6 the method to extract the ρ meson contribution is explained in details and the results are presented.

In Chapter 7 the development of a theoretical model is presented and the effect of interferences is discussed.

In Chapter 8 the experimental results obtained for the baryonic resonance contributions are compared to theoretical model simulation and with the results of transport models.

1.1 Properties of strong interactions

The strong interaction is responsible for the binding of quarks in nucleons and nuclei. Its corresponding quantum field theory is QCD [1] which describes the quark and gluon interaction. A major difference of the strong force with respect to the well understood electromagnetic interaction is its color charge [2]. In QCD, gluons are the force carrier of the strong interaction, but in contrast to the photon, the gluons also carry the color charge and can interact with each other. As shown in Figure 1.1, the QCD coupling constant (α_s) is not constant, which is also one of the characteristics of the strong interaction. The strong coupling constant is small ($\alpha_s \sim 0.1$) in the case of processes with small distances or large momentum transfers. This causes the quarks inside hadrons to behave more or less as free particles, when probed at large enough energies. This property of the strong interaction is called *asymptotic freedom* [3]. It allows us to use perturbation theory, and by this to make quantitative predictions for hard scattering cross sections in hadronic interactions. In the low-energy range, at increasing distances, α_s increases and non-perturbative mechanisms dominate which qualitatively explains that quarks are confined in hadrons [4]. However, the detailed understanding of *confinement* and the structure of hadrons is an open subject.

Due to the attractive force, bound states are created. Baryons consist of three quarks carrying different colors that add up to a color neutral object. Another typical state is a meson consisting of a quark and anti-quark pair with color and anti-color respectively. The standard model can describe mass creation by the coupling of the quarks to the Higgs field. The self interaction of this field is the so-called Higgs boson, which was discovered in 2012 at the LHC [5]. The mass of the lightest quarks that are created by the Higgs mechanism are in the order of a few MeV/c^2 . In comparison to the mass of a nucleon ($M_p = 938 \text{ MeV}/c^2$), the contributions from the Higgs field are less than one percent. As a consequence, additional sources have to contribute to the mass generation of hadrons.

In addition to the SU(3) gauge symmetry, that describes the color charges and the coupling to the exchange bosons (gluons), QCD has other approximate symmetries. Chiral symmetry describes the independence of left and right handed particles coupling in QCD in the limit of zero mass. This symmetry is *spontaneously broken* in physical states. Indeed, there is no mass degeneracy between chiral partners, which differ by the

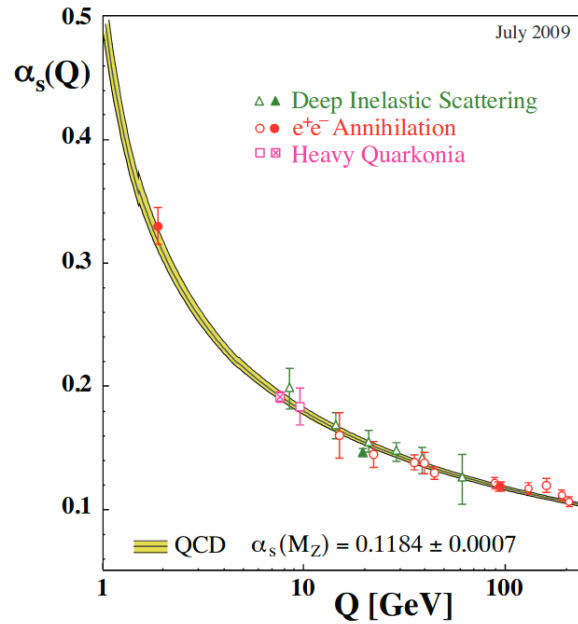


FIGURE (1.1) Measurements of the QCD strong coupling constant α_s as function of the momentum transfer Q [10]. At short distances (large momentum transfer), the strong interaction mechanism is called asymptotic freedom. At increasing distances (small momentum transfer) the mechanism is called confinement.

parity, such as the pion and the σ mesons, the $\rho(770)$ and $a_1(1260)$, the nucleon and the $N(1535)$,... One of the order parameters which quantify this chiral symmetry breaking is the quark condensate $\langle 0|q\bar{q}|0 \rangle$. Hadrons are seen as excitations of the QCD vacuum which is filled by condensates of quark-antiquark pairs which break the chiral symmetry.

The spontaneous chiral symmetry breaking is therefore an essential feature of the hadron spectrum in vacuum. In addition, a reduction of the quark condensate, as a function of increasing baryon density or temperature is predicted [6]. This chiral symmetry restoration has been shown to occur at a temperature of 160-190 MeV [7, 8] for vanishing baryonic densities using numerical computations on the lattice at finite temperatures. Lattice QCD calculations can not be performed at large baryonic densities, but models predict that the quark condensate is strongly reduced already at normal nuclear matter density [9]. Heavy ion collisions at moderate to high energies are used to measure the phase diagrams at different points (see Figure 1.12).

To explore QCD properties, one can study the spectrum of QCD states in vacuum, using elementary reactions. The properties (mass, width, decay branching ratios) of the hadrons bring detailed information on the strong interaction. One can also study the phase structure of strongly interacting matter. For this purpose, hadrons are not

considered in the QCD vacuum, but within a surrounding medium with a baryon density and/or a finite temperature using heavy-ion collisions. In the following, we will give more details about these two aspects of hadronic physics, with a focus on low energy studies.

1.2 Baryon resonances and vector mesons

1.2.1 Quark Model predictions

Baryons in the conventional Quark Model are color singlets composed of three quarks. Figure 1.2 displays the baryon octet (left) and baryon decuplet (right) built from the first generation of quarks (u , d and s). The understanding of the nucleon and the excited baryons internal structure remains a fundamental challenge in hadronic physics. In addition to the study of the nucleon which is the most intensive, the investigation of the other baryons and of their excited states (or baryonic resonances) is of utmost importance to bring information on strong interaction. The investigation of baryon resonances (i.e. short-lived excited states of the nucleon) provides access to strong interactions.

Resonances are identified as complex energy poles in the scattering matrix for a given partial wave. They manifest experimentally as peaks in excitation function located around a certain energy. They are probed in scattering experiments and are characterized by the complex pole position of the scattering amplitude and the couplings to the various channels. The region of 1-2 GeV is occupied by light-flavored baryons which are

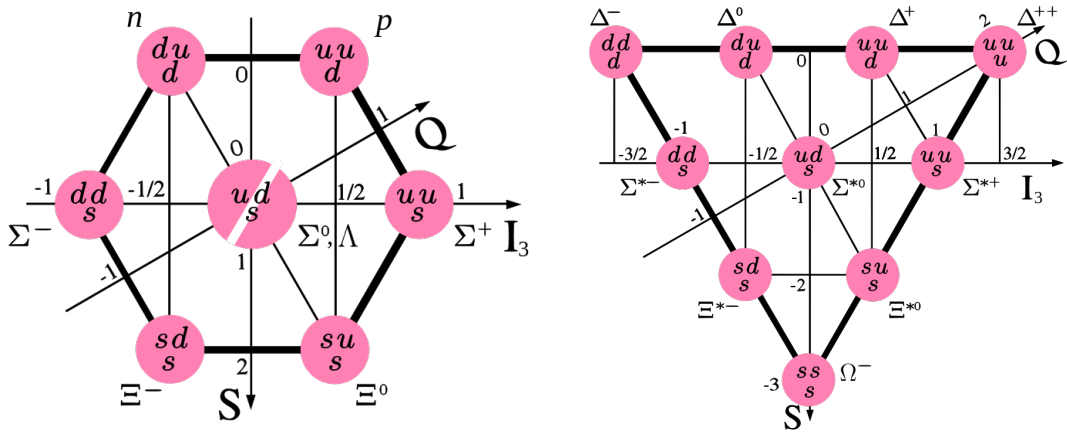


FIGURE (1.2) SU(3) multiplets of baryons made of u , d and s quarks. Left : the baryon octet ($J^P = 1/2^+$). Right : the baryon decuplet ($J^P = 3/2^+$). The valence quark content of the baryons is indicated explicitly. The S axes represent the strangeness, the I_3 axes represent the isospin and the Q axes represent the charge.

built out of the three light quarks (u , d , s) with isospin 0, 1/2, 1 or 3/2, accounting for orbital motion, a supermultiplet $SU_{flavor}(3) \times SU_{spin}(2) \times O_{space}(3)$ resulting in 434 possible resonances which highly exceeds the number of identified 112 resonances listed in the PDG [11] which came from the earlier spectroscopy results from π - and K-induced reactions (Figure 1.3). This mismatch between the theoretically predicted and experimentally observed spectroscopic densities is known in hadron physics as *"the missing resonance puzzle"*.

Up to a few years ago, it was common to label baryon resonances with the incoming πN partial wave $L_{2I,2J}$ ($N(1440)P_{11}$, $N(1520)D_{13}$, $\Delta(1232)P_{11}$...). since nearly all resonances information came from partial wave analysis (PWA) of πN elastic scattering. Most recent information comes from photon induced reactions and some resonances have a weak coupling to pion, so, nowadays the spin and parity replaced $L_{2I,2J}$ was replaced by the spin parity of the state J^P ($N(1440)1/2^+$, $N(1520)3/2^-$, $\Delta(1232)3/2^+$...). The PDG gives an evaluation status to all the N and Δ baryons from one to four stars where a **** or *** status is given to resonances which are derived from analyses of data sets that include precision differential cross sections and polarization observables, and are confirmed by independent analyses. all the others are given ** or * status [11].

1.2.2 Baryon spectroscopy

Pion-induced reactions were the first experiments to track baryon resonances. Most of the current knowledge about the light-quark baryons is a result of partial wave analysis (PWA) of πN scattering data in the reaction $\pi N \rightarrow \pi N$ and charge exchange data (e.g. $\pi^- p \rightarrow \pi^0 n$). The first experiments were performed between 1957 and 1979 at the Nimrod accelerator at Rutherford Laboratory. They focused mostly on the production of non-strange baryon resonances. Later there were many experiments that extracted cross sections with much smaller statistical and systematic uncertainties and also measured polarization observables (see [16] for the full experimental database). The most recent results published after 2000 come from experiments at the Brookhaven National Laboratory (BNL), the Tri-University Meson Facility (TRIUMF), and the Paul Scherrer Institute (PSI). In $\pi^+ p$ reactions, only Δ resonances (of isospin 3/2) can be excited. As shown in Figure 1.4, the cross sections show a prominent structure at low energies corresponding to the excitation of the $\Delta(1232)$ resonance and smaller structures for the

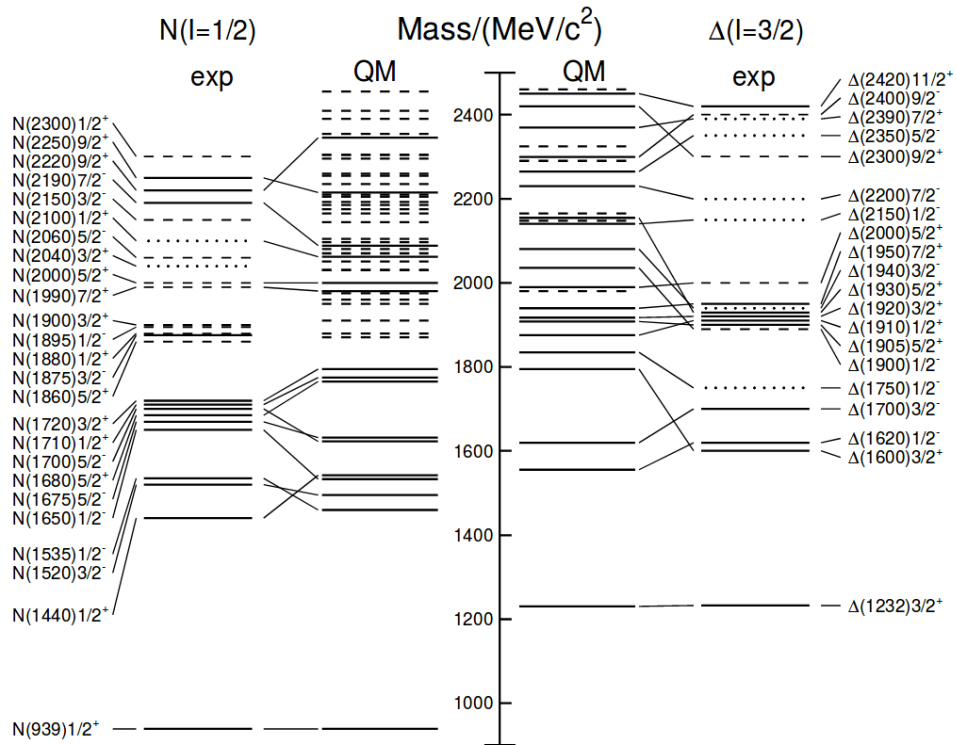


FIGURE (1.3) Excitation spectrum of the nucleon. Compared are the positions of the excited states identified in experiment, to those predicted by a relativistic quark model calculation. Left : isospin $I = 1/2$ N-states. Right : isospin $I = 3/2$ Δ -states. Experimental : (columns labeled 'exp'), three and four star states are indicated by full lines (two star dashed lines, one star dotted lines). At the very left and right of the figure, the spectroscopic notation of these states is given. Quark model [12–14] : (columns labeled 'QM'), all states for the $N = 1,2$ bands, low-lying states for the $N = 3,4,5$ bands. Full lines : at least tentative assignment to observed states, dashed lines : so far no observed counterparts. Many of the assignments between predicted and observed states are highly tentative. [11].

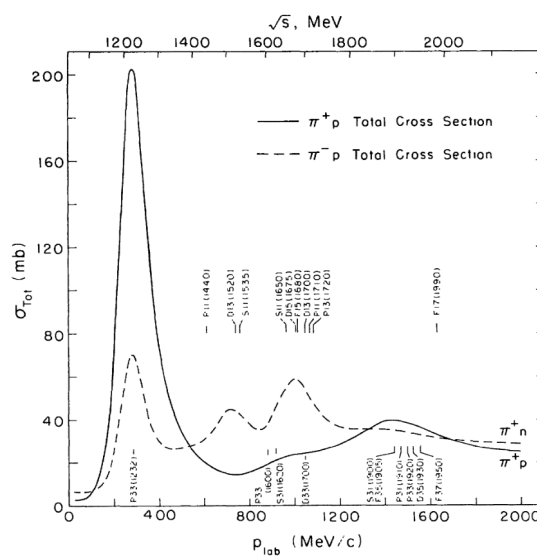


FIGURE (1.4) Total π^+p and π^+n cross sections plotted against the pion lab momentum (p_{lab}) and total center of mass energy \sqrt{s} . The positions of several N^* and Δ resonances are shown [15].

excitation of Δ s with mass around 1600 and 1900 MeV/c^2 . In the case of πn reactions, the $\Delta(1232)$ excitation is weaker, but still prominent and two other groups of resonances can be identified (the so-called second and third resonance regions, respectively around 1.5 and 1.7 GeV/c^2).

Figure 1.5 displays the cross sections for different channels in the $\pi^- p$ reaction. It can be observed that, above 1.4 GeV , inelastic channels provide an important contribution to the cross section. Their measurement is necessary to characterize the baryon spectrum, in particular for higher energies where the coupling to one pion becomes weaker. Among all inelastic channels, the production of two pions has the largest contributions. This channel is also very rich, since it provides information on the production of some mesons (f_0, ρ, \dots). With three particles in the final state, this channel is however not very easy to measure and to analyze.

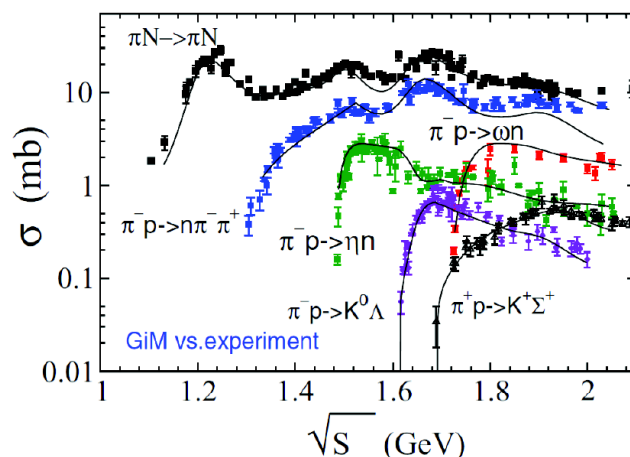


FIGURE (1.5) Total $\pi^- N$ cross sections calculated with Giessen model compared to experimental data [17].

A comparison between experimental results and theoretical models led to the above-mentioned "missing resonances" problem. It was concluded that the reason for this is their weak coupling to the πN channel. To test this hypothesis it was necessary to look for these resonances in reactions that do not involve πN initial or final state. An extensive dataset of observables in light-meson production, photo-production and electro-production reactions has been accumulated over recent years at facilities worldwide such as the GRenoble Anneau Accelérateur Laser (GRAAL), Jefferson Lab (USA), the ELectron Stretcher Accelerator (ELSA), and the MAInz MIcrotron (MAMI) facility in Europe as well as the 8 GeV Super Photon Ring (SPring-8) in Japan hosting the Laser Electron Photon Experiment (LEPS). The datasets include cross section data and

polarization observables for a large variety of final states, such as πN , ηN , ωN , $\pi\pi N$, $K\Lambda$, $K\Sigma$, etc [18]. The main goals of the recent experiments are the determination of the excited baryon spectrum and the identification of possible new symmetries in the spectrum.

Baryon resonances properties are obtained from Partial Wave Analysis, which consists in global fits of differential distributions measured in many different exit channels. PWA formalisms have been developed at several places using different techniques to extract nucleon resonance parameters. The SAID (Scattering Analysis Interactive Dial-in) group maintains an extensive database of πN , KN , and NN scattering data as well as data on the electromagnetic production of a single pseudoscalar meson [16]. SAID PWA analysis results include baryon masses and widths and the helicity amplitudes $A_{1/2}$ and $A_{3/2}$. The MAID partial wave analysis group [19] results give predictions for multipoles, amplitudes, cross sections, and polarization observables for photo- and electroproduction in the energy range from the pion threshold up to $W = 2$ GeV. Neither of these two groups treats the double-pion production channels [18]. The Bonn-Gatchina group performs combined analyses of all known data on single and double-meson photon- and pion-induced reactions they reported four new states recently [20]. The Gießen group has studied pion and photon-induced reactions for the final states γN , πN , $\pi\pi N$, ηN and ωN , within a coupled-channel phenomenological Lagrangian approach in the energy region from the pion threshold up to 2 GeV, as well as the strangeness channels $K\Lambda$ and $K\Sigma$.

Today, more pion-induced reactions need to be studied to solve the missing baryon resonances puzzle, but also simply to improve the knowledge of already observed resonances. For instance more precise low-energy data on πN elastic scattering are required for chiral perturbation theory. The available data for double pion production are extremely sparse, precise new data are needed to determine $\pi\Delta$ and ρN couplings. The HADES collaboration has started to provide such data, using the GSI pion beam [21], but there are also existing plans for meson beam facilities at J-PARC [22] or EIC [23].

1.2.3 Exotic Baryons

Quantum chromodynamics (QCD) predicts the existence the of so-called exotic hadrons with more complicated internal structures. The state is exotic in the sense that

the quantum numbers cannot be explained as a system of three quarks, or that it cannot be classified into conventional classifications (octet, decuplet). Exotic mesons may be classified such as glueballs (ggg), hybrids ($q\bar{q}gg$), and four-quark ($qq\bar{q}\bar{q}$) states, and exotic baryons as hybrids ($qqqg$), pentaquarks ($qqqq\bar{q}$) and dibaryons ($qqqqqq$). The last ones have been a hot topic for many experiments and theories since they were predicted by Dyson and Xuong in 1964 [24]. Many models and interpretations have been proposed to explain the structure of dibaryons. Some assume that they are induced through the six-quark compound systems (q^6) like in the Compound Nucleus Model in nuclear physics. In other models they are interpreted as $N\Delta$ or $\Delta\Delta$ resonances bound by a potential [25–32].

Table 1.1 shows the Dyson and Xuong SU(6) based classification and predictions of non-strange dibaryons where the D_{01} corresponds to the deuteron and the virtual NN state D_{10} , the D_{12} and D_{21} correspond to a quasibound $N\Delta$ with mass ≈ 2.15 GeV near the $N\Delta$ threshold and width $\Gamma \approx 0.12$ GeV [33], the D_{03} and D_{30} correspond to a quasibound $\Delta\Delta$ with mass ≈ 2.38 GeV and width $\Gamma \approx 0.70$ GeV.

D_{IJ}	D_{01}	D_{10}	D_{12}	D_{21}	D_{03}	D_{30}
BB'	deuteron	NN	$N\Delta$	ΔN	$\Delta\Delta$	$\Delta\Delta$
SU(3)-flavor	$\bar{10}$	27	27	35	$\bar{10}$	28
M	A	A	A + 6B	A + 6B	A + 10B	A + 10B

TABLE (1.1) Prediction of Dyson and Xuong [24] for a sextet of non-strange dibaryon states based on SU(6) symmetry. The states are denoted by D_{IJ} , where I denotes the isospin and J the total spin of the state. The masses are given by the formula $M = A + B[I(I + 1) + S(S + 1) - 2]$. Identifying A with the NN threshold mass 1878 MeV, the value $B \sim 47$ MeV was derived by assigning $D_{12} \rightarrow d\pi^+$ coupled-channel.

1.2.4 Baryon resonances in the early universe

Figure 1.6 (left) displays the main steps of the evolution of the structure of matter in the universe after the Big Bang (Quark-Gluon Plasma at about 10^{-9} s, formation of the nucleons at 10^{-9} s, of the nuclei at 10^2 s, of the atoms at 300k years). In the first μ s after the Big Bang, the transition from QGP to nucleons occurred, leading to important phenomena such as chiral symmetry breaking, hadron mass generation and confinement. It is thought [35] that the excited hadrons play an important role in this transition, as shown schematically in the phase diagram in Figure 1.6 (right).

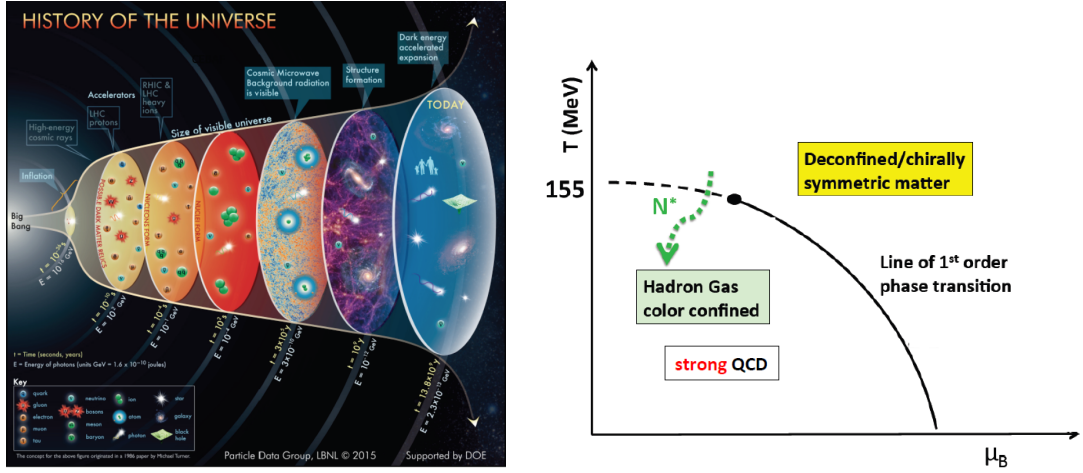


FIGURE (1.6) Left : Scheme of the evolution of the universe after the Big Bang [34]. Right : diagram showing the role of baryonic resonances in the transition between deconfined and confined phase.

1.2.5 "Resonance" matter

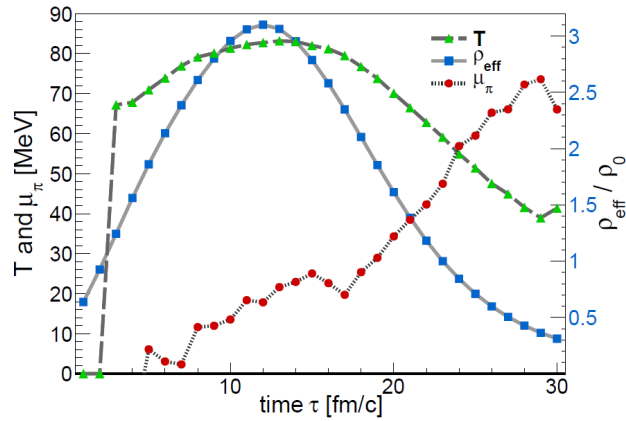


FIGURE (1.7) Evolution of average temperature (green), baryochemical potential (red) and density (blue) as a function of time in a Au+Au collision at an energy of 1.23A GeV in a coarse-grained approach based on the UrQMD transport model [36].

The role of baryonic resonances is even more obvious for the study of baryon-rich matter corresponding to the region of high μ_B of the QCD phase diagram. Such matter can be produced in collisions of heavy ions at energies around 1A GeV and above, where strongly interacting matter is substantially compressed and collective kinetic energy is dissipated into intrinsic degrees of freedom. As a result, nucleons are excited to baryonic resonances which can propagate and regenerate due to their short life time with respect to the long life-time of the dense phase in these collisions (respectively of the order of 1.5 and 15 fm/c). This is illustrated in Figure 1.7 where one can notice that the baryonic density (blue curve) reaches values close to three times the normal nuclear density and

temperatures close to 80 MeV are reached in the Au+Au reaction at 1.23A GeV. A large fraction of these baryons are baryonic resonances.

The open questions motivating the study of dense matter are for example the existence of a critical point in the QCD phase diagram, the nature of the transition between the hadronic and the partonic phase and the existence of exotic phases with mixed properties between the two phases. It is predicted that at SIS18 energies (1-2 AGeV), the fireball produced in heavy-ion collisions spends most of its time in a phase with a substantially reduced chiral condensate, which means that chiral symmetry is partially restored. The study of dense matter is therefore directly related to QCD properties.

The study of dense matter is also attractive due to the existence of dense stellar objects, as neutron stars, with densities up to 10 times the normal nuclear matter density. But moderately hot ($T < 70$ MeV) and dense matter can also be produced in the universe in the collision of compact stellar objects as recently observed thanks to the detection of gravitational waves [37].

1.2.6 Dileptons and vector meson spectral functions

meson	mass (MeV/c ²)	Γ (MeV/c ²)	c_τ (fm)	main decay	branching ratio
ρ	768	152	1.3	$\pi^+\pi^-$	$4.4 \cdot 10^{-5}$
ω	782	8.43	23.4	$\pi^+\pi^-\pi^0$	$7.2 \cdot 10^{-5}$
ϕ	1019	4.43	44.4	K^+K^-	$3.1 \cdot 10^{-4}$

TABLE (1.2) Vector mesons main characteristics

Dilepton measurements are proposed to probe the hot and dense phase of a heavy-ion collision directly. Since dileptons interact only electromagnetically and weakly, they have indeed a mean free path which is much larger than the size of the system. The radiation emitted throughout the collision can therefore be detected, starting from the early hot stage which is not accessible by measuring purely hadronic final states. In addition, they can be used to study the properties of vector mesons (Table 1.2), which have the same quantum numbers as the dileptons ($J^P = 1^-$). However, the small production rates of dileptons are a serious experimental challenge.

The early conjectures of Brown and Rho [38] and Hatsuda and Lee [39] of a decrease of hadron masses related to changes of the quark condensates in the nuclear medium

motivated experimental studies of in-medium masses of the vector mesons (ρ , ω , ϕ). In fact, the connection between chiral quark condensates and hadronic observables is model dependent, although QCD sum rules still provide useful constraints for the integral of the hadron spectral functions. Brown and Rho conjecture of dropping vector meson masses has not been confirmed experimentally and the present measurements of dilepton spectra are rather consistent with the predictions of hadronic models [40, 41] which were developed in the meantime. These models are able to describe the dielectron spectra measured at SPS [41] and RHIC [42] in a wide range of energies in terms of in-medium modifications of the ρ spectral function. The latter is related to the imaginary part of the propagator which is modified in medium due to the dressing of the pions and the coupling to baryons and mesons (see Figures 1.8 and 1.9). These modifications depend on the momentum, but also on the polarization of the vector meson. In addition, the calculations need as inputs the coupling of vector mesons to the baryonic resonances, especially at lower energies, where the hadronic matter is baryon rich. This makes a direct connection between QCD matter studies and baryon spectroscopy.

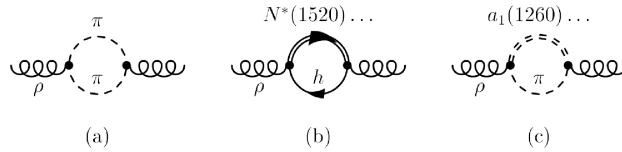


FIGURE (1.8) Dressing of the ρ in the nuclear medium via the 2π propagator (a) the coupling to baryonic resonances (b) and the coupling to mesonic resonances (c).

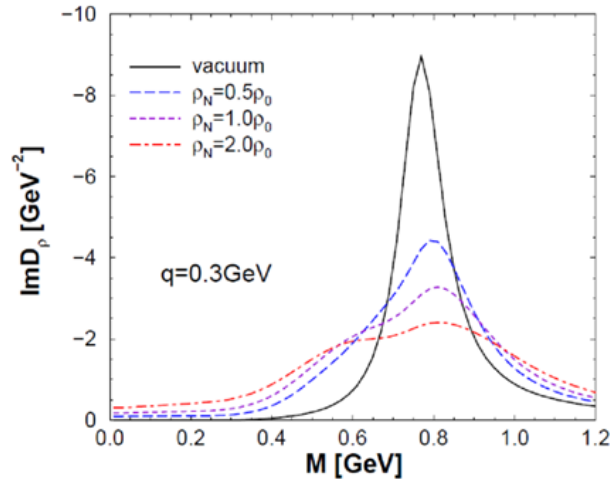


FIGURE (1.9) Imaginary part of the ρ meson propagator (or spectral function) as a function of the mass for different baryon densities [41].

1.2.7 Baryon resonance Dalitz decay and Vector Meson Dominance Model

Dileptons are also unique to study the electromagnetic properties of hadrons in vacuum. Baryonic resonances can emit an e^+e^- pair in the Dalitz decay process : $R \rightarrow Ne^+e^-$. These processes are electromagnetic processes in the time-like region, since the squared four-momentum q^2 of the involved virtual photon has a positive value

$$4m_e^2 < q^2 = M_{ee}^2 < (M_R - M_N)^2 \quad (1.1)$$

where M_{ee} is the invariant mass of the dilepton pair and M_R and M_N are the resonance and nucleon masses respectively. These processes are therefore sensitive to the baryon electromagnetic structure which can be parametrized using form-factors $F(q^2)$ depending on the value of q^2 . As sketched on Figure 1.10, Dalitz decay is complementary to electron scattering experiments, which allow to access the baryon electromagnetic structure in the space-like region ($q^2 < 0$). Dalitz decay probes in fact a limited region of q^2 (Eq. 1.1), but this region is very interesting, due to the vicinity of the vector meson poles. It therefore allows to check the Vector Meson Dominance Model, which is a simple and rather powerful form factor model. The Vector Meson Dominance Model indeed assumes that the coupling of a real (or virtual) photon to the electromagnetic hadronic current is mediated by a vector meson [43], as sketched in Figure 1.11. This makes the coupling of vector mesons to baryons an essential feature of the e^+e^- emission also in vacuum.

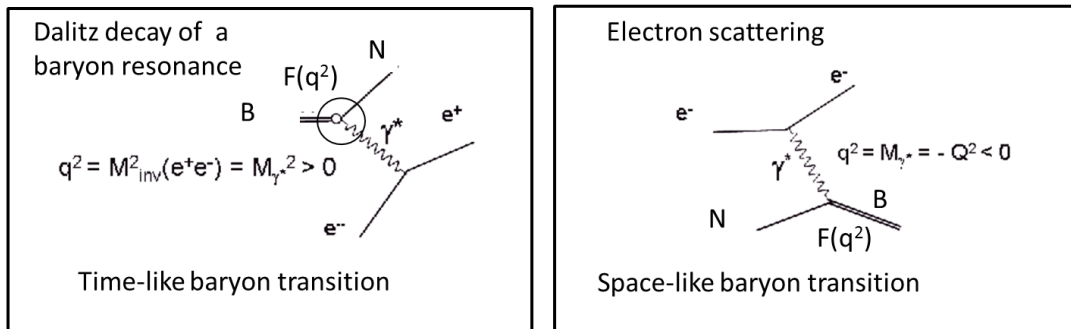


FIGURE (1.10) Left : baryon Dalitz decay gives access to form factors $F(q^2)$ in the time-like region ($q^2 > 0$). Right : electron scattering gives access to form factors in the space-like region ($q^2 < 0$).

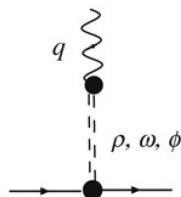


FIGURE (1.11) Sketch of Vector Meson Dominance Model.

1.3 HADES experiments

The High Acceptance Di-Electron Spectrometer (HADES) working at GSI Darmstadt is a unique detector aiming for investigations of dilepton and strangeness production in elementary and heavy ion collisions in the 1-4 AGeV energy range, it also allows for the investigation of hadron properties in nuclear matter and in elementary collisions.

1.3.1 Main motivations

The heavy-ion program of the Relativistic Heavy Ion Collider (RHIC) at BNL and of the Large Hadron Collider (LHC) at CERN concentrates on the study of matter at high temperatures and at small baryochemical potential μ_B . As shown in Figure 1.12 of the phase diagram of QCD matter as a function of temperature and baryochemical potential μ_B , different phases might exist. The transition boundary between confined matter into hadrons and the deconfined quark-gluon plasma remains unknown. Currently, HADES is the only experiment exploring the high baryochemical potential region. With SIS18, a large region in the nuclear matter phase diagram, ranging from ground state matter density ρ_0 up to about $3\rho_0$, can be accessed. Here, the matter in the central reaction volume reaches temperatures $T \leq 80$ MeV without reaching the QGP phase boundary [44]. To learn more about the microscopic structure of matter in the region of high baryochemical potential HADES pursues a strategy, which relies on systematic measurements of strangeness production and virtual photon emission in heavy-ion collisions, as well as complementary non-strange meson production measurements. Particles containing strangeness are of great interest at these energies, due to their steep excitation function, which makes them very sensitive to the conditions reached inside the fireball. As it was shown in [45], particles containing two or more strange particles are even more sensitive to the production and propagation of strangeness inside the medium. In the following, we will focus on the dielectron and pion production measurements.

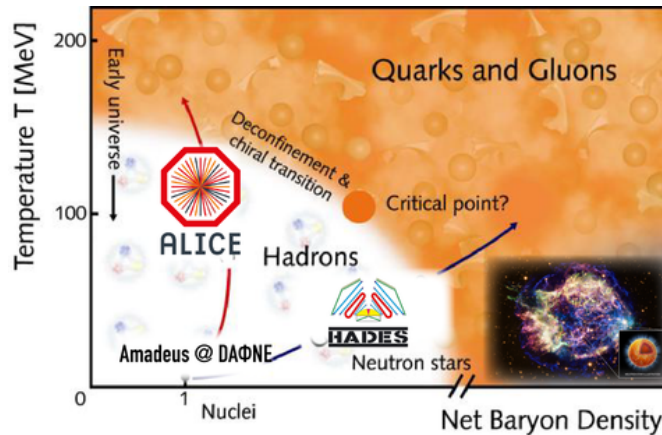


FIGURE (1.12) Schematic representation of the QCD phase diagram. The states of the strongly interacting matter as a function of the temperature T and the baryochemical potential μ_B are shown.

1.3.2 Dilepton spectroscopy in medium

The experimental program of HADES aims at a systematic study of e^+e^- pair production in heavy-ion collisions, in hadron-induced nuclear collisions ($p + A$, $\pi + A$) and in elementary reactions ($\pi + p$, $p + p$, $p + d$). With the range of energies available at GSI (protons up to 4.5 GeV, ions of 1-2A GeV and the possibility to use secondary pion beams), the interest is focused on the invariant mass region up to 1 GeV, with special interest on the vector meson (ρ , ω) properties in nuclear matter. In particular, the ρ meson is considered the ideal probe for in-medium effects due to its even shorter lifetime ($\tau_\rho = 1.3 \text{ fm}/c$) in comparison to the typical lifetime of the fireball ($\sim 10 \text{ fm}/c$) at SIS18 energies, meaning that the ρ meson decays inside the fireball. But medium effects on the ω meson are also present and are reflected in particular in the strong increase of its absorption width.

Dielectron measurements in medium have started with an investigation of the production in $^{12}\text{C} + ^{12}\text{C}$ collisions in 2002 [46, 47]. Ar + KCl collisions were measured in 2005 at 1.756 AGeV beam kinetic energy, [48] followed by Au+Au at 1.23A GeV [49] and very recently Ag+Ag at 1.65 GeV. p+Nb at 3.5 GeV [50] and $\pi + C$ at an incident pion momentum close to 0.7 GeV/c have also been measured to quantify the effects in cold nuclear matter.

1.3.3 Dilepton spectroscopy in elementary reactions

In addition to the heavy ion program, it is necessary to carry out studies of elementary NN or $N\pi$ reactions. A fundamental property of these reactions is that they do not produce a medium that can influence the structure of the hadrons via density and/or temperature effects. Such measurements are therefore used to provide model-independent reference spectra for studies of proton-nucleus or nucleus-nucleus collisions. They also provide important constraints on the contributions of various e^+e^- sources, in particular, via the measurement of exclusive channels.

The NN experiments, which have been performed with the HADES spectrometer, are listed below :

- $p + p$, $p + n$ and $d + p$ at $E_{kin} = 1.25$ GeV. These reactions have been studied for a better understanding of the contribution of Δ -Dalitz decay and NN bremsstrahlung processes to dielectron production in heavy-ion collisions [51, 52].
- $p + p$ at $E_{kin} = 2.2$ GeV. The reaction $pp \rightarrow pp\eta$ has been studied via an exclusive reconstruction of the hadronic and the dielectron decay channels [53, 54]. An inclusive measurement has been done in order to compare the dielectron spectra with $^{12}C + ^{12}C$ at 2.0 GeV [55].
- $p + p$ at $E_{kin} = 3.5$ GeV. The production of η , ω [56] and ϕ [57] mesons production was studied. Differential cross sections of light mesons are needed by theoretical models to describe the e^+e^- invariant mass spectrum, they also provide valuable information about the nature of the nucleon-nucleon interaction. One-pion production was achieved allowing for an estimate of individual baryon resonance production cross sections which are used as input to calculate the dielectron yields from $R \rightarrow pe^+e^-$. This will be discussed in more details in Sec. 1.4.3
- $\pi^- + p$ at $\sqrt{s} = 1.49$ GeV. The baryon resonances Dalitz decay in the region of the $N(1520)$ resonance and the off-shell ρ meson contribution to the dilepton production was studied [58].

1.4 One pion production in NN reactions with HADES

As mentioned above, for the dielectron production, the HADES elementary reaction program is used as a reference to the heavy ion program. But a detailed description of the

resonance excitation and their subsequent decays to pseudo-scalar and vector mesons is important for the interpretation of the elementary di-electron spectra. Baryon resonance production in NN collisions can be determined by the investigation of one-pion, two-pion or η production as a function of the excitation energy. This goal has been addressed by the HADES Collaboration in experiments with a proton kinetic beam energy of 1.25 GeV, 2.2 GeV, and 3.5 GeV and deuteron beam energy of 1.25 GeV/nucleon. We will present below some results obtained for the one pion production.

1.4.1 pp collisions at $T = 1.25$ GeV

The first HADES experiment in the NN collisions program was the pp collision at $\sqrt{s} = 2.42$ GeV, *i.e.* below the η meson production threshold in order to favor the $\Delta(1232)$ production. Two channels were studied, $pp \rightarrow pp\pi^0$ and $pp \rightarrow n\pi^+$ [52, 59], by implementing the resonance model by Teis *et al.* [60] in the framework of the PLUTO event generator [61] and the angular distribution parametrization of OPE (One Pion Exchange) model [62]. The Teis model is a well known reference, as it is the basis of several transport models. Figure 1.13 shows the $p\pi^+$ (left), $n\pi^+$ (middle), $p\pi^0$ (right) invariant mass distributions compared to the initial resonance model (A), one can clearly see that the model does not describe well the data. After the pn Final State Interaction (FSI) was implemented and the pion cut-off parameter was corrected ($\Lambda_\pi = 0.75$) the modified resonance model (B) described better the data. This was a first example of the sensitivity of HADES data and their capacity to improve models used for the production of dielectron in heavy-ion experiments.

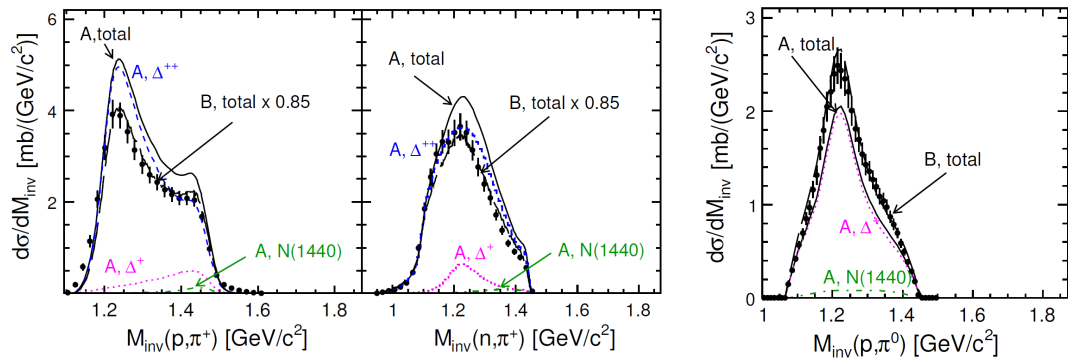


FIGURE (1.13) $p\pi^+$ (left), $n\pi^+$ (middle), $p\pi^0$ (right) invariant mass distributions compared to the resonance model (A) and the modified resonance model (B) [52]

In view of the limitations of the resonance model (does not include interferences effects, it is not sensitive to non resonant contributions), a partial wave analysis was done in collaboration with the Bonn-Gatchina group. Figure 1.14 shows $p\pi^+$ (left), $n\pi^+$ (middle), $p\pi^0$ (right) invariant mass distributions compared to PWA solution (solid black), the $\Delta(1232)$ contribution (short-dashed red) and the $N(1440)$ contribution (long-dashed blue). A detailed study of various observables indicates that the partial wave solution provides not only a better control of the underlying physics but also a better description of experimental data. The pp collisions are essentially described by two leading contributions, π^0 and $\Delta(1232)$ Dalitz decays. The results of Δ production were used for the interpretation of the $pp \rightarrow ppe^+e^-$ channel, and allowed to extract, for the first time, the branching ratio of the Δ Dalitz decay ($4.19 \pm 0.62 \times 10^{-5}$) [63].

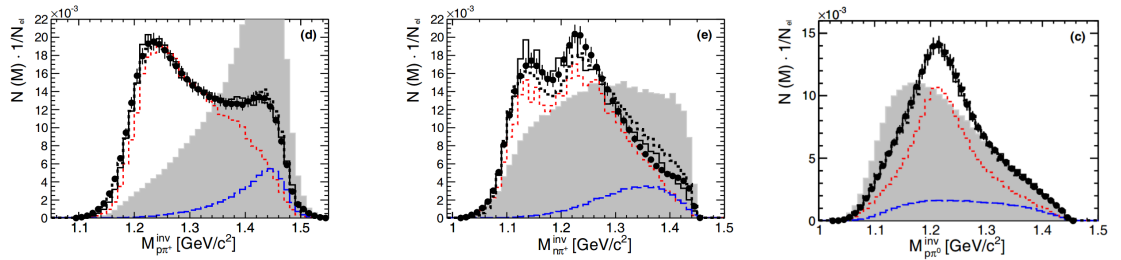


FIGURE (1.14) $p\pi^+$ (left), $n\pi^+$ (middle), $p\pi^0$ (right) invariant mass distributions compared to PWA solution (solid black), the $\Delta(1232)$ contribution (short-dashed red) and the $N(1440)$ contribution (long-dashed blue) [59].

1.4.2 pp collisions at $T = 2.2$ GeV

The exclusive hadronic channels $pp \rightarrow pp\pi^0$, $pp \rightarrow np\pi^+$ and $pp \rightarrow pp\eta$ from the pp reaction at $\sqrt{s} = 2.765$ GeV were identified with high statistics and studied in various differential distributions within the resonance model by Teis *et al.* [60]. Like in pp collisions at 1.25 GeV, the main contributing resonances are the $\Delta(1232)$ and $N(1440)$, but also higher lying resonances, mainly $N(1520)$ and $N(1535)$, play a role [64]. Figure 1.15 shows the $p\pi^0$, $p\pi^+$, $n\pi^+$ invariant mass distributions compared to the resonance model contribution (model A). The cross sections of $N(1440)$, $N(1520)$ and $N(1535)$ were increased and a non-resonant contribution, generated with a phase space distribution, was added (model B). A better description of the invariant mass distributions was obtained.

The studies of the various contributions of the model, compared to the data allowed to determine resonance cross sections on one-pion and one η production. These constraints were used for modeling the dielectron sources [64].

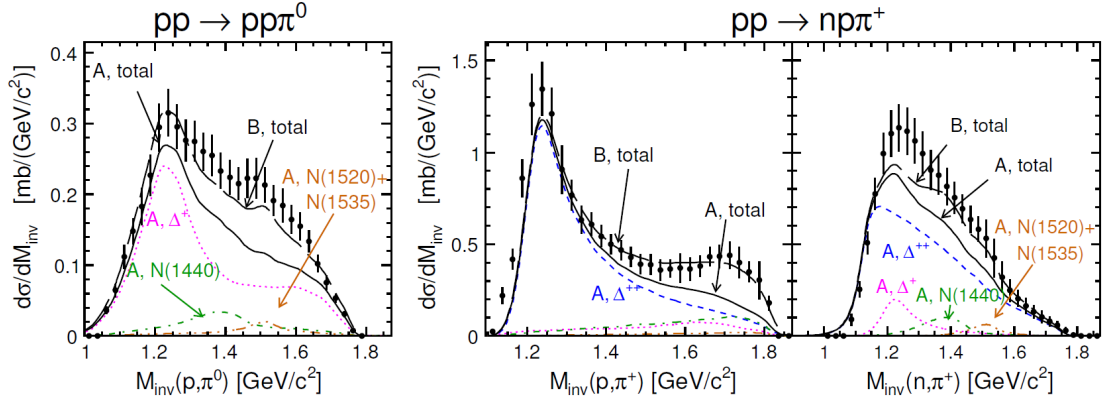


FIGURE (1.15) $p\pi^0$ (left), $p\pi^+$ (middle), $n\pi^+$ (right) invariant mass distributions compared to the resonance model contribution (model A), with contributions of $\Delta^{++}(1232)$ (dashed blue), $\Delta^+(1232)$ (dotted magenta), $N(1440)$ (dashed-dotted green), and the sum of $N(1520)$ and $N(1535)$ (solid brown). The long-dashed black curve, denoted as model B, results from the yield of N^* resonance adjustment and a small non-resonant admixture (not in the figure) [64].

1.4.3 pp collisions at $T = 3.5$ GeV

The HADES collaboration also measured the pp collision at the kinetic beam energy of 3.5 GeV. Two channels with one pion production were selected : $pp \rightarrow pp\pi^+$ and $pp \rightarrow pp\pi^0$, the analysis focused on baryon resonance excitation and decay to πN [65]. The simulations were performed by means of the PLUTO event generator [61]. A resonance cocktail model assuming that the total production cross section is given by the incoherent sum of all the baryon resonance contributions was implemented. All four-star resonances used by Teis *et al.* [60] were included. The resonances production cross sections were treated in the simulations as free parameters, and they were identified by means of the πN invariant mass distributions only. The Δ^{++} resonances were observed as peaks in the $p\pi^+$ invariant mass distribution and the Δ^+ and N^+ resonances were observed as peaks in the $n\pi^+$ and $p\pi^0$ invariant mass distributions. Figure 1.16 shows the $p\pi^0$, $p\pi^+$ and $n\pi^+$ invariant mass distributions from the one pion analysis compared to the result of simulations (dashed curve). A very good agreement between simulation and the data was achieved for these reaction channels.

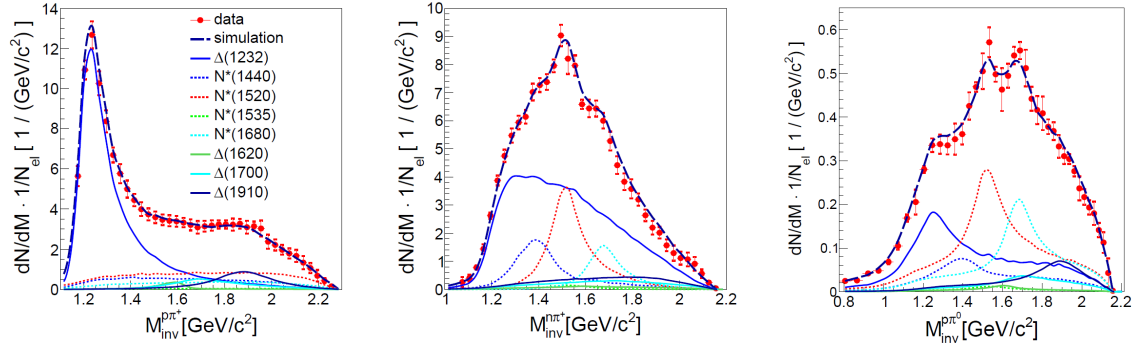


FIGURE (1.16) $p\pi^+$ (left), $n\pi^+$ (middle), $p\pi^0$ (right) invariant mass distributions from the one pion analysis compared to the result of simulations (dashed curve) [65].

The baryonic resonance contributions deduced from the one pion production channels were used as an input for the analysis of the exclusive dilepton channel $pp \rightarrow ppe^+e^-$. For each baryon, the Dalitz decay differential distributions as a function of the e^+e^- invariant mass was calculated, in the "QED" (or point-like) assumption, i.e. the form factors were deduced from the radiative decay width and their dependence as a function of $q^2 = M_{ee}^2$ was neglected [66, 67]. Figure 1.17 (a) shows the e^+e^- invariant mass distribution compared to the result of the simulations of e^+e^- production from the cocktail of baryons in the "QED" model. The peak around the vector meson pole mass is due to the ω contribution, which is also added to the simulation. An excess of the experimental yield is clearly visible below the vector meson pole. This is, however, not a surprise because one expects contributions from off-shell couplings of the resonances to the vector mesons. It is expected that such couplings modify the respective eTFF (electromagnetic Time-like Form Factor) which were assumed to be constant in the simulations. The dielectron production through the resonance decay can be factorized as a two step process, proceeding through the intermediate ρ -meson production, $R \rightarrow p\rho \rightarrow pe^+e^-$. This scheme is used in transport models. However, the calculated dielectron yield in the transport models calculations depends strongly on the $R \rightarrow p\rho$ which is relatively high compared to the new results from partial wave analysis. Also the cross sections for resonance in transport models are higher than the cross sections derived from the HADES one pion analysis. Figure 1.17 (b) shows the e^+e^- invariant mass distribution compared to simulations based on the input from GiBUU [68] (solid curve). If the cross sections extracted from the HADES simulations and the $R \rightarrow N\rho$ branching ratios from Bonn-Gatchina PWA [20] are taken (modell1), the calculation reproduces the measured yield better. Therefore, once the baryon resonance contribution is adjusted using the results of the one pion production and the coupling to the $N\rho$ channel are taken from

the most recent PWA analysis, the e^+e^- production is found to be in agreement with the Vector Meson Dominance Model. This illustrates the sensitivity of the dilepton production to these ingredients and the interest of pion production data to fix the resonance contribution. HADES data recently measured in the $\pi^-p \rightarrow \pi N$ are used in the most recent Bonn-Gatchina PWA to improve the precision on the determination of baryonic resonance couplings to $N\rho$ [21].

Another example of transport model predictions is given by the SMASH model (see Figure 1.18) [69, 70]). Here, the data are shown for the inclusive e^+e^- production in the pp reaction at 3.5 GeV and the model includes an η contribution.

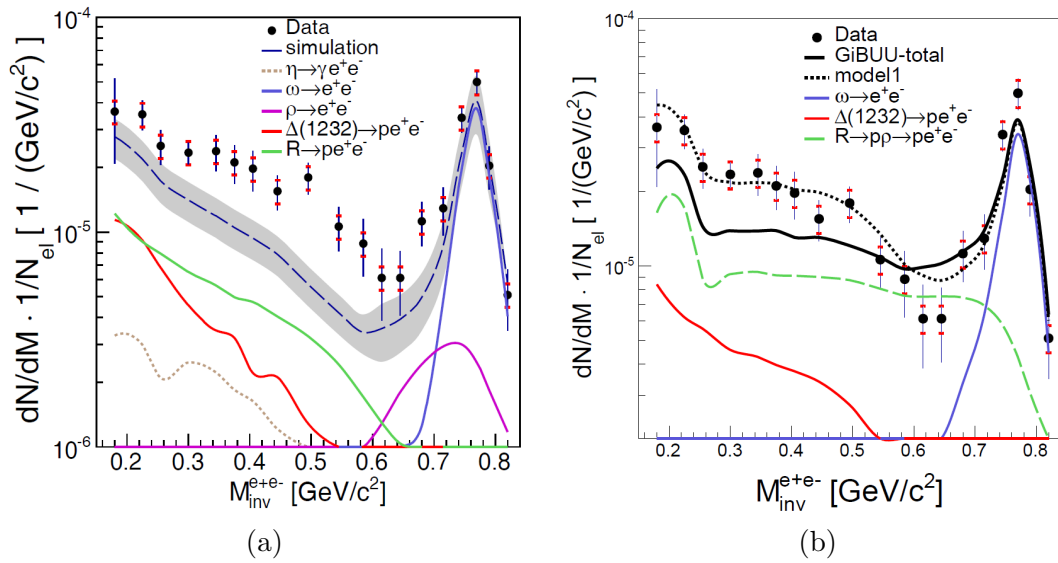


FIGURE (1.17) e^+e^- invariant mass distribution, (a) compared to the simulation result assuming a point-like $RN\gamma^*$ coupling (QED-model). The hatched area indicates the model errors [65]. (b) compared to simulations based on the input from GiBUU (solid curve). Dotted curves show results of calculations using modified cross sections and $R \rightarrow N\rho$ branching ratios from Bonn-Gatchina PWA [20].

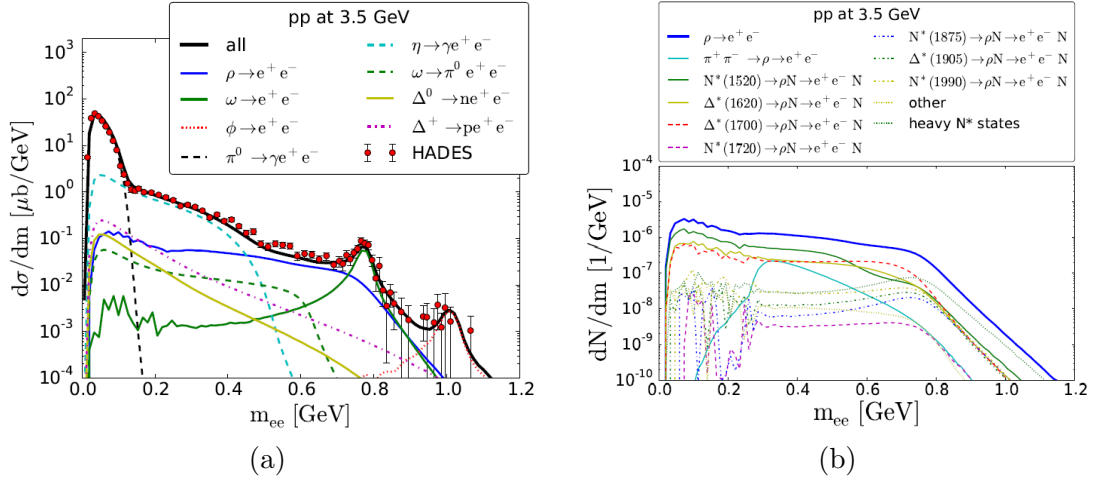


FIGURE (1.18) e^+e^- invariant mass distribution in pp collision at $T = 3.5$ GeV compared to SMASH model calculation. (a) All contributions. (b) resonances contributing to the dielectron production through the decay $R \rightarrow N\rho \rightarrow Ne^+e^-$ [70].

1.5 Double pion production in nucleon-nucleon reactions

1.5.1 Motivations

Two-pion production can bring additional information to the single pion production. As mentioned in section 1.2.2, the double pion production in pion or photon induced reactions is of special interest in view of studying the baryon excitation spectrum. In nucleon-nucleon reactions, the focus is put on studying the various production mechanisms of a two pion pair, via decay of one or two baryonic resonances or one meson. Since the single pion production is rather well known, the double pion production can be considered as a key process towards a better understanding of mechanisms which contribute to meson and dilepton production, either directly or via excitation of baryonic resonances.

In addition to the study of the decay of baryons in the $\pi\pi N$ channel, the $NN \rightarrow NN\pi\pi$ reaction allows for the study of the double resonance excitation, where each resonance decays in the πN channel. These channels are very badly known and since the double resonance excitation is also a possible source of dileptons, via the Dalitz decay of one of the resonances, it is important to have information on these processes.

Moreover, with two pions in the isospin 1 channel, the $NN \rightarrow NN\pi\pi$ reaction allows to study the production of the ρ meson and to disentangle the direct production from the production via baryonic resonances. As mentioned above, the coupling of baryonic

resonances are of high interest for a better understanding of the dilepton production in nucleon-nucleon reactions and also in nuclear matter due to the expected modifications of the ρ meson spectral functions. The production of other mesons decaying to 2π ($f_0(500)$, $f_0(980), \dots$) can also be investigated.

Finally, the two-pion production in NN collisions is also interesting for the check of existence of dibaryon resonances, which can decay, either to the $NN\pi\pi$ or to the $NN\pi$ channels.

All the above-mentioned reasons motivated the analysis of the $pp \rightarrow pp\pi^+\pi^-$ channel measured with the HADES spectrometer at GSI at an incident proton energy of 3.5 GeV

1.5.2 Existing measurements

Investigations of the double pion production in pp reactions started very early using bubble-chambers [71–75]. Most of these reactions recorded low statistics and could mostly only provide total cross sections. Recently, precise measurements of differential distributions were performed in the $pp \rightarrow pp\pi\pi$ reaction from near threshold up to $T_p = 2.2$ GeV [76, 77]. In particular the $pp \rightarrow pp\pi^+\pi^-$ reaction was measured at CELSIUS [78–81], COSY [82–84], KEK [85] and PNPI-Gatchina [86] facilities from threshold up to 1.4 GeV. The WASA collaboration also measured the $pp \rightarrow pp\pi^0\pi^0$ reaction at 1.4 GeV and $pp \rightarrow nn\pi^+\pi^+$ at 1.1 GeV. For a detailed understanding of the reaction mechanisms, it is useful to have measurements of all possible isospin channels. Two-pion production in the pn reactions has also been recently investigated in various channels at energies up to 1.5 GeV with WASA at COSY (see [87] and references therein), at Dubna [88] and with HADES, as will be discussed below in more details.

1.5.3 Theoretical developments for $NN \rightarrow NN\pi\pi$

On the theoretical side, several phenomenological models (Valencia [89], Cao *et al.* [90], modified Valencia [76] and OPER [91, 92]) have been suggested to study the double pion production in NN collisions from threshold to few GeV. Valencia and Cao *et al.* models are both Lagrangian models, while the OPER model is based on pion exchange and uses pion-nucleon amplitudes determined experimentally. More details will be given in Chapter 8 on the Cao *et al.* and OPER models which are used in this work. The

Valencia model includes contributions from $\Delta(1232)$, $N(1440)$ and $N(1520)$ resonances only. It is therefore limited to energies below 1.4 GeV and can not be used in our analysis.

1.5.4 HADES results in the $np \rightarrow np\pi^+\pi^-$ reaction at 1.25 GeV

The np interactions were studied by HADES using deuteron-proton (dp) collisions with a deuteron incident beam energy of 1.25 GeV/nucleon. The spectator proton was detected in a wall of scintillators covering small laboratory angles. The invariant mass and angular distributions were compared with three different models : the modified Valencia [93], the Cao [90], and OPER model [91].

Figure 1.19 shows the $\pi^+\pi^-$, $p\pi^-$, $p\pi^+$, $p\pi^+\pi^-$ invariant mass distributions compared to the theoretical predictions within the HADES acceptance are from OPER (solid curve), Cao (dashed curve), and modified Valencia model (long-dashed curve). The total yield was normalized to the data. The grey area shows the phase space distributions. The measured differential cross section integrated over the HADES acceptance was larger by a factor more than 2 in Cao model compared to the data, while the modified Valencia model was in better agreement. The results confirmed the dominance of the t-channel $N(1440)$ and the double $\Delta(1232)$ excitation, the contribution of a s-channel process, with an intermediate dibaryon resonance, with mass $M \sim 2.38$ GeV and width $\Gamma \sim 70$ MeV, as observed by the WASA collaboration in the reaction $pn \rightarrow d\pi^+\pi^-$ [94]. One can also add that the OPER and modified Valencia model gave the best predictions for the differential cross sections. The comparison with the Cao model demonstrated a too large $N(1440)$ contribution.

1.5.5 WASA results for the $pp \rightarrow pp\pi^+\pi^-$ reaction

The WASA collaboration developed an extensive program of measurements in the $NN \rightarrow NN\pi\pi$ and $pn \rightarrow d\pi\pi$ reactions. After the observation of the dibaryon with $I(J^P) = 0(3^+)$ in the $pn \rightarrow d\pi^0\pi^0$ reaction, as shown in Figure 1.20 [87, 96, 97], this program was focused on the search for signals of this dibaryon in other reaction channels. The subsequent measurements of the double pion channels : $pn \rightarrow d\pi^+\pi^-$ [98], $pn \rightarrow pp\pi^0\pi^-$ [99], $pn \rightarrow pn\pi^0\pi^0$ [100] and $pn \rightarrow pn\pi^+\pi^-$ [95, 101] revealed that all these reaction channels exhibit a signal of this resonance called now $d^*(2380)$.

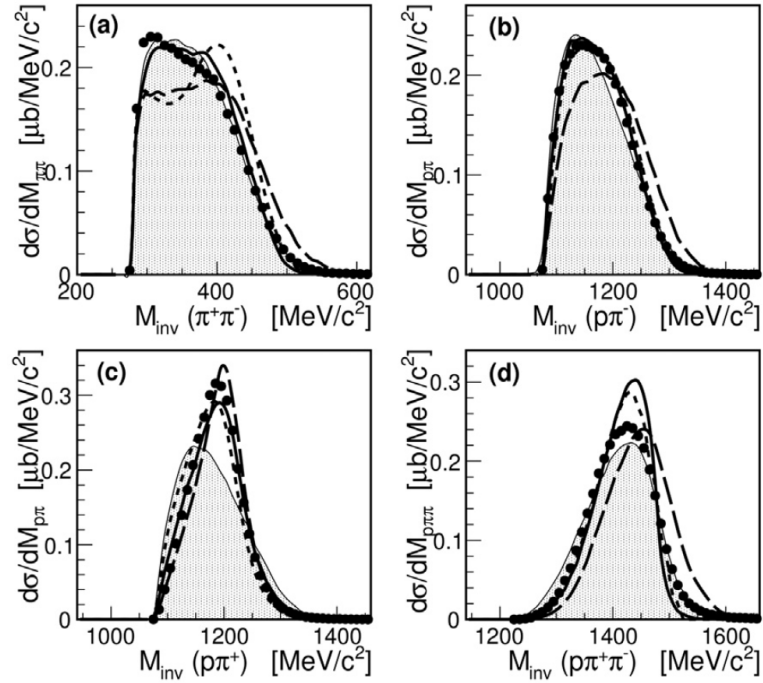


FIGURE (1.19) (a) $\pi^+\pi^-$, (b) $p\pi^-$, (c) $p\pi^+$, (d) $p\pi^+\pi^-$ invariant mass distributions for the $np \rightarrow np\pi^+\pi^-$ reaction at 1.25 GeV. The experimental data are shown by solid symbols. The theoretical predictions within HADES acceptance from OPER [91] Cao [90] and modified Valencia models [93] are given by the solid, dashed and long-dashed curves, respectively. The shaded areas show the phase-space distributions [95].

The dibaryon D_{21} on the other hand strongly favors the channel $pp\pi^+$ in its decay, as suggested by Dyson and Xuong [24], the favored production process should then be in the $pp \rightarrow pp\pi^+\pi^-$ reaction channel. Indeed, this was reported recently by the WASA collaboration, by exploiting the quasi-free scattering process $pd \rightarrow pp\pi^+\pi^- + n_{spectator}$, covering the energy region $T_p = 1.08$ -1.36 GeV. Both the differential distributions and total cross section in dependence of the incident proton energy are in agreement with predictions of a model based on the modified Valencia model [93] plus the dibaryon D_{21} resonance production according to the process $pp \rightarrow D_{21}^{++}\pi^- \rightarrow pp\pi^+\pi^-$ as shown in Figure 1.21 (solid line) [102, 103].

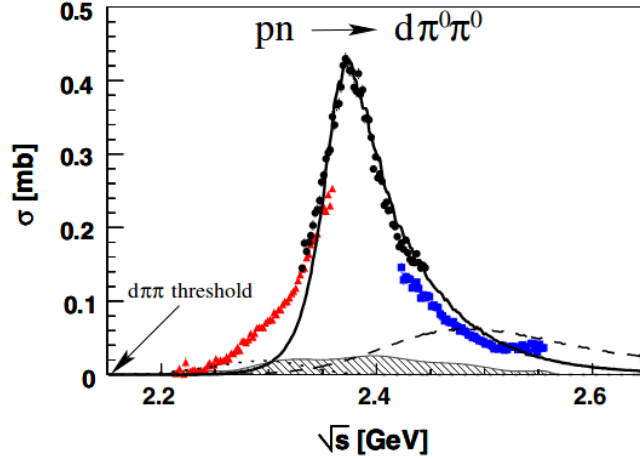


FIGURE (1.20) Total cross sections obtained from $pn \rightarrow d\pi^0\pi^0 + p_{spectator}$ for the beam energies $T_p = 1.0$ GeV (red triangles), 1.2 GeV (black dots), and 1.4 GeV (blue squares). The hatched area indicates systematic uncertainties. The drawn lines represent the expected cross sections for the $N(1440)$ excitation process (dotted) and the t-channel $\Delta\Delta$ contribution (dashed) as well as a calculation for a s-channel resonance with $M = 2.37$ GeV and $\Gamma = 68$ MeV (solid) [97].

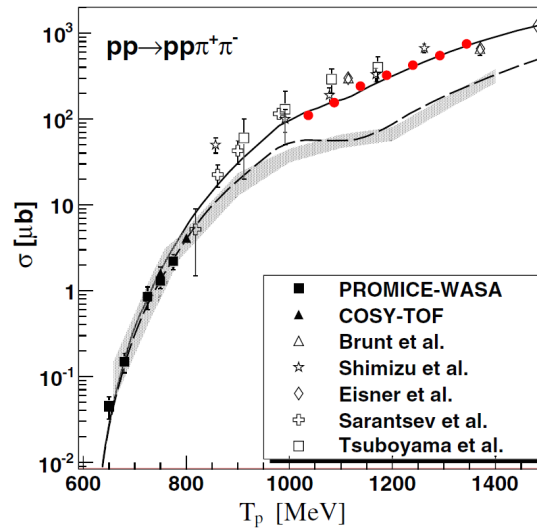


FIGURE (1.21) Total cross section as function of the incident proton energy T_p for the reaction $pp \rightarrow pp\pi^+\pi^-$. The solid red dots show results from WASA collaboration [102, 103]. Other symbols denote results from previous measurements [72, 73, 75, 78, 80–82, 85, 86]. The shaded band displays the isospin-based prediction. The dashed line gives the modified Valencia calculation [93]. The solid line is obtained, if a D_{21} resonance is added with a strength fitted to the total cross section data.

2

HADES detector

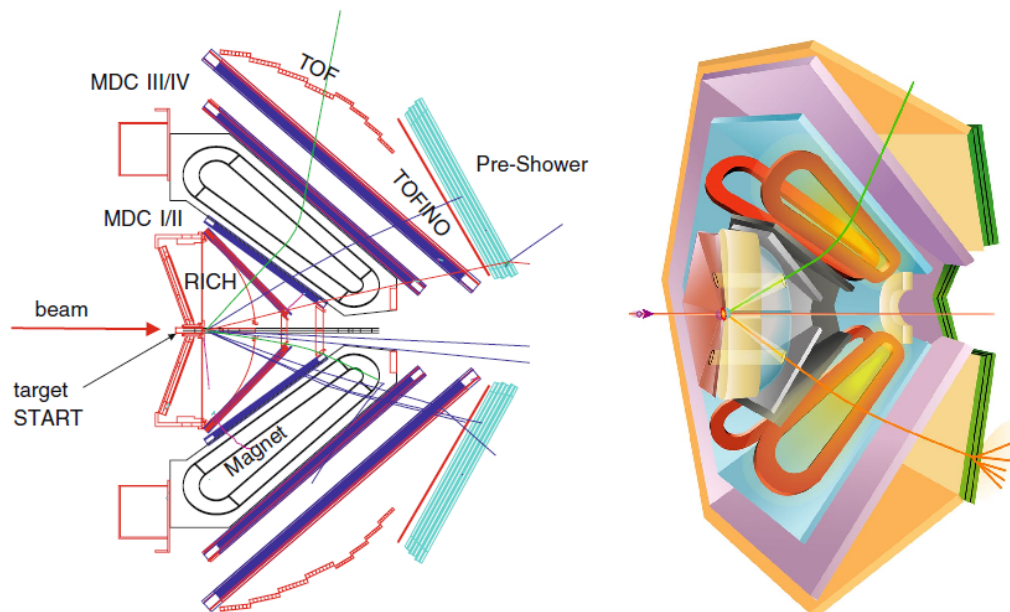


FIGURE (2.1) Left : Side view of the HADES setup. Right : The HADES spectrometer in a 3D view

The HADES (High Acceptance Di-Electron Spectrometer) experiment, is a fixed target experiment installed at the heavy-ion synchrotron SIS-18 at GSI. It was designed for the identification and invariant mass reconstruction of electron-positron pairs (e^+e^-). The main emphasis is the study of leptonic (e^+e^-) decays of light vector mesons in elementary and in heavy-ion collisions. These decays are suppressed by a factor 10^{-5} compared to hadronic decay channels, thus in order to accumulate significant statistics in a reasonable amount of time, HADES has to fulfill several conditions [104] :

- Large geometrical acceptance : to achieve good pair detection probability.
- High rate capabilities : due to the rarity of the interesting channels, the beam intensity is 10^7 particles/s.
- Trigger system : a trigger hierarchy scheme is required to find and combine the electron signatures in the various sub-detectors and to reduce the huge background created mainly by γ conversion in the detector's material or in the target.
- High granularity : in order to deal with high particles multiplicities expected in heavy-ion collision systems.
- High lepton invariant-mass resolution : in order to detect the modification of experimentally observable properties of vector mesons such as mass and width, when embedded in a dense medium. An invariant mass resolution for dileptons of 2-3% in the ρ and ω meson mass range is required to distinguish possible in-medium effects.

In order to fulfill the above requirements, the HADES spectrometer has several different specialized detectors. The spectrometer, in Fig. 2.1, is characterized by a six-fold azimuthal geometry. The polar acceptance covers from 15° to 85° , while including almost the full azimuthal acceptance [104], [105]. The HADES detector is divided into sub-detectors. Moving from the target to the direction of a typical particle trajectory, the detector consists of :

- Ring Imaging Cherenkov (RICH) detector.
- Two inner planes of Multi-wire Drift Chambers (MDCs).
- Toroidal magnetic field generated by six superconducting coils.
- Two outer planes of MDCs.
- Multiplicity Electron Trigger Array (META) ; it consists of two Time-of-Flight walls (TOF/TOFino), the first with high granularity and the second with low granularity and the Pre-Shower detector, which is placed behind the TOFino at small polar angles.

2.1 Target



FIGURE (2.2) LH₂ target used to study elementary processes [104].

For elementary interactions a liquid hydrogen (LH₂) target was used. It has been developed at IPN¹ (see Fig. 2.2). The liquid hydrogen is contained inside a cylindrical vessel (inner-vessel), 5 cm long with a diameter of 2.50 cm, covered by an aluminized Mylar foil (6 μm thick). An outer-vessel provides low interaction probabilities due to its low atomic number (Z) and provides thermal isolation to the inner-vessel, which operates at a temperature of 20 K at atmospheric pressure. The forward end cap of this cylindrical carbon fiber cylinder is also made out of a 100 μm thick Mylar foil. The system operates in vacuum. The interaction probability between beam and the window material is of the order of $\approx 0.05\%$ while the probability of interaction with the LH₂ is around 0.7% [104]. The cooling down from room temperature takes 12 hours. The cryogenic operation is controlled by a dedicated software interface.

2.2 The Ring Imaging Cherenkov detector

The Ring Imaging Cherenkov detector (RICH), shown in Fig. 2.3, is the innermost detector and surrounds the target region. It has been designed to identify electrons and positrons with momenta in the range $0.1 \text{ GeV} < p < 1.5 \text{ GeV}$. It covers the polar angle

1. Institut de physique nucléaire d'Orsay

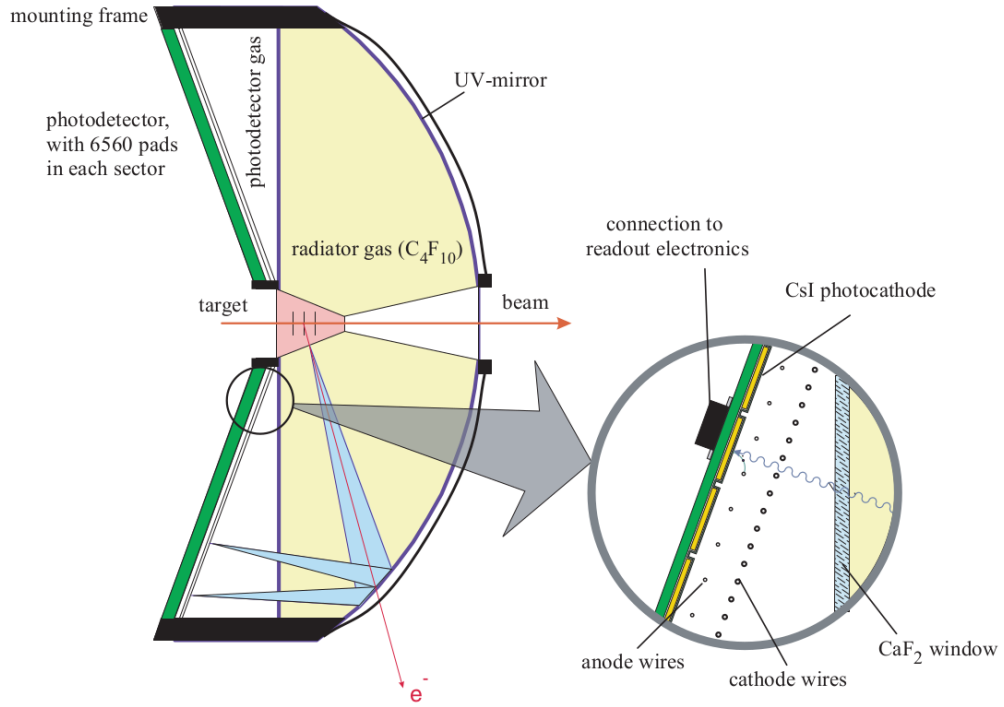


FIGURE (2.3) Schematic layout of the RICH, consisting of a Carbon shell mirror, a CaF_2 window and a photon detector.

between 18° and 85° and the full azimuthal angle [106].

When a charged particle passes through a medium with refraction index n , and its velocity β is larger than the speed of light in the medium (c/n), then a Cherenkov light is emitted at a constant opening angle θ with respect to the particle trajectory :

$$\cos\theta = \frac{1}{n\beta}$$

$$\gamma = \frac{1}{\sqrt{1-\beta^2}} \quad (2.1)$$

where β is the velocity of the particle and γ is the Lorentz factor. Hence, the particle is identified if $\beta \geq c/n$.

The radiator gas (C_4F_{10}) has a refraction index of $n = 1.00151$, which corresponds to a threshold of $\gamma \approx 18.3$. Therefore, only particles with velocity $\beta > 0.9985$ produce Cherenkov light, ensuring the hadron blindness of the detector. The minimum particle energies needed to emit Cherenkov light are $E^p \simeq 17.8$ GeV for protons, $E^\pi \simeq 2.6$ GeV for pions and for electrons $E^e \simeq 9.3$ MeV, which is far below the energy of interest. At the energies available with the SIS accelerator, the hadrons reach a γ_{max} of about 10. The estimated γ implies the hadron blindness of the detector. Hence, only electrons can

be detected in the energy of interest of the HADES physics. Electrons and positrons have a β value close to 1, and the light cone is generated along their track in the radiator.

2.3 The Multi-wire Drift Chambers

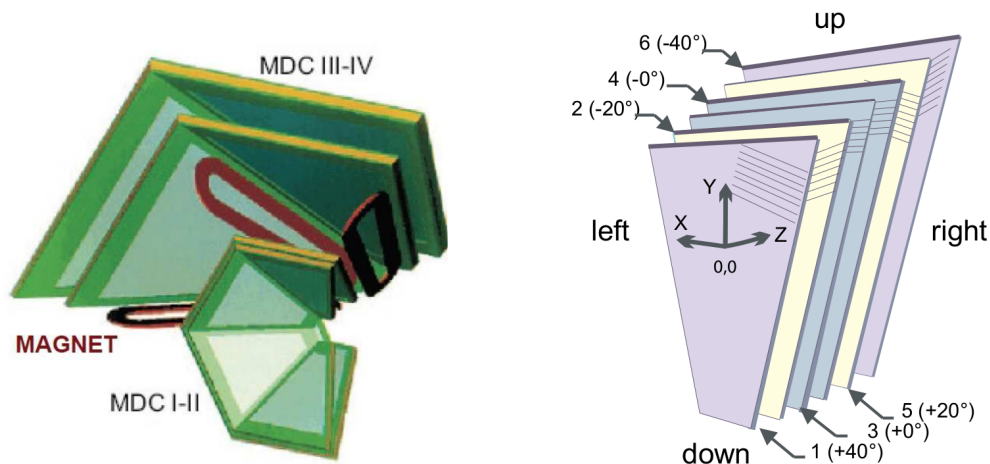


FIGURE (2.4) Schematic layout of the HADES tracking system. Left : Arrangement of the MDC chamber with respect to the magnetic coils. Right : View of the six anode wire frames inside a HADES MDC, with the respective wire angles.

In HADES the dielectron decay channel defines the decisive design and performance constraints on the Multi-wire Drift Chambers (MDCs). They consist of 24 trapezoidal planar MDCs, symmetrically arranged in six identical sectors. They provide a polar angle coverage between 18° and 85° around the beam axis, forming four tracking planes (I-IV) of increasing size. In each sector, two modules (planes I and II) are located in front of and two (planes III and IV) behind the toroidal magnetic field, in order to determine the direction of the particle track before and after the deflection in the magnetic field and thus the momentum, as shown in Fig. 2.4 left. The chambers provide active areas from 0.35 m^2 up to 3.2 m^2 and cover the same solid angle per sector.

The main feature of the design and the operation parameters of the chambers is the implementation of the low-mass concept and the position of the active detector area between the six coils of the magnet. These requirements are met by : (1) cathode and field wires made of annealed aluminum (planes I-III : bare, IV : Gold-plated) with $80 \mu\text{m}$ and $100 \mu\text{m}$ diameter, (2) a Helium-based counting gas (Helium :Isobutane = 60 :40) and (3) entrance windows made of $12 \mu\text{m}$ aluminized Mylar [104].

The MDCs are used for the tracking of charged particles and the determination of their momenta, which depend upon their deflection in the magnetic field. To cope with ambiguities (left and right ambiguities), in the track reconstruction in a high multiplicity environment of a heavy ion reaction, all chambers are composed of six sense/field wire layers oriented in five different stereo angles, $\pm 0^\circ$, $\pm 20^\circ$, $\pm 40^\circ$. This is sketched in Fig. 2.4. The essential information which the HADES spectrometer delivers is the invariant mass of dilepton pairs. The tracking system has been optimized for high electron momentum resolution [107]. In order to resolve the various vector mesons, a dilepton invariant-mass resolution of the order of the natural meson's width is required (e.g. $\delta M/M = 2-3\%$). It corresponds to a single particle momentum resolution of $\delta p/p = 1.5\%$.

The field and cathode wires are made of bare aluminum, with diameters of $100\ \mu\text{m}$ and $80\ \mu\text{m}$, respectively. The sense wires are made of gold plated tungsten with a diameter of $20\ \mu\text{m}$. All four chamber types contain about 1100 drift cells each, with increasing size, from $5\times 5\ \text{mm}^2$ (plane I) to $14\times 10\ \text{mm}^2$ (plane IV), in order to maintain the granularity and, therefore, the double hit resolution in the four detector planes, per solid angle. The chambers are filled with Ar-CO₂ mixture.

2.4 The Superconducting Magnet

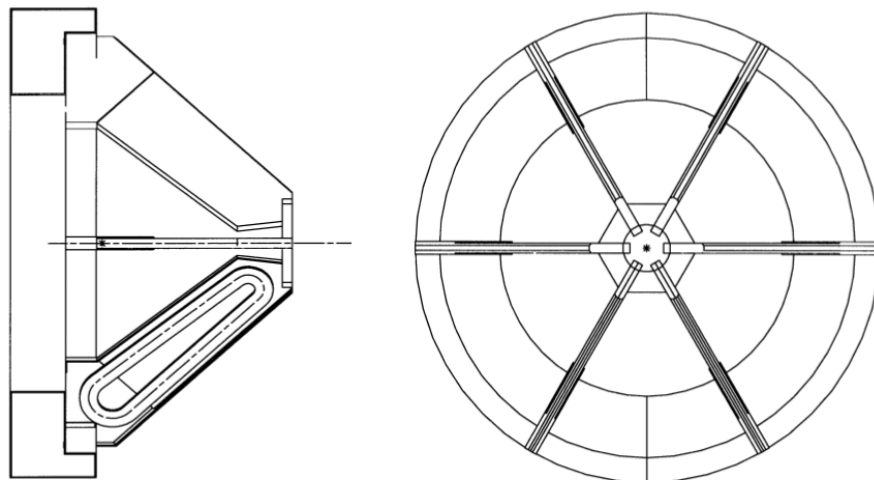


FIGURE (2.5) Left : side view of the magnet. One coil shows a cut at its central plane. Right : front view cut. [104]

The superconducting magnet ILSE (Iron-Less Superconducting Electron magnet) in Fig. 2.5, consists of six superconducting coils, surrounding the beam axis. It generates a toroidal magnetic field. The magnet should fulfill these requirements :

- It deflects charged particles, in order to measure their momenta with sufficient resolution.
- The magnetic field should not be extended up to the neighbor detectors (RICH and MDC).

The magnetic field can reach a maximum intensity of 3.7 T on the coil's surface, but not more than 0.7 T in the HADES acceptance and it is higher at smaller polar angles [104], [108]. The magnet geometry has been chosen in order to obtain the toroidal field which deflects the particles only in the polar direction θ . This results in a particle momentum kick of the order of $p_T = 50$ MeV at large polar angles and $p_T = 100$ MeV at smaller polar angles.

2.5 The Multiplicity Electron Trigger Array

The Multiplicity Electron Trigger Array (META) is positioned behind the outer MDCs. It is used for fast charged particle determination via the time-of-flight between the target and the TOF wall, of each detected particle, performing particle identification : electrons, positrons and hadrons (π , K, p). Since it is a fast detector, it is used for triggering. The META consists of two Time Of Flight detectors (TOF and TOFino) and a Pre-Shower detector covering forward polar angles (18° - 45°).

2.5.1 Time-Of-Flight Detectors : TOF and TOFino

The Time-Of-Flight (TOF) wall was designed to have the following features :

- Charged particle multiplicity determination in each event, thus providing a first level trigger decision and selecting the centrality of the events.
- It provides position information of charged particles.
- Measurement of the time-of-flight of each hitting charged particle in order to distinguish between leptons, protons, pions and kaons.
- Measurement of particle energy loss, which can be used for particle identification.

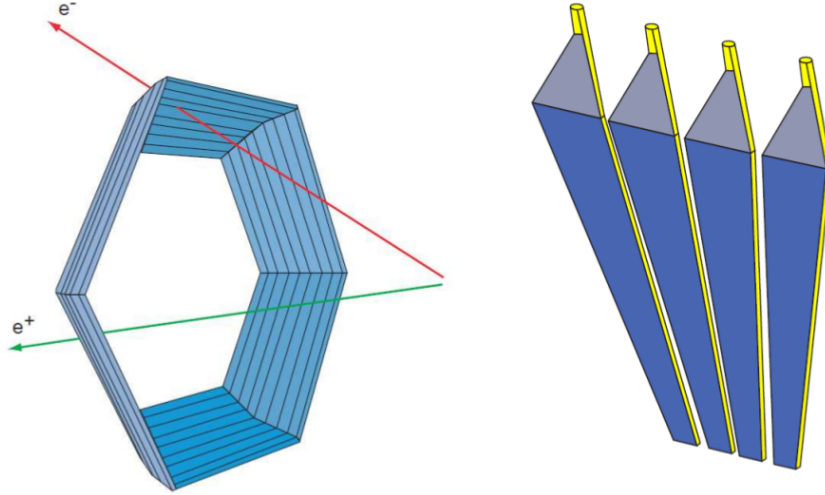


FIGURE (2.6) Schematic view of the Left :TOF and Right :TOFINO detector (one sector only).

For the time-of-flight measurements in the polar angle region from 44° to 88° , the TOF detector is used. Following the hexagonal geometry of the whole spectrometer, the TOF detector is divided into six sectors (left panel of fig.2.6). Each sector consists of 64 scintillator rods (384 rods in total) coupled on both ends to photo-multipliers (PMT). The rod length increases while ranging from the smaller to larger polar angles. This geometry allows to have a finer granularity in the forward polar angle region, where the multiplicity of produced charged particles is higher, to reduce the probability that two particles hit the same rod. The time resolution is about 150 ps.

From the measured signals the following information can be extracted : the time-of-flight (t_{tof}) of particles corresponding to the time between the reaction and the readout of the signal, the hit position on the rod (x), and the energy deposited in the rod (ΔE) with following formulas :

$$\begin{aligned}
 t_{tof} &= \frac{1}{2} \left(t_{left} + t_{right} - \frac{L}{v_{group}} \right) \\
 x &= \frac{1}{2} (t_{left} + t_{right}) \cdot v_{group} \\
 \Delta E &= k \cdot \sqrt{A_{left} A_{right}} \cdot e^{-L/2\lambda_{at}}
 \end{aligned} \tag{2.2}$$

where t_{left} and t_{right} is the time measured on the left and the right side of the rod, v_{group} is the group velocity in the rod (average velocity of light in the rod), L is the length of the rod, A_{left} left and A_{right} are the signal amplitudes at the left and the right ends of the rod, λ_{at} is the light attenuation length of the rod and k is a constant.

For time-of-flight measurements, the region of polar angle below 45° was covered by a low granularity system called TOFINO. It is divided into six sectors each consisting of four scintillator pads (see right panel of fig.2.6), arranged radially with respect to the beam axis. The basic principle is the same as for the TOF detector. In the case of the TOFINO detector, only one end is coupled to a PMT, so there is no information about the hit position. But directly behind the TOFINO detector, the Pre-Shower detector (will be described in the next section) is mounted, which provides the coordinate information of the particle hit on the paddle (x). The time-of-flight (t_{tof}) can be calculated using the following equation :

$$t_{tof} = t - \frac{x}{v_{group}} \quad (2.3)$$

where t is interval between the reaction and the arrival of the light pulse at the PMT, v_{group} the light group velocity in the pad and x the distance from the particle hit position to the PMT. The time resolution of TOFINO is about 420 ps, worse than TOF.

2.5.2 Pre-Shower detector

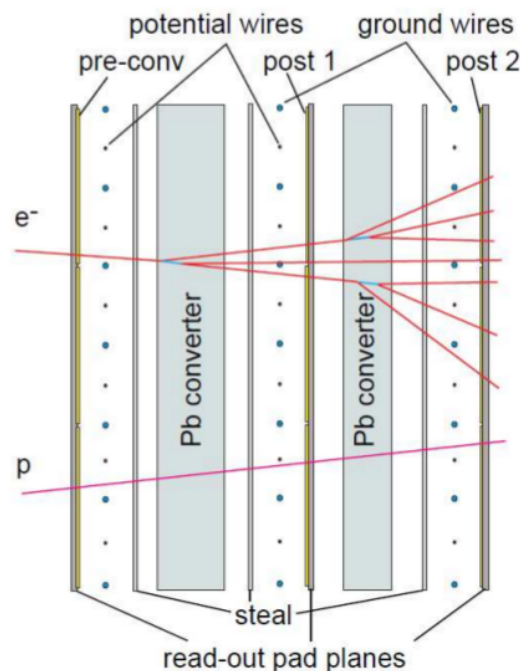


FIGURE (2.7) Side view of the Pre-Shower detector (one sector) with an example of electromagnetic shower.

Electrons and positrons induce much higher charge through interaction with matter than hadrons. They lose energy mainly by bremsstrahlung, and if the energy of the

photons emitted during this process is greater than $2m_e = 1.022$ MeV, they can generate high energy $e^+ e^-$ pairs. The result is a cascade of electrons, positrons and photons. Since the radiative energy loss per unit length ($\frac{dE}{dx}$) by photon emission, in a bremsstrahlung process, is proportional to the inverse mass squared $\frac{dE}{dx} \sim 1/m^2$, the bremsstrahlung process plays an important role mainly for light particles.

At forward polar angles, the separation of electrons from hadrons via time-of-flight measurement is more difficult than at large angles due to the higher hadron momenta and larger hits densities in the detectors. For this reason, an additional electron/hadron separation method was taken into account : an electromagnetic shower measurement in the Pre-Shower detector. The Pre-Shower detector, in Fig. 2.7, covers the polar angular region between 18° and 45° . It is composed of a stack of three Multi Wire Proportional Chambers (MWPCs) layers (pre-converter, post1-converter, post2-converter). Each chamber is filled with an Ar-Isobutan gas mixture and consists of one wire (anode/cathode) plane and two flat cathode planes. A 1 cm thick lead layer (corresponding to 2 radiation lengths) separates the chambers. Each cathode plane is subdivided into pads of different dimensions from which the induced charge signal is taken from. A charged particle, passing through a MWPC, ionizes the Ar-Isobutane gas producing avalanches of electrons, drifting towards the closest anode wire ; the positive cloud motion induces a positive charge on the nearby cathode pads, which are connected to charge sensitive pre-amplifiers. By comparing the integrated charge deposited by a track in the pre-converter and post1/post2-converters, it is possible to distinguish electromagnetic showers from hadronic tracks using momentum-dependent thresholds.

2.6 The trigger system

The trigger system of HADES is illustrated in Figure 2.8. A two level trigger system is used in the HADES experiments :

- 1st level trigger : The first level trigger (noted as LVL1) consists of a fast hard ware selection of central collisions, by measuring the hit multiplicity in META system. It is possible to apply multiplicity selections in TOF and TOFINO separately and sector-wise, in order to select only interesting decay channels, which is used for example for proton-proton elastic events.
- 2nd level trigger : The second level trigger (noted as LVL2) is based on an online

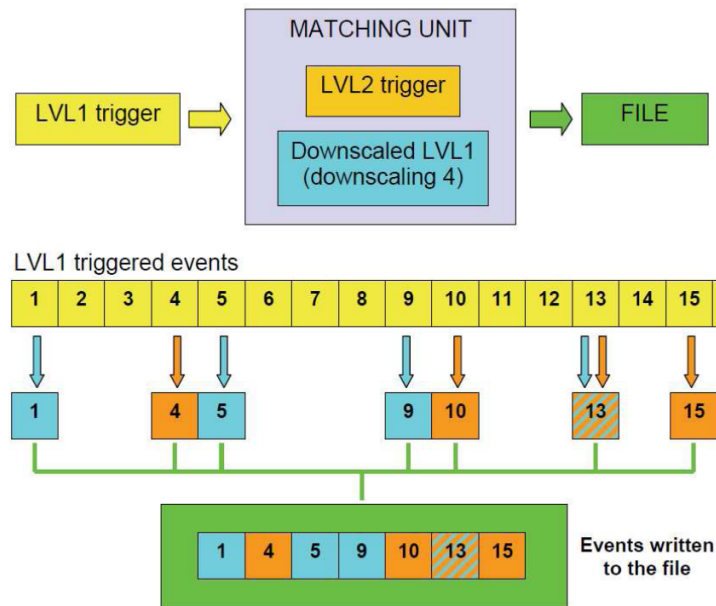


FIGURE (2.8) Sketch of the event selection used for data acquisition.

search for lepton candidates in the event. It comprises ring search in the RICH and electromagnetic shower in the Pre-Shower detection.

The downscaled LVL1 events are recorded because we are also interested in events which contain hadrons. However, the rate of hadronic events is so high that their number has to be reduced. Figure 2.8 gives a schematic explanation of the event selection used for data acquisition. The first selection of the events is done by the LVL1 trigger (yellow boxes), and they are sent to the matching unit afterwards where the downscaling factor is defined, for example factor 4 was selected for the pp experiment at $T = 3.5$ GeV. This means that one event out of four is stored (event number 1, 5, 9, 13, ...) (labelled by blue boxes), no matter the LVL2 trigger decision. In the meantime, all the events with a recognized lepton candidate are stored as well (labelled orange boxes). It can happen that an event can be at the same time downscaled by the LVL1 trigger and be accepted by LVL2 trigger, like for instance the event number 13 in the example. If we want to have the total number of the events, we must multiply the number of downscaled LVL1 events (blue boxes) by the downscaling factor 4. In this case, we obtain 16 events against 7 which are effectively stored to file. This means that in the example we found 4 events with electron candidates by storing only 7 events instead of 16. In this particular case, we have roughly saved half of the disk space, and half of the time needed for the data processing.

3

Experimental Data Analysis

3.1 Introduction

In this chapter the data analysis method developed for the selection of the $pp \rightarrow pp\pi^+\pi^-$ reaction channel is described. HADES analyses are realized within the HYDRA framework, i.e. the Hades sYstem for Data Reduction and Analysis, based entirely on ROOT. The first step, which is common for all analyses in the HADES collaboration is the production of the DST files (Data Summary Tapes) where the detector signals measured by the different sub-detectors, as the RICH, MDC, TOF/TOFINO and Pre-Shower are translated to physical information as hit coordinates, time of flight, energy loss and also reconstructed tracks in MDCs etc.

The analysis is divided into several steps (see Figure 3.1) : raw data processing, calibration, track reconstruction, particle identification and finally reaction channel selection. For the simulation part, two options are used. The first one is based on GEANT3

and contains detailed emulation of detector response including trigger conditions. The second option is based on filtering by dedicated acceptance and efficiency matrices.

DST files are input to the PAT (PostDST Analysis Tool) framework. Only interesting events are selected from the whole experimental data based on the selection of a given final reaction channel. Particle identification (PID) is performed via conditions defined on velocity and momentum correlation.

The next step in the analysis chain is provided by the Final Analysis Tool (FAT), where physical information (invariant mass, total energy, distribution angles, etc.) is extracted for the previously selected events. Based on this information, the background is also identified and removed and efficiency corrections are applied. Finally, the distributions of count rates obtained for a given reaction channel are converted to differential cross sections using normalization factors calculated from simultaneously measured pp elastic scattering events, as described in Section 3.7.

In order to calculate efficiency corrections, flat generators are used to have a good statistics of events in all bins, as will be explained in more details in Section 3.5.2. Such simulations are also used to calculate acceptance matrices (see Section 3.5.1) and to parametrize smearing functions which are used to take into account resolution effects (see Section 4.4.3). Then, simulated events are interfaced to the detector simulation package GEANT3. Their interaction with the target and detector material is calculated.

The comparison of the experimental differential distributions with the model predictions requires the use of simulations, in order to take into account experimental effects. In the analysis of simulated events the same steps are performed as in the case of experimental data (this will be the subject of Chapter 4). Events are generated, following theoretical distributions, using PLUTO++ [61, 109] a ROOT-based event generator, developed by the HADES collaboration. Then, simulated events are smeared to account for the detector resolution and filtered with acceptance matrices. More detailed description and results concerning matrices are the subject of Section 3.5.1.

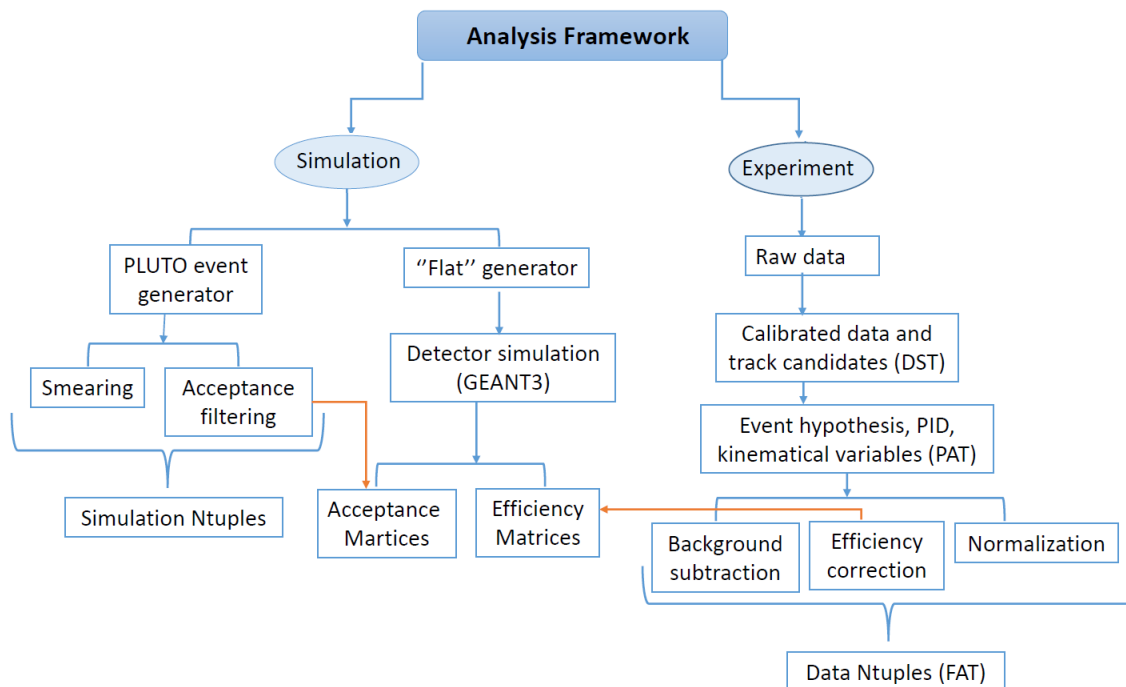


FIGURE (3.1) Data and simulation analysis flow relevant for this PhD work.

3.2 Particle reconstruction and identification

The procedure to select events corresponding to the $pp \rightarrow pp\pi^+\pi^-$ channel is to choose events with one proton, one π^+ and one π^- and check that the kinematics correspond to the $pp \rightarrow pp\pi^+\pi^-$ reaction. This choice is triggered by the fact that, due to the detector acceptance, the probability to detect two protons is very low. In the following, we will first briefly explain the method for momentum reconstruction (section 3.2.1) and time-of-flight calculation (Section 3.2.2). These information are used for the particle identification (Section 3.2)

3.2.1 Momentum reconstruction

The momentum is obtained from the deflection of particles in the magnetic field. Independent inner and outer straight track segments are reconstructed from the hit and drift time information in the pairs of drift chambers in front of and behind the field region, respectively. The mechanism of track segment reconstruction is presented in Figure 3.2. The inner and outer MDC track segments are projected and matched on "the kick plane" which is a surface, obtained from simulations, which approximates the deflection of charged particles in the HADES magnetic field just by a sudden change (a "kick")

of the trajectory occurring in the kick plane. This allows to give a crude approximation of the momentum which is used as initial value in the subsequent more refined track fitting algorithm, aiming at a final precise determination of the momentum. First the cubic spline method is applied to calculate a first approximation of the momentum. Second, based on the previous result, a fourth order Runge Kutta algorithm is used. Implementation of this method solves differential equations of motion in the known magnetic field. With such a procedure, the momentum resolutions are of the order of 1-2% for electrons, and 2-3% for pions and protons. The larger value for hadrons is mainly due to their larger average momentum, but multiple scattering also contributes significantly to the momentum.

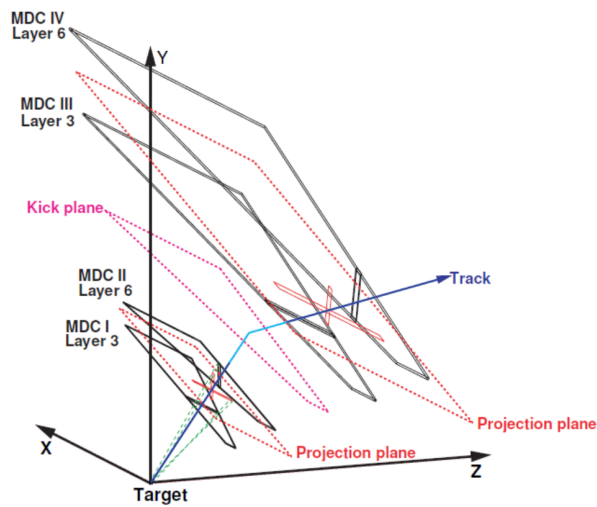


FIGURE (3.2) Illustration of the track reconstruction procedure. Only one MDC sector is shown in each layer.

3.2.2 Time of flight calculation

Usually the time of flight is calculated using the difference of arrival time between the START and the TOF detectors signals but because of the high intensity of the proton beams it was not possible in this experiment to use the START detector. As a consequence, there was no common start time reference for tracks in the same event. The start time was given for each event by the trigger signal, which was related, to the earliest signal in either TOF, TOFINO or FW detectors. The absolute time-of-flight can, however, be calculated for a defined hypothesis, where each reconstructed trajectory is assigned to a given particle species. With the known trajectory length, momentum and ideal particle mass, the time-of-flight for each particle is calculated.

$$t_i^c = \frac{l_i^{track}}{\beta \cdot c} \quad (3.1)$$

where l_i^{track} is the i -th particle track length, β is the particle velocity, it depends on the assigned ideal mass. In a general case of N particles, the reference particle has to be chosen (here, π^-). The reference time for each (i, j) pair is defined as the mean time :

$$\bar{t}_j = \frac{t_i^c + t_j^c}{2} \quad (3.2)$$

If the measured (relative) time is t_i^{exp} and t_j^{exp} , with the help of half time difference

$$\Delta t_j = \frac{t_j^{exp} - t_i^{exp}}{2} \quad (3.3)$$

the reconstructed time can be calculated as follows :

$$t_{ij}^{rec} = \bar{t}_j - \Delta t_j \quad (3.4)$$

$$t_{ii}^{rec} = \frac{\sum_j^N \bar{t}_j}{N - 1} \quad (3.5)$$

Finally, the χ_{tot}^2 for a given hypothesis is a measure which particle combination assignment is the best in terms of the reconstructed time-of-flights :

$$\chi_{tot}^2 = \sqrt{\sum_i^N \chi_i^2}, \quad \chi_i^2 = \sqrt{\sum_j^N \frac{(t_{ij}^{rec} - t_j^c)^2}{\sigma^2(TOF, TOFINO)}} \quad (3.6)$$

where $\sigma^2(TOF, TOFINO)$ is the detector time resolution for TOF and TOFINO and the sum runs over all particle species in the event. Finally, the combination with the smallest χ_{tot}^2 value is chosen.

3.2.3 Time and momentum correlation

The final step consists of a check of the correlation between the momentum and time of flight. The particle velocity is deduced using the track length and the time-of-flight.

If the mass of the particle is known the momentum is given by the relation :

$$p = \beta \times m / \sqrt{1 - \beta^2} \quad (3.7)$$

We can check that this relation is fulfilled by the momentum deduced from the tracking. The correlations between the velocity and reconstructed momentum (see Figure 3.3) for all three particles were taken into consideration to reject the wrong hypotheses. The correlation between the energy losses in MDCs and momentum was additionally applied for the final selection of the proton and π^+ . Figure 3.3 shows the limits used to accept the particles of different types and the correlation between the product of charge and momentum and the velocity β for particles selected by the event hypothesis method.

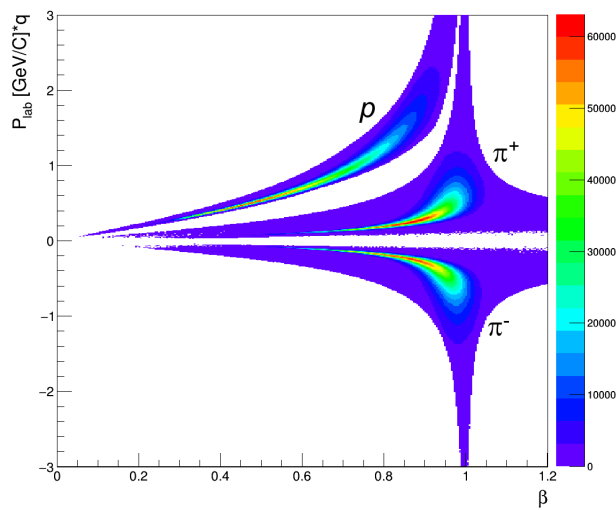


FIGURE (3.3) Experimental distribution of momentum \times charge vs beta for p, π^+ and π^- after identification using the event hypothesis method.

3.3 Event selection

In the first step, the $pp \rightarrow pp\pi^+\pi^-$ channel is selected by asking for at least one proton, one positive pion and one negative pion in the exit channel. In this case, knowing the value of the total energy, momentum and masses of the three identified particles, we can calculate the momentum and energy of the missing particle.

$$p_{tot} = p_{proj} + p_{targ}$$

$$p_{miss} = p_{tot} - p_p - p_{\pi^+} - p_{\pi^-}$$

Where p_{proj} , p_{targ} are the entrance system, projectile and target proton momenta, respectively.

In the second step, the squared missing mass of the reaction $pp \rightarrow p\pi^+\pi^-X$ is evaluated. It corresponds to the mass of the system of the missing proton and all other residual undetected particles. Figure 3.4 shows the missing mass squared spectrum, the peak at 0.88 GeV^2 corresponds to the missing proton, and the large structure in this spectrum is created by the production of an extra pion, it is the subject of a separate analysis and will not be included in this work.

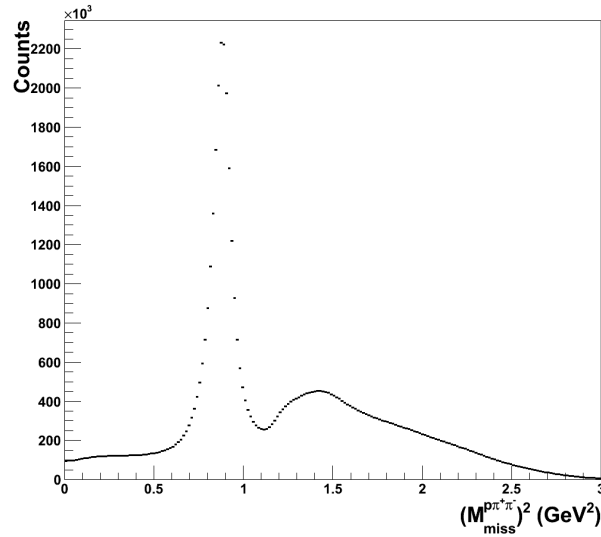


FIGURE (3.4) Missing mass squared distribution of the reaction $pp \rightarrow p\pi^+\pi^-X$.

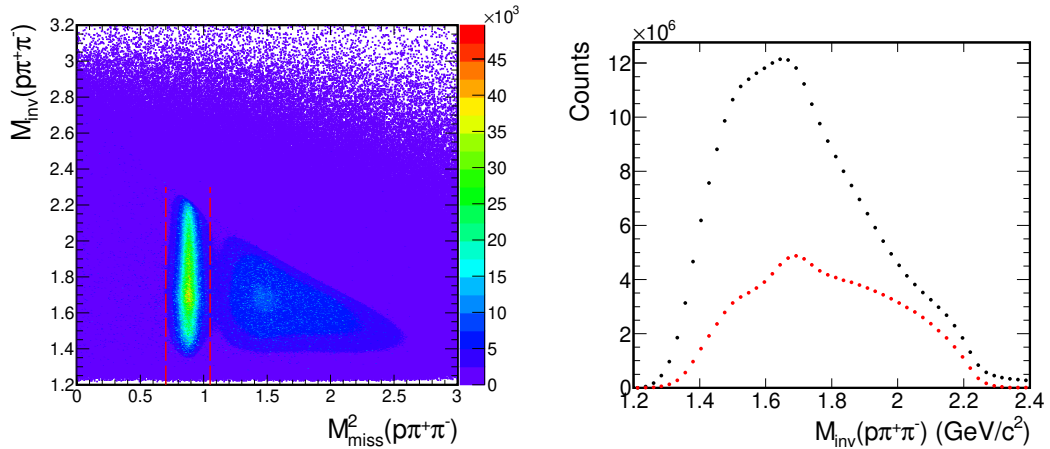


FIGURE (3.5) Left : a two-dimensional histogram showing the invariant mass as a function of the squared missing mass. The red dotted line shows the range in $M_{miss}^2(p\pi^+\pi^-)$ for selection of the $pp \rightarrow pp\pi^+\pi^-$ signal. Right : Invariant mass distribution of the $p\pi^+\pi^-$ system. Black dots show the total projection on the invariant mass, while red dots show the signal after applying the missing mass selection.

3.4 Background Subtraction

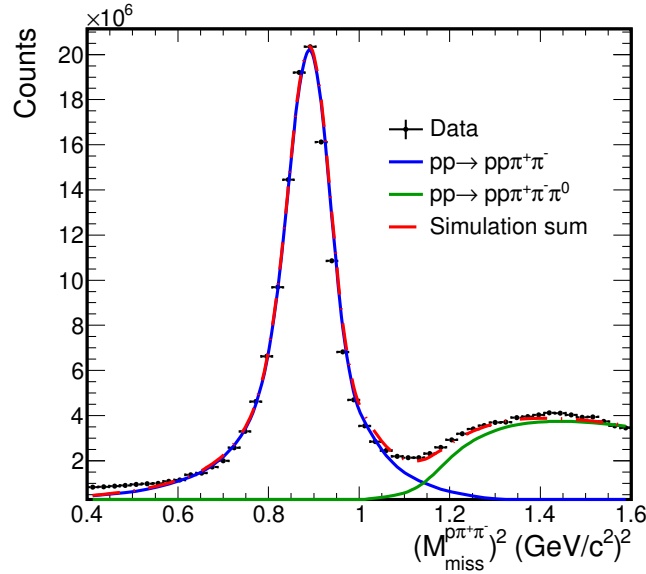


FIGURE (3.6) Squared missing mass distribution of the $p\pi^+\pi^-$ system compared to to the sum (red) of two pion production (blue) and three pion production (green) phase space simulation.

To describe the missing mass distribution we simulated the reactions $pp \rightarrow pp\pi^+\pi^-$ and $pp \rightarrow pp\pi^+\pi^-\pi^0$. For this, we used the PLUTO simulation (see Section 4.1) and generated events according to phase space. Acceptance and resolution effects were applied using acceptance matrices and smearing functions, as will be explained in detail in Section 4.4 and section 4.4.3. The comparison between data and simulation in Figure 3.6 shows a good match after adding the three pion production (green). The width of the proton peak is well described, which confirms that we have a realistic description of the resolution in the simulation. The sum of the two pion and three pion production simulation describes well the data. However, there is still an excess of data at small missing masses which is probably due to misidentified particles, noise or random coincidences.

In order to extract the yield related to the $pp\pi^+\pi^-$ final state the background had to be subtracted for each bin used for the data analysis. To do so we implemented a method where we first subtract the three pion contribution using the simulation and then we apply a weight on each event to take into account the probability that it is a signal or a background event. In detail, the procedure consists in the following different steps :

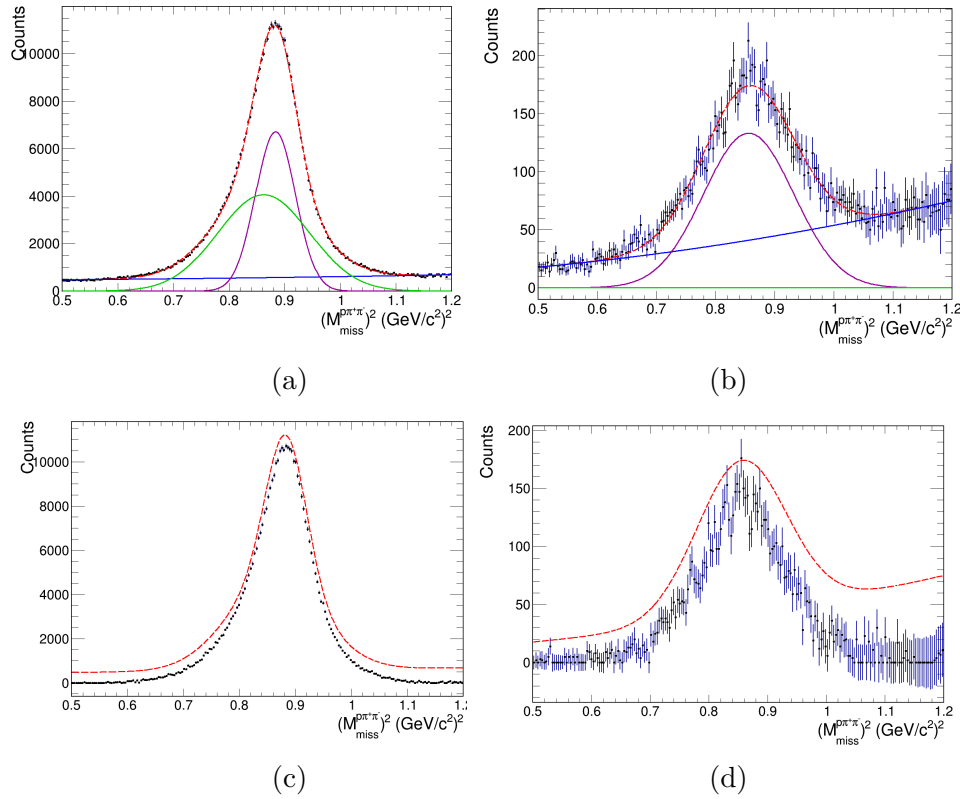


FIGURE (3.7) (a), (b) : Squared missing mass distribution of the $p\pi^+\pi^-$ system after the three pion production subtraction fitted with two Gaussians (violet and green curves) and a polynomial function (blue curve), the red curve represent the total fit, the two pictures correspond to two different cells with very different background content. (c), (d) : The squared missing mass distribution after the background subtraction, the dashed red curve shows the total events before the background subtraction.

- Create a 25×20 matrix of histograms, divide the data events into 25 bins of $M_{inv}(p\pi^-)$ and 20 bins of $\cos(\theta)_{CM}(p\pi^-)$, fill each histogram with the squared missing mass.
- Apply the same binning for the three pion production simulation.
- Subtract for each of the 25×20 cells the simulated events from the data.
- Fit the remaining data with the sum of two Gaussians and a polynomial function to take into account the remaining background.
- Subtract the fitted background from the data.
- Calculate the Q-factors that are the ratio between the background subtracted data and the raw data. The Q-factors are defined as :

$$Q_{ij} = \frac{N_{ij}^{signal}}{N_{ij}^{raw}} \quad (3.8)$$

Figure 3.7 (a) and (b) shows two examples of the signal/background fit, one with a

relatively low background and the other with relatively high background. The result of the background subtraction for each case is shown in Figure 3.7 (c) and (d) respectively.

3.5 Efficiency and Acceptance Considerations

The HADES detector has a high acceptance but still does not cover the full solid angle. In order to describe the geometrical coverage and the reconstruction efficiencies, acceptance and efficiency matrices were calculated for different particles individually. These matrices are defined in three dimensions corresponding to p (momentum), θ (polar angle) and ϕ (azimuthal angle) in the laboratory frame.

The acceptance matrices describe the geometrical acceptance of the spectrometer, while the efficiency matrices account for the detection and reconstruction losses within the detector acceptance. They are generated separately for every particle of interest via GEANT3 simulations including precise HADES electronics information and response. In addition, the same track reconstruction and particle identification algorithms are used than for real data. These matrices are functions of the particle momentum, polar and azimuthal angles, p is typically set from 0 to 5000 MeV/c with 100 MeV/c per bin for protons and from 0 to 2000 MeV/c with 40 MeV/c per bin for pions, θ from 0° to 90° with 2° per bin and ϕ from 0° to 360° with 2° per bin which corresponds to the coverage of all 6 sectors. They are created by generating with the simulation "white" particles which are distributed uniformly over all degrees of freedom in a given range. The efficiency response of the detector is computed through the "track embedding" method and is determined following different analysis steps :

- **Event Generation** : 6 "white" single particles distributions are generated (one per sector) by the PLUTO event generator [61, 109]. These events are generated taking into account the vertex coordinates (three coordinates) and the sequential number of the real event, which are stored in the output files as well. The output files produced in this step are used as input files in the next step.
- **Event Simulation** : The simulated events are propagated through the HADES spectrometer simulation using GEANT3 [110], which takes into account the spectrometer acceptance and the response of the HADES detector to the passage of charged particles. This is achieved by implementing a detailed description of the

detectors geometry and parametrization of the response of all subdetectors adjusted to real data to take into account their efficiency in a realistic way. The vertex coordinates of the simulated events which are propagated through the spectrometer are sampled from experimental distributions. The output data has the same structure as the real one, therefore it is used as input for the reconstruction programs in the same way as for the real data.

- **Event Digitization** : the resulting events were digitized and processed in order to take into account the detector and electronics response (e.g. electronics noise). The digitizers are part of the HYDRA framework and give the response of each sub-detectors. All parameters needed by the digitizers are retrieved from the ORACLE database in order to be consistent with the analysis of the real events.
- **Event Embedding** : the simulated events produced in the previous analysis steps are embedded into real data events. This is a technique to estimate the reconstruction efficiency under realistic conditions. "Realistic" means that background of the simulated tracks is as close as possible to the real one. The sequential number of the events is used to synchronize the embedded events with the real events.
- **Event Reconstruction** : the full events are reconstructed and the same cuts as applied to the real data are considered in this stage.

3.5.1 Acceptance Matrices

The events which hit the active volume of the detector are retrieved and considered as detected. The acceptance matrix is calculated using equation 3.9, as the ratio between the number of particles which fall into the detector active volume and the number of all simulated particles sent in the beginning, assuming a perfect (100%) detection efficiency. HADES has zero acceptance for any particle that is emitted from the target region with a laboratory polar angle less than approximately 15° . This means that, one can not fully reconstruct any configuration of final state particles where one or more charged particles are emitted below 15° in the polar angle.

$$F_{ACC}(p, \theta, \phi) = \frac{N_{Acc}(p, \theta, \phi)}{N_{Tot}(p, \theta, \phi)} \quad (3.9)$$

Figure 3.8 shows a two dimension projection of the acceptance matrices of the proton, π^+ and π^- .

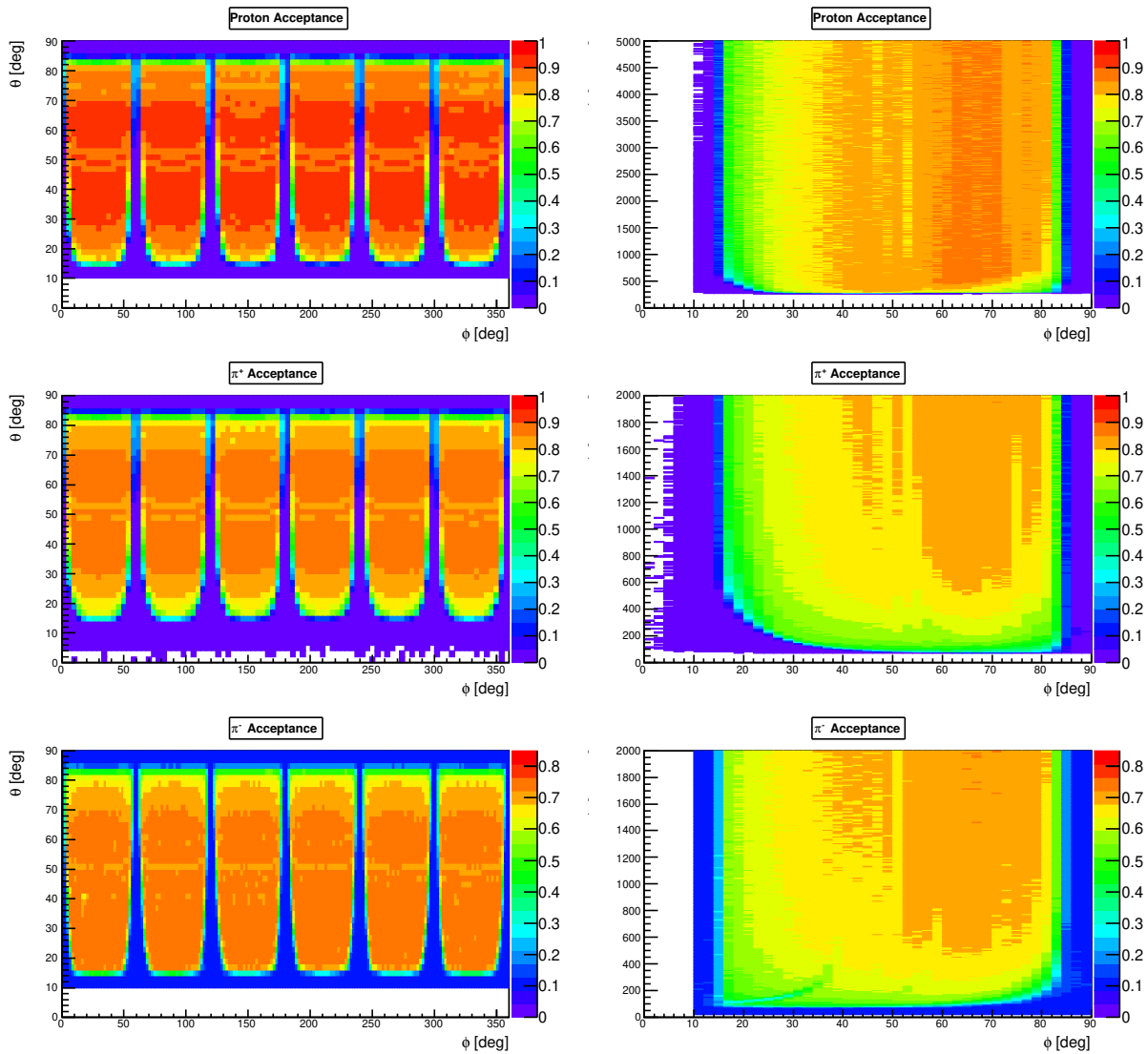


FIGURE (3.8) Projection of the three dimensional acceptance matrices for the proton, π^+ and π^- , as a function of θ and ϕ (left) and as function of p and θ (right)

3.5.2 Efficiency Matrices

The efficiency matrices are calculated as the ratio between the number of reconstructed particles ($N_{reconstructed}(p, \theta, \phi)$) and the number of particles which fall into the detector active volume ($N_{accepted}(p, \theta, \phi)$):

$$Eff(p, \theta, \phi) = \frac{N_{reconstructed}(p, \theta, \phi)}{N_{accepted}(p, \theta, \phi)} \quad (3.10)$$

For each experimental event the efficiency of the p, π^+ and π^- , is taken from the corresponding matrix. The event is then corrected with the weighting factor (efficiency correction factor) :

$$Eff_{corrected} = \frac{1}{Eff(p) \times Eff(\pi^+) \times Eff(\pi^-)} \quad (3.11)$$

Figure 3.9 shows the efficiency matrices for protons (upper row) and π^+ (middle row) and π^- (lower row), as a function of θ and ϕ (left), as function of p and θ (right). The number of positive reconstructed particles at small angles is much lower than for the negative particles. This is due to combined effect of magnetic field and the lack of acceptance at forward angles. The positive particles are indeed more sensitive to this cut, since they are bent towards the beam axis, while the negative ones are bent outwards. The borders of depressed region in proton efficiency (and acceptance) matrix correspond to decreasing polar angles when the momentum increases. This can be understood because before reaching the TOF or TOFINO detectors, the proton was bent by the magnetic field towards the beam axis depending on its momentum. The higher the proton momentum, the smaller the deviation is. The same phenomena can be found even more clearly in the case of π^+ , because the relevant momenta are smaller. This effect is not present in the case of negative particles. The acceptance is larger at momenta below 300 MeV/c for π^- than for π^+ , since π^- are bent in the magnetic field towards the detector.

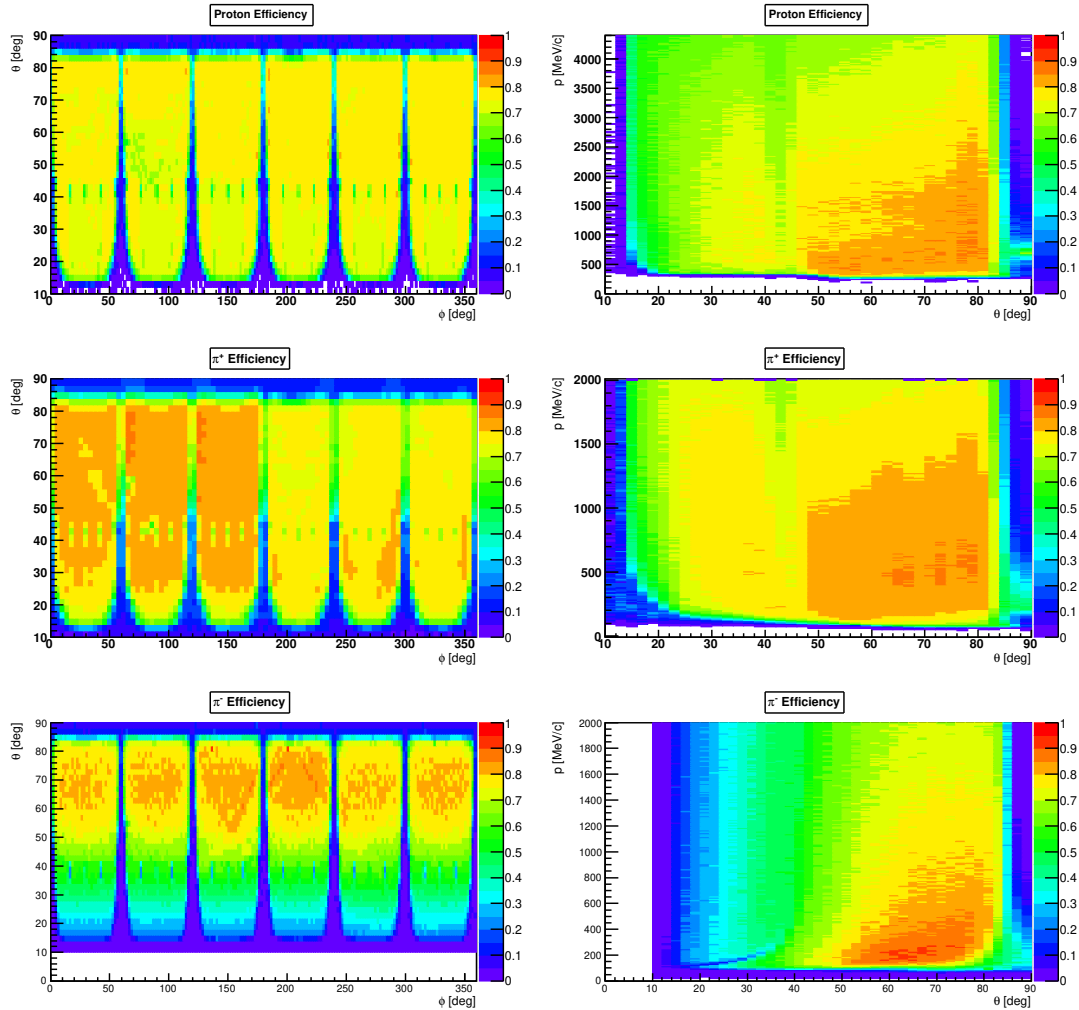


FIGURE (3.9) Projections of the three dimensional efficiency matrices for protons (upper row) and π^+ (middle row) and π^- (lower row), as a function of θ and ϕ (left), as function of p and θ (right).

3.6 Efficiency cuts

The edges of the six HADES sectors are not well described by the simulation so it was necessary to introduce a cut to exclude them from the analysis. The result of the efficiency correction is shown in two dimensional plots of momentum and polar angle in Figure 3.10 (a) and (b) for the protons, (c) and (d) for π^+ , (e) and (f) for π^- . It is visible in the plots on the left that when the particles of very low efficiency are reconstructed ($< 20\%$ for protons and $< 10\%$ for pions), the homogeneity of the distributions is distorted, as it is seen in Figure 3.10 (a) the number of protons with momentum < 0.4 GeV is overestimated. The low efficiency regions correspond to the edges of the sectors. Due to the fact that there are areas for which the geometrical acceptance of the tracks is high, but only few tracks at all are reconstructed due to the lack of efficiency. This

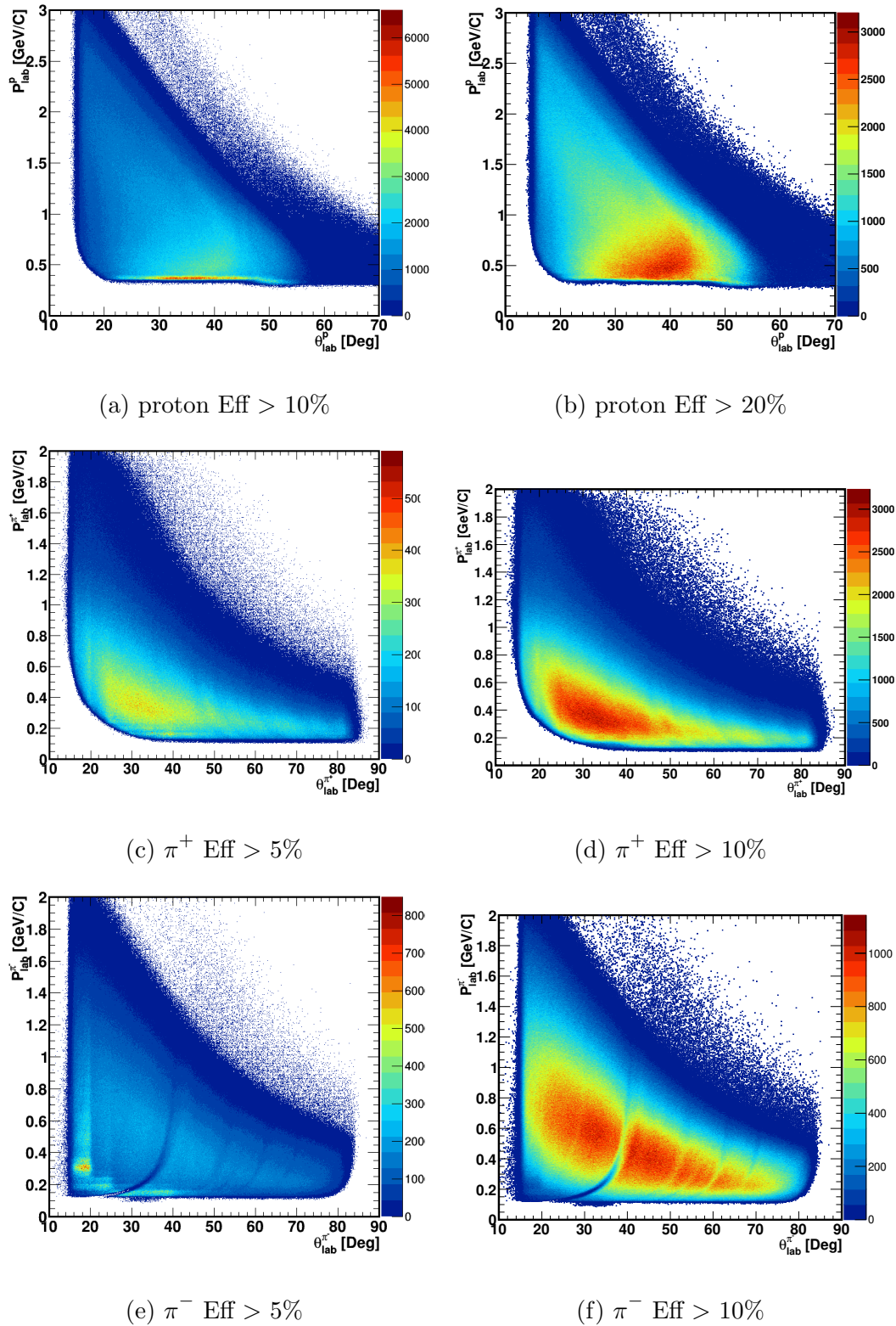


FIGURE (3.10) Data momentum as function of the polar angle θ in the Lab frame. (a) proton efficiency threshold > 5%, (b) proton efficiency threshold > 20%, (c) π^+ efficiency threshold > 5%, (d) π^+ efficiency threshold > 10%, (e) π^- efficiency threshold > 5%, (f) π^- efficiency threshold > 10%.

demonstrates that when comparing the data to simulations, it is important to restrict to regions where the efficiency is above a certain threshold. We use a 10% threshold for pions and 20% threshold for protons.

3.7 Data Normalization

The data was normalized using the number of $p-p$ elastic scattering events collected during the experimental beam time. By using the known elastic cross section we can normalize the number of events in a given bin as follows :

$$\frac{\sigma_R}{N_R} = \frac{\sigma_{el}}{N_{el}} \implies \sigma_R = N_R \frac{\sigma_{el}}{N_{el}} \quad (3.12)$$

N_{el} - number of elastic scattering events in full solid angle.

N_R - number of collisions of the reaction of interest .

σ_{el} - known cross-section of elastic scattering in full solid angle.

To select events corresponding to the proton-proton elastic scattering, relations between the angles of the two protons are used. Indeed, in the Lorentz transformation from the laboratory system to the center of mass system, the momentum component in the transverse direction to beam axis, does not change :

$$p_{lab} \sin \theta_{lab} = p_{cm} \sin \theta_{cm} \quad (3.13)$$

Whereas the momentum component in the direction of the beam axis extends relativistically :

$$p_{lab} \cos \theta_{lab} = \gamma_{cm}(p_{cm} \cos \theta_{cm} + \beta_{cm} E_{cm}) \quad (3.14)$$

Where γ_{cm} is the Lorentz factor calculated in the CM frame and β is the velocity.

In the case of proton-proton elastic scattering, the two protons have same momentum p_{cm} and energy E_{cm} in the center of mass. Therefore applying Eqs (3.13) and (3.14) to the target particle at rest leads to $\beta_{cm} = p_{cm}/E_{cm}$, thus :

$$\tan \theta_{lab} = \frac{\sin \theta_{lab}}{\cos \theta_{lab}} = \frac{\sin \theta_{cm}}{\gamma_{cm}(\cos \theta_{cm} + \beta_{cm} E_{cm}/p_{cm})} \quad (3.15)$$

If θ_{cm} is the angle of proton 1, the angle of proton 2 is : $\theta_{cm}^1 = \theta_{cm}^2 - 180^\circ$ and $\phi_1 = 180 + \phi_2$

$$\tan \theta_{lab}^1 = \frac{\sin \theta_{cm}}{\gamma_{cm}(\cos \theta_{cm} + 1)} \quad (3.16)$$

$$\tan \theta_{lab}^2 = \frac{\sin \theta_{cm}}{\gamma_{cm}(1 - \cos \theta_{cm})} \quad (3.17)$$

So :

$$\tan \theta_{lab}^1 \cdot \tan \theta_{lab}^2 = \frac{1}{\gamma_{cm}^2} \quad (3.18)$$

Elastic scattering events were selected by considering the following conditions :

- Condition of the M2 triggering system, meaning that the detector has registered exactly two charged particles.
- Coplanarity $|\phi_1 - \phi_2| = 180^\circ$
- Condition on the polar angles $\tan \theta_{lab}^1 \cdot \tan \theta_{lab}^2 = \frac{1}{\gamma_{cm}^2} = 0.349$ ($E_{lab} = 3.5$) GeV

The number of corresponding events is then integrated over the periods when the detector was perfectly working, exactly as for the analysis of the pion production channels.

3.8 Systematic errors estimation

As can be seen in Figure 3.4, the statistics in the two pion production channel is large so statistical errors are negligibly small, however systematic errors have also to be investigated. The first source of systematic errors to be considered is related to the uncertainty on the background subtraction. The latter was defined as the largest difference obtained in estimating the number of counts using various functions describing the background. From Figure 3.7 it is clear that this error depends on the bin. Our estimate is of the order of 2% for most of the bins and reaches 10% for some bins. This systematic error is propagated for each event.

As mentioned before, all the spectra are scaled by the normalization factor in order to represent differential cross sections with an integral in millibarn. As in the previous analysis [65], we consider a 7% uncertainty on the normalization factor. The error on the normalization is a global error, which affects all bins in the same way.

Another source of systematic error is the efficiency correction. The error related to the limited statistics in the simulations used for the determination of the efficiency

matrices is calculated in the efficiency correction procedure. The statistical error on the calculation of the efficiency, which is related to the statistics used in the simulation is taken into account in the efficiency correction procedure. One way to quantify systematic errors is to check the azimuthal isotropy of efficiency corrected yields. Indeed, since the beam is not polarized, there is no favoured direction in the plane perpendicular to the beam axis and the distribution of azimuthal angle should be isotropic. This means that the differences between the number of reconstructed particles in each sector should differ only due to the different efficiencies, and as a consequence, after efficiency corrections, one should ideally obtain the same yield in each sector. We chose to compare the yield in each sector to the average over all sectors. Figure 3.11 shows the ratio

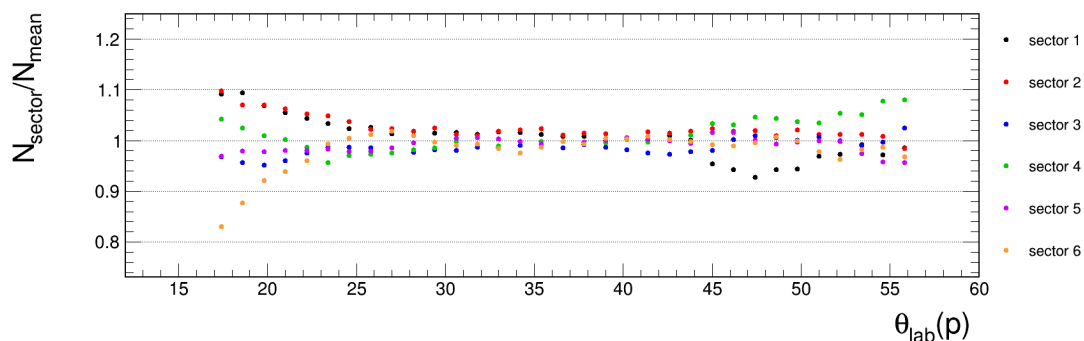


FIGURE (3.11) Ratio of counts between each sector and the average as function of θ . Each color corresponds to a sector.

between the number of counts in polar angle bins of one degree of each sector and the average as a function of the polar angle θ . It can be observed that in the region between 25 and 45 degrees, all the ratios are close to 1, with deviations smaller than 2%. Larger fluctuations exist, especially at smaller angles, which indicates some errors in the efficiency correction, however the difference remains within 10%. Since the spectra are always averaged over 6 sectors, the effect of this difference between the sectors has no effect on our analysis. However, the difference between sectors points to some limited description of the efficiency in the simulation, which might also affect the average value. Nevertheless, this effect is also reduced, thanks to our normalization procedure. Indeed it is clear from Eq(3.10) that a possible systematic error on N_{eff} will be taken into account in the normalization coefficient σ_{el}/N_{el} . However, a residual effect might subsist, due to the different kinematics of protons in the $pp \rightarrow pp\pi^+\pi^-$ reaction with respect to the elastic case and the different efficiencies for protons and pions. We therefore estimate a global residual error of 2% on the efficiency correction. To be conservative, we also include a point-to-point error of 2% to take into account the variations of the error

as a function of θ . The total error on experimental spectra includes all the systematic uncertainties summed quadratically. Point to point errors are added quadratically and

Source of systematic error	Point to point error	Global uncertainty
Background subtraction	2%-10%	1%
Efficiency correction	2%	2%
Normalization	-	7%
Total	-	7.3%

TABLE (3.1) Summary of systematic errors in the $pp \rightarrow pp\pi^+\pi^-$ reaction analysis.

included on experimental spectra. The global errors are not shown, but are taken into account when calculating integrated cross sections.

4

Simulations

4.1 The PLUTO event generator

The PLUTO event generator [61, 109] is a tool to simulate particle emission from hadronic reactions based on ROOT developed by the HADES collaboration. It allows to describe the production of particles in elementary reactions and their hadronic and leptonic decays, and also to simulate heavy-ion induced reactions. The package is entirely based on ROOT, without the need of additional packages, and uses the embedded C++ interpreter of ROOT to control the event production.

To obtain realistic simulations of hadronic interactions at low energies, the effect of the deviation of resonance shapes from fixed-width Breit-Wigner distributions is taken into account, which is typically modeled as a mass-dependence in the resonance width. The relativistic form of the Breit Wigner distribution is used :

$$g(m) = A \frac{m^2 \Gamma_{tot}(m)}{(M_R^2 - m^2)^2 + m^2 \Gamma_{tot}^2(m)} \quad (4.1)$$

Where m is the running unstable mass, and M_R is the static pole mass of the resonance. The factor A has been chosen such that the integral is statistically normalized ($\int dm g(m) = 1$). The mass-dependent width depends on the partial widths :

$$\Gamma_{tot}^2(m) = \sum_k^N \Gamma_k(m) \quad (4.2)$$

PLUTO is composed of 5 main classes :

- The PParticle class : describes the objects of particle type. It's the most elementary object of the software, it inherits from the class TLorentzVector, a quadrivector tool of ROOT. The PParticle class holds all the information of each given particle (momentum components, mass, time of decay...)
- The PChannel Class : describes the decay of a primary particle to secondary particles.
- The PReaction Class : describes a succession of channels as a chain of PChannel. This class has a *Loop()* function that generates the simulation events with the predefined statistics.
- The PDecayManager Class : allows the creation of reaction cocktails. This class is very important since it allows the generation of all the different processes that occur in the same interaction.
- The PData Class : is a data basis where all the different particles and properties are listed, such as mass, width, decay channels and branching ratios.

4.2 PLUTO Resonance Cocktail

The simulations in this thesis were performed with PLUTO. The goal is to simulate all the production processes of the proton-proton reaction at 3.5 GeV, that leads to the $pp\pi^+\pi^-$ exit channel. We consider three different processes : the excitation of one resonance, with subsequent decay into a proton and two pions ($R \rightarrow p\pi^+\pi^-$), the excitation of two resonances decaying into a proton and a pion each ($R_1, R_2 \rightarrow p\pi$), and the direct ρ meson production and decay $\rho \rightarrow \pi^+\pi^-$.

A resonance model assuming that the pion production cross section is given by the incoherent sum of various baryon resonance contributions was implemented. To generate the resonance cocktail, all the subsequent channels were simulated separately by

N Resonances	Γ_R (MeV)	BR(N $\pi\pi$) %			Δ Resonances	Γ_R (MeV)	BR(N $\pi\pi$) %		
		tot	$\Delta\pi$	$N\rho$			total	$\Delta\pi$	$N\rho$
N(1440)	350	35	25	0	$\Delta(1232)$	120	0	0	0
N(1520)	120	45	25	15	$\Delta(1600)$	350	85	75	0
N(1535)	203	5	0	2	$\Delta(1620)$	150	70	60	10
N(1650)	150	20	7	5	$\Delta(1675)$	150	55	55	0
N(1675)	150	55	5	5	$\Delta(1700)$	300	85	55	30
N(1680)	130	30	10	5	$\Delta(1720)$	150	80	0	80
N(1720)	150	80	0	80	$\Delta(1905)$	350	85	25	60
N(1860)	/	unknown	/	/	$\Delta(1910)$	250	50	50	0
N(1875)	250	< 50	40	6	$\Delta(1950)$	300	25	25	0

TABLE (4.1) List of baryonic resonances, their width and their branching ratio to the N $\pi\pi$ decay channel.

J^P	Resonance	Γ_{tot}	Branching Ratios (%)	
			$p\gamma$	$n\gamma$
1/2+	N(1440)	0.35	0.042	0.021
	N(1710)	0.1	0.026	0.01
	$\Delta(1910)$	0.25	0.1	0.1
1/2-	N(1535)	0.15	0.15	0.021
	N(1650)	0.15	0.11	0.09
	$\Delta(1620)$	0.15	0.024	0.024
3/2+	$\Delta(1232)$	0.12	0.56	0.56
	N(1720)	0.15	0.05	0.2
	$\Delta(1600)$	0.35	0.01	0.01
3/2-	N(1520)	0.12	0.51	0.42
	N(1700)	0.1	0.03	0.07
	$\Delta(1700)$	0.3	0.19	0.19
5/2+	N(1680)	0.13	0.27	0.034
	$\Delta(1905)$	0.35	0.02	0.02
5/2+	N(1675)	0.15	0.014	0.07
	$\Delta(1930)$	0.35	0.01	0.01

TABLE (4.2) The branching ratios and coupling constants for the electromagnetic transition of baryon resonances.

$pp \rightarrow ppe^+e^-$ channel . Table 4.1 presents the compilation of resonance properties, from the above mentioned resonance model.

The strategy to build a full cocktail describing our data and including both one and two resonance excitation is summarized below :

1. Starting from the list of resonances from the one pion analysis where only resonances designated conventionally as four-star by the PDG were chosen and which have the largest anticipated contribution to the production of dileptons. In order to determine this contribution, the theoretical predictions contained in the

work [67] were used, from which table 4.2, corresponding branching ratios to $N\gamma$ (columns 3 and 4) was used.

2. The double resonance production was added by considering a production of all the resonances listed in the one pion production together with $\Delta(1232)$, this choice was adopted after doing a simple 2D histogram analysis (see Figure 4.1) that shows no evidence of other Δ^{++} resonances.
3. Finally, information about heavier resonances from the $pK\Lambda$ analysis [111] were added, this step is explained in details in section 5.3.1.

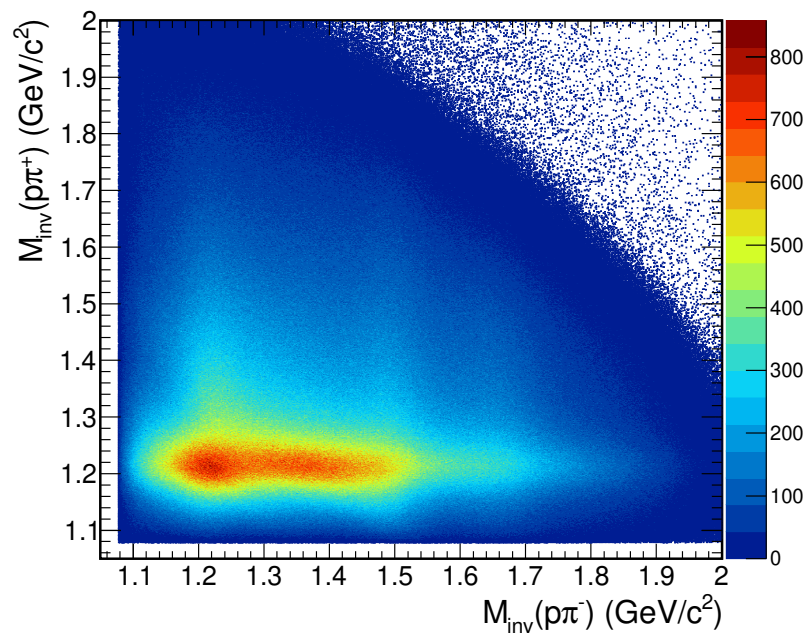


FIGURE (4.1) $p\pi^-$ Vs $p\pi^+$ invariant mass showing the three main double resonance production, $\Delta^{++}(1232)$ together with $\Delta^0(1232)$, $N^0(1532)$ and $N^0(1680)$.

Resonance	J^P	M (MeV)	Γ_R (MeV)	Decay mode	BR	Isospin
N(1440)	$1/2^+$	1440	350	$\Delta^{++}\pi^-$	17%	1/2
				$\Delta^0\pi^+$	17%	1/6
				$p\sigma$	16%	1/3
				$p\rho$	1%	1/3
N(1520)	$3/2^-$	1515	110	$\Delta^{++}\pi^-$	18%	1/2
				$\Delta^0\pi^+$	18%	1/6
				$p\rho$	12%	1/3
N(1535)	$1/2^-$	1530	150	$\Delta^{++}\pi^-$	2%	1/2
				$\Delta^0\pi^+$	2%	1/6
				$p\sigma$	3%	1/3
				$N(1440)\pi^+$	9%	1/3
N(1650)	$1/2^-$	125	150	$\Delta^{++}\pi^-$	9%	1/2
				$\Delta^0\pi^+$	9%	1/6
				$p\rho$	1%	1/3
				$N(1440)\pi^+$	8%	1/3
N(1675)	$5/2^-$	1675	145	$\Delta^{++}\pi^-$	35%	1/2
				$\Delta^0\pi^+$	35%	1/6
				$p\sigma$	5%	1/3
N(1680)	$5/2^+$	1685	130	$\Delta^{++}\pi^-$	18%	1/2
				$\Delta^0\pi^+$	18%	1/6
				$p\rho$	12%	1/3
N(1700)	$3/2^-$	1700	150	$\Delta^{++}\pi^-$	40%	1/2
				$\Delta^0\pi^+$	40%	1/6
				$p\rho$	40%	1/3
N(1710)	$1/2^+$	1710	100	$\Delta^{++}\pi^-$	6%	1/2
				$\Delta^0\pi^+$	6%	1/6
				$p\rho$	9%	1/3
				$N(1535)\pi^+$	15%	2/3
N(1720)	$1/2^+$	1720	250	$\Delta^{++}\pi^-$	20%	1/2
				$\Delta^0\pi^+$	20%	1/6
				$p\rho$	60%	1/3
N(1875)	$1/2^+$	1875	200	$\Delta^{++}\pi^-$	25%	1/2
				$\Delta^0\pi^+$	25%	1/6
				$p\rho$	60%	1/3
N(1880)	$1/2^+$	1880	300	$\Delta^{++}\pi^-$	22%	1/2
				$\Delta^0\pi^+$	22%	1/6
				$p\rho$	30%	1/3
				$p\sigma$	11%	1/3
				$N(1535)\pi^+$	8%	2/3

TABLE (4.3) List of simulated N^* resonances, their widths and their branching ratios to the $N\pi\pi$ decay channel. $N\rho$ branching ratios are taken from Bonn-Gatchina PWA.

Resonance	J^P	M (MeV)	Γ_R (MeV)	Decay mode	BR	Isospin
$\Delta(1232)$	$3/2^+$	1232	117	$p\pi^+$ $p\pi^-$	100% 100%	1 1/3
$\Delta(1600)$	$3/2^+$	1600	250	$\Delta^{++}\pi^-$ $\Delta^0\pi^+$ $N(1440)\pi^+$	70% 70% 5%	2/5 8/15 1/3
$\Delta(1620)$	$1/2^-$	1620	130	$\Delta^{++}\pi^-$ $\Delta^0\pi^+$ $p\rho$ $N(1440)\pi^+$	35% 35% 40% 5%	2/5 8/15 2/3 1/3
$\Delta(1700)$	$3/2^-$	1700	280	$\Delta^{++}\pi^-$ $\Delta^0\pi^+$ $p\rho$	10% 10% 44%	2/5 8/15 2/3
$\Delta(1905)$	$1/2^+$	1900	300	$\Delta^{++}\pi^-$ $\Delta^0\pi^+$ $p\rho$	43% 43% 47%	2/5 8/15 2/3

TABLE (4.4) List of simulated Δ^* resonances, their widths and their branching ratios to the $N\pi\pi$ decay channel. $N\rho$ branching ratios are taken from Bonn-Gatchina PWA.

4.4 Accounting for the detector geometrical effects

4.4.1 Acceptance filtering

The simulations cover the full solid angle, therefore before comparing them to HADES data all the simulations should be filtered by the acceptance matrices (see Figure 3.8). Figure 4.2 shows $\Delta^{++}\Delta^0$ and $N(1520)$ simulation before (dashed lines) and after (full lines) acceptance cuts.

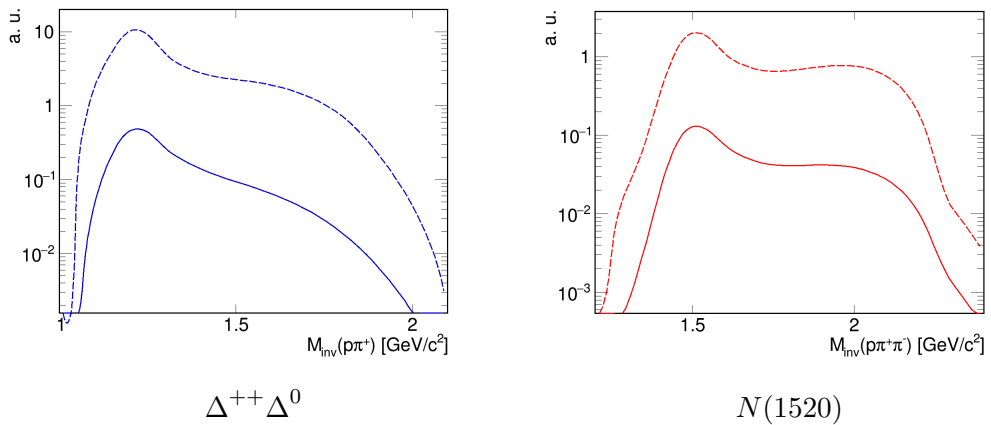
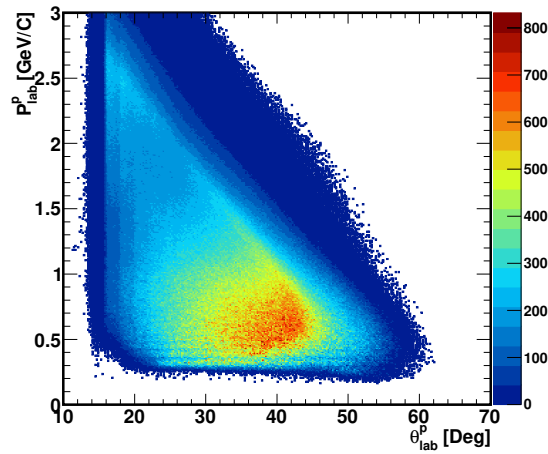


FIGURE (4.2) $\Delta^{++}\Delta^0$ (left) and $N(1520)$ (right) simulation before (dashed lines) and after (full lines) acceptance cuts.

4.4.2 Simulation efficiency cuts



(a) proton Eff > 20%

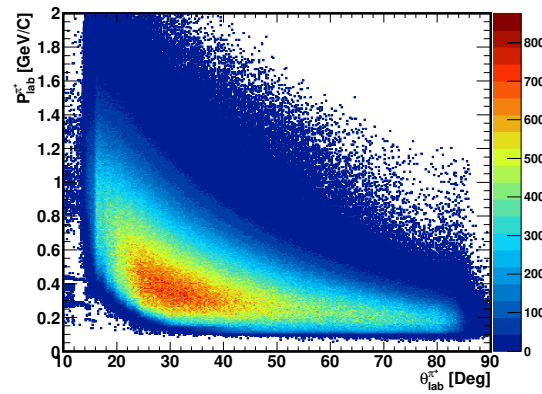
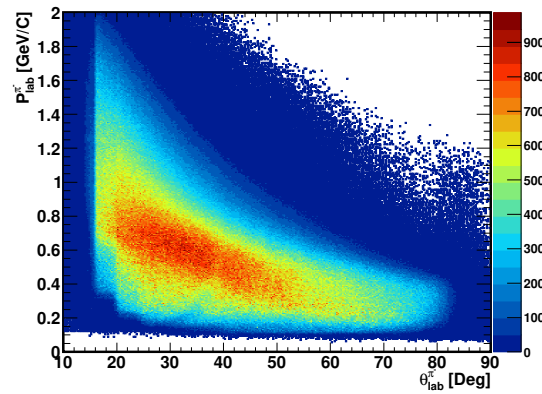
(b) π^+ Eff > 10%(c) π^- Eff > 10%

FIGURE (4.3) Simulation momentum as function of polar angle θ in the Lab frame. (a) proton efficiency threshold of 20%, (b) π^+ efficiency threshold of 10%, (c) π^- efficiency threshold of 10%.

In order to compare HADES data to our simulation, we need to treat the simulation exactly as the data. As mentioned in section 3.6, the regions where the efficiency is above a certain threshold was restricted. We used a 10% threshold for pions and 20% threshold for protons. The same restriction should be applied on the simulations. Figure 4.3 shows the momentum as function of polar angle θ in the Lab frame after applying the efficiency threshold restriction, 10% for pions and 20% for protons.

4.4.3 Momentum Smearing

For the p+p experiment at 3.5 GeV, Runge-Kutta algorithms have been employed to reconstruct the particle momentum. The resolution is dominated at low momentum by multiple scattering, consequently is particle dependent, and goes like $\frac{1}{\beta}$. The position resolution on the MDC chambers gives a contribution $\frac{\Delta p}{p}$ which is linear in momentum and particle independent. This position resolution is directly related to the drift time uncertainty, but also to the knowledge of the geometry of wires in space, and also depends on the calibration of the electronics (details can be found in [112]).

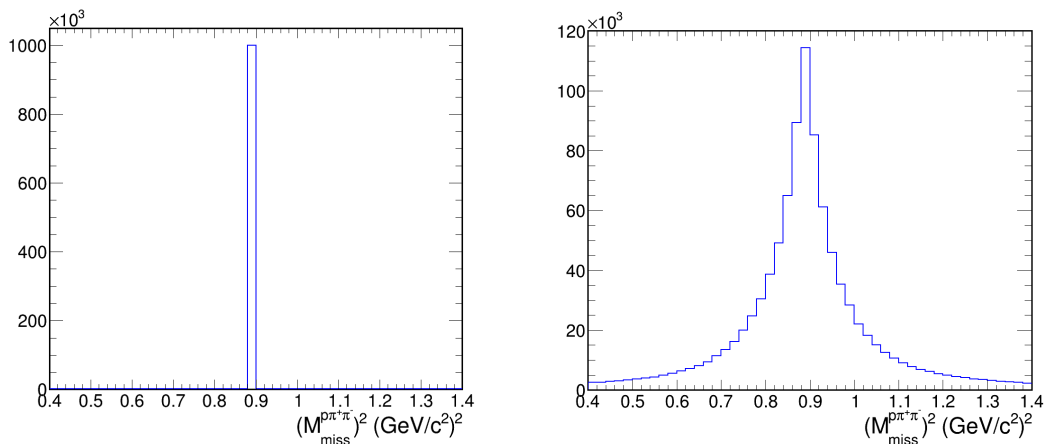


FIGURE (4.4) Squared missing mass distribution of the $p\pi^+\pi^-$ system before (left) and after (right) smearing

The resolution has been investigated using the proton-proton elastic collisions at 3.5 GeV. As the angle resolution is much better than the momentum resolution, a good estimate of the momentum (p_{cal}) of scattered protons can be calculated from their reconstructed polar angle. Using the Runge-Kutta method, we can also reconstruct the momentum (p_{RK}) from the measured drift times. By comparing these two values, the resolution $\frac{\Delta p}{p} = \frac{p_{cal} - p_{RK}}{p_{cal}}$ can be measured event by event. For each (p, θ, ϕ) cell,

the obtained values are fitted by Gaussians. The $\sigma(p, \theta, \phi)$ are then used to smear the simulation. For each event $(p_{sim}, \theta_{sim}, \phi_{sim})$ in the simulation, the simulated momentum p_{sim} is replaced by a random value p_{smear} sampled from the Gaussian distribution with mean value equals to p_{sim} and variance equals to $\sigma(p_{sim}, \theta_{sim}, \phi_{sim})$.

4.5 Angular distribution parametrization

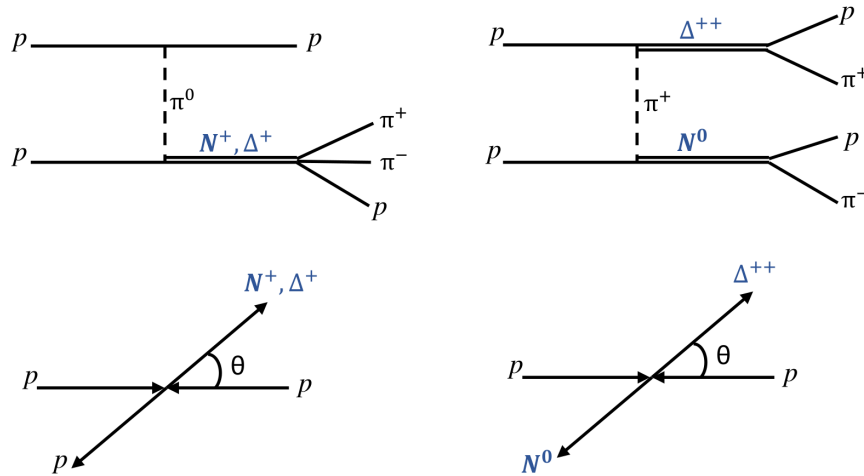


FIGURE (4.5) Top : single and double resonance production diagrams. Bottom : the same processes are illustrated in the centre of mass frame.

Figures 4.5 (top) shows the diagrams of the one and double baryon resonance production resulting from a meson exchange. Figure 4.5 (bottom) schematically shows the production of these resonances in the center of mass frame. Because there are no clear predictions about how the angular distributions should look like in these cases, it was decided to calculate these distributions based on phenomenological parameterization in the form of

$$\frac{d\sigma}{dt} \sim \frac{A}{t^\alpha} \quad (4.3)$$

where t is the Mandelstam variable or the transferred four-momentum, and is defined as follows : $t = (p_1 - p_3)^2 = (p_2 - p_4)^2$, where 1 and 2 are the indexes of the input channel particles, while 3 and 4 are the indexes of the output channel particles. In the case of the one resonance production, the four-momentum transfer can be defined as the difference between the resonance four-momentum and the projectile four-momentum (proton flying from the left in the center of mass frame), if the produced resonance flies forward. If, on the other hand, the produced resonance flies backward, we define the four-momentum transfer as the difference between the four-momentum of the resonance

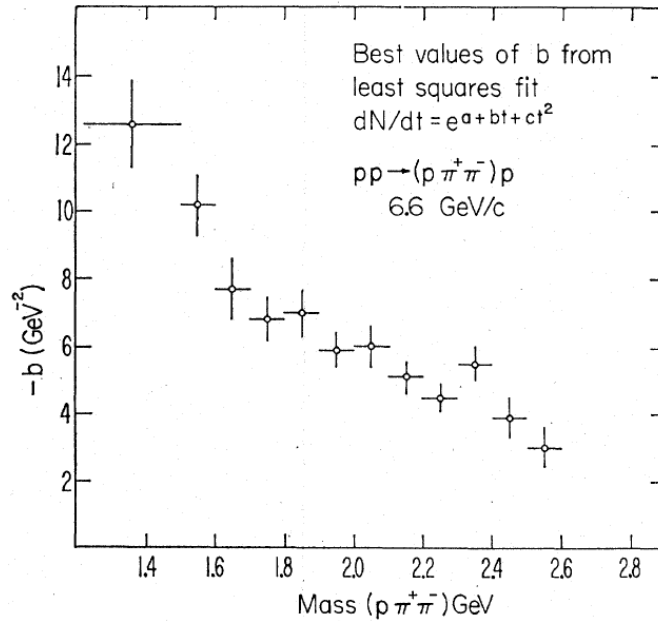


FIGURE (4.6) The value of parameter "b" of function 4.4 shown as a function of the resonances mass. (Figure taken from [113])

and of the target proton. In the case of double resonance production, the same recipe to calculate the transfer at the resonance vertex is applied. The four-momentum transfer thus is a measure of peripherality of the collision. The more peripheral the collision the smaller the absolute value of t is.

It is also worth noting the relationship between the peripheral collision and the angular distribution of the produced resonances. By parameterizing the four-momentum transfer, we therefore influence the simulated angular distributions of the produced resonances. The above parameterization based on observations from published data [113], where the authors reconstructed baryon resonances generated in proton-proton collisions at 6.6 GeV. The authors have parameterized the four-momentum transfer, using the function :

$$\frac{d\sigma}{dt} = e^{a+bt+ct^2} \quad (4.4)$$

Figure 4.6, taken from [113], shows how the parameter b changes as a function of the resonance mass. It is worth noting that the higher the resonance mass, the lower the alpha parameter and hence, the flatter the value of the function 4.4 gets. These results are consistent with the intuition which suggests that the heavier the produced resonance is, the bigger must be the absolute value of the transferred four-momentum, which means that the collision was more central, this is why large angles are being populated in the

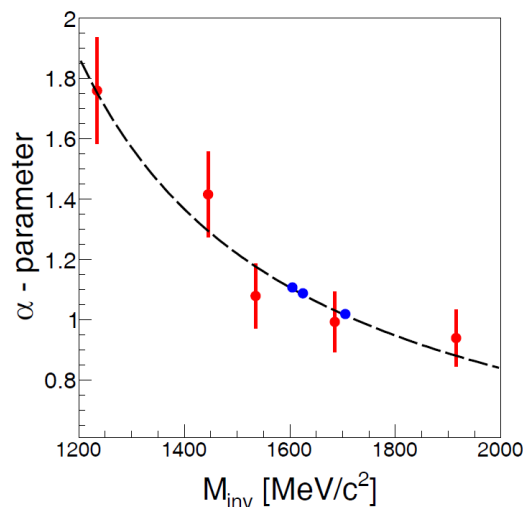


FIGURE (4.7) Dependency of the constant α from Eq.4.3 on the resonance mass obtained from fits to the data of 1π analysis [65]

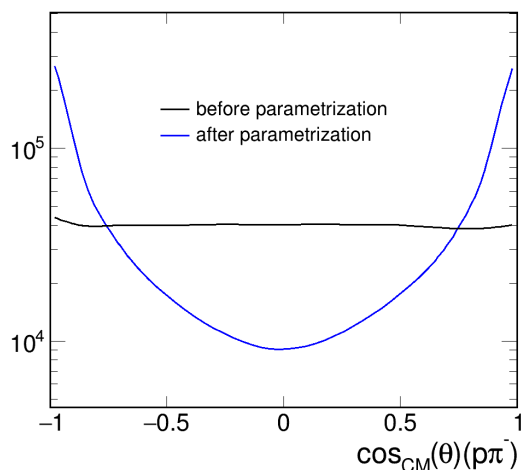


FIGURE (4.8) The results of the parameterization described in Eq.4.3 angular distribution before parameterization (black line) and after parameterization (blue line)

CM. Based on this observation, an iterative procedure to obtain the parameterization was applied in the one pion analysis. Figure 4.7 shows the dependency of the constant α on the resonance mass, this result was used to parametrize the simulation angular distributions in this work. Figure 4.8 shows an example of the $p\pi^-$ system angular distribution in the CM simulation before and after the parameterization.

4.6 Kinematics variables

Each process of a resonance production is simulated separately and the events are stored in a ROOT file containing all final state particles information. To reconstruct

the different kinematics variables (invariant masses, angular distributions...), Lorentz vectors (four-momentums) in the Lab system for both protons and pions are retrieved, One should know that in PLUTO particles are stored following the "parent" particle they originated channel. These two protons are distinguishable in the simulation. For example, in the case of the $\Delta^{++}\Delta^0$ excitation process, since in the macro, we first introduce the Δ^{++} decay and then the Δ^0 decay, the first proton stored in the ntuple is the one coming from the Δ^{++} decay and the second proton is the one coming from the Δ^0 decay. For the single resonance excitation, the second proton is the proton coming from the resonance decay since the reaction chain is written as $pp \rightarrow pN^*$. This is of course fully arbitrary but has no influence on the results, since for any comparison to the data, both protons are added.

The invariant mass of a proton-pion system is calculated as follow :

$$M_{\text{inv}}(p\pi) = (p_{p_1} + p_{\pi}).M() + (p_{p_2} + p_{\pi}).M() \quad (4.5)$$

Angular distribution in the centre of mass system are calculated after boosting the Lorentz vectors to the CM system.

5

Extraction of the baryon resonance contributions

In this chapter the analysis results for exclusive $pp \rightarrow pp\pi^+\pi^-$ channel at $\sqrt{s} = 3.18$ GeV will be discussed. The measured spectra, such as invariant mass and angular distributions, are compared in the HADES acceptance to the PLUTO simulation based on the resonance model as introduced in Chapter 4. The steps of building up the PLUTO resonances cocktail are explained in detail followed by the experimental cross sections extraction method.

5.1 Evidence for single and double baryon excitation

5.1.1 Correlations between invariant masses

As a first investigation step, we performed a two dimensional histogram analysis as shown in Figure 5.1. The aim of this analysis is to look for some resonance excitations that can show up in certain invariant mass correlations.

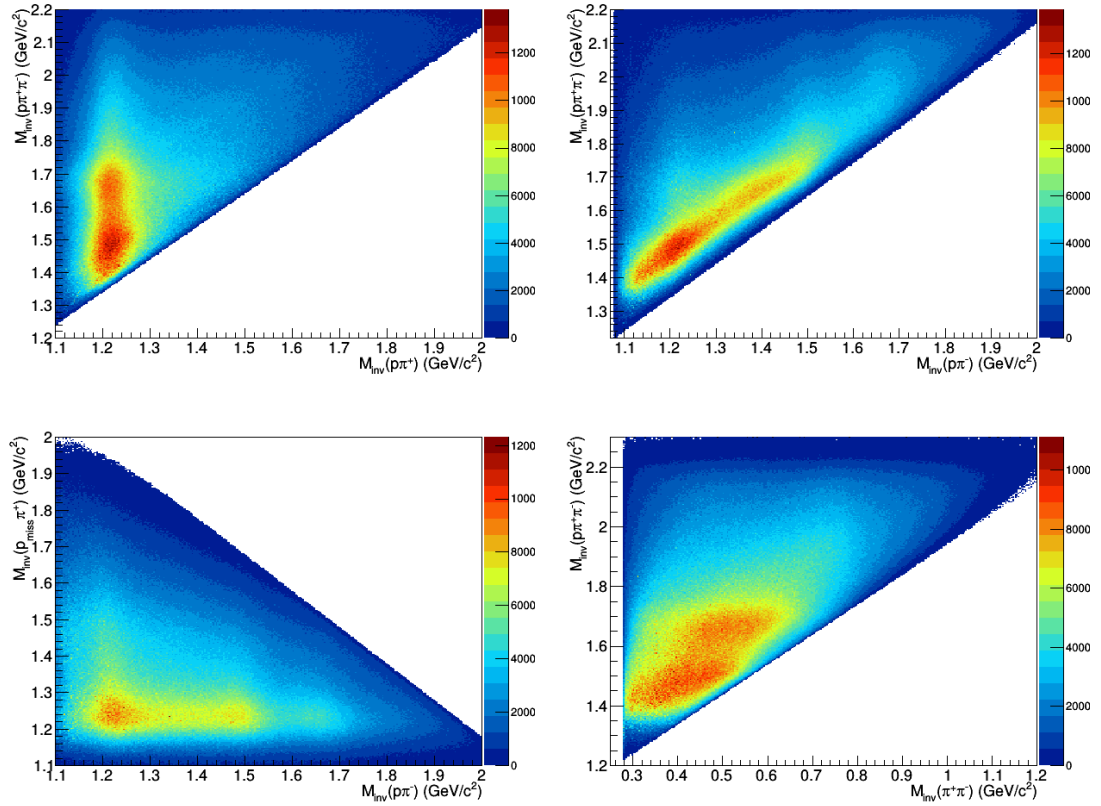


FIGURE (5.1) Top left : $M_{inv}(p\pi^+\pi^-)$ as a function of $M_{inv}(p\pi^+)$. Top right : $M_{inv}(p\pi^+\pi^-)$ as a function of $M_{inv}(p\pi^-)$. Bottom left : $M_{inv}(p\pi^+\pi^-)$ as a function of $M_{inv}(p\pi^-)$. Bottom right : $M_{inv}(p\pi^+\pi^-)$ as a function of $M_{inv}(\pi^+\pi^-)$.

The first 2D histogram displays the $M_{inv}(p\pi^+\pi^-)$ as function of $M_{inv}(p\pi^+)$ (see Figure 5.1 top left). This is an evidence for the one resonance excitation where the resonance decays to $p\pi^+\pi^-$ via an intermediate a Δ^{++} ($N^+ \rightarrow \Delta^{++}\pi^- \rightarrow p\pi^+\pi^-$) as shown by the large vertical structure around $M_{inv}(p\pi^+) = 1.2$ GeV. This is shown more clearly on the projection of $1.1 \text{ GeV} < M_{inv}(p\pi^+) < 1.3$ GeV on the $M_{inv}(p\pi^+\pi^-)$ in Figure 5.2, one can indeed see two peaks, one around 1.5 GeV and another around 1.7 GeV.

The second 2D histogram shows the correlation between the $M_{inv}(p\pi^+\pi^-)$ and the $M_{inv}(p\pi^-)$ (see Figure 5.1 top right). The comparison with the previous 2D histogram shows that the production of π^+ and π^- is not symmetric. An enhancement for $M_{inv}(p\pi^-)$ close to the Δ^0 mass is indeed clearly visible, but it is much weaker than in the $M_{inv}(p\pi^+)$ projection. This is consistent with the different isospin factors ($N^* \rightarrow \Delta^{++}\pi^- : 1/2$; $N^0 \rightarrow \Delta^-\pi^+ : 1/6$). One can also see two other vertical structures at higher $p\pi^-$ invariant mass indicating the presence of N^{*0} resonances decaying

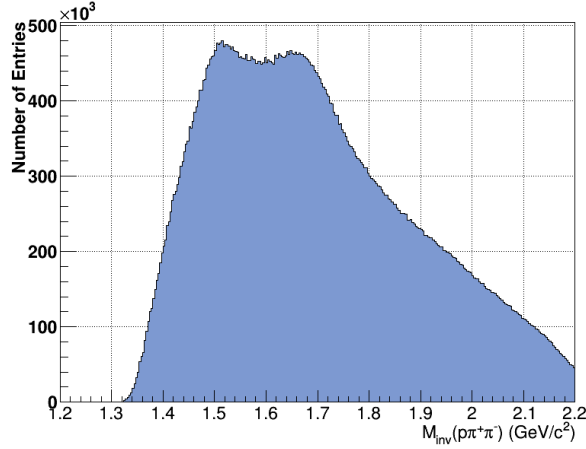


FIGURE (5.2) $1.1 \text{ GeV} < M_{inv}(p\pi^+) < 1.3 \text{ GeV}$ projection on $M_{inv}(p\pi^+\pi^-)$ showing two distinct peaks.

to $p\pi^-$. In this case, a second resonance is simultaneously excited and decays into a proton and a π^+ . To investigate this configuration, we study the correlation between the $M_{inv}(p_{miss}\pi^+)$ and the $M_{inv}(p\pi^-)$ (see Figure 5.1 bottom left). We can clearly see three vertical structures in $M_{inv}(p\pi^-)$ correlated to a horizontal structure at $M_{inv}(p_{miss}\pi^+) = 1.2 \text{ GeV}$. Figure 5.3 shows the projection on the $M_{inv}(p\pi^-)$, three peaks appear, one around 1.2 GeV, another around 1.5 GeV and a last one around 1.7 GeV. This clearly suggest the excitation of the Δ^{++} together with a Δ^0 or a N^{*0} in the second or third resonance region.

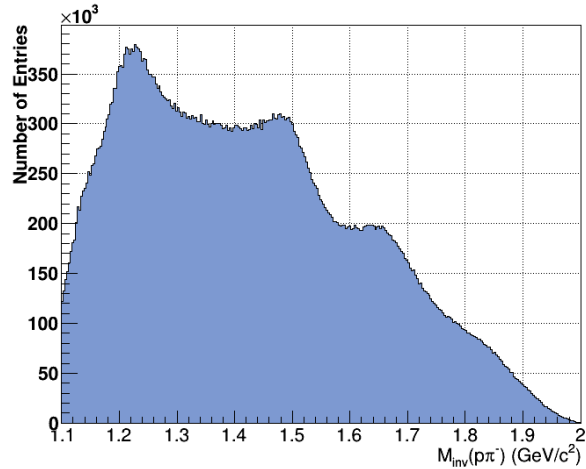


FIGURE (5.3) $1.2 \text{ GeV} < M_{inv}(p_{miss}\pi^+) < 1.3 \text{ GeV}$ projection on $M_{inv}(p\pi^-)$ showing three distinct peaks.

The fourth and the last 2D histogram is the $M_{inv}(p\pi^+\pi^-)$ as function of $M_{inv}(\pi^+\pi^-)$ (see Figure 5.1 bottom right). No clear peak appears around the ρ meson mass ($M_\rho = 0.77 \text{ GeV}$). This confirms that the production of the ρ meson is a small part of the cross section. The two structures at low $\pi^+\pi^-$ invariant mass are due to the decay of

resonances of the second and third resonance region into a nucleon and two pions, where the $M_{inv}(\pi^+\pi^-)$ and $M_{inv}(p\pi^+\pi^-)$ are correlated. Figure 5.4 shows the projection of $M_{inv}(p\pi^+\pi^-) > 1.6$ GeV on $M_{inv}(\pi^+\pi^-)$ a large peak around 0.75 GeV appears which could be a signature of the ρ meson production, this will be discussed in chapter 6.

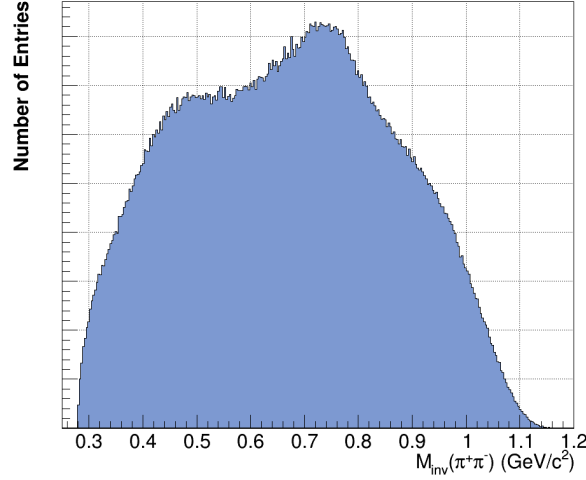


FIGURE (5.4) $M_{inv}(p\pi^+\pi^-) > 1.6$ GeV projection on $M_{inv}(\pi^+\pi^-)$ showing a large peak at 0.75 GeV.

5.1.2 Comparing data to phase space distributions

The main distributions that will be discussed in this chapter are the four invariant mass spectra : $M_{inv}(p\pi^+\pi^-)$, $M_{inv}(p\pi^+)$, $M_{inv}(p\pi^-)$, $M_{inv}(\pi^+\pi^-)$ shown in Figure 5.5 compared to $pp \rightarrow pp\pi^+\pi^-$ phase space simulation (yellow area) and the four angular distribution spectra : $\cos\theta_{CM}(p\pi^+\pi^-)$, $\cos\theta_{CM}(p\pi^+)$, $\cos\theta_{CM}(p\pi^-)$, $\cos\theta_{CM}(\pi^+\pi^-)$ in Figure 5.6 also compared to $pp \rightarrow pp\pi^+\pi^-$ phase space simulation (yellow area). The comparison to phase space confirms the presence of resonance excitations as one can see in the invariant mass distributions phase space does not show any structure contrary to data. The backward/forward peaking in angular distribution is a signature of NN peripheral collisions, the data shows a backward peaking, the forward one being suppressed due to HADES acceptance. Phase space distributions are not flat due to acceptance cuts, but the backward peaking is clearly missing, proving that it is not due to the detector acceptance effects. In the following, and in the rest of this thesis, the experimental data are shown in the HADES acceptance.

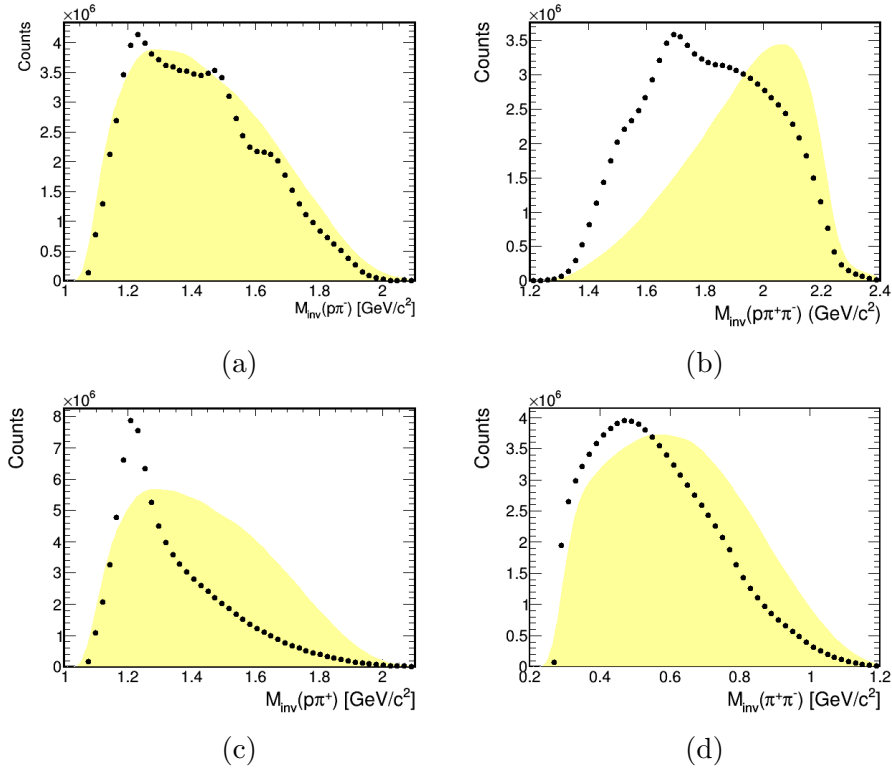


FIGURE (5.5) (a) $(p\pi^-)$, (b) $(p\pi^+)$, (c) $(p\pi^+\pi^-)$, (d) $(\pi^+\pi^-)$ invariant mass distributions compared to $pp \rightarrow pp\pi^+\pi^-$ phase space simulation (yellow area) in HADES acceptance

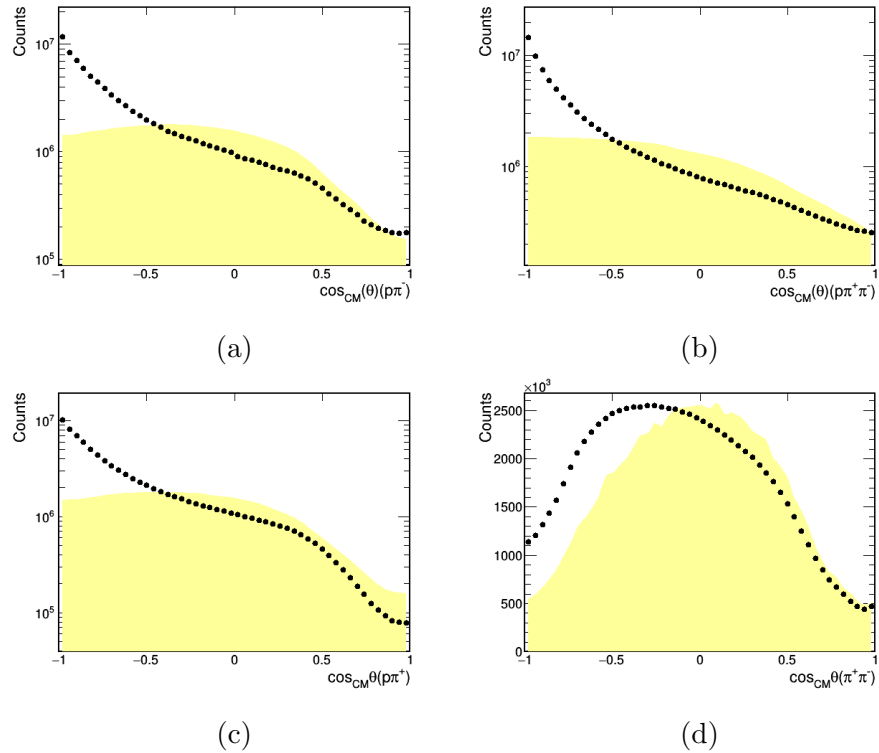


FIGURE (5.6) (a) $(p\pi^-)$, (b) $(p\pi^+)$, (c) $(p\pi^+\pi^-)$, (d) $(\pi^+\pi^-)$ center of mass angular distributions compared to $pp \rightarrow pp\pi^+\pi^-$ phase space simulation (yellow area) in HADES acceptance

5.2 Comparing Data with PLUTO simulation

A simple comparison of HADES data with our PLUTO resonance cocktail was done based on the attempt to describe the shapes of angular distributions in the center of mass frame and invariant mass distributions shown in Figures 5.5 and 5.6 to eventually extract all the contributing processes cross sections.

5.2.1 Comparing with one resonance production model

We started by comparing our data to the resonance model established using the one pion analysis [65] without any modifications. Table 5.1 shows the list of baryonic resonances with their former cross sections extracted from one pion analysis. At this level the model represents only the one resonance production ($pp \rightarrow pN^+$, $pp \rightarrow p\Delta^+$).

Resonance	$\Gamma_{N\pi\pi}/\Gamma_{tot}(\%)$	σ_R [mb]
$N(1440)$	65	1.50 ± 0.37
$N(1520)$	55	1.8 ± 0.3
$N(1535)$	46	0.15 ± 0.05
$\Delta(1600)$	15	$< 0.24 \pm 0.10$
$\Delta(1620)$	25	$< 0.10 \pm 0.03$
$N(1650)$	45	$< 0.81 \pm 0.13$
$N(1675)$	45	$< 1.65 \pm 0.27$
$N(1680)$	65	$< 0.9 \pm 0.15$
$N(1720)$	20	$< 4.4 \pm 0.7$
$\Delta(1700)$	15	$< 0.45 \pm 0.16$
$\Delta(1905)$	15	$< 0.85 \pm 0.53$
$\Delta(1910)$	25	$< 0.38 \pm 0.16$

TABLE (5.1) Cross sections in units of mb for the single positively charged resonances extracted from the one pion analysis [65] $pp \rightarrow n p \pi^+$ and $pp \rightarrow p p \pi^0$.

It can be deduced from the comparison of the invariant mass spectra shown in Figure 5.7, that the one resonance production reproduces only about 30% of the measured 2 pion channel yield. The total one resonance simulation curve (dashed green) (see Figure 5.7 left) does not show the resonant structures at $M_{inv}(p\pi^-) > 1.4$ GeV and in Figure 5.7 (right) it shows only resonant structures, while the non-resonant contribution to $M_{inv}(p\pi^+\pi^-)$ is clearly missing, which confirms the need to implement the double resonance production.

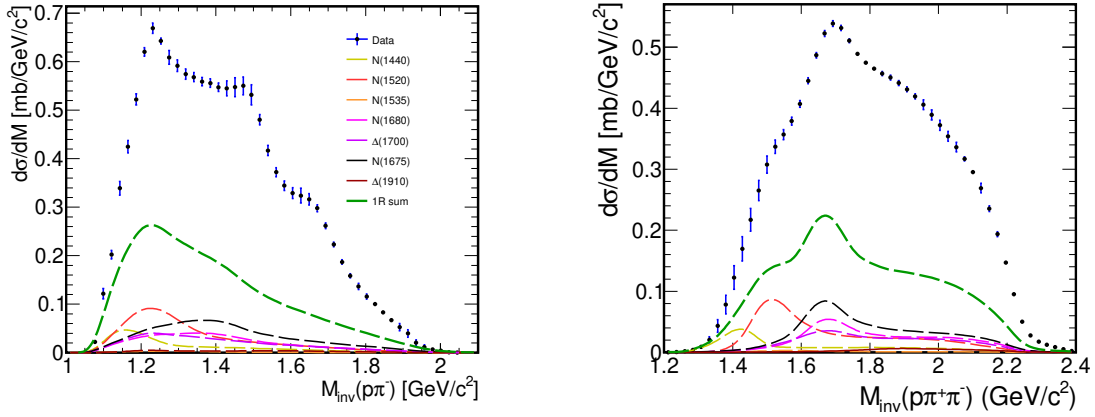


FIGURE (5.7) $p\pi^-$ invariant mass (left) and $p\pi^+\pi^-$ invariant mass (right) compared to the One resonance production simulation (dashed green)

5.2.2 Implementation of the double resonance contribution

As mentioned chapter 4, the double resonance excitations were added to the PLUTO resonance cocktail by considering the possible excitation of all the resonances in Table 5.1 together with a $\Delta^{++}(1232)$ since as shown in Section 5.1.1 the $M_{inv}(p_{miss}\pi^+)$ vs. $M_{inv}(p\pi^-)$ suggests the excitation of the Δ^{++} together with a Δ^0 or a N^{*0} .

Figure 5.8 shows the $(p\pi^-)$, $(p\pi^+\pi^-)$, $(p\pi^+)$ and $(\pi^+\pi^-)$ invariant masses distributions together with a comparison to the PLUTO resonance cocktail. Error bars include statistical and systematic errors where the former ones are negligible while the latter ones are mainly due to background subtraction and efficiency corrections. The cocktail includes the list of one resonance production ($pp \rightarrow pN^+$, $pp \rightarrow p\Delta^+$) taken from the one pion analysis [65], [111] with the former cross sections, and the double resonance production ($pp \rightarrow \Delta^{++}N^0$) where the given cross sections were set primarily manually (see Section 5.3.1).

The prominent peaks of $M_{inv}(p\pi^-)$ and $M_{inv}(p\pi^+)$ around $1.23 \text{ GeV}/c^2$ in Figures 5.8 (a) and (c) confirm the dominance of $\Delta^{++}(1232)$ and $\Delta^0(1232)$. The other two peaks around $1.52 \text{ GeV}/c^2$ and $1.68 \text{ GeV}/c^2$ of $M_{inv}(p\pi^-)$ are an evidence for the double resonance excitations $pp \rightarrow \Delta^{++}N^0(1520)$ and $pp \rightarrow \Delta^{++}N^0(1680)$. The absence of other peaks in $M_{inv}(p\pi^+)$ indicates that heavy Δ^{++} resonances do not contribute, meaning that all the double resonance productions are a $\Delta^{++}(1232)$ together with a N resonance.

The prominent peak of $M_{inv}(p\pi^+\pi^-)$ around $1.7 \text{ GeV}/c^2$ in Figure 5.8 (b) is a mixture of few heavy resonances ($N(1675)$, $N(1680)$, $N(1700)$, $\Delta(1700)$, $N(1720)$). The width

of this peak can only be reproduced by combining the resonances with mass around 1.7 GeV/c², however the highest contributions come from $N(1675)$ and $N(1680)$.

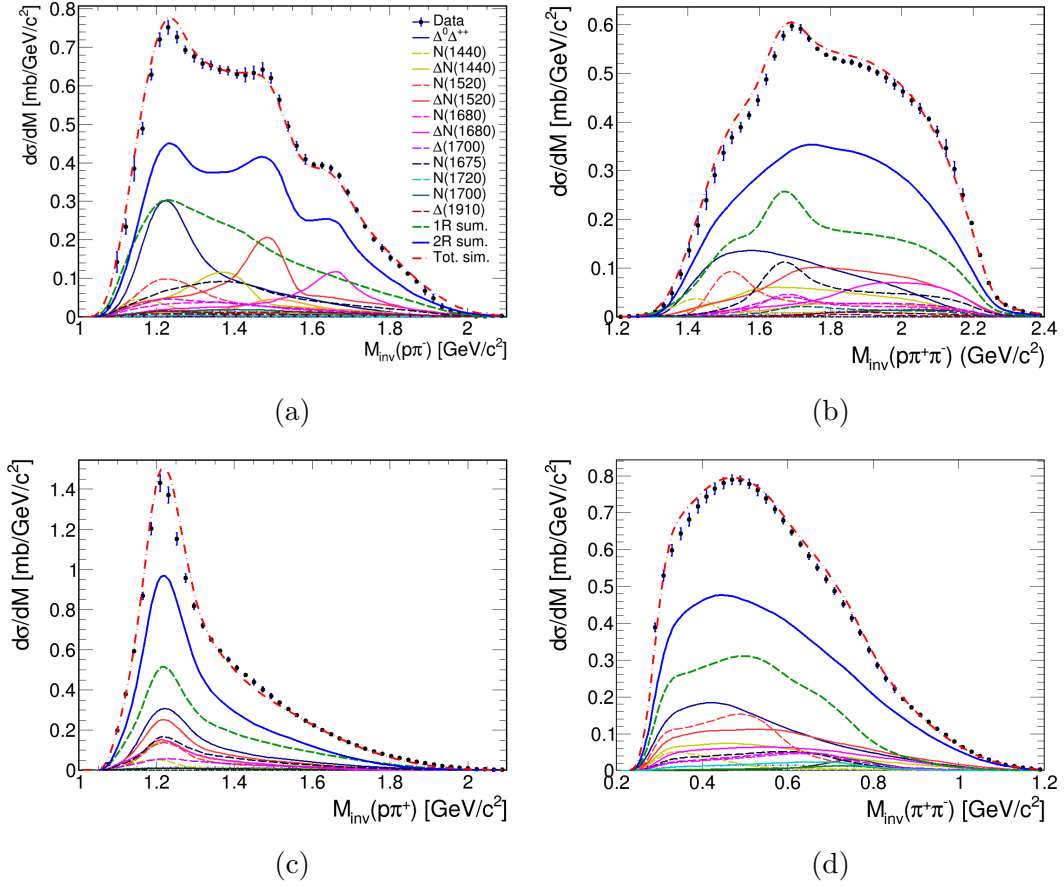


FIGURE (5.8) (a) $p\pi^-$, (b) $p\pi^+\pi^-$, (c) $p\pi^+$, (d) $p\pi^+\pi^-$ invariant mass distributions compared to the result of simulations (dashed red curves) assuming an incoherent sum of the resonance contributions shown by separate curves as indicated in the legend.

5.2.3 Sensitivity of the data to the cocktail parameters

The $p\pi^+\pi^-$ squared missing mass distribution is shown in the Figure 5.9. It peaks at the squared proton mass as expected, showing that the $pp \rightarrow pp\pi^+\pi^-$ reaction has been measured. The position and width of the proton peak is well reproduced by the PLUTO resonance cocktail which confirms the efficiency of the background subtraction strategy and the realistic description of the resolution by the simulation.

Figure 5.10 shows the four main angular distributions studied in this analysis. Our PLUTO resonance cocktail provides a reasonable description of the shape of these spectra. Some discrepancies can, however, still be found in the forward part of the CM frame, after some investigations it turned out that the acceptance matrices (see Figure 3.8) do

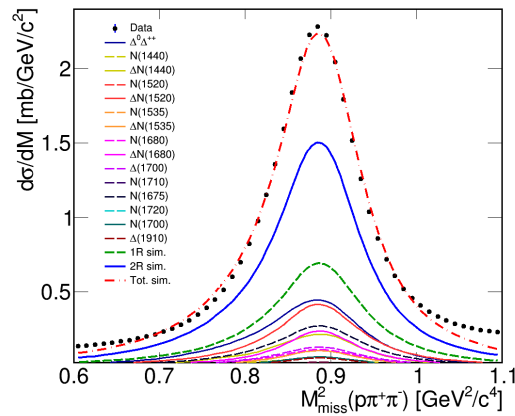


FIGURE (5.9) Squared missing mass distribution of the $p\pi^+\pi^-$ system compared to PLUTO resonances cocktail (dashed red).

not reconstruct well the particles that are emitted at a laboratory polar angle less than approximately 18° . An acceptance cut $\theta < 18^\circ$ is necessary since this detector region is not well described by simulations, one can clearly see the enhancement in Figure 4.3 at small polar angles high momentum, the effect of this enhancement is shown in angular distributions (see Figure 5.10). Figures 5.15 (e-h) show the four main angular distributions after the $\theta < 18^\circ$ cut.

The data is also sensitive to the simulation parameters. Figure 5.11 shows the $p\pi^-$ invariant mass distribution compared to old simulation with the contributions of $N(1520)$ with $M = 1520$ MeV and $\Gamma = 120$ MeV. The updated simulation of $N(1520)$ with $M = 1515$ MeV and $\Gamma = 110$ MeV (last PDG estimate [11]) fits perfectly the data (see Figure 5.15 (a)).

This aspect is also the reason why we could include both $N^+(1675)$ and $N^+(1680)$ resonances, their cross sections were given in the one pion analysis [65] only as an upper limit. To prove the presence of both resonances in this reaction, two comparisons were performed, in the first one only the $N^+(1675)$ was added, the result is shown in Figure 5.12(a), we can clearly see the shift to the left of the peak (dashed red curve). In the second one only $N^+(1680)$ was added, the result is shown in Figure 5.12(b), one can clearly see that the simulation cocktail with only $N^+(1680)$ doesn't fit the data.

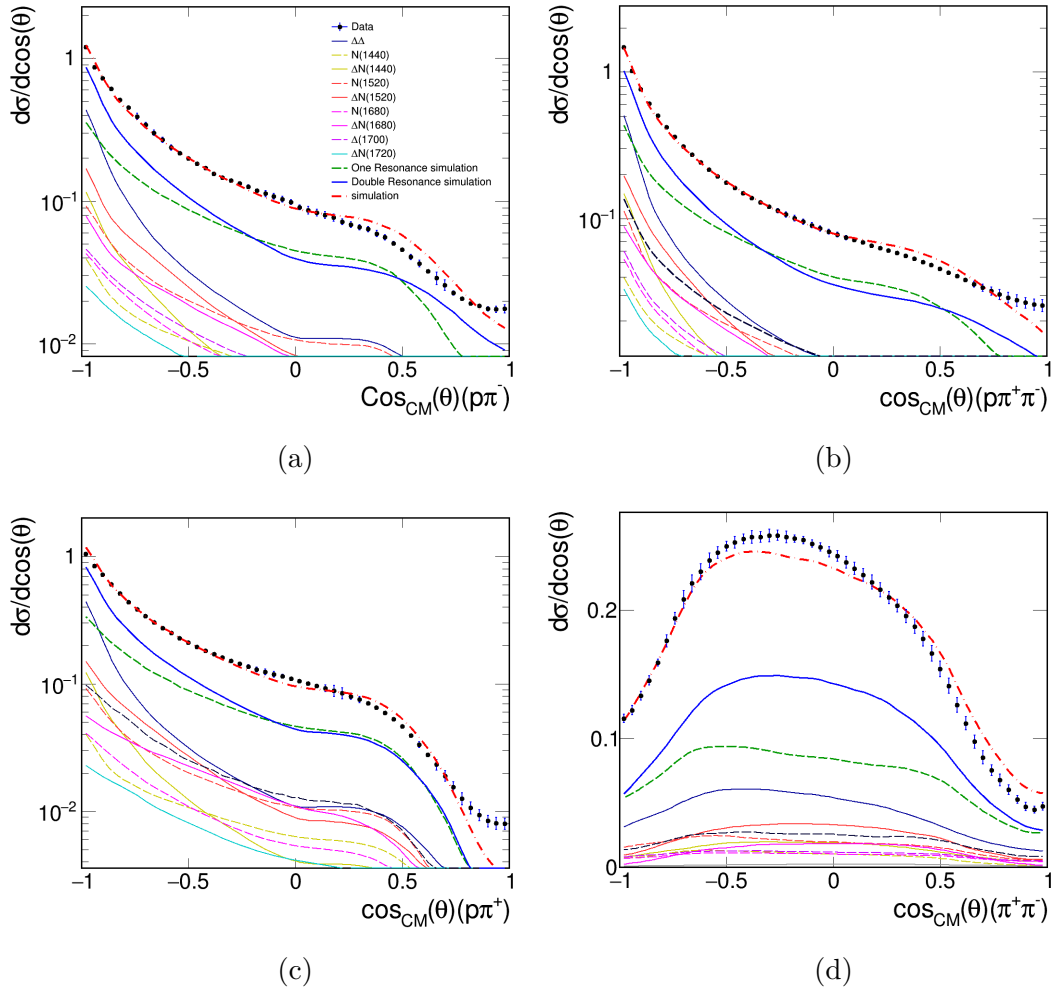


FIGURE (5.10) (a) $(p\pi^-)$, (b) $(p\pi^+)$, (c) $(p\pi^+\pi^-)$, (d) $(p\pi^+\pi^-)$ angular distributions compared to the result of simulations (dashed red curves) assuming an incoherent sum of the resonance contributions shown by separate curves as indicated in the legend.

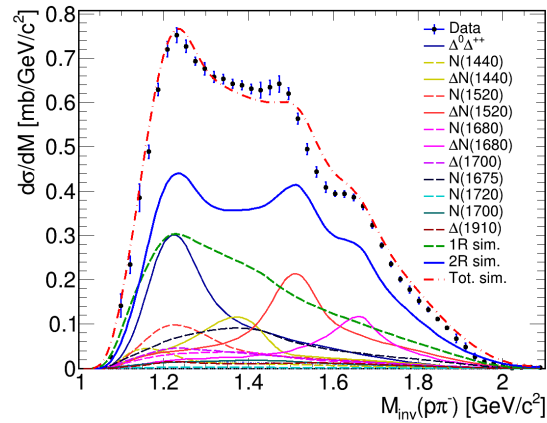


FIGURE (5.11) $p\pi^-$ invariant mass distribution with the contribution of $N(1520)$ with mass 1520 MeV and width 120 MeV

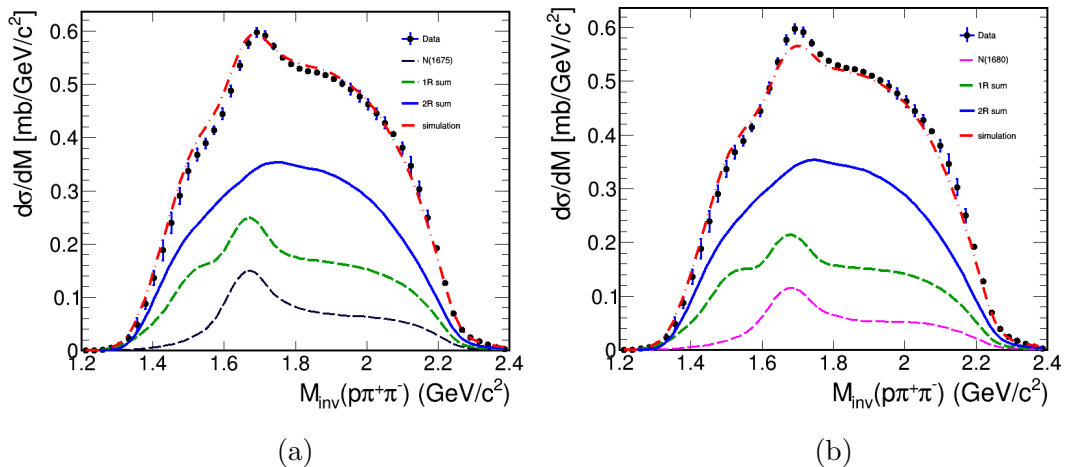


FIGURE (5.12) (a) $(p\pi^+\pi^-)$ invariant mass distribution compared to a resonance cocktail without $N(1680)$ contribution, (b) without $N(1675)$ contribution.

5.3 Extraction of the Cross Sections

In order to obtain the value of cross-sections of the different contributions, the following strategy was adopted :

5.3.1 Manually adjusted cross sections

As mentioned in Section 5.2.1, the one resonance production cross sections were taken from the one pion analysis [65] (see Table 5.1). These cross sections were extracted for the production of the positively charged resonance, so they can be directly used in our analysis, together with the branching ratio towards $N\pi\pi$. Some groups of resonances could not be separated in the one pion analysis. In these cases the resonance with the largest coupling to pion and dielectron channels (in bold) was used in simulations of Ref.[65] and only upper limits of the cross-sections were set. In our analysis, the cross-sections contributions of resonances for which only an upper limit were adjusted to the data.

The analysis presented in [111] allowed to extract amplitudes for the excitation of various resonances in the $pp \rightarrow pK\Lambda$ channel, which we convert into cross sections for the $pp \rightarrow pp\pi^+\pi^-$ using the branching ratios to $N\pi\pi$ and $pK\Lambda$, $\sigma_{p\pi\pi} = \frac{\Gamma_{N\pi\pi}}{\Gamma_{K\Lambda}} \sigma_{pK\Lambda}$. As can be observed in Table 5.2, this results have large error bars. This uncertainty is mainly due to the bad knowledge of the $K\Lambda$ branching ratios, but the systematic error in the determination of the $pK\Lambda$ amplitudes also plays a role. Despite these large errors,

the $pK\Lambda$ channel gives some information for the excitation of the five heavy resonances $N(1650)$, $N(1710)$, $N(1720)$, $N(1875)$, $N(1880)$. For two of these resonances, only an upper limit could be extracted from the one pion analysis [65]. These upper limits were still compatible with the results deduced from the $pK\Lambda$ analysis.

Resonance	$\Gamma_{K\Lambda}/\Gamma_{tot}(\%)$	$\sigma(N^* \rightarrow pK\Lambda)[\mu b]$	$\Gamma_{N\pi\pi}/\Gamma_{tot}(\%)$	$\sigma(N^* \rightarrow p\pi\pi)[\mu b]$
$N^*(1650)$	7 ± 4	$8.6 \pm 0.6 \pm 2.1$	38 ± 4	27.0 ± 17.1
$N^*(1710)$	15 ± 10	$11.7 \pm 1.0 \pm 2.8$	23 ± 10	23.4 ± 19.6
$N^*(1720)$	4 ± 1	$2.4 \pm 1.3 \pm 0.4$	70 ± 20	42.0 ± 19.5
$N^*(1875)$	4 ± 2	$1.5 \pm 1.3 \pm 0.4$	70 ± 20	26.5 ± 27.0
$N^*(1880)$	2 ± 1	$14.9 \pm 0.2 \pm 3.6$	55 ± 25	409.7 ± 294.0

TABLE (5.2) Cross sections in units of μb for the single positively charged resonances extracted from $pp \rightarrow pK\Lambda$ analysis (third column) normalized to the $p\pi\pi$ channel (fifth column). $K\Lambda$ BR (second column), $N\pi\pi$ BR (forth column) taken from the PDG [11]

Then, the double resonance production cross-sections were adjusted to reproduce the data, the double $\Delta^{++}(1232)\Delta^0(1232)$ being the most important channels of this type, followed by $\Delta^{++}(1232)N^0(1440)$, $\Delta^{++}(1232)N^0(1520)$, $\Delta^{++}(1232)N^0(1680)$, the other double resonances don't show any evidence of contribution as it will be shown below.

A first adjustment of the cross sections was done manually. The $p\pi^-$ invariant mass distribution is mainly used to adjust the cross sections of the different double resonance productions, then the unknown cross sections for the excitation of heavy baryons are adjusted at best to fit the $p\pi^+\pi^-$ invariant mass distribution. The manually adjusted cross sections are given in Table 5.3. The $\tilde{\chi}^2$ test result is : $\tilde{\chi}^2/n_d = 7.9$, where n_d is the number of degrees of freedom. $n_d = 50$ bins - 25 contributions = 25.

5.3.2 Automatic fitting procedure

In a second step, a $\tilde{\chi}^2$ minimization was performed to find corrections with respect to the cross sections values obtained in the manual adjustment. The fit parameters being the correction factors for the cross-sections. We used ROOT class MINUIT, a system for function minimization and analysis of the parameter errors and correlations [114]. The function to minimize is :

$$\tilde{\chi}^2 = \sum_i^N \left(\frac{z_i - \sum_j^m a_j R_{ij}}{\sigma_i} \right)^2 \quad (5.1)$$

Where z_i is the integrated experimental cross section in the bin i , σ_i is the error for the bin i , R_{ij} are the integrated simulation cross section, and a_j are the correction factors to be extracted.

The invariant mass spectra $M(p\pi^+)$, $M(p\pi^-)$, $M(p\pi^+\pi^-)$ and $M(\pi^+\pi^-)$ were used in this minimization. The minimization was done using MIGRAD, a minimization subroutine based on a variable metric method. It is extremely fast near a minimum but slower if the function is badly behaved. It uses the first derivatives of the function, which may either be supplied by the user or estimated by MINUIT [114].

Resonance	Manual σ [mb]	Parameter	Error
$\Delta^{++}\Delta^0$	3.45	1.08	0.04
$\Delta^{++}N^0(1440)$	1.5	0.54	0.03
$\Delta^{++}N^0(1520)$	1.6	0.94	0.03
$\Delta^{++}N^0(1535)$	0.15	0.99	0.06
$\Delta^{++}N^0(1680)$	0.8	1.00	0.02
$\Delta^{++}\Delta^0(1600)$	0.04	0.05	0.001
$\Delta^{++}\Delta^0(1620)$	0.05	0.1	0.003
$\Delta^{++}N^0(1650)$	0.01	0.02	0.002
$\Delta^{++}\Delta^0(1700)$	0.06	0.06	0.005
$\Delta^{++}N^0(1720)$	0.01	0.02	0.001
$\Delta^+(1600)$	0.04	0.04	0.003
$\Delta^+(1620)$	0.1	0.50	0.02
$N^+(1675)$	0.8	1.31	0.02
$N^+(1680)$	1.0	0.86	0.07
$N^+(1700)$	0.15	1.26	0.13
$\Delta^+(1910)$	0.015	3.0	0.4
$N^+(1650)$	0.027	0.99	0.01
$N^+(1710)$	0.024	0.98	0.02
$N^+(1720)$	0.042	1.02	0.02
$N^+(1875)$	0.027	1.01	0.01
$N^+(1880)$	0.41	1.00	0.01

TABLE (5.3) χ^2 minimization correction parameters, Red rows : non contributing resonances. Cyan rows : fixed parameters.

The minimization was done in three steps. This was necessary since the total number of selected contributions was 25. In the first step we fixed 4 contributions : $N(1440)$, $N(1520)$, $N(1535)$ and $\Delta(1700)$ and we kept the 21 left contributions as free parameters, starting with the cross section values in Table 5.3. The minimization resulted in correction factors smaller than 0.1 for the following contributions : $\Delta^{++}\Delta^0(1600)$, $\Delta^{++}\Delta^0(1620)$, $\Delta^{++}N^0(1650)$, $\Delta^{++}\Delta^0(1700)$, $\Delta^{++}N^0(1720)$ and $\Delta^+(1600)$ (See Table 5.3 red rows). Hence, they were considered as non contributing, since their initial cross

sections were already very small (below $0.05 \mu\text{b}$) and the final result is compatible with zero within 1 or 2 σ .



FIGURE (5.13) Minimization parameter correlation matrix for 15 parameters. First column : global correlation.

In the second step the minimization algorithm was run again with 15 free parameter. The result showed that the resonances of the $pK\Lambda$ analysis have a correction parameter very close to 1 (See Table 5.3 cyan rows). The errors on the different parameters are also listed. Figure 5.13 shows the correlation matrix of the 15 parameters, the correlation parameters of these resonances (See Table 5.3 cyan rows) are relatively low, which confirms that the information deduced for these resonances is very valuable. To check the stability of the fit with respect to the contributions of these heavy resonances, we fixed their cross sections to the central values of the $pK\Lambda$ analysis, which allows to perform a last minimization. In this case, we obtain a better $\tilde{\chi}^2$ ($\tilde{\chi}^2/n_d = 5.1$), which is expected due to the lower number of parameters. Most importantly, the values of the cross sections are compatible with the ones from the previous fit. So for the third step,



FIGURE (5.14) Minimization parameter correlation matrix for 10 parameters. First column : global correlation.

the minimization algorithm was run with only 10 free parameters, the calculated parameters are listed in Table 5.3 (white rows). Figure 5.14 shows the correlation matrix of these 10 parameters, this matrix is important because it indicates the reliability of the minimization for example there is no correlation coefficient that is exactly equal to zero or very close to one (0.99).

The final result of the extracted cross sections of the 19 contributions in pp collision at 3.5 GeV is given in Table 5.4 (second column). The $\tilde{\chi}^2$ test result is : $\tilde{\chi}^2/n_d = 1.23$. The errors represent the quadratic sum of the fit error and the error on the branching ratios from the PDG, the global systematic error coming from the normalization is not shown. To obtain the cross sections in the $p\pi^+\pi^-$ channel (fourth column) we multiplied the resonances cross sections (σ_R) by the corresponding $N\pi\pi$ branching ratio and isospin factor (third column). The errors come from the fitting procedure uncertainty. The total

cross section for $pp \rightarrow pp\pi^+\pi^-$ reaction at $T_p = 3.5$ GeV deduced from this analysis is : $\sigma_{tot} = 3.51 \pm 0.15$ mb. Figure 5.15 represents the best fit of the four invariant mass distributions and the four angular distributions.

Resonance	σ_R [mb]	$BR_{N\pi\pi} \times I$	$\sigma_R^{p\pi^+\pi^-}$ [mb]
$N^+(1440)$	1.5 ± 0.4	0.17 ± 0.04	0.250 ± 0.017
$N^+(1520)$	1.8 ± 0.3	0.16 ± 0.03	0.29 ± 0.016
$N^+(1535)$	0.15 ± 0.03	0.023 ± 0.005	0.0030 ± 0.0002
$\Delta^+(1620)$	0.05 ± 0.01	0.44 ± 0.09	0.022 ± 0.002
$N^+(1650)$	0.027 ± 0.008	0.09 ± 0.02	0.002 ± 0.0001
$N^+(1675)$	1.05 ± 0.23	0.25 ± 0.05	0.26 ± 0.004
$N^+(1680)$	0.80 ± 0.08	0.016 ± 0.02	0.128 ± 0.011
$N^+(1700)$	0.10 ± 0.025	0.4 ± 0.1	0.04 ± 0.004
$\Delta^+(1700)$	0.45 ± 0.13	0.38 ± 0.10	0.17 ± 0.02
$N^+(1710)$	0.024 ± 0.008	0.09 ± 0.03	0.002 ± 0.0001
$N^+(1720)$	0.045 ± 0.005	0.33 ± 0.03	0.0148 ± 0.0003
$N^+(1875)$	0.027 ± 0.013	0.36 ± 0.17	0.0097 ± 0.0004
$N^+(1880)$	0.41 ± 0.20	0.16 ± 0.07	0.066 ± 0.003
$\Delta^+(1905)$	0.045 ± 0.005	0.56 ± 0.06	0.025 ± 0.003
$\Delta^{++}\Delta^0$	3.7 ± 0.15	0.33 ± 0.0	1.22 ± 0.05
$\Delta^{++}N^0(1440)$	0.81 ± 0.13	0.36 ± 0.05	0.54 ± 0.01
$\Delta^{++}N^0(1520)$	1.50 ± 0.10	0.46 ± 0.03	0.37 ± 0.02
$\Delta^{++}N^0(1535)$	0.46 ± 0.10	0.30 ± 0.06	0.138 ± 0.003
$\Delta^{++}N^0(1680)$	0.80 ± 0.07	0.43 ± 0.03	0.34 ± 0.01

TABLE (5.4) Cross sections in units of mb for the single and double resonances production in pp collisions extracted from $pp \rightarrow pp\pi^+\pi^-$ analysis. The errors represent the quadratic sum of the fit error and the error on the branching ratios. The resonances cross sections for the channel $pp\pi^+\pi^-$ are given in the last column by multiplying $\sigma_R \times BR_{N\pi\pi} \times I$. The errors represent the uncertainty on the fitting procedure.

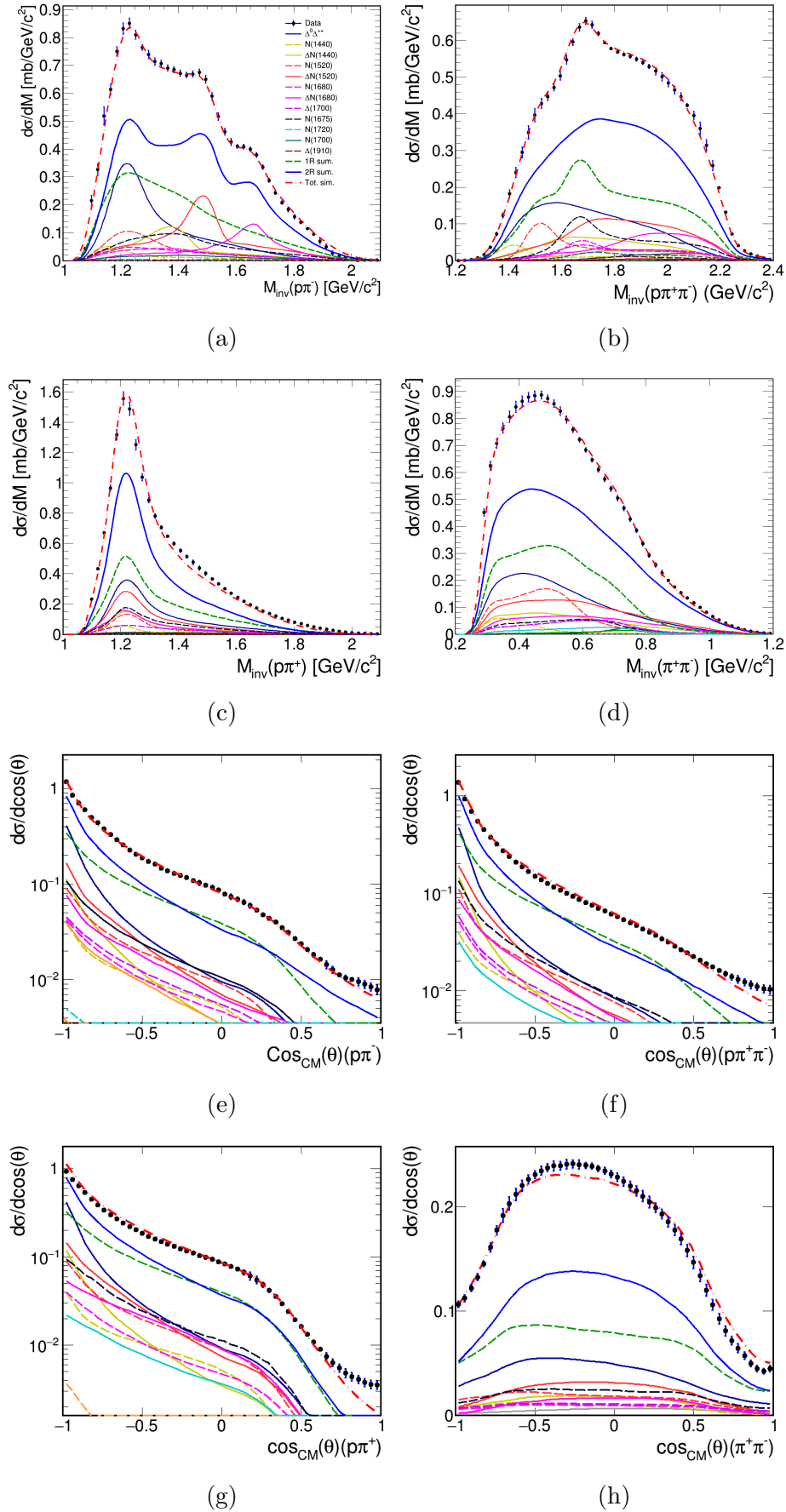


FIGURE (5.15) (a) $p\pi^-$, (b) $p\pi^+\pi^-$, (c) $p\pi^+$, (d) $p\pi^+\pi^-$ invariant mass distributions and (e) ($p\pi^-$), (f) ($p\pi^+$), (g) ($p\pi^+\pi^-$), (h) ($p\pi^+\pi^-$) angular distributions compared to PLUTO resonance cocktail best fit (dashed red curves) assuming an incoherent sum of the resonance contributions shown by separate curves as indicated in the legend.

5.3.3 Impact of the results for dielectron production

With respect to the one pion analysis [65], the two pion analysis allowed to extract more precise cross sections for $N(1440)$, $N(1520)$, $N(1535)$ and $\Delta(1700)$ contributions. As shown in Table 5.4 the errors for these resonances were reduced by a factor 3. This is due to the large sensitivity of the $p\pi^+\pi^-$ invariant mass distribution to these contributions. In addition, for the excitation of higher lying resonances, only upper limits of the cross sections were extracted from the one pion analysis. Due to the high $2\pi N$ branching ratios, cross sections values could be extracted, which are consistent with these upper values.

Also the obtained results with the minimization method are compatible with the $pK\Lambda$ analysis [111]. Indeed, although the cross sections of the heavy resonances ($N(1650)$, $N(1710)$, $N(1720)$, $N(1875)$ and $N(1880)$) are relatively small, our data is still sensitive to their contribution, any small excess will distort the $p\pi^+\pi^-$ invariant mass distribution above $1.8 \text{ GeV}/c^2$.

It was also possible to extract cross sections for double resonance excitation. Although the applied model assumes a simplified reaction mechanism ignoring interferences between various intermediate states it describes the data surprisingly well. However the effect of the interferences will be discussed in Chapter 7.

These results are very valuable since they add some missing building blocks for the dilepton production. As mentioned in Section 1.4.3 the resonances cocktail obtained from the one pion analysis [65] was used for the interpretation of the exclusive dilepton channel $pp \rightarrow ppe^+e^-$. More precisely, for each resonance the differential Dalitz decay width was calculated as a function of the e^+e^- invariant mass and all these contributions were added to generate the e^+e^- mass distribution. By doing this, electromagnetic form factors were assumed to be the same as for the radiative decays (point-like assumption), which means that for a given transition, the Dalitz decay yield is just proportional to the radiative decay branching ratio. The shape of the distribution depends however on the spin and parity of the transition. This work [65] could be updated, using the new values of resonance contributions deduced from the two pion analysis. In addition, in the meantime, a more precise information on the radiative decay width of some baryonic resonances is available in the PDG, which can also be used. Table 5.5 summarizes the new inputs for a dilepton cocktail. The cross sections are the result of our analysis and the

branching ratios are updated from [67] using the new values of radiative decay branching ratios from the PDG [11]. Such inputs could therefore be used to produce a new cocktail of point-like resonance Dalitz decay and e.g. to update the simulation results in Figure 1.17 (a). This detailed calculation is outside of the scope of this work and could be the subject of further studies. Since the one resonance production cross sections are compatible with [65] and most of the radiative decay branching ratios stayed within the error bars, we expect mainly a reduction of the uncertainties for the simulations of $pp \rightarrow ppe^+e^-$.

Also, the inputs for both one and two resonance excitations could be used for a simulation of the baryonic contribution to the inclusive $pp \rightarrow e^+e^-X$ reaction [115] where one resonances decays to Ne^+e^- and the other decays to a hadronic channel.

Resonance	σ_R [mb]	$BR_{QED}^{pe^+e^-}$
$N^+(1440)$	1.5 ± 0.4	3.06×10^{-6}
$N^+(1520)$	1.8 ± 0.3	3.13×10^{-6}
$N^+(1535)$	0.15 ± 0.03	1.66×10^{-5}
$\Delta^+(1620)$	0.05 ± 0.01	1.73×10^{-6}
$N^+(1650)$	0.027 ± 0.008	8.74×10^{-6}
$N^+(1675)$	1.05 ± 0.23	1.45×10^{-6}
$N^+(1680)$	0.80 ± 0.08	1.92×10^{-5}
$N^+(1700)$	0.10 ± 0.025	2.19×10^{-6}
$\Delta^+(1700)$	0.45 ± 0.13	2.98×10^{-5}
$N^+(1710)$	0.024 ± 0.008	2.91×10^{-6}
$N^+(1720)$	0.045 ± 0.005	1.09×10^{-5}
$\Delta^+(1905)$	0.045 ± 0.005	7.31×10^{-6}

TABLE (5.5) Cross sections in units of mb for the single resonances extracted from this analysis and their updated QED branching ratios.

5.4 Dibaryon investigation

In this part we investigate about the isotensor dibaryon D_{21} with quantum numbers $IJ^P = 21^+$ reported recently by WASA at COSY [102, 103] with mass $M = 2140 \pm 10$ MeV and width $\Gamma = 110 \pm 10$ MeV in their measurements of quasi free $pp \rightarrow pp\pi^+\pi^-$ reaction by means of pd collisions at $T_p = 1.2$ GeV. Because of its isospin $I = 2$, this state cannot be excited directly by incident NN collisions, but only by the production of an additional pion, which carries away one unit of isospin. By isospin selection the decay of an isotensor $N\Delta$ state will dominantly proceed into the purely isotensor $pp\pi^+$

channel. Hence the $pp \rightarrow pp\pi^+\pi^-$ reaction is the ideal place to look for the process $pp \rightarrow D_{21}^{++++}\pi^- \rightarrow pp\pi^+\pi^-$ [103].

Figure 5.16 (a) shows the $pp\pi^+$ invariant mass distribution measured in our experiment. Since we select the $pp \rightarrow pp\pi^+\pi^-$ reaction by detecting the two pions and one proton, this invariant mass is simply the missing mass of the reaction $pp \rightarrow \pi^- X$. No structure is visible for this spectrum at low $M_{inv}(pp\pi^+)$ invariant masses where the dibaryon is expected to show up. To further investigate the presence of the D_{21} dibaryon in more details, we simulated the process $pp \rightarrow D_{21}^{++++}\pi^- \rightarrow \Delta^{++}p\pi^- \rightarrow pp\pi^+\pi^-$, where D_{21}^{++++} is a dibaryon with $M = 2140$ MeV and $\Gamma = 110$ MeV using phase-space and added this contribution to our resonance cocktail.

Figure 5.16 (a) shows the $M_{inv}(pp\pi^+)$ distribution compared to the resonance cocktail (dashed red curve) including the D_{21}^{++++} contribution. The same figure is shown in logarithmic scale (see Figure 5.16 (b)) to bring out the dibaryon contribution (violet curve). The $\tilde{\chi}^2$ minimization method was used to extract the dibaryon cross section, the result is $\sigma_{D_{21}} = 0.3 \pm 0.1 \mu\text{b}$.

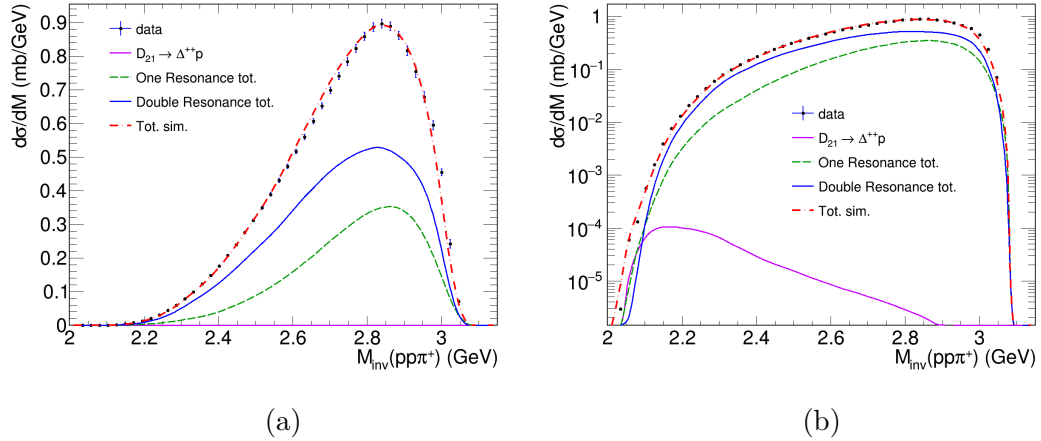


FIGURE (5.16) (a) $(pp\pi^+)$ invariant mass distribution compared to PLUTO resonance cocktail (dashed red) + the D_{21} dibaryon (violet). (b) same in logarithmic scale.

Taking into account the hypothesis that the dibaryon is masked by the high background of the single and double resonance contributions we applied the following invariant mass cuts : $M_{inv}(p\pi^+) < 1.25$ GeV, $M_{inv}(p\pi^-) > 1.4$ GeV and $M_{inv}(p\pi^+\pi^-) > 1.7$ GeV. These cuts do not affect the dibaryon distribution but reduce the background by a factor 10 as shown in Figure 5.17. The $\tilde{\chi}^2$ minimization method gave the same fit result $\sigma_{D_{21}} = 0.3 \pm 0.1 \mu\text{b}$. This cross section is much lower than in WASA analysis at $T_p =$

1.2 GeV (see Figure 1.21). However, this result should rather be considered as an upper limit, since this part of the spectrum is very sensitive to resolution effects.

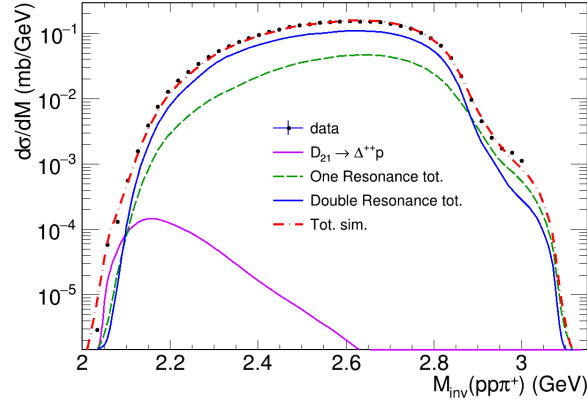


FIGURE (5.17) (a) $(pp\pi^+)$ invariant mass distribution in logarithmic scale compared to PLUTO resonance cocktail (dashed red) + the D_{21} dibaryon (violet) reduced by a factor 10 after invariant mass cuts.

One could also investigate the D_{21}^+ dibaryon that can be produced in the process $pp \rightarrow D_{21}^+\pi^+ \rightarrow \Delta^0 p\pi^+ \rightarrow pp\pi^+\pi^-$ but due to isospin coupling the branching via Δ^0 is very small. Indeed the Clebsch-Gordon coefficients are :

$$D_{21}^{++++} \rightarrow \Delta^{++}\pi^+ : |2, 2\rangle = 1 \left| \frac{3}{2}, \frac{3}{2} \right\rangle \left| \frac{1}{2}, \frac{1}{2} \right\rangle$$

$$\Delta^{++} \rightarrow p\pi^+ : \left| \frac{3}{2}, \frac{3}{2} \right\rangle = 1 \left| \frac{1}{2}, \frac{1}{2} \right\rangle |1, 1\rangle$$

$$D_{21}^+ \rightarrow \Delta^0\pi^+ : |2, 0\rangle = \sqrt{\frac{1}{2}} \left| \frac{3}{2}, -\frac{1}{2} \right\rangle |1, 1\rangle$$

$$\Delta^0 \rightarrow p\pi^- : \left| \frac{3}{2}, -\frac{1}{2} \right\rangle = \sqrt{\frac{1}{3}} \left| \frac{1}{2}, \frac{1}{2} \right\rangle |1, -1\rangle$$

which leads to the following cross sections relation :

$$\frac{\sigma_{(D_{21}^+ \rightarrow \Delta^0 \pi^+)}}{\sigma_{(D_{21}^{++++} \rightarrow \Delta^{++} \pi^+)}} = \frac{1}{6} \quad (5.2)$$

6

Extraction of the light meson contributions

6.1 Introduction

Other interesting processes contributing to the double pion production final state are the production of light mesons that decay to the $\pi^+\pi^-$ channel. Considering the energy available in our experiment, three mesons can be produced :

- $f_0(500)$ or σ ($M = 400\text{-}550$ MeV, $\Gamma = 400\text{-}700$ MeV).
- $\rho(770)$ ($M = 769$ MeV, $\Gamma = 150$ MeV).
- $f_0(980)$ ($M = 990 \pm 20$ MeV, $\Gamma = 10$ to 100 MeV).

Data for the production of these mesons in pp reactions exist only in the case of the ρ meson, which is expected to be the most strongly produced, albeit with a cross section of the order of only 100 μb , i.e. much lower than the excitation of baryonic resonances. In this chapter we first present the detailed analysis and results for the ρ meson production, since it is of a particular interest for the dilepton analysis and for the transport models and then investigate possible contributions of the f_0 mesons

6.2 ρ meson

It has to be noted that our simulation used for the extraction of the baryonic resonance contribution included the ρ meson production in two different processes :

1. A production via excitation of a baryonic resonance, i.e $pp \rightarrow pN^*$, $N^* \rightarrow p\rho \rightarrow p\pi^+\pi^-$. In this case, the branching ratios were taken from the Bonn-Gatchina PWA (see Table 6.1).
2. A direct contribution, simulated according to phase space with a cross section of $80 \mu b$, in agreement with existing experiments.

Our aim is now to extract more precisely this direct ρ contribution by using cuts to suppress $\pi^+\pi^-$ production from baryons. We will also discuss the ambiguities related to this distinction between "resonance- ρ " and "direct- ρ " production, since the amplitudes of both contributions should in principle interfere.

Resonance	Bonn-Gatchina $N\rho(\%)$	PDG $N\rho(\%)$	σ_ρ^R [μb]
$N(1440)$	< 1	< 8	0
$N(1520)$	12 ± 2	15-25	72 ± 12
$N(1535)$	3 ± 1	< 4	1.5 ± 0.5
$N(1675)$	< 1	$< 1-3$	0
$N(1680)$	12 ± 2	3-15	32 ± 5
$N(1700)$	45 ± 15	< 35	15 ± 5
$N(1720)$	60 ± 18	70-85	9 ± 3
$N(1875)$	60 ± 14	seen	5.4 ± 1.2
$N(1880)$	30 ± 8	-	41 ± 10
$\Delta(1700)$	44	30-55	66 ± 7
$\Delta(1905)$	47	< 60	6.7 ± 0.6

TABLE (6.1) Branching ratios for decay of the resonances into $N\rho$ channel, from Bonn-Gatchina PWA and the PDG.

6.2.1 ρ meson signal extraction

The invariant mass distribution of the pion pair from the light mesons decay is swamped by the background from the pion pairs that stem from the reactions $pp \rightarrow \Delta R \rightarrow pp\pi^+\pi^-$ and $pp \rightarrow pR \rightarrow pp\pi^+\pi^-$. As shown in Figure 5.15 (d), the $\pi^+\pi^-$ invariant mass does not show an evidence of the ρ^0 meson production. Therefore in order to extract the ρ^0 meson signal we had to apply specific kinematical cuts that reduce the resonances background.

The first cut was applied on the $p\pi^+$ and $p\pi^-$ invariant mass distribution in order to reduce the background related to the Δ^{++} and Δ^0 production. Events with invariant mass for both $p\pi^+$ and $p\pi^-$ lower than $1.3 \text{ GeV}/c^2$ were rejected. Figure 6.1 (a) shows by black lines the cut on the experimental distributions which are mainly due to the double- Δ contribution since it has the highest cross section (see table 5.4) and (b) shows the rejected events in ρ meson simulation. With such conditions 70% of the $\pi^+\pi^-$ pairs were rejected, whereas the simulation showed that only 2% of those from ρ^0 simulation are rejected. Figure 6.2 shows the $\pi^+\pi^-$ invariant mass distribution after applying the first kinematical cut compared to the total simulation (dashed red) built as explained in Chapter 5 with baryonic resonances contributions from Table 5.4 and a direct ρ contribution simulated with phase space distributions with a cross section of $80 \text{ } \mu\text{b}$. A structure near the ρ^0 mass $0.77 \text{ GeV}/c^2$ is now visible.

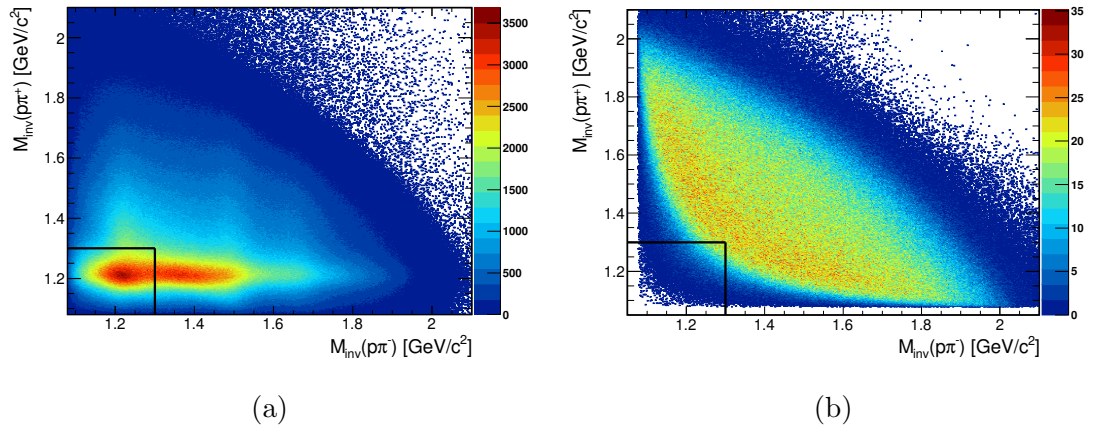


FIGURE (6.1) $p\pi^+$ invariant mass as function of $p\pi^-$ invariant mass (a) for data and (b) for ρ meson simulation. The black lines demonstrate the first kinematical cut which rejects event with $M_{inv}(p\pi^+) < 1.3 \text{ GeV}/c^2$ and $M_{inv}(p\pi^-) < 1.3 \text{ GeV}/c^2$.

In the case of one or two baryon resonance excitation, it is expected that the angular distribution of protons is very forward/backward peaked and due to the acceptance cuts, most protons are detected at backward CM angles, i.e. rather large lab angles. A much flatter proton angular distribution, closer to phase space is expected for the ρ production. Due to the Lorentz boost, the corresponding protons are expected at forward angles in the laboratory, as illustrated in Figure 6.3 (a). By applying a threshold on the angle of the detected proton at 30° in the laboratory, we can expect to suppress significantly events from the resonance production and in a much smaller amount events from the ρ meson production. This is illustrated in Figure 6.3 (a) and (b), where the cut is shown by black lines. With such condition 15% more of the $\pi^+\pi^-$ pairs were rejected, and

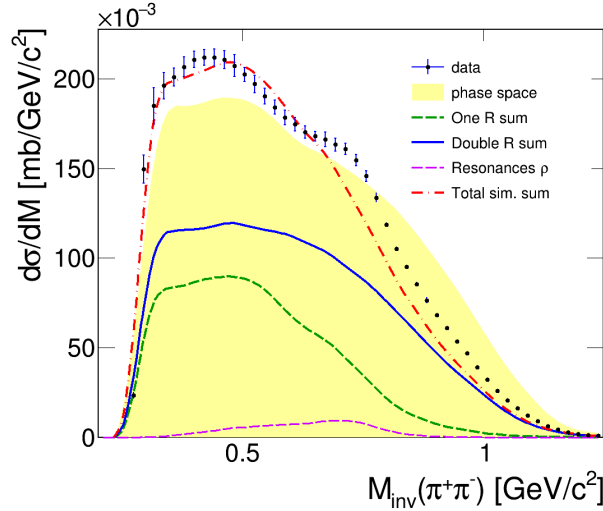


FIGURE (6.2) $\pi^+\pi^-$ invariant mass distribution after applying the kinematical cut $M_{inv}(p\pi^+) < 1.3 \text{ GeV}/c^2$ and $M_{inv}(p\pi^-) < 1.3 \text{ GeV}/c^2$, compared to phase space (yellow area) and resonance cocktail (dashed red). ρ coming from resonances is shown in dashed violet. The solid blue line represent the sum of double resonance excitation and the dashed green represent the sum of one resonance excitation.

3% from the ρ simulation. Figure 6.4 shows the $\pi^+\pi^-$ invariant mass distribution after applying both kinematical cuts compared to the predictions of our resonance model. The structure near the ρ^0 mass of $0.77 \text{ GeV}/c^2$ is enhanced, and this is obviously due to the ρ meson since it is completely absent in phase the space simulation (yellow area). The whole spectrum is very well reproduced by our resonance cocktail shown as a red line. The data are therefore in agreement with the cross section of $80 \mu\text{b}$. However, in our simulation, the ρ meson is produced according to phase space. In Section 6.2.3, we will extract the angular distribution and provide a precise estimate of the ρ production cross section.

6.2.2 ρ spectral function

In Figure 6.4, one can also compare the $\pi^+\pi^-$ invariant mass for the ρ meson produced by the decay of the resonances (dashed violet curve) and the Breit-Wigner like distribution of the direct ρ contribution. One can first notice that the former is strongly cut due to the selection applied to suppress the baryonic resonance contribution. Most importantly, it is very clear that the spectral function of the ρ produced from the baryonic resonance cocktail is highly distorted with respect to the Breit-Wigner. This is due to the coupling to the light baryonic resonances, which have a pole mass well below the pole mass of the ρ meson and can couple only to ρ mesons in the low mass tail.

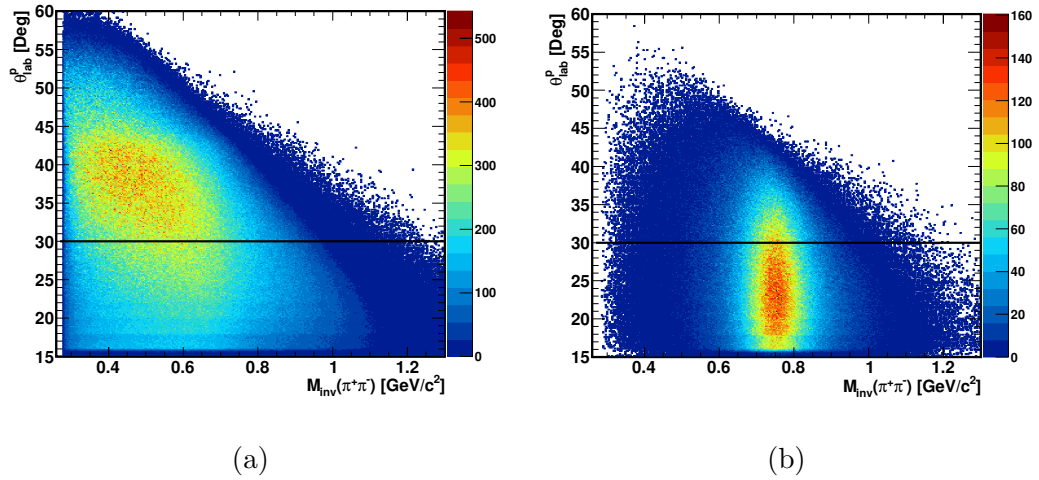


FIGURE (6.3) θ proton in the lab distribution as function of $\pi^+\pi^-$ invariant mass (a) for data and (b) for ρ meson production simulation. The black lines demonstrate the second kinematical cut that rejects events with $\theta_{lab}(p) > 30^\circ$.

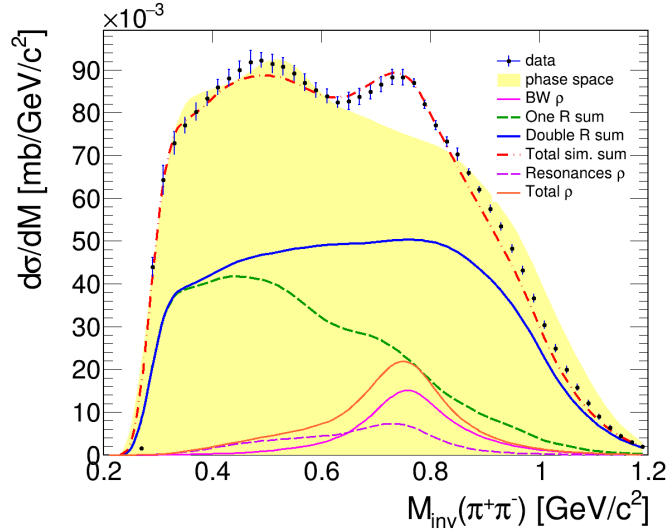


FIGURE (6.4) $\pi^+\pi^-$ invariant mass distribution after applying the kinematical cuts $M_{inv}(p\pi^+) < 1.3 \text{ GeV}/c^2$, $M_{inv}(p\pi^-) < 1.3 \text{ GeV}/c^2$ and $\theta_{lab}(p) < 30^\circ$, compared to phase space (yellow area) and resonance cocktail (blue + dashed green) + Breit-Wigner ρ (pink). ρ coming from resonances is shown in dashed violet.

This means that the ρ meson spectral function is modified by the coupling with baryon resonances already in pp reactions. Since medium effects on the ρ meson are expected to further modify the spectral function, our study is therefore very important in this context as a reference for "vacuum" modifications.

To illustrate this, we plot in Figure 6.5 the correlation between $(p\pi^+\pi^-)$ invariant mass and $(\pi^+\pi^-)$ invariant mass. This figure shows three structures, two oblique structures, with invariant masses around 1.5 and 1.7 GeV/c^2 , corresponding to the excitation of resonances in the second and third resonance region. Following our results of Chapter

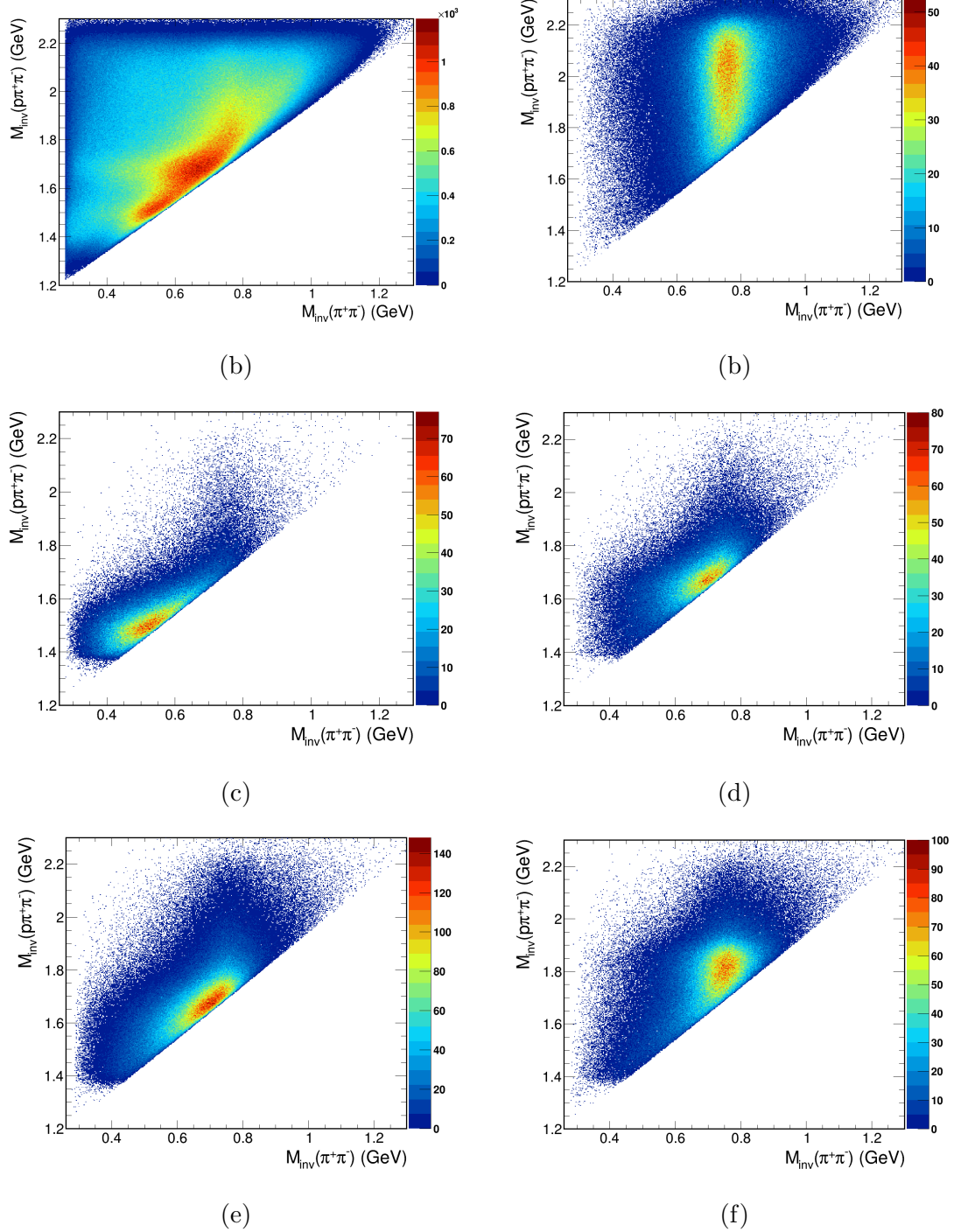


FIGURE (6.5) $(p\pi^+\pi^-)$ invariant mass as function of $(\pi^+\pi^-)$ invariant mass after the kinematical cut that rejects events with $\theta_{lab}(p) > 30^\circ$. (a) data, (b) $\rho \rightarrow \pi^+\pi^-$, (c) $N(1520) \rightarrow p\rho$, (d) $N(1680) \rightarrow p\rho$, (e) $N(1720) \rightarrow p\rho$, (f) $N(1880) \rightarrow p\rho$.

5, we know that the main contributing resonances in these regions are respectively the $N(1520)$ and $N(1680)$. In this case, since the pole mass of these resonances are below the ρ mass pole, only ρ mesons in the low mass tail can be produced. For a given mass of the baryon, the highest $\pi^+\pi^-$ invariant masses, i.e. closest to the ρ meson pole mass are

enhanced, but the maximum value of the invariant mass is limited by the available phase space for the decay. Due to this correlation between the mass of the baryons and the mass of the $\pi^+\pi^-$ pair. This is why these contribution appear as oblique bands in Figure 6.5(Data). This behavior is confirmed by the distributions obtained for simulations for the $N(1520)$, $N(1680)$ and $N(1720)$, shown in Figures 6.5 (c,d,e).

The third structure is a vertical band located at $\pi^+\pi^-$ masses around the ρ meson mass and with $p\pi^+\pi^-$ invariant masses spread around $1.8 \text{ GeV}/c^2$. These $\pi^+\pi^-$ pairs can be due to the production of ρ by resonances with masses well above the ρ meson mass, for example $N(1880)$, which has a mass about $160 \text{ MeV}/c^2$ above the threshold for the ρ meson at the pole mass. This is illustrated in Figure 6.5 (f). The decay of $N(1880)$ appears as a broad spot around $M_{inv}(p\pi^+\pi^-) = 1880 \text{ MeV}/c^2$ and $M_{inv}(\pi^+\pi^-) = 770 \text{ MeV}/c^2$, $\pi^+\pi^-$ invariant mass distribution is centered around the ρ meson mass. The direct ρ production can also contribute in this region. It is expected to produce a vertical structure centered on the ρ meson mass ($769 \text{ MeV}/c^2$), with no structure for the $p\pi^+\pi^-$ invariant mass distribution as illustrated in Figure 6.5 (b) which shows the result obtained for the simulation of the direct ρ production.

6.2.3 ρ meson angular distribution

In [116], the production of vector mesons via baryonic resonances was not considered and two different graphs were invoked : nucleonic currents (Figure 6.6 a) where the ρ is emitted from a ρNN vertex and mesonic currents (Figure 6.6 b) where the ρ is emitted from a ρMM vertex, where M is a meson exchanged between the two interacting protons. Polar angle differential cross sections have been proposed [116] as a sensitive observable to extract the strength of nucleonic and mesonic currents and detailed calculations were performed for the ω production [116]. It was shown that mesonic currents lead to a flat angular distribution in the center of mass, while the distribution for nucleonic currents is predicted to be forward/backward peaked. No calculation exist to our knowledge for the ρ meson production, but we can expect the same qualitative trend. However, we can observe that, since the coupling of ρ^0 to $\pi^0\pi^0$ is forbidden, the ρ meson can not be produced via pion exchange. It still can be produced by the exchange of heavier mesons, but this will be less probable. So, it is expected that the direct ρ meson production will proceed dominantly via nucleonic currents. It can also be added that, nucleonic currents

should be treated coherently with baryonic resonance contributions, involving a MNR vertex instead of MNN .

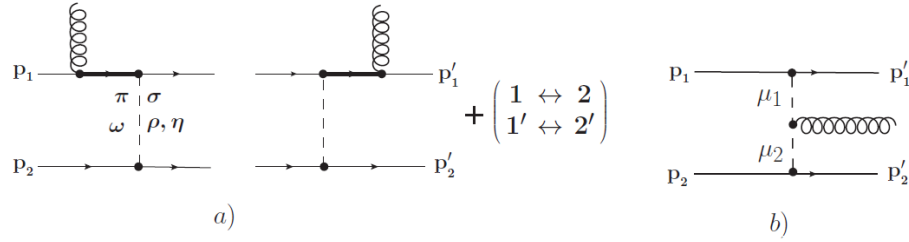


FIGURE (6.6) Feynman diagrams for the nucleonic current (a) and mesonic current (b) contributing to meson production in NN reactions.

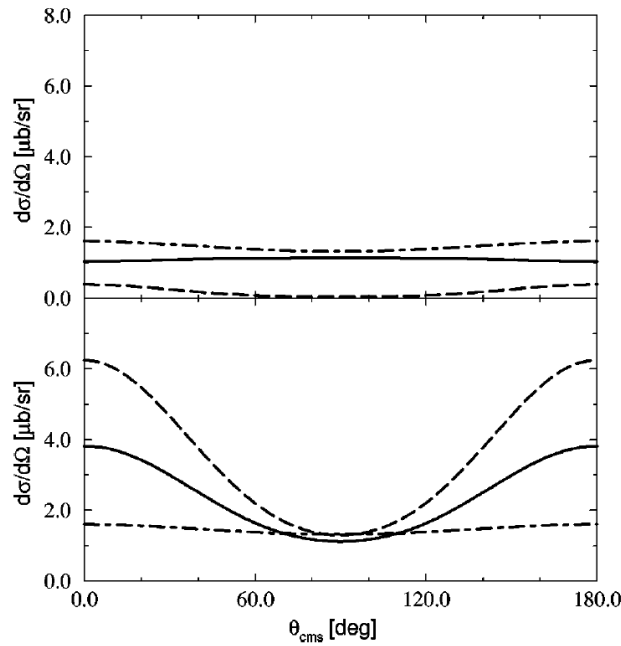


FIGURE (6.7) Angular distribution of the emitted ω meson in the reaction $pp \rightarrow pp\omega$ at the energy $T_p = 2.2$ GeV [116]. The lower figure shows the result where the nucleonic current is larger than the mesonic current (NC > MC) whereas the upper graph contains the results where the nucleonic current is smaller than the mesonic current (NC < MEC). The dash-dotted line is the contribution of the mesonic current, the long-dashed line is the contribution of the nucleonic current and the full line is the total result.

The DISTO collaboration has studied the ρ meson production in the $pp \rightarrow pp\pi^+\pi^-$ channel at $p_{\text{beam}} = 3.67$ GeV/c [117] by fitting the $\pi^+\pi^-$ invariant mass distribution for equal bins in $\cos_{CM}\theta$ with a Breit-Wigner ρ and a third order polynomial background normalized to the same maximum of experimental data (see Figure 6.8 (a)). The DISTO collaboration has reported an anisotropy of the ρ meson polar angle θ_ρ^{cm} . Such behavior

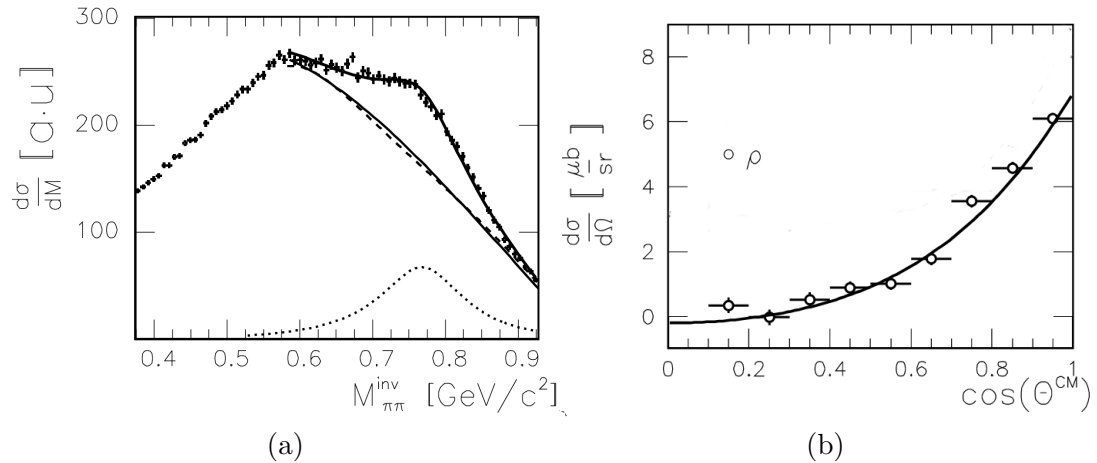


FIGURE (6.8) (a) $\pi^+\pi^-$ invariant mass distribution measured for $\cos_{CM}\theta > 0.5$. The solid line shows the fit using a relativistic Breit-Wigner function added onto a third order polynomial for the background. The dotted line shows the meson line shape, and the dashed line presents the $M_{inv}(\pi^+\pi^-)$ distribution obtained for $\cos_{CM}\theta < 0.4$ normalized to the same maximum. (b) the ρ^0 (circles) differential cross sections as a function of the meson CM emission polar angle. The solid line show fits using the first three even Legendre polynomials [117].

was described with a fit using the first three even Legendre-polynomials :

$$\frac{d\sigma_\rho}{d\Omega} \propto (2 \pm 0.2)P_0 + (4.4 \pm 0.2)P_2 + (0.8 \pm 0.2)P_4 \quad (6.1)$$

Figure 6.8 (b) shows the ρ^0 (circles) production cross section extracted in this experiment as a function of $\cos\theta_{CM}$, the polar angle in the center of mass system of the meson.

We followed the DISTO analysis procedure in order to extract the angular distribution for the ρ^0 production in our experiment and to calculate the total production yield. However, instead of using a polynomial fit for the background below the ρ meson peak, we used the PLUTO resonance cocktail, which gives a good approximation of the experimental yield and takes into account structures due to the baryonic resonance contribution. In the model, the direct ρ production proceeds via phase-space and the ρ mass distribution is taken as a Breit-Wigner. As mentioned before the simulation was performed with a starting value of 80 μb which gave a good agreement for the $\pi^+\pi^-$ total invariant mass distribution (Figure 6.4). In order to extract the direct ρ production angular distribution, the simulated yield, was adjusted to fit the experimental spectrum in each bin. In this way, the direct ρ production acceptance corrected cross section could be extracted in each bin.

The $\pi^+\pi^-$ invariant mass distributions are displayed in Figure 6.9 in comparison

to the resonance cocktail for 10 bins in $\cos\theta_{CM}$ from -1 to 1. The adjusted direct ρ contribution is shown as a pink curve. A good description of the data is obtained, which confirms that also detailed differential distributions for the production of $\pi^+\pi^-$ pairs are well described by the model. Still some structures are not predicted, for example around 0.9 GeV/c² for backward and forward angles.

The distributions obtained for the simulation of the $pp \rightarrow pp\pi^+\pi^-$ reaction according to phase space are also shown in the picture as a yellow area, and are normalized arbitrary for each bin. They present some structures which are only due to the acceptance and selection cuts. However, the latter do not affect the region of the ρ peak. It is however preferred to use the resonance cocktail than a simple phase space distribution, or a polynomial fit to extract the ρ contribution, since it gives a global good description of the data. The dashed violet curve illustrates the resonance- ρ , which, as mentioned above is wider and extends in the low mass region due to the kinematical limits for light resonances ($N(1520)$, $N(1535)$...) decaying to ρ meson. The orange curve is the total ρ , obtained by adding the resonance and the direct contributions. The advantage of this method to extract the ρ contribution is that it takes into account the baryonic resonance decays in the ρN channel. However, this contribution is model dependent. It depends on the values of the baryonic resonance production cross sections, which were adjusted mainly to the $p\pi^+\pi^-$ invariant mass distributions and on the branching ratios to ρN which are taken in our approach from the Bonn-Gatchina PWA (Table 6.1). In addition, previous extractions of the ρ production cross sections were based on a Breit-Wigner mass distribution for the ρ meson, which takes into account only the production via decay of heavy baryonic resonances, for which the ρ spectral function is not too much distorted by the available phase space.

Therefore, we used a second method to extract the ρ contribution, where we removed from the cocktail the decay of baryons to ρN before adjusting the cross section for the $pp \rightarrow pp\rho$ process to reproduce the data in the region of the ρ peak. In this case, as shown in Figure 6.10, the cocktail underestimates the yield, in particular in the region of small $\pi^+\pi^-$ invariant masses, but a good description of the ρ peak is achieved with the simulation with a Breit-Wigner ρ . The ρ yield extracted by this fit is of course higher than in the first fit where part of the yield in this region was included in the cocktail, via the decay of heavy baryons in the ρN channel.

Figure 6.11 shows the "direct" and "Breit-Wigner" ρ^0 production cross sections obtained using the two different fits as function of $\cos\theta_{CM}$. The error bars reflect the statistical and systematic errors which are equal to the quadratic sum of the global systematic error on the background and the error on the ρ fit in each bin of $\cos\theta_{CM}$. It is important to note that the yields are within errors, perfectly symmetric around $\cos\theta_{CM} = 0$, even for the most extreme bins, where the acceptance at forward angle is strongly reduced. This is not a trivial result, since the measured yields are highly distorted by the acceptance and selection cuts. It gives additional proof of the consistency of the extraction of the ρ^0 yield. The distributions were fitted with the sum of the first three even Legendre polynomials and the following result was obtained :

$$\frac{d\sigma_{\rho}^{direct}}{d\Omega} = (7.1 \pm 0.2)P_0 + (2.4 \pm 0.3)P_2 - (0.7 \pm 0.3)P_4 \quad (6.2)$$

$$\frac{d\sigma_{\rho}^{BW}}{d\Omega} = (9.9 \pm 0.2)P_0 + (3.9 \pm 0.2)P_2 - (1.6 \pm 0.3)P_4 \quad (6.3)$$

The above results indicate a contribution of partial waves up to $L = 2$ in the production of the ρ -meson. The angular distribution for ρ^0 production exhibits a significant forward peaking, suggesting a dominance of the nucleonic current characterized by a dipole $\propto \cos^2\theta_{CM}$ dependence [116]. This is consistent with the fact that π exchange is suppressed in this channel. As expected, the "Breit-Wigner" ρ has a steeper distribution than the direct ρ , since it includes baryonic resonance contributions which are expected to be forward/backward peaked.

It is also interesting to compare these numbers to DISTO results (Eq. 6.1). For such comparison, it is more relevant to use the "Breit-Wigner" ρ results than the "direct" ρ , since the DISTO experiment did not subtract the contribution of ρ meson production via baryonic resonances. The P_0 coefficient is simply related to the cross section, which is about a factor five larger at our energy. The anisotropy of the distribution is measured by the ratio of the P_2 and P_0 coefficients which are respectively about 2.2 and 0.39 for the DISTO and HADES experiments. The angular distribution in the case of HADES is clearly much flatter. For the sake of completeness, Figure 6.12 shows the differential cross section for the total ρ production (resonance- ρ + direct- ρ) as function of $\cos\theta_{CM}$, the polar angle in the CM system of the meson.

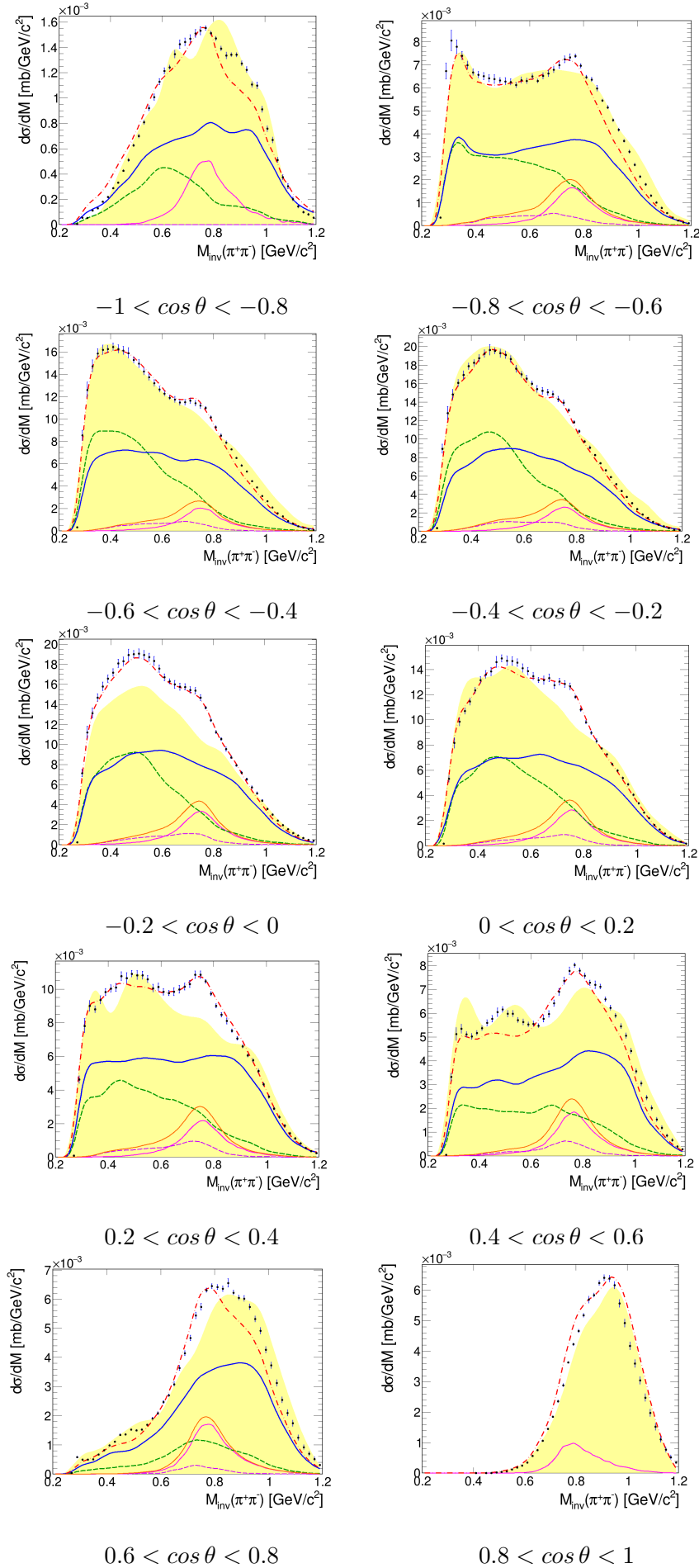


FIGURE (6.9) $\pi^+\pi^-$ invariant mass distributions obtained in ten different CM angular bins as indicated in the figure. Phase space yield is adjusted arbitrarily. (Legend : see Figure 6.2).

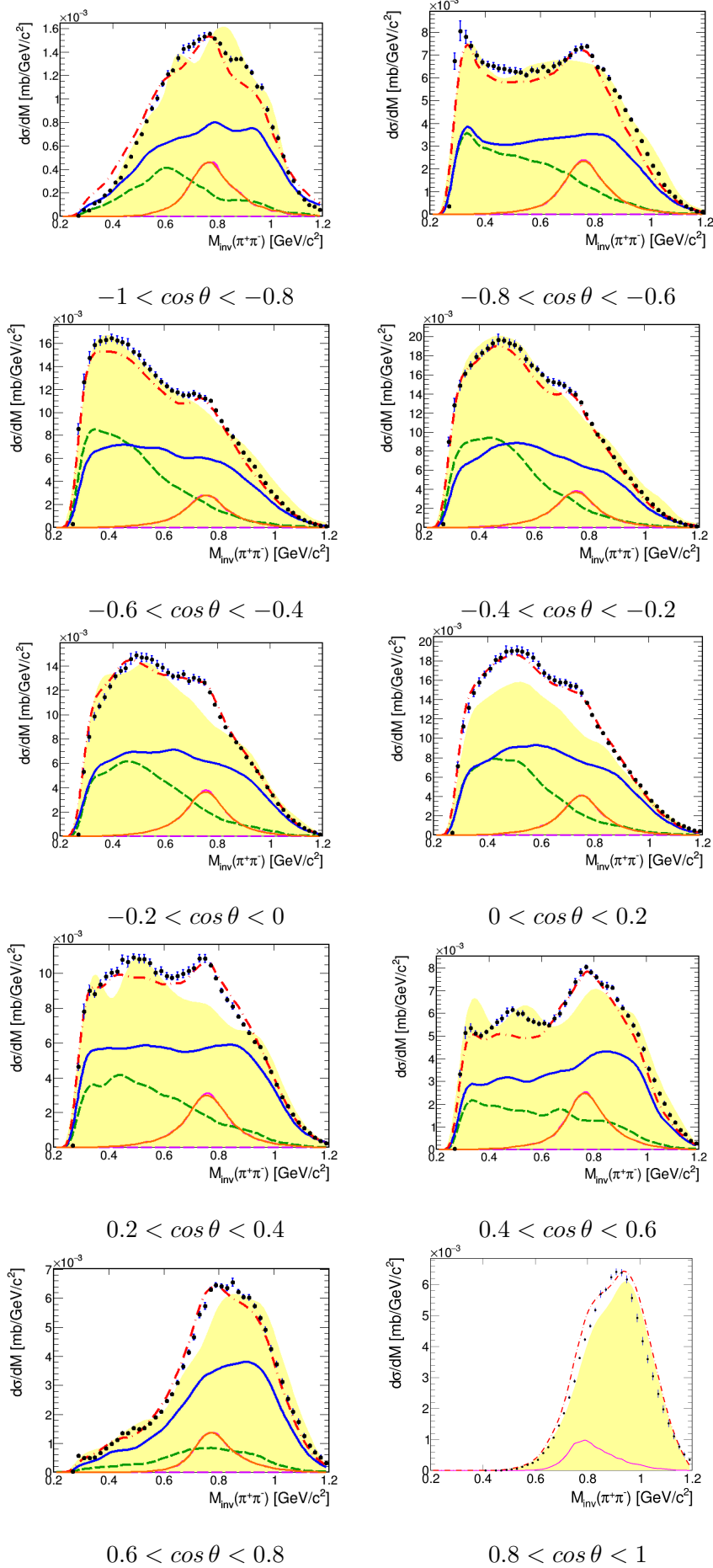


FIGURE (6.10) $\pi^+\pi^-$ invariant mass distributions obtained in ten different CM angular bins as indicated in the figure. Phase space yield is adjusted arbitrarily. (Legend : see Figure 6.2).

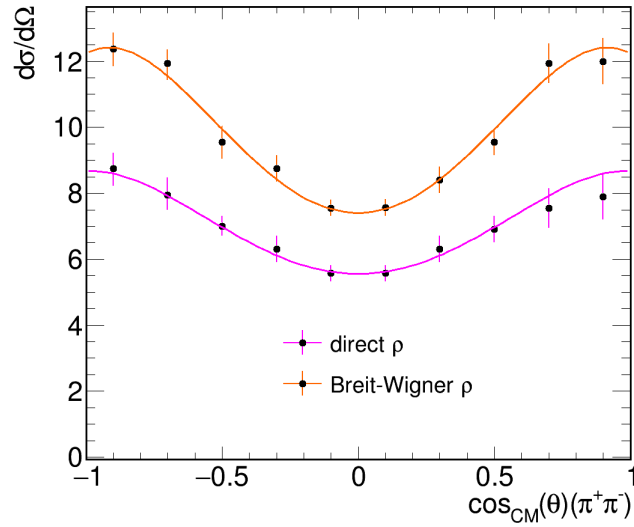


FIGURE (6.11) The ρ differential cross section as function of the meson CM angle. The solid lines show fits using the first three even Legendre polynomials. Pink curve represents the direct ρ production to be added to the resonance- ρ production. Orange curve represents the ρ signal extracted using a Breit-Wigner ρ .

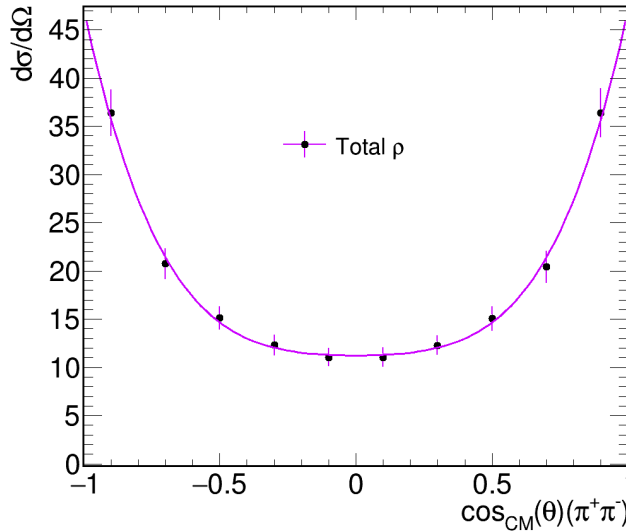


FIGURE (6.12) The total ρ (resonance- ρ + direct ρ) differential cross section as a function of the meson polar angle in CM.

6.2.4 Total cross sections

By integrating the differential cross sections extracted in our experiment, we obtain for the direct contribution (Eq. 6.2) :

$$\sigma_{\rho}^{direct} = 89.2 \pm 6.7 \text{ } \mu\text{b.}$$

This cross section should be associated with the "resonance- ρ " cross section from our

model, which derived from the resonances cross sections listed in Table 5.4 and $N\rho$ Bonn-Gatchina branching ratios listed in Table 6.1 and is equal to :

$$\sigma_{\rho}^R = 248.9 \pm 51.8$$

The total ρ production cross section is therefore :

$$\sigma_{\rho}^{tot} = 338.1 \pm 74.7 \text{ } \mu\text{b.}$$

By integrating the differential cross section of Eq.6.3, we obtain for the Breit-Wigner ρ :

$$\sigma_{\rho}^{BW} = 124.4 \pm 9.1 \text{ } \mu\text{b.}$$

Since most experiments were using a Breit-Wigner fit to extract the ρ contribution, we compare our result for σ_{ρ}^{BW} with world data in Figure 6.13. The open circles represent inclusive production cross sections ($pp \rightarrow \rho X$), the red open circle represents HADES inclusive ρ production in pp at $T_p = 3.5$ GeV, extracted after fitting $pp \rightarrow ppe^+e^-X$ with PYTHIA + PLUTO simulation [115]. The full circles correspond to exclusive productions ($pp \rightarrow pp\rho$), the first full dot represents DISTO result [117] and the blue dot represents our result. The dot at slightly higher energy show a smaller cross section but it has a very high error. This comparison validates our result.

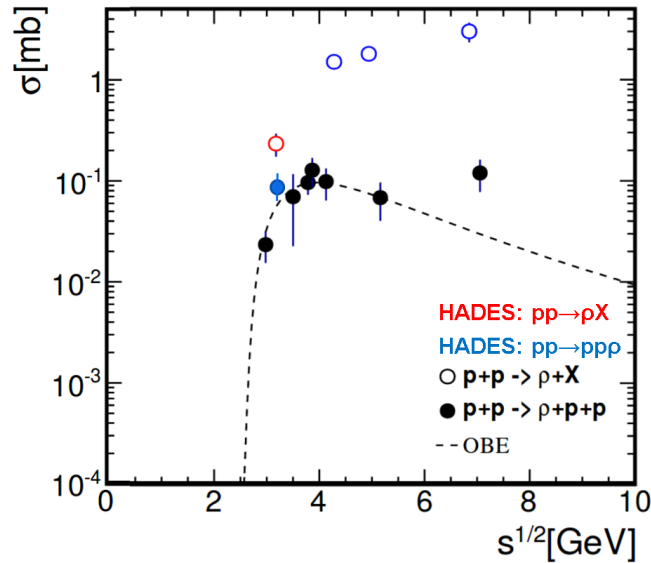


FIGURE (6.13) ρ production cross section in pp collisions world data. Inclusive (circles), exclusive (full dots), OBE model (dashed line). The blue full dot shows the exclusive Breit-Wigner ρ cross section from this work. The red circle shows inclusive ρ cross section from [115].

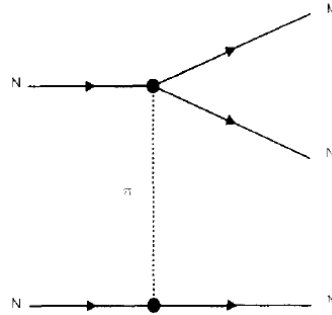
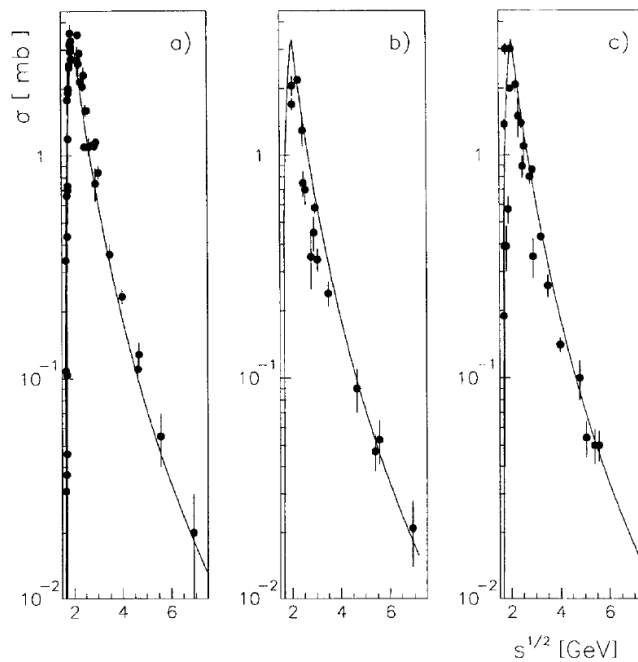
6.2.5 Comparing ρ result with theoretical models

FIGURE (6.14) Diagram for one pion exchange in the calculation of [118].

The calculations that we found in the literature for the $pp \rightarrow pp\rho$ reaction in our energy domain were not aiming at a very detailed description of the ρ production mechanism, but rather at providing realistic inputs for elementary processes for heavy-ion collisions. In particular, these models focused on reproducing total cross sections, but did not attempt to describe the production angular distribution of the ρ [119].

Sibirtsev parametrization : The calculation of [118] is based on the one pion exchange approximation (Figure 6.14). At a given proton-proton center of mass energy \sqrt{s} , corresponding to an incident proton momentum p_i , the $pp \rightarrow pp\rho$ cross section is expressed as a function of the $\pi N \rightarrow \rho N$ as follows :

FIGURE (6.15) Cross sections for the reactions $\pi^- p \rightarrow \rho^0 n$ (a), $\pi^- p \rightarrow \rho^- p$ (b) and $\pi^+ p \rightarrow \rho^+ p$ (c). Experimental points are from [120]. Picture from [118].

$$\begin{aligned} \sigma(pp \rightarrow pp\rho) = & \frac{3m_N^2}{2\pi^2 p_i^2 \sqrt{s}} \int_{W_{min}}^{W_{sup}} kW^2 dW \\ & \times \sigma(\pi^0 p \rightarrow \rho^0 p, W) \int_{t^-}^{t^+} \frac{f_{\pi NN}}{\mu^2} F^2(t) D^2(t) t dt \end{aligned} \quad (6.4)$$

Here t is the four momentum transfer between the two nucleons at the πNN vertex (bottom vertex in figure 6.14) and W is the invariant mass of the πN system at the ρ production vertex, which ranges from :

$$W_{min} = m_N + m_\rho \quad \text{to} \quad W_{max} = \sqrt{s} - m_N \quad (6.5)$$

with m_N and m_ρ the masses of the nucleon and ρ meson respectively.

$F(t)$ and $D(t)$ are the πNN vertex and pion propagator functions. The main ingredient of the calculation is the $\pi N \rightarrow \rho N$ cross section. The latter is parametrized as a function of \sqrt{s} using a fit to existing data measured with charged pion beams, as shown in figure 6.15, using the following expression :

$$\begin{aligned} \sigma(\pi^\pm N \rightarrow \rho N) &= 9.27(\sqrt{s} - \sqrt{s_0}) [mb] \quad \text{for} \quad \sqrt{s} < 2 GeV \\ &= 64.1s^{-2.11} [mb] \quad \text{for} \quad \sqrt{s} \geq 2 GeV. \end{aligned} \quad (6.6)$$

and the production induced by π^0 , which is relevant in the case of the pp reaction, was deduced from the relation :

$$\sigma(\pi^0 N \rightarrow \rho^0 p) = \frac{1}{2} \left[\sigma(\pi^- p \rightarrow \rho^- p) + \sigma(\pi^+ p \rightarrow \rho^+ p) - \sigma(\pi^- p \rightarrow \rho^0 n) \right] \quad (6.7)$$

It has to be noted that Eq. 6.4 neglects interference effects between the four possible graphs corresponding to the exchange of the two nucleons in the entrance or exit channels. In addition, the dependence of the $\pi N \rightarrow \rho N$ cross section as a function of the four momentum transfer between the two nucleons at the πNN vertex is averaged out. In this calculation, the mechanism for the ρ production at the $\pi NN\rho$ vertex is not explicit and in principle it includes both resonant and non-resonant processes. However, since the ρ production cross sections were obtained from data above threshold using a Breit-Wigner shape for the ρ meson spectral function, the contribution of low baryonic

resonances was excluded, or at least strongly underestimated, as mentioned in Section 6.2.3.

Along this line, the model should be compared to the "Breit-Wigner" extraction of the ρ production cross section. We can first notice, that the model describes the measured cross sections up to $\sqrt{s} = 5$ GeV rather well. In particular, the DISTO point, measured many years after the publication of the model fits well on the curve. Our measurement of the Breit-Wigner ρ only is also in quite satisfactory agreement with this prediction. It can also be observed that, as expected, the model strongly under predicts our estimate for the total ρ production, which includes the production from light baryon resonances.

BUU model : Figure 6.16 shows the result of a BUU model [121] developed by a Budapest-Dresden group in comparison with the DISTO measurement. As expected, the prediction extends below threshold and overestimates the DISTO measurement, which can be easily explained, since, as already mentioned, the experimental extraction suppresses the contribution of light baryons. However, we were surprised to read in the paper that the ρ production cross section in the model has been readjusted to reproduce the data, which, in our opinion amounts to underestimate the total ρ contribution. Moreover, at our energy, the model underestimates the ρ production cross section value.

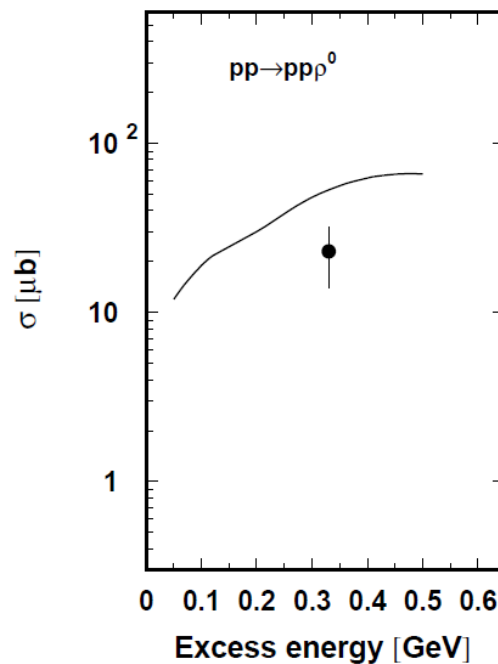


FIGURE (6.16) Predictions for the $pp \rightarrow pp\rho$ production cross sections from [121] are compared to the measurement of [119].

HSD model : The Sibirtsev parametrization is used in the HSD (Hadron-String-Dynamics) transport model to calculate the exclusive "non-resonant" ρ production in nucleon nucleon collisions. In addition, a contribution of ρ meson via the $N(1520)$ resonance is added [122] (see Figure 6.17). The solid line represent the parametrization of the inclusive $pp \rightarrow \rho X$ cross sections, while the dashed lines stand for the exclusive cross sections. The exclusive $pp \rightarrow pp\rho$ is denoted "non-resonant" because the authors consider explicitly the possible contribution of the $N(1520)$ to the ρ production via the process $pp \rightarrow N(1520)p \rightarrow \rho pp$. The $N(1520)$ cross section is taken from Teis *et al.* [60] and the $N\rho$ branching ratio from [123]. The cross section for $N(1520) \rightarrow p\rho$ given by the model is $30 \mu\text{b}$ which is more than a factor 2 lower than our result ($72 \mu\text{b}$, see Table 6.1). The red dot indicate the Breit-Wigner ρ cross section from this work which is slightly higher than the model parametrization.

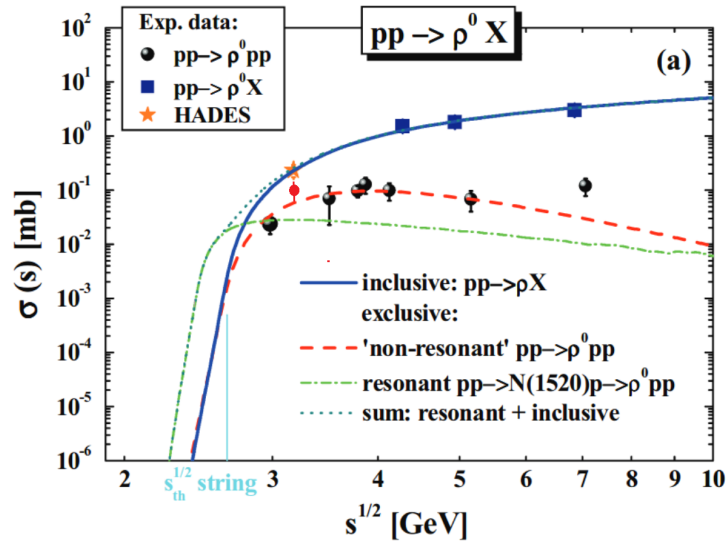


FIGURE (6.17) The production cross sections for the channel $pp \rightarrow pp\rho X$ as a function of the center of mass energy \sqrt{s} . The solid blue line represent the parametrization of the inclusive ρ cross sections, while the dashed red line stand for the exclusive "non-resonant" cross sections. The dash-dotted green line shows the contribution from the $N(1520)$ resonance to the ρ production via the process $pp \rightarrow N(1520)p \rightarrow \rho pp$. The stars indicate the inclusive cross sections extrapolated from the dielectron data by the HADES [115]. The red dot indicates the Breit-Wigner ρ cross section from this work.

UrQMD, GiBUU and SMASH : In most other transport models, the production of the ρ mesons in our energy range is realized exclusively via resonance decay, where many resonances are taken into account. The production cross section should therefore be consistent with our estimate for the total ρ production. The values for the ρ production in UrQMD, GiBUU and SMASH are $565 \mu\text{b}$, $423 \mu\text{b}$ and $140 \mu\text{b}$ in comparison to our

total value of $338.1 \pm 74.7 \mu\text{b}$ (see Table 6.2). Both results from the GiBUU and UrQMD models are very high compared to our result for the total exclusive ρ cross section even though these models do not include a direct ρ contribution, while SMASH result is more than a factor 2 lower. Figure 6.18 from [70] shows the exclusive ρ production in dashed lines (with and without the $N(1520)$ which has the highest contribution), it should be mentioned here that these curves represent the exclusive ρ coming from the decay of baryonic resonances. Hence, it can not be compared to the empty data points. Figure 6.19 shows the individual contributions of various resonances to the ρ production, which are all higher than the individual contributions deduced in this work.

Model	σ [μb]
OBE	70
BUU	63
GiBUU	423
UrQMD	565
SMASH	140
PLUTO cocktail	338.1 ± 74.7

TABLE (6.2) Cross sections in units of μb for exclusive $pp \rightarrow pp\rho$.

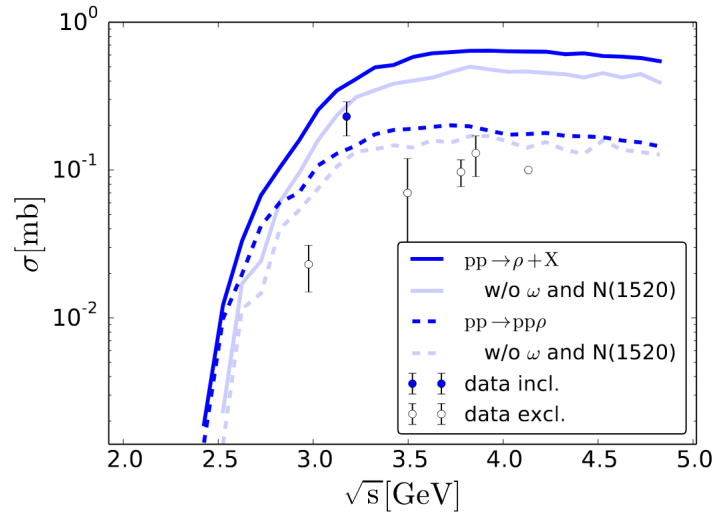


FIGURE (6.18) Cross sections for exclusive ($pp \rightarrow pp\rho$) and inclusive ($pp \rightarrow pp\rho X$) ρ meson production in pp collisions [70]. Empty data points from [120, 124].

Perspectives on model description of ρ production : In transport model calculations, the ρ yield depends both on the production cross section of the various resonances, which are fitted to available data of meson production and on the $N\rho$ branching ratios, which were taken from the PDG. From the detailed analysis of the one-pion production channel [126], we already learned that some adjustments were needed for the resonance production cross sections in the UrQMD and GiBUU model. As already said,

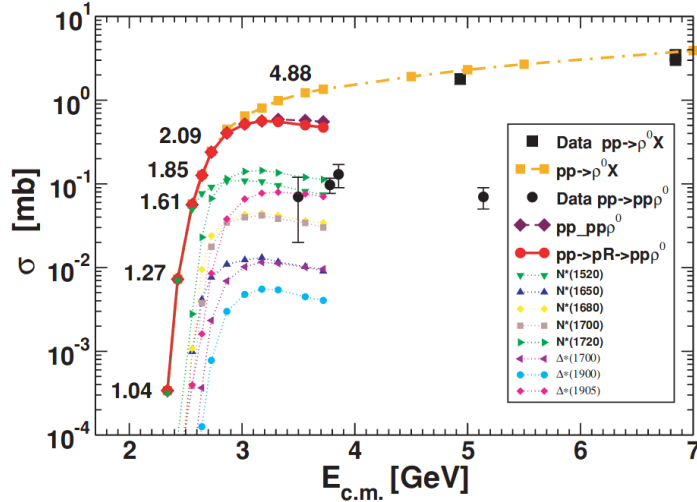


FIGURE (6.19) Cross sections for exclusive ($pp \rightarrow pp\rho^0$) and inclusive ($pp \rightarrow pp\rho^0 X$) ρ^0 meson production in pp collisions in comparison to experimental data. The contribution of the most important resonances to the resonant exclusive production is additionally shown [125].

our two-pion measurements can also be used to update the inputs for the production of the heaviest baryons, which can not be constrained with sufficient precision from the one-pion production (see Section 5.3). We will discuss in more detail in Chapter 8 the predictions of transport models for the resonance cross sections and the comparison to the values extracted in our analysis. We also mentioned that the knowledge of $N\rho$ branching ratios is very unsatisfactory and can not be anymore taken from the PDG. The inputs of the resonance models should therefore be updated with the values of the most recent PWA, eg. Bonn-Gatchina [127].

It would be also very interesting to have a full microscopic model for the ρ production including both resonant and non resonant contributions and with predictions of the $\pi^+\pi^-$ angular distributions and invariant mass distributions. The development of a Lagrangian model for the $pp \rightarrow pp\rho$ has started by M. Zetenyi in Budapest and the results should be available soon.

Finally, considering the difficulty to extract a reliable ρ production cross section, since the spectral function is distorted due to the coupling to light baryons, we would like to insist on the necessity for the models to directly use as a benchmark the $\pi^+\pi^-$ invariant mass distributions, after the kinematical cuts needed to enhance the ρ production.

6.3 $f_0(500)$ meson or σ

The σ meson, its modern name being $f_0(500)$, got its name from the light scalar-isoscalar field that was postulated 60 years ago to explain the inter nucleon attraction [128]. To describe chiral symmetry in pion-pion interactions, this field was soon included within the Linear Sigma Model [129] which is a simple realization of a spontaneous chiral symmetry breaking, where all fields but the σ become Goldstone bosons, i.e. pions. Generically, the σ , having the vacuum quantum numbers, plays a relevant role for the understanding of the QCD spontaneous chiral symmetry breaking.

As it is mentioned in the literature, the precise $f_0(500)$ pole is difficult to establish because of its large width, and because it can certainly not be modeled by a naive Breit-Wigner resonance, but only with a mathematically rigorous definition through its associated pole in the complex plane, whose position s_R is related to the resonance mass and width as $\sqrt{s_r} \cdot M_R - i\Gamma_R/2$. Most of the analyses listed under $f_0(500)$ agree on a pole position near $(500 - i250 \text{ MeV})$.

Using a simple description of the $f_0(500)$ as a Breit-Wigner resonance with mass $M = 500 \text{ MeV}$ and width $\Gamma = 500 \text{ MeV}$, we added to our PLUTO resonance cocktail the $f_0(500)$ meson simulation simply using phase space. Figure 6.20 shows the $\pi^+\pi^-$ invariant mass spectrum after adding the $f_0(500)$ meson contribution with a total cross section of $1 \mu\text{b}$. We consider that this is an approximate upper value for the production of the $f_0(500)$ meson in our pp reaction at 3.5 GeV .

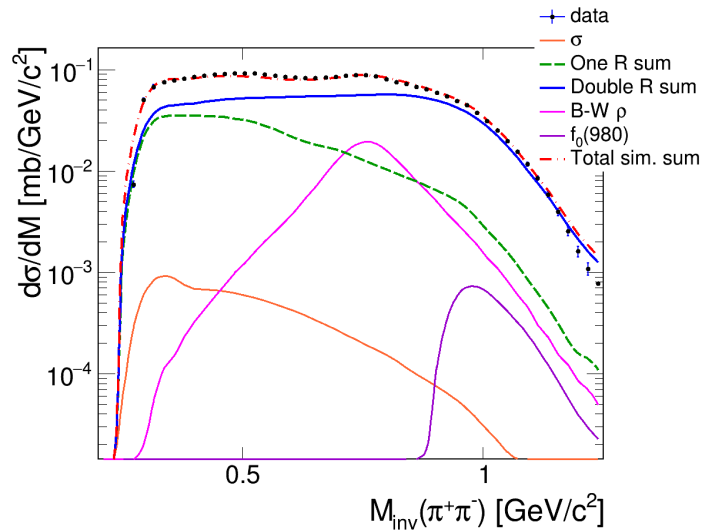


FIGURE (6.20) The $\pi^+\pi^-$ invariant mass after adding the $f_0(500)$ and $f_0(980)$ mesons contribution with a total cross section of $1 \mu\text{b}$

6.4 $f_0(980)$ meson

The status of the $f_0(980)$ meson is still an open problem in particle physics. In the 1996 Review of Particle Physics, the $f_0(980)$ decay modes were announced as $78.1 \pm 2.4\%$ for the $\pi\pi$ and $21.9 \pm 2.4\%$ for the $K\bar{K}$ -channel. These information have however been removed from the PDG2018. However, it has to be noted that the $f_0(980) \rightarrow \pi\pi$ mode is established as dominant, while the $f_0(980) \rightarrow K\bar{K}$ mode is stated as seen.

In 1999 the $f_0(980)$ meson production cross section in πN and NN reactions within the meson-exchange model was calculated by E.L. Bratkovskaya *et al.* and the possibility for $f_0(980)$ observation via the $K\bar{K}$ decay mode in proton-proton collisions was investigated [130]. Using a fit to the data on the $p\pi \rightarrow f_0(980)n \rightarrow K\bar{K}n$ cross section they extracted the following $f_0(980)$ meson properties :

$$Br(f_0(980) \rightarrow \pi\pi) = 98\%$$

$$Br(f_0(980) \rightarrow K\bar{K}) = 2\%$$

$$\Gamma_{tot} = 44.3 MeV$$

It has to be noted that the PDG [11] does not give any value for these branching ratios

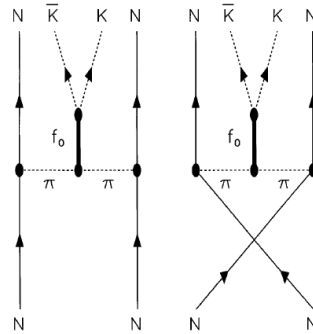


FIGURE (6.21) The diagrams for $NN \rightarrow NN f_0 \rightarrow NN K\bar{K}$ [130], which are the same for $pp \rightarrow pp f_0 \rightarrow pp \pi\pi$

and has an estimate for the total width between 10 and 100 MeV. Figure 6.21 shows the production mechanism Feynman diagrams for the $NN \rightarrow NN f_0 \rightarrow NN K\bar{K}$ and $pp \rightarrow pp f_0 \rightarrow pp \pi\pi$ reactions used in [130]. The result of the calculation from [130] is shown in Figure 6.22 by the dotted line and without form factor by the solid line. The experimental data are taken from [124] while the dashed line shows the corresponding calculation within the one-boson exchange model from [131]. The calculation gives $\sigma(f_0 \rightarrow K\bar{K}) =$

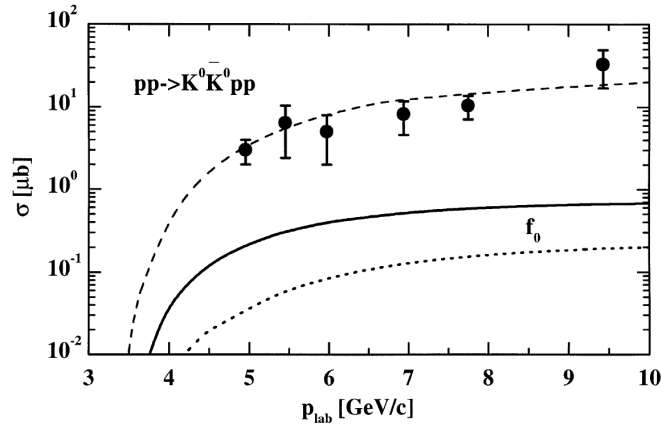


FIGURE (6.22) The $pp \rightarrow pp f_0 \rightarrow pp K K$ cross section calculated from [130] (dotted line) and without form factor (solid line). The experimental data are taken from [124] while the dashed line shows the corresponding calculation within the one-boson exchange model from [131]

0.0137 μb at $p_{lab} = 4.33$ GeV, hence, we can easily deduce that $\sigma(f_0 \rightarrow \pi^+ \pi^-) = 0.685$ μb .

To check the consistency of our data with this prediction, we added to our PLUTO resonance cocktail the $f_0(980)$ meson simulation. Figure 6.20 shows the $\pi^+ \pi^-$ invariant mass spectrum after adding the $f_0(980)$ meson contribution with a total cross section of 1 μb . This value is compatible with the result from [130]. However it should be taken as a very rough estimation of the upper limit of the $f_0(980)$ cross section in the pp reaction at 3.5 GeV.

7

Theoretical development of a Lagrangian model

In the previous chapters, we have used a simple model to analyze the data, which is based on PLUTO simulations and consists in an incoherent sum of many contributions, which are considered as independent. In addition, this model uses phenomenological inputs for the angular distributions. In order to check the validity of the inputs of our model, we developed, thanks to the collaboration with Jacques Van de Wiele, a Lagrangian model for some graphs contributing to the $pp \rightarrow pp\pi^+\pi^-$ reaction. In this chapter, we describe this theoretical work, quantify the effect of interferences and compare the differential distributions obtained with the Lagrangian model and the PLUTO model.

7.1 General expression of the differential cross section

The differential cross section for a collision of the type $a + b \rightarrow 1 + \dots + n$ is given by

$$\frac{d\sigma}{d\Phi_n(p_a, p_b, \dots, p_n)} = \frac{(2\pi)^4}{4\sqrt{(p_a \cdot p_b)^2 - m_a^2 m_b^2}} |\mathcal{M}|^2 \quad (7.1)$$

where : p_i is the four-momentum of particle i , $d\Phi_n(p_a, p_b, \dots, p_n)$ is the phase-space element and \mathcal{M} is the matrix element of the transition amplitude summed over the spins of the final state particles and averaged over the spins of the initial state particles. In the case of a process with 4 particles in the final state (our case) the differential cross section can be expressed as (see Appendix A) :

$$\frac{d^8\sigma}{d\Omega_1 dE_1 d\Omega_2 dE_2 d\Omega_3} = \frac{1}{64(2\pi)^8} \frac{p_1 p_2}{p_a m_b} \sum_{p_3} \frac{p_3^3 |\mathcal{M}_{total}|^2}{|E_4 p_3^2 + E_3 [p_3^2 - (\mathbf{p}_3 \cdot (\mathbf{p}_a - \mathbf{p}_1 - \mathbf{p}_2))]|} \quad (7.2)$$

In the calculation of the total cross section all the amplitudes for all the possible diagrams with the same final state should be summed.

$$|\mathcal{M}_{total}|^2 = (\mathcal{M}_1 + \mathcal{M}_2 + \dots + \mathcal{M}_n)(\mathcal{M}_1^* + \mathcal{M}_2^* + \dots + \mathcal{M}_n^*) \quad (7.3)$$

i.e.

$$|\mathcal{M}_{total}|^2 = \sum |\mathcal{M}_i|^2 + \sum_{ij} \mathcal{M}_i \mathcal{M}_j^* + \sum_{ij} \mathcal{M}_j \mathcal{M}_i^* \quad (7.4)$$

The first term is the sum of squared amplitudes which would correspond to the cross section in the case of summing processes incoherently. The last two terms represent the interference effect, which can either increase the total cross section (constructive interference) or decrease it (destructive interference).

7.2 Model Formalism

7.2.1 Choice of Feynman graphs

We developed a Lagrangian model for the reaction $pp \rightarrow pp\pi^+\pi^-$ at an incident proton energy of 3.5 GeV including two processes, on one hand the excitation of two deltas ($\Delta^{++}(1232)\Delta^0(1232)$) and on the other hand the excitation of the $N^+(1520)$ resonance. In the first case, the π^+ and π^- are produced respectively by the decay of the Δ^{++} ($\Delta^{++} \rightarrow p\pi^+$) and of the Δ^0 ($\Delta^0 \rightarrow p\pi^-$) and in the second case, they are produced by the decay of the $N(1520)$. This choice is driven by the observation (see Chapter 5) that these two contributions are dominating in the $pp \rightarrow pp\pi^+\pi^-$ channel at 3.5 MeV.

For the $N^+(1520)$ decay, three channels are considered :

$$N^+(1520) \rightarrow \Delta^{++}\pi^-$$

$$N^+(1520) \rightarrow \Delta^0\pi^+$$

$$N^+(1520) \rightarrow p\rho^0$$

The corresponding graphs are depicted in Figure 7.1 and Figure 7.2. The graphs labeled (a) and (b) correspond to the exchange of the beam and target protons, with four-momenta respectively p_a and p_b . In addition, the protons in the exit channel are identical particles so their indistinguishability must be taken into account. Since protons are fermions, the amplitude must be antisymmetric with respect to the exchange of the two protons, so the "exchange" diagrams corresponding to the exchange of p_1 and p_2 were added in the model.

7.2.2 Lagrangians

We used the Lagrangians for Meson-Baryon-Baryon interaction, which are the same as those used in Cao *et al.* Effective Lagrangian Model [90].

The πNN interaction Lagrangian is give by :

$$\mathcal{L}_{\pi NN} = -\frac{f_{\pi NN}}{m_\pi} \bar{N} \gamma_5 \gamma_\mu \boldsymbol{\tau} \cdot \partial^\mu \boldsymbol{\pi} N. \quad (7.5)$$

where N and \bar{N} represent the nucleon field in the spin-isospin space, $f_{\pi NN}$ is a coupling constant. The γ_5 matrix compensates the negative parity of the pion. The isospin operators $\boldsymbol{\tau}$ are the Pauli's matrices.

The $\pi n\Delta$ interaction Lagrangian is given by :

$$\mathcal{L}_{\pi\Delta N} = g_{\pi\Delta N} \bar{\Delta}^\mu g_{\mu\nu} \mathbf{T}^\dagger \cdot \partial^\nu \boldsymbol{\pi} N + h.c \quad (7.6)$$

For the $\pi NN(1520)$ interaction we use the pion-nucleon-spin-3/2 resonance Lagrangian given by :

$$\mathcal{L}_{\pi NR}^{3/2^-} = g_{\pi NR} \bar{N} \gamma_5 \gamma_\mu \boldsymbol{\tau} \cdot \partial^\mu \partial^\nu \boldsymbol{\pi} R_\nu + h.c \quad (7.7)$$

The $\rho NN(1520)$ interaction Lagrangian is given by :

$$\mathcal{L}_{\rho NR}^{3/2^-} = g_{\rho NR} \bar{N} \boldsymbol{\tau} \cdot \boldsymbol{\rho}^\mu R_\mu + h.c \quad (7.8)$$

The $\pi\Delta N(1520)$ interaction Lagrangian is given by :

$$\mathcal{L}_{\pi\Delta R}^{3/2^-} = g_{\pi\Delta R} \bar{\Delta}^\mu \gamma_\nu \mathbf{T}^\dagger \cdot \partial^\nu \boldsymbol{\pi} R_\mu + h.c \quad (7.9)$$

The process where the ρ meson decays into two pions is described by :

$$\mathcal{L}_{\rho\pi\pi} = g_{\rho\pi\pi} \boldsymbol{\pi} \times \partial_\mu \boldsymbol{\pi} \cdot \boldsymbol{\rho}^\mu. \quad (7.10)$$

where R_μ and Δ_μ , are the Rarita-Schwinger fields for the spin-3/2 resonance and $\Delta(1232)$, respectively. \mathbf{T}^\dagger is the isospin transition operator from isospin-1/2 to isospin-3/2. μ, ν are Lorentz indices. $\boldsymbol{\pi}, \boldsymbol{\rho}$, are the pion and ρ meson fields; h.c. stands for hermitian conjugate.

The coupling constants are taken from [132, 133].

$$f_{\pi NN}^2/4\pi = 0.078$$

$$g_{\rho NN}^2/4\pi = 0.9$$

$$f_{\pi\Delta\Delta} = 4f_{\pi NN}/5$$

The coupling constants $g_{\Delta N\pi}, g_{N^*N\pi}, g_{N^*N\rho}, g_{N^*\Delta\pi}$ are also taken from [132]. They are related to the corresponding decay widths and the values are listed in Table 7.1.

Resonance	Decay mode	$g^2/4\pi$
$\Delta^*(1232)$	$N\pi$	19.54
$N^*(1520)$	$N\pi$	1.73
	$N\rho$	1.32
	$\Delta\pi$	0.01

TABLE (7.1) The coupling constants for $\Delta^*(1232)$ and $N^*(1520)$ [132].

7.2.3 Form factors

Form factors are added at each vertex to take into account the finite size of the hadrons and suppress momentum transfers larger than a given cut-off. For the nucleon-nucleon-meson vertices, form factors are chosen as :

$$F_M^{NN}(q_M^2) = \left(\frac{\Lambda_M^2 - m_M^2}{\Lambda_M^2 - q_M^2} \right)^n \quad (7.11)$$

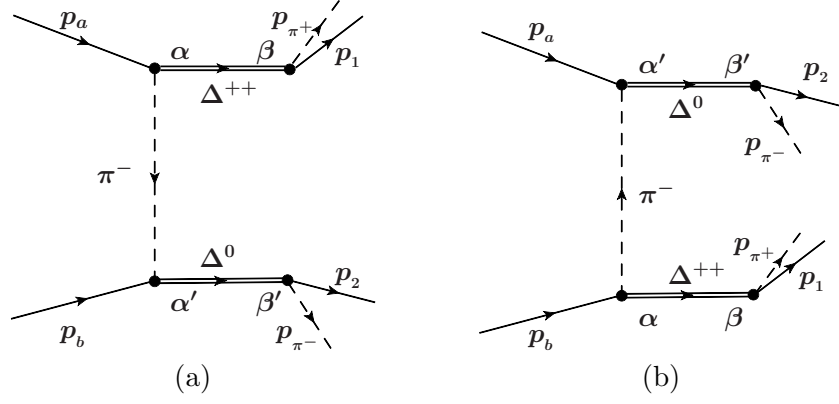


FIGURE (7.1) Feynman diagrams for $pp \rightarrow pp\pi^+\pi^-$ with intermediate $\Delta^{++}(1232)\Delta^0(1232)$. The antisymmetrization graphs corresponding to the exchange of the identical protons p_1 and p_2 are taken into account but are not shown.

where q_M , m_M and Λ_M are the four-momentum, mass and cutoff parameters for the exchanged meson, respectively. $n = 1$ and $\Lambda_\pi = 1.0$ for pions, $n = 2$ and $\Lambda_\rho = 1.0$ for the ρ meson.

For the resonance-nucleon-meson vertices, form factors are calculated as follows :

$$F_M^{RN}(q_M^2) = \left[\frac{(\Lambda_M^*)^2 - m_M^2}{(\Lambda_M^*)^2 - q_M^2} \right]^n \quad (7.12)$$

where $n = 1$ (monopole form factors) if the resonance has an isospin $1/2$ (N^*) and $n = 2$ (dipole form factors) if the resonance has an isospin $3/2$ (Δ), and $\Lambda_\pi^* = \Lambda_\rho^* = 1.0$ GeV. The form factors for the resonance and nucleon are taken as :

$$F_R(q^2) = \frac{\Lambda_R^4}{\Lambda_R^4 + (q^2 - M_R^2)^2} \quad (7.13)$$

where $\Lambda_\Delta = 1.0$ GeV and $\Lambda_N = 0.8$ GeV.

7.2.4 Propagators

The propagators of the exchanged meson, nucleon pole, and resonance can be written as [132, 134] :

$$G_\pi(q_\pi) = \frac{i}{q_\pi^2 - m_\pi^2} \quad (7.14)$$

$$G_R^{3/2}(q) = \frac{-i(\not{q} + M_R)G_{\mu\nu}(q)}{q^2 - M_R^2 + iM_R\Gamma_R} \quad (7.17)$$

where $\not{q} = \gamma^\mu q_\mu$ and γ^μ are Dirac matrices and Γ_R is the total width of the corresponding resonance, and $G_{\mu\nu}(q)$ is calculated as :

$$G_{\mu\nu}(q) = -g_{\mu\nu} + \frac{1}{3}\gamma_\mu\gamma_\nu + \frac{1}{3M_R}(\gamma_\mu q_\nu - \gamma_\nu q_\mu) + \frac{2}{3M_R^2}q_\mu q_\nu \quad (7.18)$$

7.3 Amplitude Calculation

The amplitudes for a given diagram are calculated using the Feynman rules [135]. The ingredients are the spinors of the interacting particles, the form factors and propagators introduced in the sections 7.2.3 and 7.2.4, as well as vertex functions which can be derived from the Lagrangians defined in Section 7.2.2 using Feynman rules.

7.3.1 Double Δ production

To explain how the calculation is performed, we take the example of the Feynman diagram (a) in Figure 7.1. It can be written as :

$$\begin{aligned} \mathcal{M}(m_1, m_2, m_a, m_b) = & \bar{u}_1(p_1, m_1) \underbrace{V(\Delta^{++ \beta} \rightarrow p_1 + p_{\pi^+})}_{(a)} \underbrace{i P_F^{\alpha \rightarrow \beta}(\Delta^{++}, p_{\Delta^{++}} = p_1 + p_{\pi^+})}_{(b)} \\ & \underbrace{V(p_a \rightarrow \Delta^{++ \alpha} + \pi^-)}_{(c)} u_a(p_a, m_a) \underbrace{i P_F(\pi^-, \tilde{p}_{\pi^-})}_{(d)} \bar{u}_2(p_2, m_2) \underbrace{V(\Delta^0 \beta' \rightarrow p_2 + p_{\pi^-})}_{(e)} \\ & \underbrace{i P_F^{\alpha' \rightarrow \beta'}(\Delta^0, p_{\Delta^0} = p_2 + p_{\pi^-})}_{(f)} \underbrace{V(p_b + \tilde{p}_{\pi^-} \rightarrow \Delta^0 \alpha')}_{(g)} u_b(p_b, m_b) \end{aligned} \quad (7.19)$$

In addition to the kinematical variables, the amplitudes depend on the spin projections of all particles in the exit channel. m_i represents the spin of proton i . p_i denotes the four-momentum of particle i :

$$\left\{ \begin{array}{l} p_{\Delta^{++}} = p_1 + p_{\pi^+} \\ p_a = p_{\Delta^{++}} + \tilde{p}_{\pi^-} \\ p_{\Delta^0} = p_2 + p_{\pi^-} = \tilde{p}_{\pi^-} + p_b \end{array} \right\} \quad (7.20)$$

$u_i(p_i, m_i)$ are the Dirac spinors for incoming proton i , $\bar{u}_i(p_i, m_i)$ are the Dirac spinors for outgoing proton and V are the vertices calculated as follows :

$$V(\Delta^{++\beta} \rightarrow p_1 + \pi^+) = \frac{g_{\pi\Delta N}}{m_\pi} F_\Delta(q^2 = (p_1 + p_{\pi^+})^2) (p_{\pi^+})_\beta \quad (a) \quad (7.21)$$

$$V(p_a \rightarrow \Delta^{++\alpha} + \tilde{p}_{\pi^-}) = \frac{g_{\pi\Delta N}}{m_\pi} F_\Delta(q^2 = (p_a - \tilde{p}_{\pi^-})^2) F_\pi^{\Delta N}(\tilde{p}_{\pi^-}^2) (\tilde{p}_{\pi^-})_\alpha \quad (c) \quad (7.22)$$

$$V(\Delta^0\beta' \rightarrow p_2 + \pi^-) = -\frac{g_{\pi\Delta N}}{m_\pi} \sqrt{\frac{1}{3}} F_\Delta(q^2 = (p_2 + p_{\pi^-})^2) (p_{\pi^-})_{\beta'} \quad (e) \quad (7.23)$$

$$V(p_b + \tilde{p}_{\pi^-} \rightarrow \Delta^0\alpha') = \frac{g_{\pi\Delta N}}{m_\pi} \sqrt{\frac{1}{3}} F_\Delta(q^2 = (p_b + \tilde{p}_{\pi^-})^2) F_\pi^{\Delta N}(\tilde{p}_{\pi^-}^2) (\tilde{p}_{\pi^-})_{\alpha'} \quad (g) \quad (7.24)$$

The isospin factors are 1 for $\Delta^{++} \rightarrow p\pi^+$ and $\sqrt{\frac{1}{3}}$ for $\Delta^0 \rightarrow p\pi^-$. $F_\Delta(q^2)$ and $F_\pi^{\Delta N}(q^2)$ are the form factors given in Eq (7.13) and Eq (7.12) respectively. $P_F^{\alpha\rightarrow\beta}(\Delta^{++}, p_{\Delta^{++}})$ and $P_F^{\alpha'\rightarrow\beta'}(\Delta^0, p_{\Delta^0})$ are the Δ propagators given in Eq (7.17) and $P_F(\pi, q)$ is the pion propagator given in Eq (7.14).

We contract as much as possible the different terms to make the calculations faster.

● Final expression

After computing the different terms in Eq (7.19) we obtain :

$$\begin{aligned} & \mathcal{M}(m_1, m_2, m_a, m_b) \\ &= \bar{u}_1(p_1, m_1) \mathbf{\Gamma}(a)(b)(c) u_a(p_a, m_a) \left[\frac{i}{\tilde{p}_{\pi^-}^2 - m_\pi^2} \right] \bar{u}_2(p_2, m_2) \mathbf{\Gamma}(e)(f)(g) u_b(p_b, m_b) \quad (7.25) \end{aligned}$$

where : $\Gamma_{(a)(b)(c)}$ and $\Gamma_{(e)(f)(g)}$ are 2×2 matrices

$$\begin{aligned} \Gamma_{(a)(b)(c)} = & \left[\frac{g_{\pi\Delta N}}{m_\pi} F_\Delta(q^2 = (p_1 + p_{\pi^+})^2) \right] \left[\frac{g_{\pi\Delta N}}{m_\pi} F_\Delta(q^2 = (p_a - \tilde{p}_{\pi^-})^2) F_\pi^{\Delta N}(\tilde{p}_{\pi^-}^2) \right] \\ & \left[-i \frac{(\not{p}_{\Delta^{++}} + M_\Delta)}{p_{\Delta^{++}}^2 - M_\Delta^2 + i M_\Delta \Gamma_\Delta} \right] \left[(p_{\pi^+} \cdot \tilde{p}_{\pi^-}) - \frac{1}{3} \not{p}_{\pi^+} \not{\tilde{p}}_{\pi^-} - \frac{\not{p}_{\pi^+} (\tilde{p}_{\pi^-} \cdot p_{\Delta^{++}})}{3 M_\Delta} \right. \\ & \left. + \frac{\not{\tilde{p}}_{\pi^-} (p_{\pi^+} \cdot p_{\Delta^{++}})}{3 M_\Delta} - \frac{2(p_{\pi^+} \cdot p_{\Delta^{++}}) (\tilde{p}_{\pi^-} \cdot p_{\Delta^{++}})}{3 M_\Delta^2} \right] \end{aligned} \quad (7.26)$$

$$\begin{aligned} \Gamma_{(e)(f)(g)} = & \left[-\frac{g_{\pi\Delta N}}{m_\pi} \sqrt{\frac{1}{3}} F_\Delta(q^2 = (p_2 + p_{\pi^-})^2) \right] \left[\frac{g_{\pi\Delta N}}{m_\pi} \sqrt{\frac{1}{3}} F_\Delta(q^2 = (p_b + \tilde{p}_{\pi^-})^2) F_\pi^{\Delta N}(\tilde{p}_{\pi^-}^2) \right] \\ & \left[-i \frac{(\not{p}_{\Delta^0} + M_\Delta)}{p_{\Delta^0}^2 - M_\Delta^2 + i M_\Delta \Gamma_\Delta} \right] \left[(p_{\pi^-} \cdot \tilde{p}_{\pi^-}) - \frac{1}{3} \not{p}_{\pi^-} \not{\tilde{p}}_{\pi^-} - \frac{\not{p}_{\pi^-} (\tilde{p}_{\pi^-} \cdot p_{\Delta^0})}{3 M_\Delta} \right. \\ & \left. + \frac{\not{\tilde{p}}_{\pi^-} (p_{\pi^-} \cdot p_{\Delta^0})}{3 M_\Delta} - \frac{2(\tilde{p}_{\pi^-} \cdot p_{\Delta^0})}{3 M_\Delta^2} \right] \end{aligned} \quad (7.27)$$

The amplitude for the graph (b) in Figure 7.1 is calculated in a similar way. The amplitudes for the antisymmetrization diagrams corresponding to the exchange of protons 1 and 2 are also taken into account with a negative sign.

7.3.2 N(1520) production followed by decay to $\Delta\pi$

The amplitude for the Feynman diagram (1-a) in Figure 7.2 can be written as :

$$\begin{aligned} \mathcal{M}(m_1, m_2, m_a, m_b) = & \bar{u}_1(p_1, m_1) \underbrace{V(\Delta^0 \beta' \rightarrow p_1 + p_{\pi^-})}_{(a)} \underbrace{i P_F^{\alpha' \rightarrow \beta'}(\Delta^0, p_{\Delta^0} = p_1 + p_{\pi^-})}_{(b)} \\ & \underbrace{V(D_{13}^+ \beta \rightarrow \Delta^0 \alpha' + p_{\pi^+})}_{(c)} \underbrace{i P_F^{\alpha \rightarrow \beta}(D_{13}^+, p_{D_{13}^+})}_{(d)} \underbrace{V(p_a \rightarrow D_{13}^+ \alpha + \pi^0)}_{(e)} u_a(p_a, m_a) \\ & \underbrace{i P_F(\pi^0, p_{\pi^0})}_{(f)} \bar{u}_2(p_2, m_2) \underbrace{V(p_b + \pi^0 \rightarrow p_2)}_{(g)} u_b(p_b, m_b) \end{aligned} \quad (7.28)$$

with

$$\left\{ \begin{array}{l} p_{\Delta^0} = p_1 + p_{\pi^-} \\ p_{D_{13}^+} = p_1 + p_{\pi^-} + p_{\pi^+} \\ p_{\pi^0} = p_2 - p_b = p_a - (p_1 + p_{\pi^-} + p_{\pi^+}) \end{array} \right\} \quad (7.29)$$

The vertices and propagators in Eq (7.28) are calculated as follows :

$$V(\Delta^0 \beta' \rightarrow p_1 + \pi^-) = -\frac{g_{\pi\Delta N}}{m_\pi} \sqrt{\frac{1}{3}} F_\Delta(q^2 = (p_1 + p_{\pi^-})^2) (p_{\pi^-})_{\beta'} \quad (a) \quad (7.30)$$

$$V(D_{13}^+ \beta \rightarrow \Delta^0 \alpha' + \pi^+) = -\frac{g_{\pi\Delta D_{13}}}{m_\pi} F_{D_{13}}(q^2 = p_{D_{13}^+}^2) F_\Delta(q^2 = p_{\Delta^0}^2) \sqrt{\frac{1}{3}} \not{p}_{\pi^+} g_{\beta\alpha'} \quad (c) \quad (7.31)$$

$$V(p_a \rightarrow D_{13}^+ \alpha + \pi^0) = -\frac{g_{\pi N D_{13}}}{m_\pi} F_{D_{13}}(q^2 = p_{D_{13}^+}^2) F_{\pi^0}^{D_{13}N}(p_{\pi^0}^2) \gamma^5 \not{p}_{\pi^0} (p_{\pi^0})_\alpha \quad (e) \quad (7.32)$$

$$V(p_b + \pi^0 \rightarrow p_2) = -\frac{f_\pi}{m_\pi} F_{\pi^0}^{NN}(p_{\pi^0}^2) \gamma^5 \not{p}_{\pi^0} \quad (g) \quad (7.33)$$

The propagators $P_F^{\alpha' \rightarrow \beta'}(\Delta^0, p_{\Delta^0})$ and $P_F^{\alpha \rightarrow \beta}(D_{13}^+, p_{D_{13}^+})$ are given in Eq (7.17) and the pion propagator is given in Eq (7.14).

● Final expression

After computing the different terms in Eq (7.28) we obtain :

$$\begin{aligned} \mathcal{M}(m_1, m_2, m_a, m_b) &= \bar{u}_1(p_1, m_1) \mathbf{\Gamma}(a) (b) (c) (d) (e) u_a(p_a, m_a) \frac{i}{p_{\pi^0}^2 - m_{\pi^0}^2} \\ &\quad \bar{u}_2(p_2, m_2) \left[-\frac{f_\pi}{m_\pi} F_{\pi^0}^{NN}(p_{\pi^0}^2) \gamma^5 \not{p}_{\pi^0} \right] u_b(p_b, m_b) \end{aligned} \quad (7.34)$$

where $\mathbf{\Gamma}(a) (b) (c) (d) (e)$ is a 2×2 matrix

$$\begin{aligned} \mathbf{\Gamma}(a) (b) (c) (d) (e) &\equiv C_{\pi^- \Delta^0 p_1} C_{\pi^+ \Delta^0 D_{13}} C_{\pi^0 p_a D_{13}} \\ &\quad \tilde{\mathbf{P}}_F(p_{\Delta^0}) \left[-i \frac{\left[\sum_{k=1}^{49} \mathcal{P}_k(\Delta^0, p_{\pi^+}, D_{13}^+, p_{\pi^0}, p_{\pi^-}) \right] \gamma^5 \not{p}_{\pi^0}}{p_{D_{13}^+}^2 - M_{D_{13}}^2 + i M_{D_{13}} \Gamma_{D_{13}}} \right] \end{aligned} \quad (7.35)$$

$$C_{\pi^-\Delta^0 p_1} = -\frac{g_{\pi\Delta N}}{m_\pi} \sqrt{\frac{1}{3}} F_\Delta(p_{\Delta^0}^2) \quad (7.36)$$

$$C_{\pi^+\Delta^0 D_{13}} = -\frac{g_{\pi\Delta D_{13}}}{m_\pi} F_{D_{13}}(p_{D_{13}^+}^2) F_\Delta(p_{\Delta^0}^2) \sqrt{\frac{1}{3}} \quad (7.37)$$

$$C_{\pi^0 p_a D_{13}} = -\frac{g_{\pi N D_{13}}}{m_\pi^2} F_{D_{13}}(p_{D_{13}^+}^2) F_{\pi^0}^{D_{13}N}(p_{\pi^0}^2) \quad (7.38)$$

$F_{\pi^0}^{NN}(p_{\pi^0}^2)$ and $F_{\pi^0}^{D_{13}N}(p_{\pi^0}^2)$ are the pion form factors given in Eq (7.11) and Eq (7.12) respectively. $F_{D_{13}}(p_{D_{13}^+}^2)$ and $F_\Delta(p_{\Delta^0}^2)$ are the form factors given in Eq (7.13).

$$\tilde{\mathbf{P}}_F(p_{\Delta^0}) = -i \frac{(\not{p}_{\Delta^0} + M_\Delta)}{p_{\Delta^0}^2 - M_\Delta^2 + i M_\Delta \Gamma_\Delta} \quad (7.39)$$

$$\sum_{k=1}^{49} \mathcal{P}_k(\Delta^0, p_{\pi^+}, D_{13}^+, p_{\pi^0}, p_{\pi^-}) = \left[\sum_{i=1}^7 \tilde{\mathbf{G}}_\beta^{(i)}(\Delta^0, p_{\pi^+}) \right] \left[\sum_{j=1}^7 \tilde{\mathbf{H}}^{(j)\beta}(D_{13}^+, p_{\pi^0}) \right] \quad (7.40)$$

$$\begin{aligned} \sum_{i=1}^7 \tilde{\mathbf{G}}_\beta^{(i)}(\Delta^0, p_{\pi^+}) &= \tilde{\mathbf{G}}_\beta(\Delta^0, p_{\pi^+}) = \not{p}_{\pi^+} (p_{\pi^-})_\beta - \frac{2}{3} \not{p}_{\pi^-} (p_{\pi^+})_\beta + \frac{1}{3} \not{p}_{\pi^-} \not{p}_{\pi^+} \gamma_\beta \\ &- \frac{\not{p}_{\pi^-} \not{p}_{\pi^+} (p_{\Delta^0})_\beta}{3 M_\Delta} + \frac{2 (p_{\pi^-} \cdot p_{\Delta^0}) (p_{\pi^+})_\beta}{3 M_\Delta} - \frac{(p_{\pi^-} \cdot p_{\Delta^0}) \not{p}_{\pi^+} \gamma_\beta}{3 M_\Delta} \\ &- \frac{2 (p_{\pi^-} \cdot p_{\Delta^0}) \not{p}_{\pi^+} (p_{\Delta^0})_\beta}{3 M_\Delta^2} \end{aligned} \quad (7.41)$$

$$\begin{aligned}
\sum_{j=1}^7 \widetilde{\mathbf{H}}^{(j)\beta}(D_{13}^+, p_{\pi^0}) &= (\not{p}_{D_{13}^+} + M_{D_{13}}) \widetilde{\mathbf{G}}^\beta(D_{13}^+, p_{\pi^0}) \\
&= -\frac{2}{3} p_{D_{13}^+}^\beta \not{p}_{\pi^0} - \frac{2 p_{D_{13}^+}^\beta (p_{D_{13}^+} \cdot p_{\pi^0})}{3 M_{D_{13}}} + (p_{\pi^0})^\beta (\not{p}_{D_{13}^+} + M_{D_{13}}) + \frac{1}{3} \gamma^\beta (\not{p}_{D_{13}^+} - M_{D_{13}}) \not{p}_{\pi^0} \\
&\quad + \frac{\gamma^\beta (\not{p}_{D_{13}^+} - M_{D_{13}}) (p_{D_{13}^+} \cdot p_{\pi^0})}{3 M_{D_{13}}} + \frac{p_{D_{13}^+}^\beta (\not{p}_{D_{13}^+} + M_{D_{13}}) \not{p}_{\pi^0}}{3 M_{D_{13}}} \\
&\quad - \frac{2 p_{D_{13}^+}^\beta (p_{D_{13}^+} \cdot p_{\pi^0}) (\not{p}_{D_{13}^+} + M_{D_{13}})}{3 M_{D_{13}}^2} \tag{7.42}
\end{aligned}$$

The amplitude for the graph (1-b) in Figure 7.2 is calculated in a similar way. The amplitudes for the antisymmetrization diagrams corresponding to the exchange of protons 1 and 2 are also taken into account with a negative sign.

7.3.3 N(1520) production followed by decay to $p\rho$

The amplitude for the Feynman diagram (3-a) in Figure 7.2 can be written as :

$$\begin{aligned}
\mathcal{M}(m_1, m_2, m_a, m_b) &= \bar{u}_1(p_1, m_1) \underbrace{V(\rho^{0\beta'} \rightarrow \pi^+ + \pi^-)}_{(a)} \underbrace{i P_F^{\alpha' \rightarrow \beta'}(\rho^0, p_{\rho^0} = p_{\pi^+} + p_{\pi^-})}_{(b)} \\
&\quad \underbrace{V(D_{13}^{+\beta} \rightarrow p_1 + \rho^{0\alpha'})}_{(c)} \underbrace{i P_F^{\alpha \rightarrow \beta}(D_{13}^+, p_{D_{13}^+})}_{(d)} \underbrace{V(p_a \rightarrow D_{13}^{+\alpha} + \pi^0)}_{(e)} \\
&\quad \underbrace{u_a(p_a, m_a) i P_F(\pi^0, p_{\pi^0})}_{(f)} \underbrace{\bar{u}_2(p_2, m_2) V(p_b + \pi^0 \rightarrow p_2)}_{(g)} u_b(p_b, m_b) \tag{7.43}
\end{aligned}$$

with

$$\left\{ \begin{array}{l} p_{\rho^0} = p_{\pi^+} + p_{\pi^-} \\ p_{D_{13}^+} = p_1 + p_{\pi^-} + p_{\pi^+} \\ p_{\pi^0} = p_2 - p_b = p_a - (p_1 + p_{\pi^-} + p_{\pi^+}) \end{array} \right\} \tag{7.44}$$

$$V(\rho^{0\beta'} \longrightarrow \pi^+ + \pi^-) = i g_{\rho\pi\pi} F_{\rho}^{\rho\pi\pi}(p_{\rho}^2) [(P_{\pi^+})_{\beta'} - (P_{\pi^-})_{\beta'}] \quad (a) \quad (7.45)$$

$$V(D_{13}^{+\beta} \longrightarrow \rho^{0\alpha'} + p) = i g_{D_{13}\rho N}^* F_{\rho}^{D_{13}N}(p_{\rho}^2) F_{D_{13}}(p_{D_{13}}^2) g_{\beta\alpha'} \quad (c) \quad (7.46)$$

$$V(p_a \rightarrow D_{13}^+ \alpha + \pi^0) = -\frac{g_{\pi ND_{13}}}{m_{\pi}^2} F_{D_{13}}(q^2 = p_{D_{13}}^2) F_{\pi^0}^{D_{13}N}(p_{\pi^0}^2) \gamma^5 \not{p}_{\pi^0} (p_{\pi^0})_{\alpha} \quad (e)(7.47)$$

$$V(p_b + \pi^0 \rightarrow p_2) = -\frac{f_{\pi}}{m_{\pi}} F_{\pi^0}^{NN}(p_{\pi^0}^2) \gamma^5 \not{p}_{\pi^0} \quad (g) \quad (7.48)$$

$P_F^{\alpha'\beta'}(\rho^0, p_{\rho^0})$ and $P_F^{\alpha\rightarrow\beta}(D_{13}^+, p_{D_{13}^+})$ and $P_F(\pi^0, p_{\pi^0})$ are the propagators given in Eq (7.15), Eq (7.17) and Eq (7.14) respectively.

● Final expression

After computing the different terms in Eq (7.43) we obtain :

$$\begin{aligned} \mathcal{M}(m_1, m_2, m_a, m_b) &= \bar{u}_1(p_1, m_1) \Gamma_{(a)(b)(c)(d)(e)} u_a(p_a, m_a) \\ &\quad \frac{i}{p_{\pi^0}^2 - m_{\pi^0}^2} \bar{u}_2(p_2, m_2) \left[-\frac{f_{\pi}}{m_{\pi}} F_{\pi^0}^{NN}(p_{\pi^0}^2) \gamma^5 \not{p}_{\pi^0} \right] u_b(p_b, m_b) \end{aligned} \quad (7.49)$$

where $\Gamma_{(a)(b)(c)(d)(e)}$ is a 2×2 matrix

$$\Gamma_{(a)(b)(c)(d)(e)} \equiv C_{\rho\pi\pi} C_{D_{13}\rho N} C_{\pi ND_{13}} \left[i \frac{1}{p_{\rho}^2 - m_{\rho}^2} \right] P_F(D_{13}^+) \mathcal{H}(h, p_{D_{13}^+}, p_{\pi^0}) \gamma^5 \not{p}_{\pi^0} \quad (7.50)$$

$$C_{\rho\pi\pi} = i g_{\rho\pi\pi} F_{\rho}^{\pi\pi}(p_{\rho}^2) \quad (7.51)$$

$$C_{D_{13}\rho N} = i g_{D_{13}\rho N}^* F_{\rho}^{D_{13}N}(p_{\rho}^2) F_{D_{13}}(p_{D_{13}}^2) \quad (7.52)$$

$$C_{\pi ND_{13}} = -\frac{g_{\pi ND_{13}}}{m_{\pi}^2} F_{D_{13}}(q^2 = p_{D_{13}^+}^2) F_{\pi^0}^{D_{13}N}(p_{\pi^0}^2) \quad (7.53)$$

$F_{\pi^0}^{D_{13}N}(p_{\pi^0}^2)$ and $F_{\rho}^{D_{13}N}(p_{\rho}^2)$ are the form factors given in Eq (7.12). $F_{D_{13}}(p_{D_{13}^+}^2)$ and $F_{\pi^0}^{NN}(p_{\pi^0}^2)$ are the form factors given in Eq (7.13) and Eq (7.11) respectively.

$$h = -(p_{\pi^+} - p_{\pi^-}) + \frac{(p_{\pi^+} - p_{\pi^-})}{m_\rho^2}. \quad (7.54)$$

$$\mathbf{P}_F(D_{13}^+) = -i \frac{(\not{p}_{D_{13}^+} + M_{D_{13}})}{p_{D_{13}^+}^2 - M_{D_{13}}^2 + i M_{D_{13}} \Gamma_{D_{13}}} \quad (7.55)$$

$$\mathcal{H}(h, p_{D_{13}^+}, p_{\pi^0}) \equiv -\frac{1}{3} \not{h} \not{p}_{\pi^0} - \frac{\not{h} (p_{D_{13}^+} \cdot p_{\pi^0}) - \not{p}_{\pi^0}}{3 M_{D_{13}}} - \frac{2 (p_{D_{13}^+} \cdot p_{\pi^0})}{3 M_{D_{13}}^2} \quad (7.56)$$

The amplitude for the graph (3-b) in Figure 7.1 is calculated in a similar way. The amplitudes for the antisymmetrization diagrams corresponding to the exchange of protons 1 and 2 are also taken into account with a negative sign.

7.4 Numerical calculation result and discussion

7.4.1 Building an event generator

For each process the amplitudes of all the different diagrams should be added. For the final state, the fact that the detector does not distinguish between the spin states of the outgoing particles means that what is measured are all possible combinations of spin final states. The matrix element squared is :

$$|\mathcal{M}_{total}|^2 = \sum_s |\mathcal{M}_1(s_1, \dots, s_n) + \mathcal{M}_2(s_1, \dots, s_n) + \dots + \mathcal{M}_n(s_1, \dots, s_n)|^2 \quad (7.57)$$

where \mathcal{M}_i is the matrix element for each Feynman diagram and s_i is the spin state.

Once the amplitude is calculated, it can then be injected in Eq (7.2). To obtain the differential distributions as a function of one variable, one needs to integrate over all the other variables, but it is extremely difficult to determine phase-space limits due to the complexity of the equations. In addition, we want to take into account the effect of acceptance cuts on the differential distributions, which makes the integration limits even more difficult to calculate. Therefore, it is more appropriate to use an event generator. We used the PLUTO event generator [61, 109] to generate a million phase space events

for the reaction $pp \rightarrow pp\pi^+\pi^-$. The respective distributions are given by Eq (7.2) where the transition amplitude is equal to 1. To generate events according to our model, we then just have to parametrize each event with the squared amplitude calculated from our model. The kinematical variables and the weight are stored in a Ntuple, which makes it very easy to plot any distribution and to apply acceptance or efficiency cuts, in the same way as for the previous simulations described in Chapter 4.

7.4.2 Differences with the resonance cocktail model

In the following, we will discuss some results of the calculation and compare them with the results of our PLUTO resonance model. Let's start by reminding the differences between the two approaches.

The PLUTO resonance cocktail is basically a phase space event generator modified by weighting functions. The mass distributions (see Eqs (4.1),(4.2)) of the baryonic resonances and mesons are taken into account using Breit-Wigner weights which play the same role as the propagators (Eqs (7.11), (7.12), (7.13)) used in the Lagrangian model. However, while in the Lagrangian model, fixed width were used for simplicity, in PLUTO the resonances widths are mass dependent, for the decay $R \rightarrow m_1 + m_2$, the width is given by :

$$\Gamma_{m_1 m_2}^k(m) = x_{M_R}(m) \left(\frac{q_{m_1 m_2}^R(m)}{q_{m_1 m_2}^R(M_R)} \right)^{2L+1} \left(\frac{\nu_{m_1 m_2}^R(m)}{\nu_{m_1 m_2}^R(M_R)} \right) \Gamma_R^k \quad (7.58)$$

where the subscript R refers to the resonance corresponding to the static mass pole for the decay mode in hand with mass M_R and width Γ_R^{tot} , m denotes the running Breit-Wigner mass. The dependence on the two decay products with mass m_1 and m_2 enters via the terms $q^R(m)$ and $q^R(M_r)$, namely the momenta of one out of the two decay products in the rest frame of the parent resonance R . L is the transferred orbital angular momentum and k denotes the decay mode. ν is the cutoff parametrization that is used :

$$\nu_{m_1 m_2}^R(m) = \frac{\beta^2}{\beta^2 + (q_{m_1 m_2}^R(m))^2} \quad (7.59)$$

and the parameter $\beta = 300$ MeV for $\Delta(1232)$, among with the phase space factor :

$$x_{M_R}(m) = \frac{M_R}{m} \quad (7.60)$$

For higher baryon resonances, the following parametrization is applied :

$$\beta = (M_R - m_1 - m_2)^2 + \frac{(\Gamma_R^{tot})^2}{4}, \quad x = 1 \quad (7.61)$$

The most important difference is due to the fact that there is no explicit interaction in our resonance model. All the dynamics of the reaction are parametrized in the very simple t -weight (see Section 4.5), which suppresses large transfers at the baryon excitation vertex. This weight therefore plays the same role as the vertex form factors but it is expressed in a different way. In addition, in the Lagrangian model, the vertex functions induce an additional kinematical factor, which depends explicitly on the exchanged particle (π, ρ, \dots) and on the spin of the baryon, according to the Lagrangians (Section 7.2.2). This aspect is completely absent in PLUTO resonance model and may induce significant differences. In PLUTO resonance cocktail, the different transfer dependence for the excitation of the resonance on the projectile or target nucleon is taken into account by applying two different weights depending on the center-of-mass angle of the excited baryon, but this is a simple assumption. In the Lagrangian model, the direct and exchange graphs are explicitly taken into account with their respective form factor. The global amplitude takes into account the two graphs coherently, i.e. including interferences between the amplitudes for each graph.

7.4.3 Results of the Lagrangian model

As mentioned above in Section 4.5, in PLUTO simulations, the angular distribution were calculated based on a phenomenological parametrization (see Eq (4.3)). To compare the centre of mass angular distribution of PLUTO with our Lagrangian model, particles four-momenta were boosted to the center of mass frame using Lorentz boosts. Figure 7.3 shows the center of mass angular distribution of the final state for the two processes $pp \rightarrow \Delta^{++}(1232)\Delta^0(1232)$ and $pp \rightarrow pN^+(1520)$ compared to the parameterized PLUTO simulation (green curve). In both figures we see that our model angular distribution shows a somewhat less steep behavior as PLUTO simulation. It is however very satisfactory to see that the global trend is very similar and this can be taken as a validation of the parameterization that was applied.

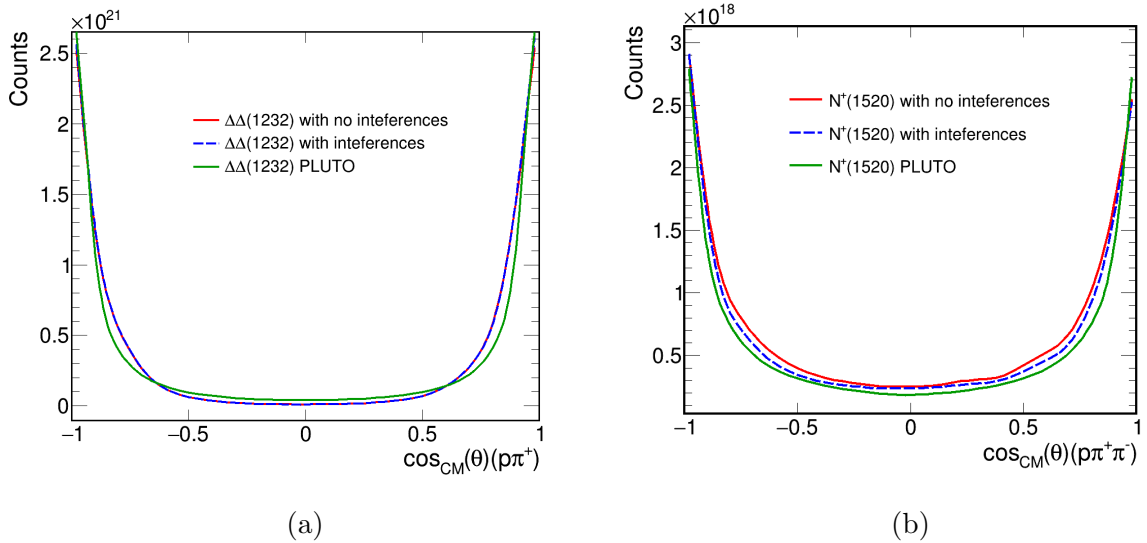


FIGURE (7.3) (a) $pp \rightarrow \Delta^{++}(1232)\Delta^0(1232) (p\pi^+)$ centre of mass angular distribution, (b) $pp \rightarrow pN^+(1520) (p\pi^+\pi^-)$ centre of mass angular distribution compared to the parameterized PLUTO simulation (green).

The invariant mass distributions obtained with the Lagrangian model for $N(1520)$ and the double- Δ production processes are shown in Figure 7.4 and Figure 7.5 in comparison with the PLUTO results. Here, we are only interested in the shapes of the distributions, the spectra are normalized such that their integral is the same. The main features of the spectra are similar. However, it is noticeable that the resonant peaks are narrower in the case of PLUTO calculation and shifted towards lower mass values by about 10 MeV. In fact, the peaks in the Lagrangian model exactly peak at the pole of the resonances. This difference might be due to both the choice of fixed or mass dependent width (see sec.7.4.2) or to the different expressions of the vertex form factors and phenomenological t -weight. Indeed, the former which is used in the Lagrangian model is maximum at a momentum transfer corresponding to the pole mass, while the t -weight used in the resonance model decreases monotonically with t . This enhances small momentum transfers and may cause the invariant mass shift. Further differences can arise from the fixed widths used in the Lagrangian model. We have shown in Chapter 5 that the position of the invariant mass peaks is very well reproduced by our PLUTO resonance model. We therefore conclude that the phenomenological t -weight gives a more realistic approach than the Lagrangian model with vertex form factors.

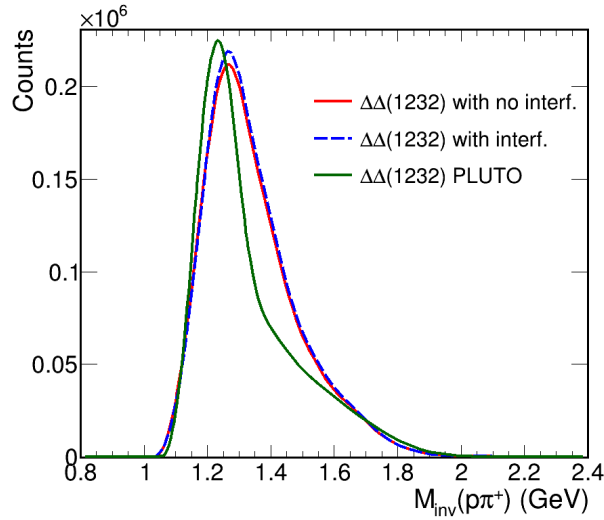


FIGURE (7.4) $p\pi^-$ invariant mass distribution in HADES acceptance for the $pp \rightarrow \Delta^{++}(1232)\Delta^0(1232)$ channel. Comparison between "full" calculation (dashed blue) and "no interference" calculation (red) and PLUTO simulation (green).

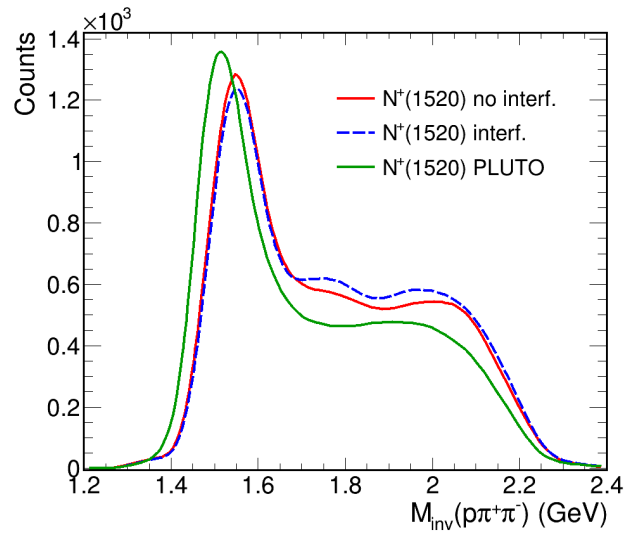


FIGURE (7.5) $p\pi^+\pi^-$ invariant mass distribution in HADES acceptance for the $pp \rightarrow pN^+(1520)$ channel. Comparison between "full" calculation (dashed blue) and "no interference" calculation (red) and PLUTO simulation (green).

7.5 Interference effect

To see the effect of interferences we compare two calculations :

- **Full calculation** : where the squared amplitude is computed as follows :

$$|\mathcal{M}_{total}|^2 = \sum_s |\mathcal{M}_1 + \mathcal{M}_2 + \dots + \mathcal{M}_n|^2 \quad (7.62)$$

- **No interference calculation** : where the squared amplitude is computed as follows :

$$|\mathcal{M}_{total}|^2 = |\mathcal{M}_1(s_1)|^2 + \dots + |\mathcal{M}_1(s_n)|^2 + \dots + |\mathcal{M}_n(s_1)|^2 + \dots + |\mathcal{M}_n(s_n)|^2 \quad (7.63)$$

were \mathcal{M}_1 is the amplitude for diagram (a) in Figure 7.1, \mathcal{M}_2 is the amplitude for diagram (b) in Figure 7.1, \mathcal{M}_3 and \mathcal{M}_4 are the amplitudes for the antisymmetrization diagrams of (a) and (b) respectively. Same for diagrams in Figure 7.2, where we have 12 amplitudes in total. This leads to a coherent sum of cross sections in the "full calculation" case, and an incoherent sum of cross sections in the "no interference calculation" case which corresponds to the cross section calculated in our PLUTO model.

The result of our test model is shown separately for the double $\Delta(1232)$ production and the $N(1520)$ resonance production in Figure 7.4, Figure 7.5 and for the full model in Figure 7.6.

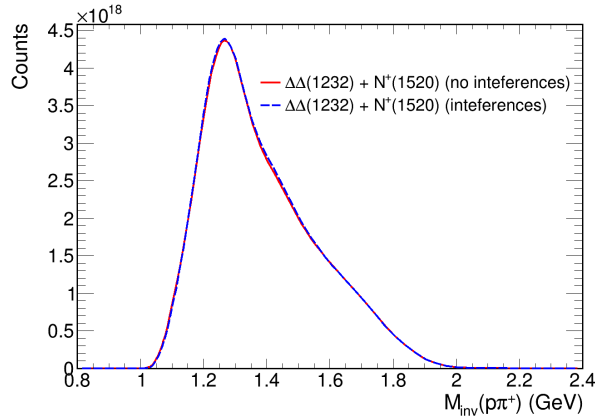


FIGURE (7.6) $p\pi^+$ invariant mass distribution in HADES acceptance for the $pp \rightarrow \Delta^{++}(1232)\Delta^0(1232)$ and $pp \rightarrow pN^+(1520)$ channels. Comparison between "full" calculation (dashed blue) and "no interference" calculation (red).

The analysis of the result was separated in two steps. In the first step we investigated for one channel the effect of the interferences between the different Feynman diagrams which contribute to the same process (graphs (a),(b) in Figure 7.1 and antisymmetrization graphs for $\Delta^{++}\Delta^0$ and graphs (a-e) in Figure 7.2 for $N^+(1520)$ and antisymmetrization graphs). The results show that the interference effect is very small in both cases. For the double $\Delta(1232)$ the effect is about 0.7% in full acceptance and the interference is constructive (see Figure 7.4). In HADES acceptance however, it gets slightly higher, about 1.4%. For the $N(1520)$ the effect is about 7% in full acceptance and the interference is constructive. It gets much lower in HADES acceptance, about 2% (see Figure 7.5).

The fact that the effect of interference is different when acceptance cuts are applied just reflects that the interferences depend on the range of kinematical variables over which the amplitudes are integrated. The lower effect of the interferences in the case of the double- Δ production is probably due to the fact that the different graphs have small kinematical overlap. For example, the π^+ is boosted in the forward direction for graph (a) and in the backward direction for graph (b). One can expect a larger kinematical overlap for the graphs corresponding to the decay of the $N(1520)$, where the angular distributions are wider due to the three body decays when pions are emitted from the same excited nucleon.

In the second step we studied the full calculation and investigated the effect of interferences between the two channels $pp \rightarrow \Delta^{++}\Delta^0$ and $pp \rightarrow pN^+(1520)$. The result shows that the interference is constructive also in this case, but still negligible, about 1.5% in HADES acceptance (see Figure 7.6). The effect of interferences is also shown for the angular distributions in Figure 7.3. It can also be observed that the effect is small.

It has to be noted that whether the interference are constructive or destructive depends on the particular choice of the amplitude, in particular, the relative sign of the coupling constants. Since the choice made here for all the model parameters is the same as in Cao *et al.* Lagrangian model [90], it validates their approximation of neglecting the interferences.

8

Comparison to theoretical models

In this chapter we present a direct comparison of differential spectra for the exclusive channel $pp \rightarrow pp\pi^+\pi^-$ with theoretical models predictions (OPER [91] and Cao *et al.* Lagrangian model [90]). We also compare the baryonic resonances contributions extracted from our data to the predictions of transport models : UrQMD and GiBUU [69].

In order to perform a proper comparison of differential spectra measured with HADES, with OPER and Cao *et al.* Lagrangian model, events generated with the models have been filtered with the HADES acceptance filters and smeared as explained in section 4.4.

8.1 OPER model

During this work we collaborated with A.P. Jerusalemov to compare OPER model simulation to our data. OPER stands for **One Pion Exchange Reggiezed** and it

is based on Regge theory [136]. The models of Regge pole exchange are based on the method of complex momenta and consider an exchange in t-channel by a virtual state R that has quantum numbers of particle (resonances) with variable spin and is on some trajectory $\alpha_R(t)$ named Regge trajectory.

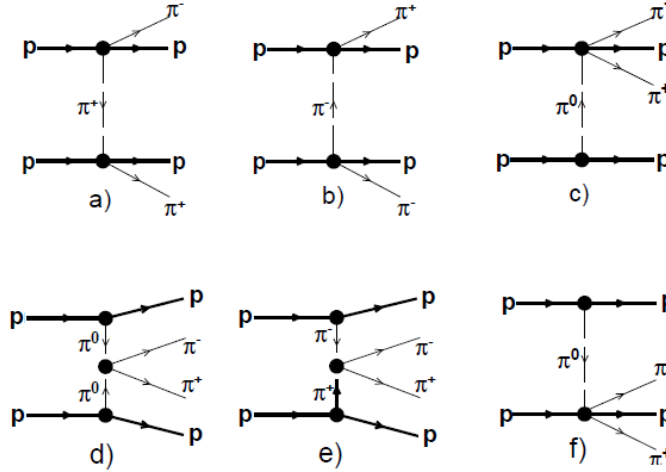


FIGURE (8.1) OPER Feynman diagrams for the reaction $pp \rightarrow pp\pi^+\pi^-$

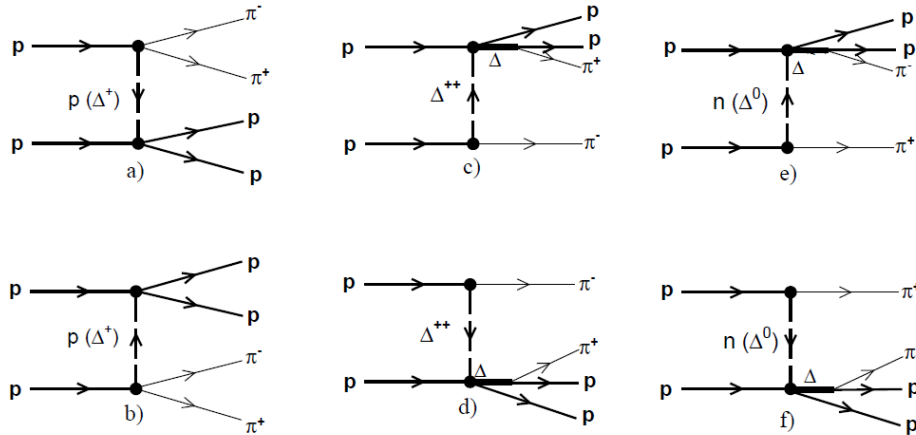


FIGURE (8.2) One baryon exchange (OBE) Feynman diagrams for the reaction $pp \rightarrow pp\pi^+\pi^-$

Figure 8.1 shows the OPER diagrams for the reaction $pp \rightarrow pp\pi^+\pi^-$. The diagrams (a) and (b) describe the production of the double-resonances that decay to $N\pi$. The parameters of the resonances were taken from PWA. The amplitudes $T_{N\pi \rightarrow N\pi}$ were used as vertex functions, hence, all possible double resonance excitations are included. The diagrams (c) and (f) describe the production of the one resonances that decay to $N\pi\pi$. The parameters of these resonances were taken from PDG. The amplitudes $T_{N\pi \rightarrow N\pi\pi}$ were used as vertex functions [137]. The diagrams (d) and (e) ("hanged diagrams")

describe $\pi\pi \rightarrow \pi\pi$ scattering, the study [92] has shown that the "hanged" diagrams contribution in the np reaction cross-section at momenta $p_0 < 10$ GeV/c is negligible and the interference between the other diagrams is very small. The one baryon exchange (OBE) diagrams shown in Figure 8.2 were also taken into account in the framework of this model.

The OPER model does not provide absolute cross sections, so in order to compare to HADES data all OPER calculations are normalized to the experimental yield measured in acceptance. Figure 8.3 represents the $p\pi^-$, $p\pi^+\pi^-$, $p\pi^+$ and $\pi^+\pi^-$ invariant mass distributions. The solid red lines are the results of OPER model calculations. The $p\pi^-$ invariant mass (see Figure 8.3 a) shows the same three peaks as in the data, however the one at $M_{inv}(p\pi^-)$ close to the $\Delta(1232)$ mass is too large, which means that the double- Δ contribution is overestimated. The $p\pi^+\pi^-$ invariant mass distribution (see Figure 8.3 (b)) is not well described by the OPER model, it shows two peaks : one around 1.6 GeV that can only be due to the $\Delta(1600)$ and another around 1.8 GeV that can only come from the excitation of the higher-laying resonances $N(1875)$ and $N(1880)$ which is not compatible with our results. As shown in Table 5.4, from the analysis of our data we deduced that the $\Delta(1600)$ resonance does not contribute and the $N(1875)$ and $N(1880)$ contributions are negligible. The OPER model predicts that $pp \rightarrow pp\pi^+\pi^-$ reaction occurs mostly with an intermediate Δ^{++} , either via a double- Δ excitation or via a resonance that decays in $\Delta^{++}\pi^-$, which is consistent with our analysis. This is why the $p\pi^+$ invariant mass (see Figure 8.3 (c)) is perfectly well described by the OPER model, Finally the $\pi^+\pi^-$ invariant mass (see Figure 8.3 d) is rather well described.

Figure 8.4 represents the $p\pi^-$, $p\pi^+\pi^-$, $p\pi^+$ and $\pi^+\pi^-$ angular distributions in the center of mass reference frame compared to the results of OPER model calculations. $p\pi^-$, $p\pi^+\pi^-$ and $p\pi^+$ angular distributions in Figure 8.4 (a), (b) and (c) respectively are not well described by OPER model calculations, they show a steeper backward/forward behavior, this may be due to the overestimation of the double- Δ excitation, which is expected to have a steeper angular distribution than the distribution of heavier baryonic resonances. The $\pi^+\pi^-$ angular distributions in Figure 8.4(d) is also not well described by the OPER model calculations, this shape is a signature for the one resonance excitation as shown by our PLUTO resonance cocktail (see Figure 5.15 (h) dashed green curve), this proves that the one resonance excitation is overestimated compared to the double resonance excitation.

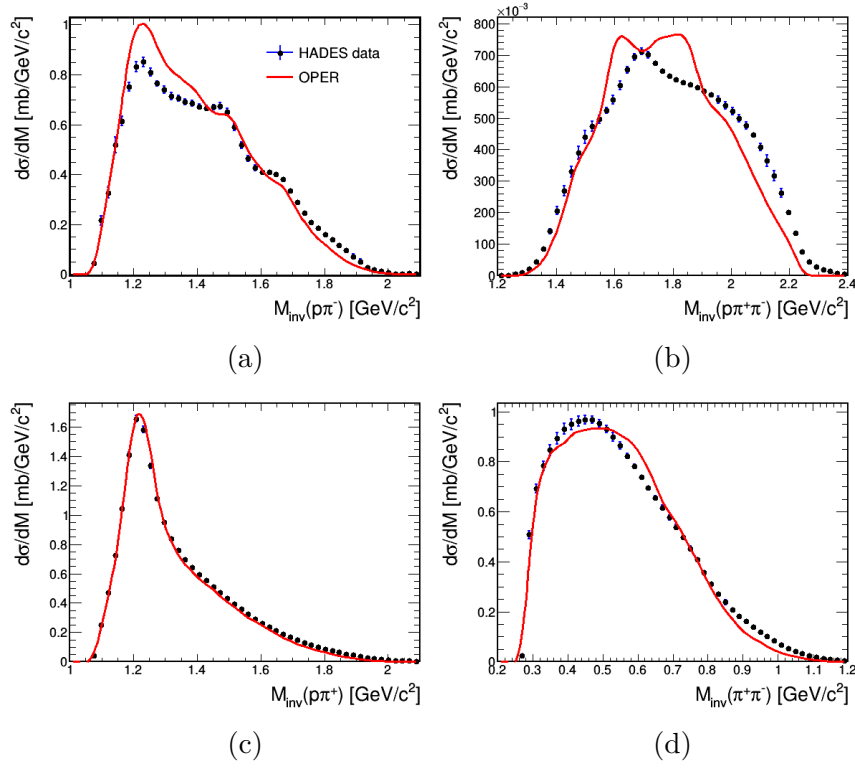


FIGURE (8.3) (a) $p\pi^-$, (b) $p\pi^+\pi^-$, (c) $p\pi^+$, (d) $\pi^+\pi^-$ invariant mass distributions compared to the result of OPER model simulation (red curves) normalized to the data.

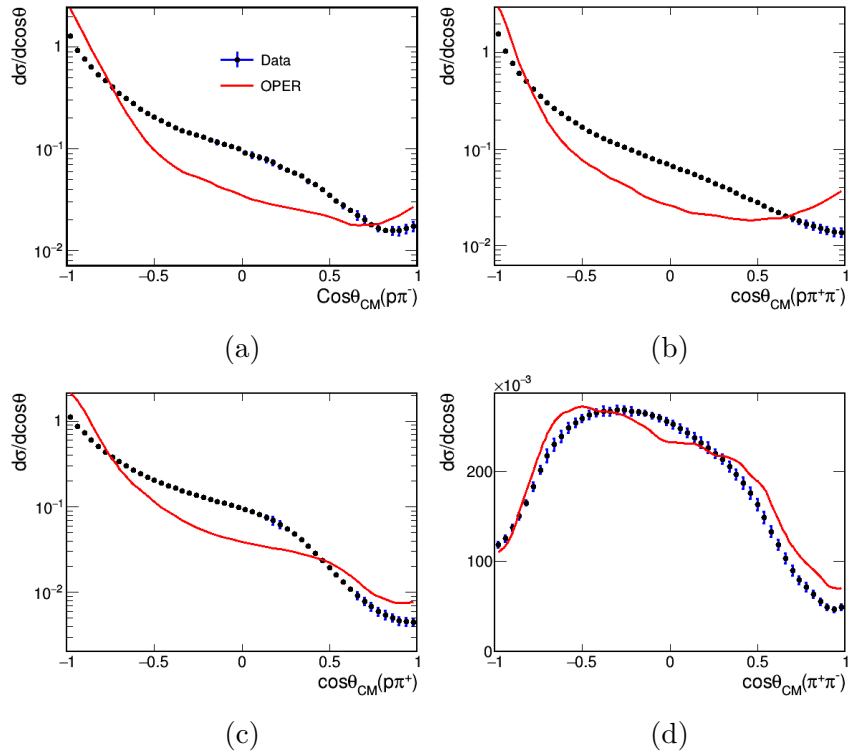


FIGURE (8.4) (a) $p\pi^-$, (b) $p\pi^+\pi^-$, (c) $p\pi^+$, (d) $\pi^+\pi^-$ CM angular distributions compared to the result of OPER model simulation (red curves) normalized to the data.

8.2 Cao Lagrangian Model

We also collaborated with Xu Cao from Institute of Modern Physics, China, to compare his effective Lagrangian model to our data. In this model the resonances with mass up to 1.72 GeV are incorporated with their properties taken from PDG 2010 [138] in an effective Lagrangian model with the motivation to give a reasonable explanation to the six isospin channels $NN \rightarrow NN\pi\pi$ and get better understanding of the dynamics for this kind of reaction [90]. The form factors of the resonances are the same as in our Lagrangian model (see 7), and the values of the cutoff were adjusted to fit the data from [78–83, 86, 139] at beam energies from threshold up to 2.2 GeV. Figure 8.5 shows Cao Lagrangian model calculation result for the channel $pp \rightarrow pp\pi^+\pi^-$.

Figure 8.6 shows the Feynman diagrams of this model, (1) and (2) represent the one resonance production with a meson exchange (π , σ , ρ or η) and the decay to a nucleon and a meson (σ or ρ) ($R \rightarrow NM$). (3) and (4) represent the one resonance (or nucleon pole) production with a meson exchange (π , σ , ρ or η) and the decay to a $\Delta\pi$ (or N pole) ($R_1 \rightarrow R_2\pi$). (5) and (6) represent the double resonance production

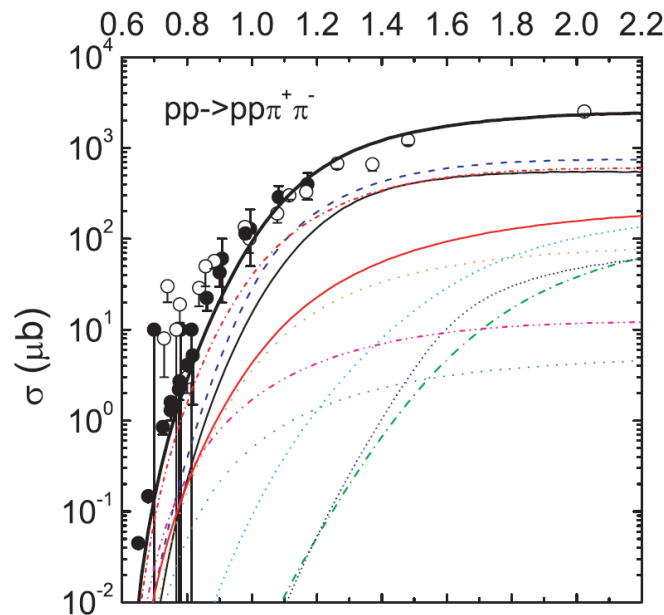


FIGURE (8.5) Total cross sections of $pp \rightarrow pp\pi^+\pi^-$ compared to predictions of Cao *et al.* Lagrangian model [90]. The black solid, red short-dash-dotted, blue dashed, orange dotted, green dotted, cyan short-dashed, green dash-dotted, royal short-dotted, magenta dash-dot-dotted, bold red, and bold solid curves correspond to contribution from double- Δ , $N(1440) \rightarrow N\sigma$, $N(1440) \rightarrow \Delta\pi$, $\Delta \rightarrow \Delta\pi$, $\Delta \rightarrow N\pi$, $\Delta(1600) \rightarrow \Delta\pi$, $\Delta(1600) \rightarrow N(1440)\pi$, $\Delta(1620) \rightarrow \Delta\pi$, nucleon pole, $N \rightarrow \Delta\pi$ and the full contributions, respectively. The solid circles and triangles represent the data from [78–83, 86, 139].

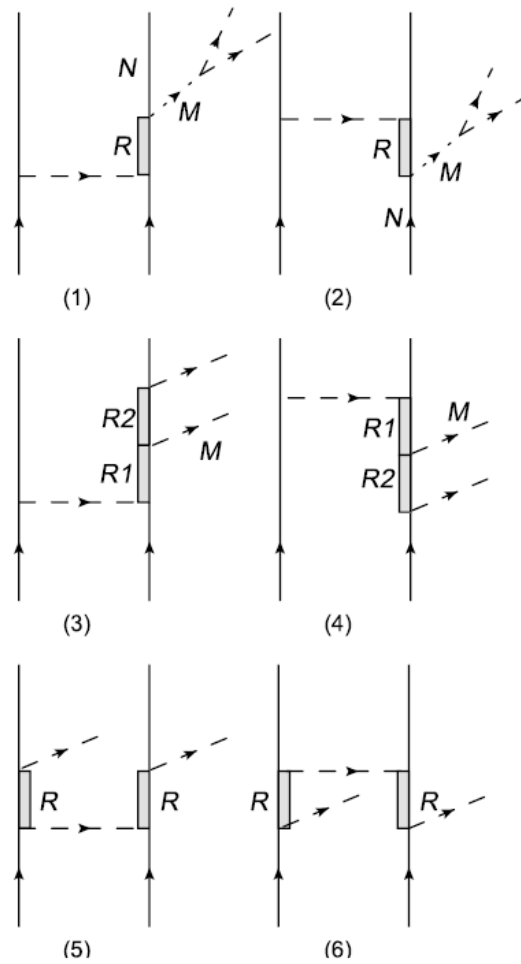


FIGURE (8.6) Feynman diagrams taken into account in Cao *et al.* Lagrangian model [90] for $NN \rightarrow NN\pi\pi$ [90]. The solid, dashed and dotted lines stand for the nucleon, mesons and intermediate σ (or ρ) meson. The shading histograms represent the intermediate resonances or nucleon poles. $R \rightarrow NM$, $R1 \rightarrow R2M$ and double-R are used to label (1)(2), (3)(4) and (5)(6), respectively.

where only the double- $\Delta(1232)$ contribution was considered. Interference terms among different diagrams are not included.

The prediction for the total production is 11.5 mb, which is much higher than our estimate. Therefore, in order to compare HADES data to Cao *et al.* Lagrangian model calculations, all the contributions were normalized to the experimental cross section. The contributions of different decay channels and different meson exchange are provided separately. The contributions for a given resonance excited by different meson exchanges are summed when comparing to data. However, to give an idea of the contributions corresponding to the different meson exchanges, Figure 8.7 shows the result for $p\pi^-$ invariant mass distribution in Cao *et al.* Lagrangian model calculation for the different exchanged mesons (π , σ , ρ and η). It should be mentioned that ρ -exchange is the most

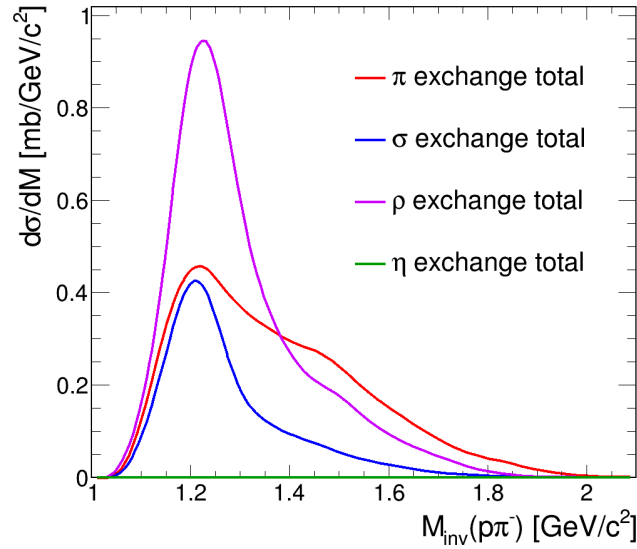


FIGURE (8.7) $p\pi^-$ invariant mass distribution in Cao *et al.* Lagrangian model calculation for the different exchanged mesons π , σ , ρ and η .

important contribution to this channel followed by π -exchange contrary to what was deduced for energies up to 2.2 GeV [90]. This higher contribution of ρ -exchange at higher energies makes sense since the larger momentum transfers available at higher energies favors ρ -exchange. Then comes σ -exchange and η -exchange is very negligible. The model calculation results show that the following contributions are very negligible : double N-pole, N-pole σ , $N(1520)$, $N(1535)$, $N(1675)$, $N(1680)$, $\Delta(1620)$, $N(1650)$ and $N(1700)$ either because of their small branching ratios to the double-pion channel or because their excitation is suppressed because they correspond to higher partial waves.

Figure 8.8 represents the $p\pi^-$, $p\pi^+\pi^-$, $p\pi^+$ and $\pi^+\pi^-$ invariant mass distributions compared to Cao *et al.* Lagrangian model calculations (dotted dashed red line). The visible contributions come from : double- $\Delta(1232)$, $N(1710) \rightarrow \Delta\pi$, $N(1710) \rightarrow N\rho$, $N(1440) \rightarrow N\sigma$ (σ exchange), $N(1440) \rightarrow \Delta\pi$ (σ exchange), $N(1720) \rightarrow N\rho$ (pion exchange), $\Delta(1600) \rightarrow \Delta\pi$ (pion exchange), $\Delta(1700) \rightarrow \Delta\pi$ (pion exchange).

As we can see the data are not well represented by the model. In the $p\pi^-$ invariant mass distribution (see Figure 8.8 a) the model shows only one peak at 1.2 GeV, this is due to the fact that only the double- $\Delta(1232)$ contribution was considered. Our data show clearly that $\Delta(1232)N(1520)$ and $\Delta(1232)N(1680)$ should be added. The $p\pi^+\pi^-$ invariant mass distribution (see Figure 8.8 b) shows two peaks at 1.45 GeV and 1.7 GeV coming from a very high contribution of the resonances $N(1440)$ decaying to $\Delta\pi$ and $N\sigma$

with a σ -meson exchange, $N(1710)$ decaying to $\Delta\pi$ and $N\rho$ with a ρ meson exchange and $N(1720)$ decaying to $N\rho$ with a pion exchange. In the $p\pi^+$ invariant mass distribution (see Figure 8.8 c) the peak at the $\Delta(1232)$ mass is not fully reproduced by the model due to the underestimation of the double resonance excitation, which according to our analysis, mainly involves a $\Delta^{++}(1232)$ contribution and the high decay of resonances to $N\rho$ instead of $\Delta\pi$. The $\pi^+\pi^-$ invariant mass distribution (see Figure 8.8 d) shows a large peak around the ρ -meson mass due to the high decay of $N(1710)$ and $N(1720)$ $N\rho$. It also shows that the $N(1440)$ excitation is overestimated and the $N(1520)$ is very negligible.

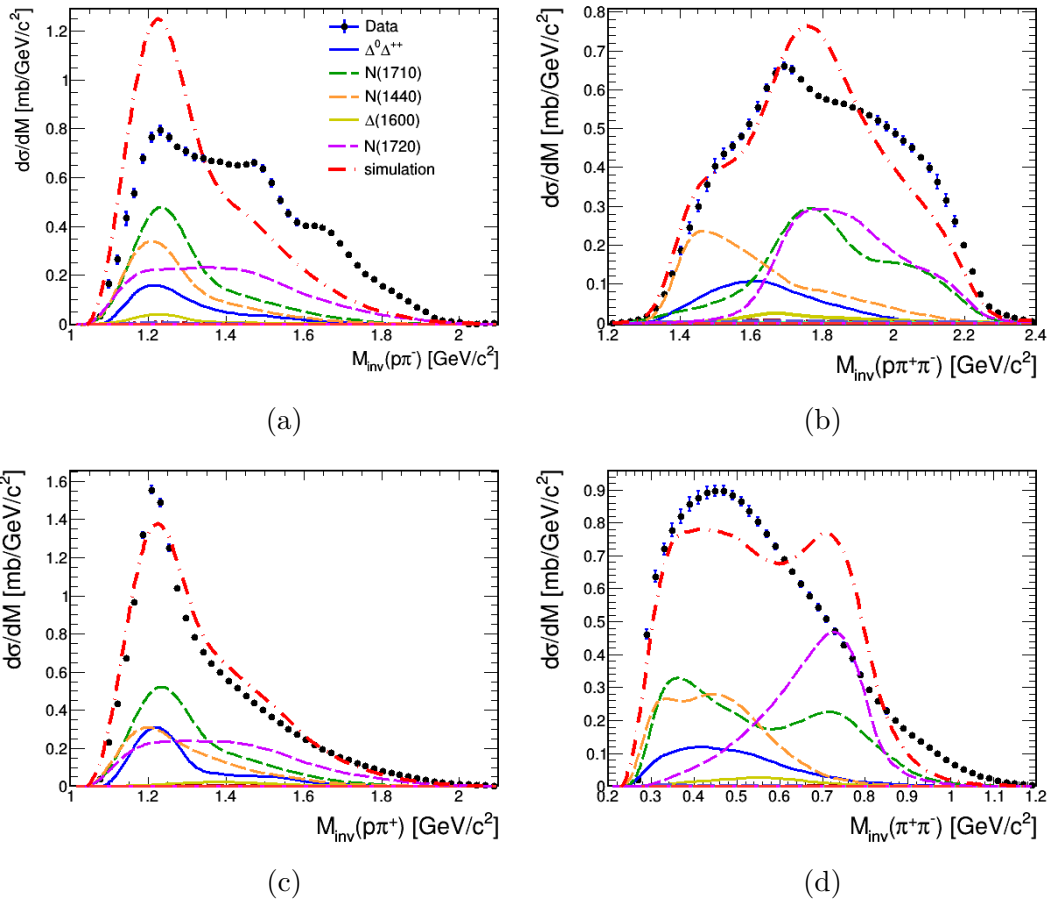


FIGURE (8.8) (a) $p\pi^-$, (b) $p\pi^+\pi^-$, (c) $p\pi^+$, (d) $\pi^+\pi^-$ invariant mass distributions compared to the result of Cao *et al.* Lagrangian model calculations (red curves). A global normalization factor is applied to the simulation in order to match the total experimental yield in HADES acceptance.

Figure 8.9 represents the $p\pi^-$, $p\pi^+\pi^-$, $p\pi^+$ and $\pi^+\pi^-$ angular distributions in the center of mass reference frame compared to the results of Cao *et al.* Lagrangian model calculations. It is interesting to note that the angular distributions for the double- Δ excitation is much steeper than for the single resonance excitation and the slope of the

angular distributions is also decreasing with the mass of the baryon. These two features are in qualitative agreement with our PLUTO resonance cocktail model. However, the double- Δ and $N(1440)$ contribution is much steeper in Cao *et al.* model. In comparison to the data, the theoretical $p\pi^-$, $p\pi^+\pi^-$ and $p\pi^+$ angular distributions are in general too steep. The $\pi^+\pi^-$ angular distribution (see Figure 8.9 d) is not well described which is also probably due to the too steep angular distribution for the light baryon production.

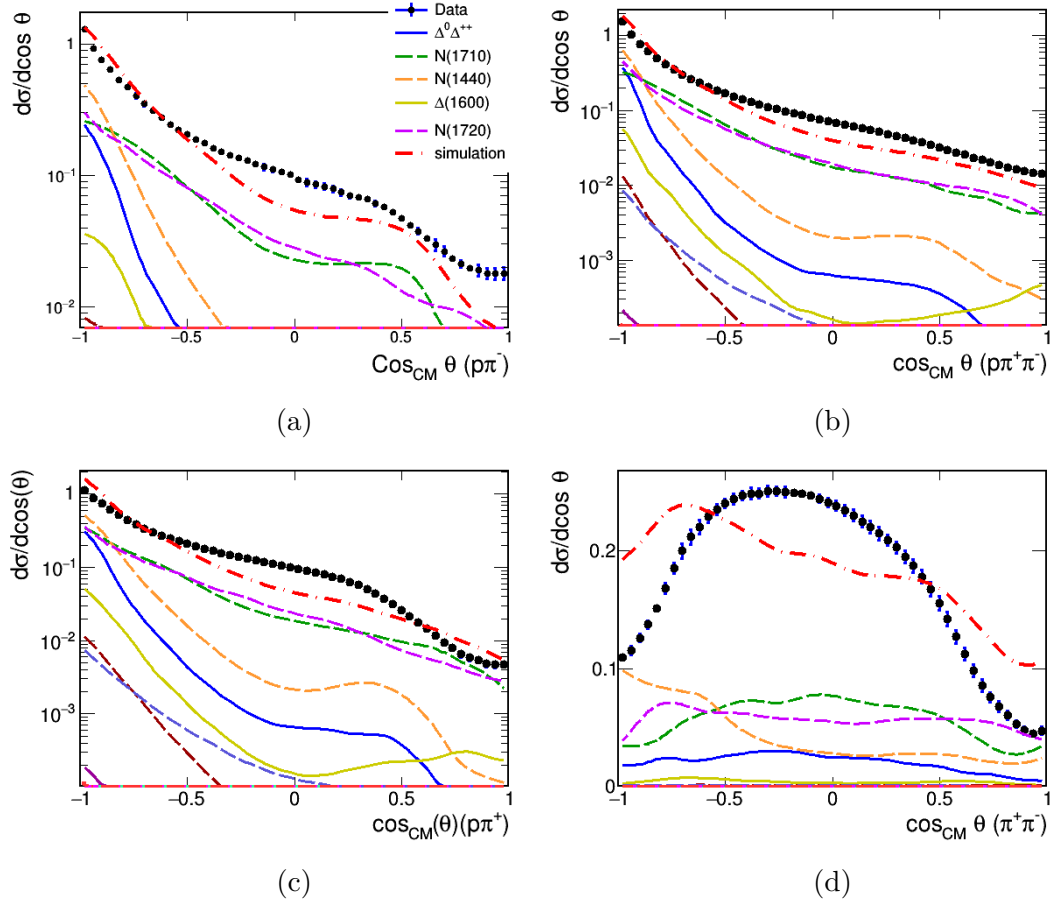


FIGURE (8.9) (a) $p\pi^-$, (b) $p\pi^+\pi^-$, (c) $p\pi^+$, (d) $\pi^+\pi^-$ CM angular distributions compared to the result of Cao *et al.* model calculations (red curves). The same normalization factor as in Figure 8.8 is applied to the simulation.

In summary, it seems that, to extend the model at higher energies, in addition to the double- Δ , also the $\Delta(1232)N(1520)$, $\Delta(1232)N(1520)$ and $\Delta(1232)N(1680)$ should be added to the model. In addition, our data shows evidence for a strong $N(1675)$ and $N(1680)$ excitation, which is absent in the model. Finally, the decay branching ratios to $N\rho$ from PDG 2010 [138] used in the model provide a too large ρ meson contribution.

8.3 GiBUU model

GiBUU (Giessen Boltzmann-Uehling-Uhlenbeck) transport model is a tool for the numerical simulation of nuclear reactions that provides a unified framework for various types of elementary reactions on nuclei as well as heavy-ion collisions in a broad energy range. This model takes care of the correct transport-theoretical description of the hadronic degrees of freedom in nuclear reactions, including the propagation, collisions and decays of particles. The GiBUU model currently contains around 30 nucleon resonance. All the resonances are taken from the partial-wave analysis of Manley [140]. The low-energy part of the nucleon-nucleon collision is given by a resonance model based on Teis analysis [60], in which all collision cross sections are assumed to be dominated by the excitation of baryon resonances [141].

Both one and double resonance excitation were considered in GiBUU model, the one resonance excitation channels $NN \rightarrow N\Delta$ and $NN \rightarrow NN^*, N\Delta^*$ were already included in Teis analysis based on existing data in 1992 of heavy-ion collisions in the energy range of 1-2 GeV/A. Most of the resonance production matrix elements are adopted from Teis. However, a few modifications were made in GiBUU model. In particular the contributions of the $N(1675)$, $\Delta(1600)$ and $\Delta(1910)$ were reduced in favor of the $N(1440)$ and double- Δ contributions, since they were extremely large in Teis analysis. This gives an improved threshold behavior of the 2π production channels [69]. The double resonance production $NN \rightarrow \Delta\Delta$ and $NN \rightarrow \Delta N^*, \Delta\Delta^*$ is performed in a phase-space approach, analogous to the one resonance excitation [69]. The GiBUU model cross sections for the two-pion production in proton-proton collisions is shown in Figure 8.10, the availability of the $\pi^+\pi^-$ final state data allows for a proper evaluation of the \sqrt{s} dependence [141].

The total cross section for the $pp \rightarrow pp\pi^+\pi^-$ channel calculated by GiBUU model is $\sigma_{pp \rightarrow pp\pi^+\pi^-}^{GiBUU} = 3.595$ mb, it is in good agreement with our result $\sigma_{HADES} = 3.89 \pm 0.15$ mb. The single and double resonance production cross sections are listed in table 8.2, the result shows that GiBUU model is missing the double resonance production $\Delta N(1440)$ and the one resonance productions $N(1875)$ and $N(1880)$, it also highly underestimates the $N(1520)$, $N(1680)$, $\Delta N(1520)$ and $\Delta N(1680)$ productions, and overestimates the $N(1440)$ production.

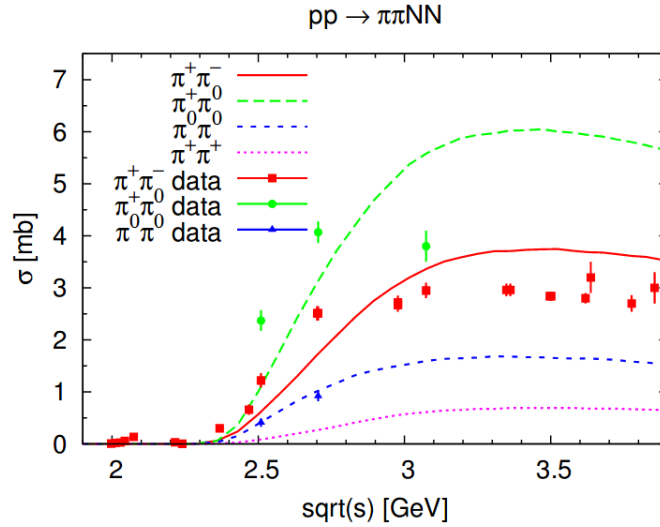


FIGURE (8.10) GiBUU cross sections for double pion production in proton-proton collisions [141]. Data from [142].

8.4 UrQMD model

The UrQMD-model (microscopic Ultra-relativistic Quantum Molecular Dynamics model) [143] is a hadronic non-equilibrium transport approach based on the quantum molecular dynamics concept. It includes all baryons and mesons with masses up to 2.2 GeV. The dynamics of reactions in a nuclear collision are described in terms of a n-particle phase-space distribution.

In UrQMD, the excitation of non-strange resonances is subdivided into 6 classes : $NN \rightarrow N\Delta(1232)$, $NN \rightarrow NN^*$, $NN \rightarrow N\Delta^*$, $NN \rightarrow \Delta(1232)\Delta(1232)$, $NN \rightarrow \Delta(1232)N^*$ and $NN \rightarrow \Delta(1232)\Delta^*$. For each of these classes specific assumptions are made with regard to the form of the matrix-element $|\mathcal{M}(m_3, m_4)|^2$. Figure 8.11 shows the UrQMD model total cross sections for the excitation of the different resonance classes. Figure 8.12 shows the UrQMD cross sections for the exclusive $pN(1440)$, $pN(1520)$, $pN(1680)$, $pN(1700)$ channels compared to data.

The total cross section for the $pp \rightarrow pp\pi^+\pi^-$ channel calculated by UrQMD model is $\sigma_{pp \rightarrow pp\pi^+\pi^-}^{UrQMD} = 3.11$ mb, it is slightly lower than our result $\sigma_{HADES} = 3.89 \pm 0.15$ mb. The one and double resonance production cross sections extracted from UrQMD model calculations are listed in Table 8.2. The contributions of the $N(1440)$ and $N(1520)$ are much closer to our estimate than GiBUU results. However, UrQMD model is missing the contributions of $N(1720)$, $N(1875)$ and $N(1880)$ and the double resonance production $\Delta N(1440)$ and $\Delta N(1535)$, it also highly underestimates the double- $\Delta(1232)$ production

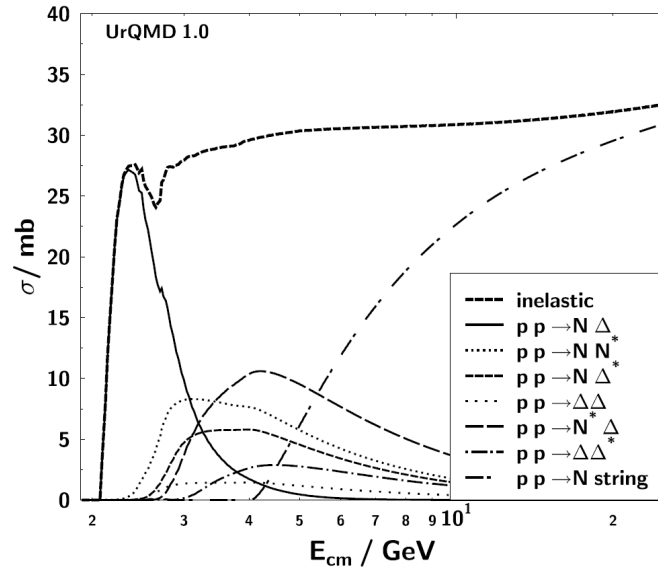


FIGURE (8.11) Inelastic proton-proton cross section in UrQMD, subdivided into the classes $NN \rightarrow N\Delta(1232)$, $NN \rightarrow NN^*$, $NN \rightarrow N\Delta^*$, $NN \rightarrow \Delta(1232)\Delta(1232)$, $NN \rightarrow \Delta(1232)N^*$ and $NN \rightarrow \Delta(1232)\Delta^*$ [143].

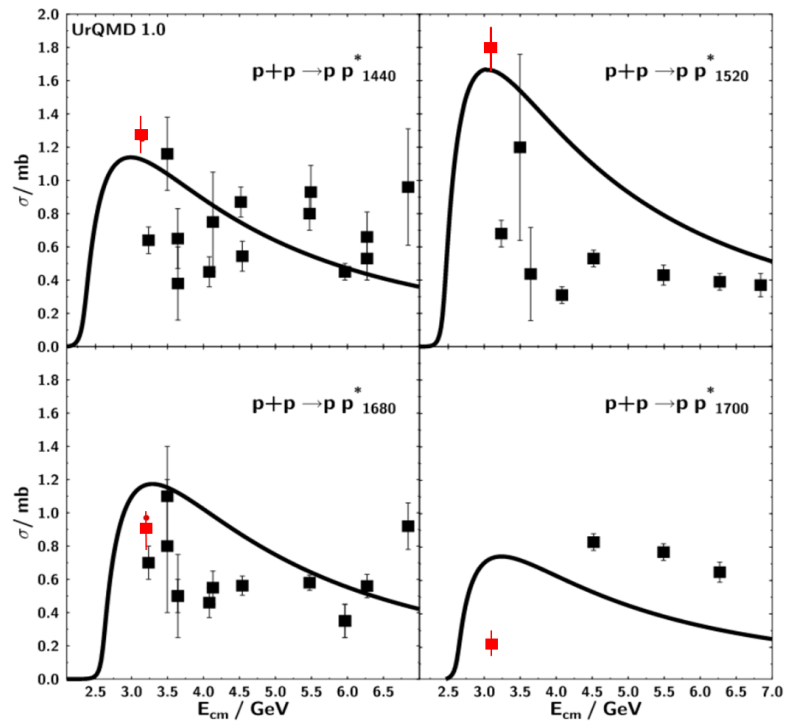


FIGURE (8.12) UrQMD parametrization for exclusive $pN(1440)$, $pN(1520)$, $pN(1680)$, $pN(1700)$ compared to data [120]. Red squares represent this work results.

and it predicts that the total one resonance production is higher than the total double resonance production which is not compatible with our result.

8.5 SMASH model

SMASH (Simulating Many Accelerated Strongly interacting Hadrons) [144] which is a new hadronic transport approach for the dynamical description of collisions at low and intermediate beam energies and dilute non-equilibrium stages of heavy-ion collisions. It constitutes a solution of the non-equilibrium dynamics of hadrons in the regime where the inelastic interactions are treated by resonance excitations and decays with vacuum properties.

The model includes all well known hadronic resonances listed by the PDG [34] up to a mass of 2.35 GeV. All resonances are assumed to have a Breit-Wigner shape and the partial widths are calculated following the framework of Manley *et al.* [140]. In NN collisions, both one resonance production processes ($NN \rightarrow NN^*, N\Delta, N\Delta^*$) and double resonance production processes ($NN \rightarrow \Delta\Delta, \Delta N^*, \Delta\Delta^*$) are taken into account. For $NN \rightarrow N\Delta$, amplitudes are calculated from [62] in the one-boson-exchange (OBE) model. In the other cases, constant matrix elements are used, i.e. only phase space energy dependence is accounted for [70, 144]. Figure 8.13 shows elastic and inelastic proton-proton cross section in SMASH compared to data from [34]. The first inelastic channel that opens up is the excitation of a single Δ resonance. At higher energies it is followed by the excitation of heavier resonance states (N^* and Δ^*) as well as double-resonance excitations.

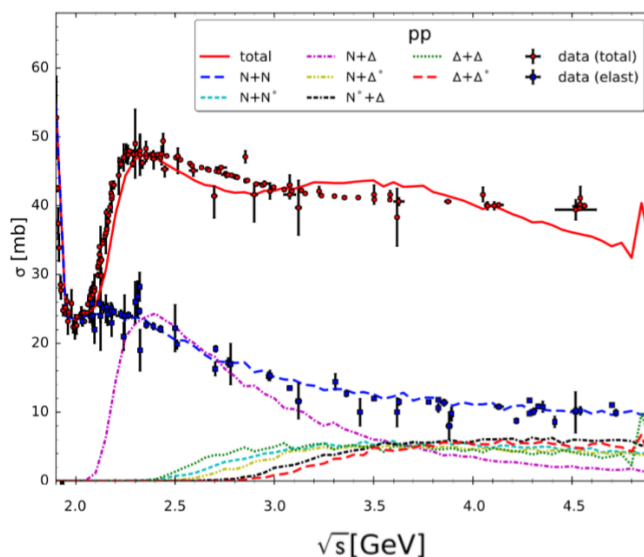


FIGURE (8.13) Elastic and inelastic proton-proton cross section in SMASH [144] compared to data from [34].

The total cross section for the $pp \rightarrow pp\pi^+\pi^-$ channel calculated by SMASH model is $\sigma_{pp \rightarrow pp\pi^+\pi^-}^{SMASH} = 2.73$ mb [145], it is lower than our result $\sigma_{HADES} = 3.51 \pm 0.15$ mb . The single and double resonance production cross sections are listed in Table 8.2 (last column) [145], these cross sections represent the resonances contributions to the channel $pp \rightarrow pp\pi^+\pi^-$, hence they should be compared to the cross sections extracted from our data that are listed in the fifth column. The result shows that SMASH model includes resonances excitations up to $N(2220)$ which could not be identified in our analysis and are absent in the two other transport models. Also the model clearly underestimates the contribution of the light resonances $N(1440)$ and $N(1520)$ and $N(1535)$. The list of double resonances contributing is compatible with our result, however, the cross sections are about 3 times lower, except for the double- Δ which is slightly lower.

Model	$\sigma_{\pi^+\pi^-}^{tot}$ [mb]
HADES	3.89 ± 0.15
GiBUU	3.595
UrQMD	3.11
SMASH	2.73

TABLE (8.1) Total cross sections in units of mb for the $pp \rightarrow pp\pi^+\pi^-$ channel at $T_p = 3.5$ GeV obtained from transport models compared to HADES.

Channel	σ_{HADES}^R	σ_{GiBUU}^R	σ_{UrQMD}^R	$\sigma_{HADES}^{\pi^+\pi^-}$	$\sigma_{SMASH}^{\pi^+\pi^-}$
$N^+(1440)$	1.5 ± 0.4	3.58	1.15	0.25 ± 0.017	0.04
$N^+(1520)$	1.8 ± 0.3	0.26	1.7	0.29 ± 0.016	0.07
$N^+(1535)$	0.15 ± 0.03	0.54	0.8	0.003 ± 0.0002	-
$\Delta^+(1600)$	-	0.14	0.4	-	-
$\Delta^+(1620)$	0.05 ± 0.01	0.097	0.2	0.022 ± 0.002	0.058
$N^+(1650)$	0.027 ± 0.008	0.22	0.4	0.002 ± 0.0001	-
$N^+(1675)$	1.05 ± 0.23	0.75	1.2	0.26 ± 0.004	0.13
$N^+(1680)$	0.80 ± 0.08	0.22	1.2	0.128 ± 0.011	0.10
$N^+(1700)$	0.10 ± 0.025	-	0.75	0.04 ± 0.004	0.12
$\Delta^+(1700)$	0.45 ± 0.13	0.055	0.35	0.17 ± 0.02	0.067
$N^+(1710)$	0.024 ± 0.008	-	-	0.002 ± 0.0001	-
$N^+(1720)$	0.045 ± 0.005	0.14	0.68	0.0148 ± 0.0003	0.07
$N^+(1875)$	0.027 ± 0.013	-	-	0.0097 ± 0.0004	0.069
$N^+(1880)$	0.41 ± 0.20	-	-	0.066 ± 0.003	-
$\Delta^+(1905)$	0.045 ± 0.005	0.047	0.25	0.025 ± 0.003	0.10
$\Delta^+(1910)$	-	0.14	0.08	-	-
$\Delta^+(1920)$	-	-	-	-	0.04
$\Delta^+(1930)$	-	-	-	-	0.05
$\Delta^+(1950)$	-	-	-	-	0.04
$N^+(1990)$	-	-	-	-	0.08
$N^+(2060)$	-	-	-	-	0.03
$N^+(2120)$	-	-	-	-	0.033
$N^+(2190)$	-	-	-	-	0.035
$N^+(2220)$	-	-	-	-	0.032
$\Delta^{++}\Delta^0$	3.7 ± 0.15	3.55	1.5	1.22 ± 0.05	1.0
$\Delta^{++}N^0(1440)$	0.81 ± 0.13	-	-	0.54 ± 0.01	0.075
$\Delta^{++}N^0(1520)$	1.50 ± 0.10	0.34	0.92	0.37 ± 0.02	0.14
$\Delta^{++}N^0(1535)$	0.46 ± 0.10	1.60	-	0.138 ± 0.003	0.049
$\Delta^{++}N^0(1650)$	-	0.26	-	-	0.048
$\Delta^{++}N^0(1675)$	-	-	-	-	0.097
$\Delta^{++}N^0(1680)$	0.80 ± 0.07	0.24	0.62	0.34 ± 0.01	0.12
$\Delta^0\Delta^{++}(1620)$	-	0.17	-	-	-
$\Delta^{++}\Delta^0(1620)$	-	0.16	-	-	-
$\Delta^{++}N^0(1720)$	-	0.15	-	-	-
$\Delta^{++}\Delta^0(1700)$	-	0.089	-	-	-
$\Delta^0\Delta^{++}(1700)$	-	0.085	-	-	-

TABLE (8.2) Cross sections in units of mb for the single and double resonance production in pp collision extracted from our data (second column) compared to GiBUU model (third column), UrQMD model (fourth column). Cross sections in the $pp \rightarrow pp\pi^+\pi^-$ channel (fifth column) compared to SMASH model [145].

8.6 Conclusion on data/model comparison

In conclusion, our data could be compared to the predictions of both dedicated models for the $NN \rightarrow NN\pi\pi$ reaction and of transport models. The Cao *et al.* and OPER dedicated models have more solid theoretical basis, since they use respectively Lagrangians and PWA amplitudes. However, the predictions are not yet satisfactory and we hope this will motivate further theoretical works. For the Cao *et al.* model, part of the discrepancy is just due to the fact that the model was aiming at describing $NN \rightarrow NN\pi\pi$ reactions up to an incident energy of 2.2 GeV and does not include the heaviest baryonic resonances.

Transport models parameters have been mostly adjusted up to now to one pion and 2π total cross section data, together with differential distributions in the region where the $\Delta(1232)$ dominates. These models differ by the size of the excitation of resonances heavier than $\Delta(1232)$ and of the double resonance contributions. Our data, which provide precise differential cross sections allow for a test of these ingredients and could be used to update the models. This can be useful to revisit the predictions for the e^+e^- production measured by HADES in the pp and $p\text{Nb}$ reactions at 3.5 GeV [50, 65]. It is also very important to provide more precise predictions for dielectron production in heavy-ion reactions, in view of the upcoming HADES and CBM experiments with the SIS100 beams of the FAIR facility, where heavy-ion beams of a few GeV/nucleon will be available.

9

Conclusion

Exclusive measurements in proton-proton reactions at a kinetic energy of 3.5 GeV ($\sqrt{s} = 3.18$ GeV) were presented in this thesis. This work is realized in the framework of the HADES experiment. The main objective is to study the role of baryonic resonances and ρ meson in these reactions. Such information has a strong impact for predictions of meson and dielectron production in elementary or heavy-ion reactions at a few GeV/nucleon. The $\pi^+\pi^-$ channel is indeed unique to investigate single and double baryon resonance excitations as well as the ρ meson production, either in a direct process or via excitation and decay of a baryon resonance.

The extraction of the signal for $\pi^+\pi^-$ production was based on the detection of one proton, one π^+ and one π^- in the HADES detector and the calculation of the missing mass. Efficiency corrections were performed using efficiency matrices calculated by GEANT3. Statistical errors are negligible and systematic errors are mainly due to the efficiency corrections which are based on simulations and to normalization. A simple model based on PLUTO event generator was built for the interpretation of the data,

including three main types of contributions summed incoherently : the production of one resonance decaying into $p\pi^+\pi^-$ and the excitation of two resonances, decaying respectively into $p\pi^+$ and $p\pi^-$ and the direct ρ production. Consistently with the analysis of one pion production measured in the same reaction with HADES, which was the subject of a previous analysis, a phenomenological modeling of the resonances angular distribution depending on the four-momentum transfer was implemented to take into account the anisotropic emission in the proton proton center-of-mass frame. It was found in the one pion analysis that the anisotropy of the distribution decreases with increasing resonance mass. Such behavior is expected since the production of heavier resonances requires a larger four-momentum transfer. A similar behavior was considered in the case of the double resonance excitation.

A fitting procedure was developed, using as constraint the information obtained by the HADES collaboration for the single resonance excitation from one pion and one kaon production in the same experiment. The results of our analysis allowed to extract the contribution of several heavy resonances for which only an upper limit was extracted from the one pion analysis ($\Delta(1620)$, $N(1675)$, $N(1680)$, $\Delta(1910)$) and to reduce the uncertainty on the excitation of lighter resonances ($N(1440)$, $N(1520)$, ...). The double resonance excitation was extracted for the first time. Among all the identified contributions, the main ones are the double $\Delta(1232)$ excitation and the $N(1520)$ excitation. An attempt to extract the dibaryon D_{21} contribution reported by WASA collaboration was done, however, no signal is seen. For a dibaryon of mass $M = 2140$ MeV and width $\Gamma = 110$ MeV, an upper limit for the cross section of $0.3 \mu\text{b}$ is obtained.

The contribution of the exclusive ρ meson production was also extracted after applying the needed kinematical cuts. To determine the ρ production angular distribution, the differential cross section was extracted in each bin of $\pi^+\pi^-$ angle in the center of mass, This distribution was fitted with Legendre polynomials and integrated to calculate the total cross section. The angular distribution is forward/backward peaked, but the anisotropy is much smaller than the result measured by the DISTO collaboration at beam energy of 2.85 GeV. The contribution of baryonic resonances to the ρ production is discussed using our cocktail of baryonic resonances, where branching ratios are taken from the Bonn-Gatchina PWA. While the details of this contribution depend on these branching ratios of baryonic resonances to the $N\rho$ channels, it appears clearly that the Breit-Wigner spectral function commonly used to extract the ρ meson production

strongly underestimates the total ρ production. This is due to the distortion of the ρ spectral function for the production from light baryons (i.e. $N(1520)$). This "resonance" ρ contribution is discussed and compared to existing models. This work points to the necessity for the models to fit directly the $\pi^+\pi^-$ invariant mass distribution and not only the ρ cross section measurements. We also tried to extract the contribution of $f_0(500)$ and $f_0(980)$ since their dominant decay channel is $\pi\pi$. No signal is observed, and rough estimates for the upper limits of the cross sections are set to 5 μb for $f_0(500)$ and 1 μb for $f_0(980)$.

To look at our analysis of the $pp \rightarrow pp\pi^+\pi^-$ reaction based on a incoherent sum of contributions in a more theoretical perspective, we developed with Jacques Van De Wiele a Lagrangian model which takes into account the main contributions, the double $\Delta(1232)$ excitation and the $N(1520)$ excitation. It allows to compare the results of our simple resonance model with a model based on quantum field theory and to test the interferences effects. While some differences are visible, the main features are very similar. In overall, our empirical model seems to give a better description of the data. The Lagrangian model predicts a negligible interference effect.

Then, we compared our experimental data to existing dedicated models for the $NN \rightarrow NN\pi\pi$ reaction. We first collaborated with A. Jerusalimov to compare the OPER model to our data. It was found that the model overestimates the double- Δ excitation, $\Delta(1600)$ and other higher lying resonances of mass around 1.8 GeV in comparison to the other contributions. We also collaborated with Xu Cao to compare Cao *et al.* Lagrangian model to our data. The comparison showed that the double resonance excitation is underestimated since only the double- $\Delta(1232)$ excitation is included in the calculations. This is due to the fact that the model had been developed to describe the NN reaction below 2.2 GeV. It also shows that the $N(1440)$, $N(1710)$ and $N(1720)$ excitations are overestimated and $N(1520)$ is missing. We hope this work will motivate further theoretical works.

The resonance contributions extracted from the data analysis were also compared to inputs of transport models calculations (GiBUU, UrQMD and SMASH), None of them provides results which are fully compatible with our analysis. The double- Δ contribution is best reproduced in GiBUU and SMASH and the $N(1440)$, $N(1520)$ and $N(1675)$ are best predicted by UrQMD. The confrontation of the experimental results to the

predictions of existing theoretical models shows the necessity to take into account these new data.

The work presented in this PhD demonstrates that the $pp \rightarrow pp\pi^+\pi^-$ reaction at 3.5 GeV is a powerful tool to constrain the models used to describe the elementary processes. In particular, this channel is very sensitive to the single and double baryonic resonance excitation, as well as the ρ meson production which are important sources of dielectrons. These data should therefore serve as a benchmark for models and be helpful e.g. to make a more detailed description of existing HADES data for the e^+e^- production in $p + p$ or $p + Nb$ at 3.5 GeV or to provide realistic predictions for future HADES or CBM heavy-ion experiments at FAIR at a few GeV per nucleon.



Four-body final state

The differential cross section for $2 \rightarrow 4$ scattering process

$$a + b \rightarrow 1 + 2 + 3 + 4$$

Depends on eight independent variables. It can be written as :

$$d^8\sigma = \frac{1}{|\mathbf{v}_a - \mathbf{v}_b|} \frac{1}{4E_a E_b} \int |\mathcal{M}|^2 (2\pi)^4 \delta^4(p_a + p_b - p_1 - p_2 - p_3 - p_4) d^4p_1 d^4p_2 d^4p_3 d^4p_4 \quad (\text{A.1})$$

In the lab frame we have :

$$\begin{aligned} E_b &= m_b \\ |\mathbf{v}_a - \mathbf{v}_b| &= \frac{p_a}{E_a} \\ |\mathbf{v}_a - \mathbf{v}_b| E_a E_b &= p_a m_b \end{aligned}$$

Where $p = |\mathbf{p}|$ is the 3-momentum

$$d^3\mathbf{p} = p^2 dp d\Omega = p E dE d\Omega \quad (\text{A.2})$$

$$d^8\sigma = \frac{1}{|\mathbf{v}_a - \mathbf{v}_b|} \frac{1}{4E_a E_b} \int |\mathcal{M}|^2 (2\pi)^4 \delta(p_a + p_b - p_1 - p_2 - p_3 - p_4) \frac{d^3\mathbf{p}_1}{(2\pi)^3 2E_1} \frac{d^3\mathbf{p}_2}{(2\pi)^3 2E_2} \frac{d^3\mathbf{p}_3}{(2\pi)^3 2E_3} \frac{d^3\mathbf{p}_4}{(2\pi)^3 2E_4} \quad (\text{A.3})$$

$$d^8\sigma = \frac{1}{64(2\pi)^8} \frac{1}{4p_a m_b} p_1 E_1 dE_1 d\Omega_1 p_2 E_2 dE_2 d\Omega_2 \frac{1}{E_1 E_2} \int |\mathcal{M}|^2 \frac{d^3\mathbf{p}_3}{E_3} \frac{d^3\mathbf{p}_4}{E_4} \delta(p_a + p_b - p_1 - p_2 - p_3 - p_4) \quad (\text{A.4})$$

$$\frac{d^8\sigma}{dE_1 d\Omega_1 dE_2 d\Omega_2} = \frac{1}{64(2\pi)^8} \frac{p_1 p_2}{4p_a m_b} \int |\mathcal{M}|^2 \frac{d^3\mathbf{p}_3}{E_3} \frac{d^3\mathbf{p}_4}{E_4} \delta(p_a + p_b - p_1 - p_2 - p_3 - p_4) \quad (\text{A.5})$$

Where

$$E_3 = \sqrt{p_3^2 + m_3^2} \quad E_4 = \sqrt{p_4^2 + m_4^2} \quad (\text{A.6})$$

$$\delta(p_a + p_b - p_1 - p_2 - p_3 - p_4) = \delta(E_a + m_b - E_1 - E_2 - E_3 - E_4) \delta(\mathbf{p}_a + \mathbf{p}_b - \mathbf{p}_1 - \mathbf{p}_2 - \mathbf{p}_3 - \mathbf{p}_4) \quad (\text{A.7})$$

When integrating over $d^3\mathbf{p}_4$

$$\begin{aligned} & \int |\mathcal{M}|^2 \frac{d^3\mathbf{p}_3}{E_3} \frac{d^3\mathbf{p}_4}{E_4} \delta(p_a + p_b - p_1 - p_2 - p_3 - p_4) \\ &= \int |\mathcal{M}|^2 \frac{d^3\mathbf{p}_3}{E_3} \frac{1}{E_4} \delta(E_a + m_b - E_1 - E_2 - E_3 - E_4) \end{aligned} \quad (\text{A.8})$$

Where

$$E_4 = \sqrt{p_4^2 + m_4^2} = \sqrt{(\mathbf{p}_a - \mathbf{p}_1 - \mathbf{p}_2 - \mathbf{p}_3)^2 + m_4^2} \quad (\text{A.9})$$

We choose to integrate over \mathbf{p}_3 . We have

$$\frac{d^3 \mathbf{p}_3}{E_3 E_4} = d\Omega_3 \frac{p_3^2 dp_3}{E_3 E_4} \quad (\text{A.10})$$

$$E_4 = \sqrt{(\mathbf{p}_a - \mathbf{p}_1 - \mathbf{p}_2)^2 + m_4^2 + p_3^2 - 2\mathbf{p}_3 \cdot (\mathbf{p}_a - \mathbf{p}_1 - \mathbf{p}_2)} \quad (\text{A.11})$$

By using

$$\int \delta[f(\mathbf{p}_3)] d\mathbf{p}_3 = \sum_{\mathbf{p}_3} \frac{\delta(\mathbf{p} - \mathbf{p}_3)}{\left| \frac{\partial f}{\partial \mathbf{p}} \right|_{\mathbf{p}_3}} \quad (\text{A.12})$$

$$\begin{aligned} & \delta(E_a + E_b - E_1 - E_2 - E_3 - E_4) = \\ & \delta\left(E_a + E_b - E_1 - E_2 - \sqrt{p_3^2 + m_3^2} - \sqrt{(\mathbf{p}_a - \mathbf{p}_1 - \mathbf{p}_2 - \mathbf{p}_3)^2 + m_4^2}\right) = \\ & \delta\left(E_a + E_b - E_1 - E_2 - \sqrt{p_3^2 + m_3^2} - \sqrt{(\mathbf{p}_a - \mathbf{p}_1 - \mathbf{p}_2)^2 + p_3^2 + m_4^2 - 2\mathbf{p}_3 \cdot (\mathbf{p}_a - \mathbf{p}_1 - \mathbf{p}_2)}\right) \end{aligned}$$

Equation A.5 becomes

$$\frac{d^8 \sigma}{dE_1 d\Omega_1 dE_2 d\Omega_2 d\Omega_3} = \frac{1}{64(2\pi)^8} \frac{p_1 p_2}{4p_a m_b} \sum_{p_3} \frac{p_3^3 |\mathcal{M}|^2}{|p_3^2 E_4 + E_3 [p_3^2 - \mathbf{p}_3 \cdot (\mathbf{p}_a - \mathbf{p}_1 - \mathbf{p}_2)]|} \quad (\text{A.13})$$

Bibliographie

- [1] F. Halzen and Alan D. Martin. *Quarks Leptons : An introductory course in modern particle physics*. 1984.
- [2] O. W. Greenberg. Spin and unitary-spin independence in a paraquark model of baryons and mesons. *Phys. Rev. Lett.*, 13 :598–602, 1964.
- [3] David J. Gross and Frank Wilczek. Ultraviolet behavior of non-abelian gauge theories. *Phys. Rev. Lett.*, 30 :1343–1346, 1973.
- [4] Kenneth G. Wilson. Confinement of quarks. *Phys. Rev. D*, 10 :2445–2459, 1974.
- [5] S. Chatrchyan et al. Observation of a new boson at a mass of 125 gev with the cms experiment at the lhc. *Physics Letters B*, 716 :30–61, 2012.
- [6] S. Klimt, M. Lutz, and W. Weise. Chiral phase transition in the SU(3) Nambu and Jona- Lasinio model. *Phys. Lett.*, B249 :386–390, 1990.
- [7] Y. Aoki, G. Endrodi, Z. Fodor, S. D. Katz, and K. K. Szabo. The order of the quantum chromodynamics transition predicted by the standard model of particle physics. *Nature*, 443 :675–678, 2006.
- [8] Y. Aoki, Z. Fodor, S. D. Katz, and K. K. Szabo. The QCD transition temperature : Results with physical masses in the continuum limit. *Phys. Lett.*, B643 :46–54, 2006.
- [9] Bernd-Jochen Schaefer, Jan M. Pawłowski, and Jochen Wambach. The Phase Structure of the Polyakov–Quark-Meson Model. *Phys. Rev.*, D76 :074023, 2007.

- [10] V. et al. Khachatryan. Constraints on parton distribution functions and extraction of the strong coupling constant from the inclusive jet cross section in pp collisions at $\sqrt{s} = 7$ tev. *Eur. Phys. J. C*, 75 :288, 2015.
- [11] M. Tanabashi et al. Review of particle physics. *Phys. Rev. D*, 98 :030001, 2018.
- [12] W. Roberts S. Capstick. Quasi-two-body decays of nonstrange baryons. *Phys. Rev. D*, 49 :4570–4586, 1994.
- [13] W. Roberts S. Capstick. New baryons in the $\delta\eta$ and $\delta\omega$ channels. *Phys. Rev. D*, 57 :4301–4309, 1998.
- [14] W. Roberts S. Capstick. Strange decays of nonstrange baryons. *Phys. Rev. D*, 58 :074011, 1998.
- [15] Daniel R. Marlow et al. Pion Scattering From C and Ca at 800-MeV/c. *Phys. Rev.*, C30 :1662, 1984.
- [16] SAID Group. <http://gwdac.phys.gwu.edu/>.
- [17] V. Shklyar, H. Lenske, and U. Mosel. 2π production in the Giessen coupled-channel model. *Phys. Rev.*, C93(4) :045206, 2016.
- [18] V. Crede and W. Roberts. Progress towards understanding baryon resonances. *Rept.Prog.Phys.*, 76 :076301, 2013.
- [19] MAID Group. <http://www.kph.uni-mainz.de/MAID/>.
- [20] A.V. Anisovich et al. Properties of baryon resonances from a multichannel partial wave analysis. *Eur.Phys.J.*, A48 :15, 2012.
- [21] I. CiepaÅ, W. Przygoda, and A. V. Sarantsev. Partial wave analysis of HADES data for two-pion production in pion-nucleon reactions. *EPJ Web Conf.*, 199 :02001, 2019.
- [22] Hiroyuki Sako et al. Baryon spectroscopy in $(\pi,2\pi)$ reactions with 10^6 Hz pion beams at J-PARC. *PoS*, INPC2016 :266, 2017.
- [23] William J. Briscoe et al. Physics opportunities with meson beams. *Eur. Phys. J.*, A51(10) :129, 2015.

- [24] F.J. Dyson and N.-H. Xuon. $Y = 2$ states in $su(6)$ theory. *Phys. Rev. Lett.*, 13 :815, 1964.
- [25] D. B. Lichtenberg, E. Predazzi, D. H. Weingarten, and J. G. Wills. Quark-cluster model of dibaryon resonances. *Phys. Rev. D*, 18 :2569–2573, 1978.
- [26] J. L. Ping, H. X. Huang, H. R. Pang, Fan Wang, and C. W. Wong. Quark models of dibaryon resonances in nucleon-nucleon scattering. *Phys. Rev. C*, 79 :024001, 2009.
- [27] V.I. Kukulín, P. Grabmayr, A. Faessler, Kh.U. Abraamyan, M. Bashkanov, H. Clement, T. Skorodko, and V.N. Pomerantsev. Experimental and theoretical indications for an intermediate \ddot{I} -dressed dibaryon in the nn interaction. *Annals of Physics*, 325 :1173 – 1189, 2010.
- [28] A. Gal and H. Garcilazo. Three body calculation of the $\Delta\Delta$ dibaryon candidate $d_{03}(2370)$. *Phys. Rev. Lett.*, 111 :172301, 2013.
- [29] Three-body model calculations of $n\delta$ and $\delta\delta$ dibaryon resonances. *Nuclear Physics A*, 928 :73 – 88, 2014.
- [30] Hongxia Huang, Jialun Ping, and Fan Wang. Dynamical calculation of the $\Delta\Delta$ dibaryon candidates. *Phys. Rev. C*, 89 :034001, 2014.
- [31] Woosung Park, Aaron Park, and Su Hounng Lee. Dibaryons in a constituent quark model. *Phys. Rev. D*, 92 :014037, 2015.
- [32] J. Huang, H.and Ping, X. Zhu, and F. Wang. Possible existence of a dibaryon candidate $N\Delta (D_{21})$. *Phys. Rev. C*, 98 :034001, 2018.
- [33] Richard A. R.A. Arndt, John S. Hyslop, and L. David Roper. Nucleon-nucleon partial-wave analysis to 1100 mev. *Phys. Rev. D*, 35 :128–144, 1987.
- [34] K.A. Olive et al. Review of Particle Physics. *Chin.Phys.*, C38 :090001, 2014.
- [35] Volker D. Burkert. N^* Experiments and Their Impact on Strong QCD Physics. *Few Body Syst.*, 59(4) :57, 2018.
- [36] T. Galatyuk, P. M. Hohler, Ralf R., F. Seck, and J. Stroth. Thermal dileptons from Coarse-Grained transport as fireball probes at SIS energies. *Eur. Phys. J.*, A52(5) :131, 2016.

- [37] B. P. Abbott et al. GW170817 : Observation of Gravitational Waves from a Binary Neutron Star Inspiral. *Phys. Rev. Lett.*, 119 :161101, 2017.
- [38] G. E. Brown and Mannque Rho. Scaling effective Lagrangians in a dense medium. *Phys. Rev. Lett.*, 66 :2720–2723, 1991.
- [39] Tetsuo Hatsuda and Su Houng Lee. QCD sum rules for vector mesons in nuclear medium. *Phys. Rev.*, C46 :34–38, 1992.
- [40] R. Rapp, G. Chanfray, and J. Wambach. Rho meson propagation and dilepton enhancement in hot hadronic matter. *Nucl. Phys.*, A617 :472–495, 1997.
- [41] R. Rapp and J. Wambach. Low mass dileptons at the CERN-SPS : Evidence for chiral restoration? *Eur. Phys. J.*, A6 :415–420, 1999.
- [42] R. Rapp and H. van Hees. Thermal Electromagnetic Radiation in Heavy-Ion Collisions. *Eur. Phys. J.*, A52(8) :257, 2016.
- [43] J. J. Sakurai. Vector-meson dominance and high-energy electron-proton inelastic scattering. *Phys. Rev. Lett.*, 22(18) :981–984, May 1969.
- [44] T. Galatyuk et al. HADES overview. *Nucl. Phys. A*, 931 :41, 2014.
- [45] M. Lorenz. *Vector meson production in p+Nb reactions and statistical particle production in Ar+KCl collisions*. PhD thesis, Goethe-Universität, Frankfurt, 2012.
- [46] G. Agakichiev et al. Study of dielectron production in C+C collisions at 1 AGeV. *Phys. Lett.*, B663 :43, 2008.
- [47] G. Agakichiev et al. Dielectron production in C-12 + C-12 collisions at 2-AGeV with HADES. *Phys. Rev. Lett.*, 98 :052302, 2007.
- [48] G. Agakishiev et al. Dielectron production in Ar+KCl collisions at 1.76A GeV. *Phys. Rev.*, C84 :014902, 2011.
- [49] J. Adamczewski-Musch et al. Probing dense baryon-rich matter with virtual photons. Accepted for Publication in Nature Physics, 2019.
- [50] G. Agakishiev et al. First measurement of low momentum dielectrons radiated off cold nuclear matter. *Phys. Lett.*, B715 :304–309, 2012.

- [51] H. Kuc. *Di-pion and di-electron production in quasi-free np reactions with HADES*. PhD thesis, Paris-Sud university, France, 2014.
- [52] T. Liu. *Exclusive measurements with the spectrometer HADES in proton-proton reactions at 1.25 GeV*. PhD thesis, Paris-Sud XI university, France, 2010.
- [53] S. Spataro. *Characterization of the HADES spectrometer in pp collisions at 2.2 GeV : elastic scattering and exclusive η reconstruction*. PhD thesis, Università di Catan, 2006.
- [54] A. Rustamov. *Exclusive η Meson Reconstruction in Proton-Proton Collisions at 2.2 GeV with the HADES Spectrometer and High Resolution Tracking*. PhD thesis, Technische Universität Darmstadt, Germany, 2006.
- [55] B. Sailer. *Inklusive e^+e^- Paarproduktion in bpp-Reaktionen bei $E_{kin} = 2.2$ GeV*. PhD thesis, Technischen Universität Munchenn, 2006.
- [56] K. Teilab. *The production of η and ω mesons in 3.5 GeV p+p interaction in HADES*. PhD thesis, Goethe-Universität, Frankfurt, 2011.
- [57] M. Palka. *ϕ meson production in pp reactions at 3.5 GeV with HADES Detector*. PhD thesis, Jagiellonian University, Cracow, 2011.
- [58] F. Scozzi. *Studying excited states of the nucleon with the HADES detector at GSI*. PhD thesis, Université Paris-Saclay, Technische universitat Darmstadt, 2018.
- [59] G. Agakishiev et al. Analysis of pion production data measured by HADES in proton-proton collisions at 1.25 GeV. *Eur. Phys. J.*, 51 :137, 2015.
- [60] S. Teis et al. Pion production in heavy ion collisions at sis energies. *Z. Phys.*, A356 :421, 1997.
- [61] I. Frohlich et al. Pluto : A Monte Carlo Simulation Tool for Hadronic Physics. *PoS ACAT*, 2007.
- [62] V. Dmitriev, O. Sushkov, and C. Gaarde. Delta formation in the $^1\text{H}(^3\text{He,t}) \Delta^{++}$ reaction at intermediate energies. *Nucl. Phys.*, A459 :503–524, 1986.
- [63] J. Adamczewski-Musch et al. $\Delta(1232)$ Dalitz decay in proton-proton collisions at T=1.25 GeV measured with HADES at GSI. *Phys. Rev.*, C95(6) :065205, 2017.

- [64] G. Agakishiev et al. Inclusive dielectron production in proton-proton collisions at 2.2 GeV beam energy. *Phys. Rev.*, C85 :054005, 2012.
- [65] G. Agakishiev et al. Baryon resonance production and dielectron decays in proton-proton collisions at 3.5 GeV . *Eur. Phys. J. A*50 82, 2014.
- [66] M. Zetenyi and G. Wolf. Baryonic contributions to the dilepton spectrum of nucleon nucleon collisions. *Phys. Rev.*, C67 :044002, 2003.
- [67] M. Zetenyi and Gy. Wolf. Dilepton decays of baryon resonances. *Heavy Ion Phys.*, 17 :27–39, 2003.
- [68] O. Buss et al. Transport-theoretical description of nuclear reactions. *Phys. Rep.*, 512 :1, 2012.
- [69] J. Weil, H. V. Hees, U. Mosel. Dilepton production in proton-induced reactions at SIS energies with the GiBUU transport model. *Eur. Phys. J.*, A48 :111, 2012.
- [70] J. Staudenmaier, J. Weil, V. Steinberg, S. Endres, and H. Petersen. Dilepton production and resonance properties within a new hadronic transport approach in the context of the GSI-HADES experimental data. *Phys. Rev.*, C98 :054908, 2018.
- [71] L.G. Dakhno et al. Measurement of cross-sections of meson pair production in nucleon nucleon collisions below 1 GeV and isospin analysis. *Sov. J. Nucl. Phys.*, 37 :540, 1983.
- [72] D. C. Brunt et al. Inelastic reactions in proton-deuteron scattering at 1.825 and 2.11 GeV/c. *Phys. Rev.*, 187 :1856, 1969.
- [73] F. Shimizu et al. Study of pp intercalations in the momentum range 0.9-GeV/c to 2.0-GeV/c. *Nucl. Phys.*, A389 :445, 1982.
- [74] E. Pickup, D. K. Robinson, and E. O. Salant. Three-pion mass distributions and the η meson. *Phys. Rev. Lett.*, 8(8) :329–332, Apr 1962.
- [75] A. M. Eisner, E. L. Hart, R. I. Louttit, and T. W. Morris. Proton-proton scattering at 1.48 bev. *Phys. Rev.*, 138(3B) :B670–B677, May 1965.
- [76] T. Skorodko, M. Bashkanov, D. Bogoslawsky, H. Calen, H. Clement, et al. Two-Pion Production in Proton-Proton Collisions : Experimental Total Cross Sections and their Isospin Decomposition. *Phys.Lett.*, B 679 :30–35, 2009.

- [77] I. Koch. *Measurements of $2\pi^0$ and $3\pi^0$ Production in Proton-Proton Collisions at a Center of Mass Energy of 2.465 GeV*. PhD thesis, uppsala university, Sweden, 2004.
- [78] W. Brodowski et al. Exclusive measurement of the $pp \rightarrow pp\pi^+\pi^-$ reaction near threshold. *Phys.Rev.Lett.*, 88 :192301, 2002.
- [79] et al. E. Doroshkevich. Study of baryon and search for dibaryon resonances by the $pp \rightarrow pp\pi^+\pi^-$ reaction. *Eur. Phys. J. A*, 18 :71â176, 2003.
- [80] J. Johanson et al. Two-pion production in protonâproton collisions near threshold. *Nuclear Physics A*, 712 :75 – 94, 2002.
- [81] J. Patzold, M. Bashkanov, R. Bilger, W. Brodowski, H. Calen, et al. Study of the $pp \rightarrow pp\pi^+\pi^-$ reaction in the low-energy tail of the Roper resonance. *Phys.Rev.*, C67 :052202, 2003.
- [82] S. Abd El-Bary et al. Two-Pion Production in Proton-Proton Collisions with Polarized Beam. *Eur. Phys. J.*, A37 :267, 2008.
- [83] S. Abd El-Samad et al. Single-Pion Production in pp Collisions at 0.95 GeV/c (II). *Eur. Phys. J.*, A39 :281–289, 2009.
- [84] S. et al. Dymov. Observation of an ABC effect in proton-proton collisions. *Phys.Rev.Lett.*, 102 :192301, 2009.
- [85] T. Tsuboyama et al. Double-pion production induced by deuteron-proton collisions in the incident deuteron momentum range 2.1 – 3.8GeV/c. *Phys. Rev. C*, 62 :034001, 2000.
- [86] V.V. Sarantsev et al. Measurement of the cross sections for $\pi^+\pi^-$ production in pp collisions at energies below 1 gev. *Phys. Atom. Nucl.*, 70 :1998, 2007.
- [87] P. Adlarson et al. Measurement of the $\vec{n}p \rightarrow d\pi^0\pi^0$ reaction with polarized beam in the region of the $d^*(2380)$ resonance. *Eur. Phys. J.*, A 52 :147, 2016.
- [88] A. P. Jerusalimov, A. V. Belyaev, V. P. Ladygin, A. K. Kurilkin, A. Yu. Troyan, and Yu. A. Troyan. Study of the reaction $np\vec{I} \hat{a} np\vec{I}^+\vec{I}^{\hat{a}}$ at 1.0 and 1.5 GeV. *Eur. Phys. J.*, A51(7) :83, 2015.

- [89] L. Alvarez-Ruso, E. Oset, and E. Hernandez. Theoretical study of the $N N \rightarrow N N \pi \pi$ reaction. *Nucl.Phys.*, A633 :519–546, 1998.
- [90] Xu Cao, Bing-Song Zou, and Hu-Shan Xu. Phenomenological analysis of the double-pion production in nucleon-nucleon collisions up to 2.2 gev. *Phys. Rev. C*, 81 :065201, 2010.
- [91] A.P. Jerusalimov. Analysis of the Reaction : $np \rightarrow np\pi^+\pi^-$ from the Point of View of Oper-Model. 2012.
- [92] A.P. Jerusalimov. Contribution of the "hanged" diagrams into the reaction $np \rightarrow np\pi^+\pi^-$. 2012.
- [93] T. Skorodko, M. Bashkanov, D. Bogoslawsky, H. Calen, H. Clement, et al. $\Delta\Delta$ Excitation in Proton-Proton Induced $\pi^0\pi^0$ Production. *Phys.Lett.*, B695 :115–123, 2011.
- [94] M. Albaladejo and E. Oset. Combined analysis of the $pn \rightarrow d\pi^+\pi^-$ and $pn \rightarrow pn\pi^+\pi^-$ cross sections and implications for the interpretation of the $pn \rightarrow d\pi^+\pi^-$ data. *Phys. Rev. C*, 88 :014006, 2013.
- [95] G. Agakishiev et al. Study of the quasi-free $np \rightarrow np\pi^+\pi^-$ reaction with a deuterium beam at 1.25 GeV/nucleon. *Phys. Lett.*, B750 :184–193, 2015.
- [96] M. Bashkanov, Chr. Bargholtz, M. Berlowski, D. Bogoslawsky, H. Calen, et al. Double-Pionic fusion of nuclear systems and the ABC effect : Approaching a puzzle by exclusive and kinematically complete measurements. *Phys.Rev.Lett.*, 102 :052301, 2009.
- [97] P. Adlarson et al. Abashian-booth-crowe effect in basic double-pionic fusion : A new resonance? *Phys. Rev. Lett.*, 106 :242302, 2011.
- [98] P. Adlarson et al. Isospin Decomposition of the Basic Double-Pionic Fusion in the Region of the ABC Effect. *Phys. Lett. B*, 721 :229–236, 2013.
- [99] P. Adlarson et al. Measurement of the $pn \rightarrow pp\pi^0\pi^-$ reaction in search for the recently observed resonance structure in $d\pi^0\pi^0$ and $d\pi^+\pi^-$ systems. *Phys. Rev. C*, 88 :055208, 2013.

- [100] P. Adlarson et al. Measurement of the $np \rightarrow np\pi^0\pi^0$ reaction in search for the recently observed $d^*(2380)$ resonance. *Physics Letters B*, 743 :325, 2015.
- [101] T. Skorodko H. Clement, M. Bashkanov. From CELSIUS to COSY : on the observation of a dibaryon resonance. *Phys. Scr.*, T 166 :014016, 2015.
- [102] P. Adlarson et al. Isotensor dibaryon in the $pp \rightarrow pp\pi^+\pi^-$ reaction? *Phys. Rev. Lett.*, 121 :052001, 2018.
- [103] P. Adlarson et al. Examination of the production of an isotensor dibaryon in the $pp \rightarrow pp\pi^+\pi^-$ reaction. *Phys. Rev. C*, 99 :025201, 2019.
- [104] G. Agakishiev et al. The High-Acceptance Dielectron Spectrometer HADES. *Eur. Phys. J. A41* :243-277, 2009.
- [105] HADES Collaboration. A Proposal for a High Acceptance Di-Electron Spectrometer. *GSI, Darmstadt*, 1994.
- [106] K. Zeitelhack et al. The HADES RICH Detector, *Nucl. Inst. and Meth. A433*, 201, 1999.
- [107] J. Markert. Untersuchung zum Ansprechverhalten der Violdrathdriftkammern niedriger Massenbelegung des HADES Experimentes. *Ph.D. Thesis*, 2005.
- [108] T. Bretz. Magnetfeldeigenschaften der Spektrometer HADES. *Ph.D. Thesis*, 2003.
- [109] I. Frohlich et al. Design of the Pluto Event Generator. *17th International Conference on Computing in High Energy and Nuclear Physics*, 2009.
- [110] <http://consult.cern.ch/writeup/geant/>.
- [111] R. Munzer et al. Determination of N^* amplitudes from associated strangeness production in p+p collisions. *Phys. Lett. B* 785, 574â580, 2018.
- [112] Emilie Morinière. *Contribution à l'analyse de réactions de production de dileptons en collision proton-proton avec HADES*. PhD thesis, Université Paris Sud, 2008.
- [113] E. Colton and P. E. Schlein. Reaction $pp \rightarrow pp\pi^+\pi^-$ at 6.6 GeV/c. *Phys. Rev. D* 3, 1063, 1971.

- [114] F. James and M. Roos. Minuit - a system for function minimization and analysis of the parameter errors and correlations. *Computer Physics Communications*, 10 :343–367, 1975.
- [115] G. Agakishiev et al. Inclusive dielectron spectra in p+p collisions at 3.5 GeV. *Eur. Phys. J.*, A48 :64, 2012.
- [116] K. Nakayama et al. Production of ω mesons in proton-proton collisions. *Phys. Rev. C*, 57 :1580, 1998.
- [117] F. Balestra et al. ρ^0 meson production in the $pp \rightarrow pp\pi^+\pi^-$ reaction at 3.67 GeV/c. *Phys. Rev. Lett.*, 89 :092001, 2002.
- [118] A. A. Sibirtsev. Heavy meson production cross-sections from proton proton collisions. *Nucl. Phys.*, A604 :455–465, 1996.
- [119] F. Balestra et al. ρ^0 meson production in the $pp \rightarrow pp\pi^+\pi^-$ reaction at 3.67 GeV/c. *Phys. Rev. Lett.*, 89 :092001, 2002.
- [120] V. Flaminio, W. G. Moorhead, Douglas R. O. Morrison, and N. Rivoire. Compilation of Cross-sections. Pion Induced Reactions. *CERN-HERA-84-01*, 1984.
- [121] H. W. Barz, B. Kämpfer, Gy. Wolf, and M. Zetenyi. Propagation of vector-meson spectral-functions in a BUU type transport model : Application to di-electron production. *The Open Nuclear & Particle Phys. J.*, 3 :1–15, 2010.
- [122] E. L. et al. Bratkovskaya. System size and energy dependence of dilepton production in heavy-ion collisions at 1-2 GeV/nucleon energies. *Phys. Rev. C*, 87 :064907, 2013.
- [123] The spectral function of the rho meson in nuclear matter. *Nuclear Physics A*, 632 :109 – 127, 1998.
- [124] H. Schopper. *Total cross-sections for reactions of high energy particles : (including elastic, topological, inclusive and exclusive reactions)*, volume 12 of (*Landolt-Barnstein. New series. Group 1 Nuclear and particle physics, I/12-B*). 1988.
- [125] K. Schmidt et al. Production and evolution path of dileptons at energies accessible to the HADES detector. *Phys. Rev.*, C79 :064908, 2009.

- [126] G. Agakishiev et al. Baryon resonance production and dielectron decays in proton-proton collisions at 3.5 GeV. *Eur. Phys. J.*, A50 :82, 2014.
- [127] V. V. Sarantsev. private communication.
- [128] M. H. Johnson and E. Teller. Classical field theory of nuclear forces. *Phys. Rev.*, 98 :783–787, 1955.
- [129] M. Levy M. Gell-Mann. The axial vector current in beta decay. *Nuovo Cim.*, 16 :705â726, 1960.
- [130] L.A. Kondratyuk A. Sibirtsev E.L. Bratkovskaya, W. Cassing. On the possibility of f_0 observation in low energy pp collisions. *Eur. Phys. J. A*, 4 :165â170, 1999.
- [131] A. Sibirtsev, W. Cassing, and U. Mosel. Heavy meson production in proton - nucleus reactions with empirical spectral functions. *Z. Phys.*, A358 :357–367, 1997.
- [132] Ch. Elster R. Machleidt, K. Holinde. The bonn meson-exchange model for the nucleonânucleon interaction. *Physics Reports*, 149 :1–89, 1987.
- [133] A. Engel, R. Shyam, U. Mosel, and A. K. Dutt-Mazumder. Pion production in proton-proton collisions in a covariant one-boson-exchange model. *Nuclear Physics A*, 603 :387–414, 1996.
- [134] K Tsushima, A Sibirtsev, and A W Thomas. Kaon properties and cross sections in the nuclear medium. *Journal of Physics G : Nuclear and Particle Physics*, 27 :349–354, 2001.
- [135] M. E. Peskin and D. V. Schroeder. *An Introduction to quantum field theory*. Addison-Wesley, Reading, USA, 1995.
- [136] P. D. B. Collins. *An Introduction to Regge Theory and High Energy Physics*. Cambridge Monographs on Mathematical Physics. Cambridge University Press, 1977.
- [137] A.P. Jerusalimov. Di-pion production in np-interaction at intermediate energies. *Proceedings of science*, 2014.
- [138] K. Nakamura et al. Review of particle physics. *J. Phys. G*, 37 :075021, 2010.

-
- [139] T. Skorodko, M. Bashkanov, D. Bogoslawsky, H. Calen, F. Cappellaro, et al. Excitation of the Roper resonance in single- and double-pion production in nucleon-nucleon collisions. *Eur.Phys.J.*, A35 :317–319, 2008.
- [140] D.M. Manley and E.M. Saleski. Multichannel resonance parametrization of πN scattering amplitudes. *Phys.Rev.*, D45 :4002–4033, 1992.
- [141] J. Weil. Vector Mesons in Medium in a Transport Approach. *Ph.D. Thesis*, 2013.
- [142] A. Baldini, V. Flaminio, W.G. Moorhead, Douglas R.O. Morrison, and H. (Ed) Schopper. Numerical data and functional relationships in science and technology. GRP. 1 : Nuclear and particle physics. Vol. 12. *Landolt Börnstein new series*, 1988.
- [143] et al. S.A.Bass. Microscopic models for ultrarelativistic heavy ion collisions. *Prog. Part. Nucl. Phys.*, 41 :225, 1998.
- [144] J. Weil et al. Particle production and equilibrium properties within a new hadron transport approach for heavy-ion collisions. *Phys. Rev.*, C94 :054905, 2016.
- [145] Jan Staudenmaier. private communication.

Résumé en Français

L'objectif principal des expériences avec le détecteur HADES (High Acceptance Di-Electron Spectrometer) est l'étude de la matière hadronique, dans la région de forte densité (jusqu'à trois fois la densité nucléaire normale) et de températures modérées, ($T < 100$ MeV), accessible en utilisant des collisions d'ions lourds à des énergies incidentes de l'ordre de 1 à 4A GeV.

En 2007, la collaboration HADES a mesuré à GSI, des collisions de protons avec une énergie cinétique du projectile égale à 3,5 GeV. Le but principal de cette expérience était de mesurer des paires électron-positron (appelées di-électrons). Cependant, HADES, est aussi un détecteur très performant pour la mesure des hadrons chargés tels que des protons et des pions, ce qui offre la possibilité d'effectuer des mesures complémentaires importantes pour l'interprétation de la production des paires e^+e^- . Ainsi, l'analyse des "hadrons" permet d'étudier les principaux mécanismes de réaction aux énergies de GSI et notamment le rôle des résonances baryoniques, et de déterminer les sections efficaces de processus qui sont des sources importantes de paires e^+e^- .

Dans le cadre de cette thèse, nous présentons l'analyse du canal exclusif $pp \rightarrow pp\pi^+\pi^-$ à une énergie cinétique de 3,5 GeV. L'objectif principal est d'étudier le rôle des résonances baryoniques et du méson ρ dans ces réactions. Ces informations ont un impact important sur les prévisions de la production de mésons et de diélectrons dans les réactions élémentaires ou d'ions lourds à quelques GeV/nucléon. Le canal $\pi^+\pi^-$ est en effet unique pour étudier les excitations d'une ou deux résonances baryoniques ainsi que la production de mésons ρ , soit directement, soit par l'excitation et la décroissance d'une résonance baryonique.

L'extraction du signal pour la production de $\pi^+\pi^-$ était basée sur la détection d'un proton, un π^+ et un π^- dans le détecteur HADES et le calcul de la masse manquante. Les corrections d'efficacité ont été effectuées à l'aide de matrices d'efficacité calculées avec GEANT3. Les erreurs statistiques sont négligeables et les erreurs systématiques sont principalement dues aux corrections d'efficacité basées sur des simulations et à la normalisation. Un modèle simple basé sur le générateur d'événements PLUTO a été construit pour l'interprétation des données, en considérant trois types de contributions sommées de manière incohérente : la production d'une résonance décroissant en $p\pi^+\pi^-$, l'excitation de deux résonances, décroissant respectivement en $p\pi^+$ et $p\pi^-$ et la production directe du méson ρ . Conformément à l'analyse de la production d'un pion mesurée dans la même réaction avec HADES, qui a fait l'objet d'une analyse précédente, une modélisation phénoménologique de la distribution angulaire des résonances en fonction du transfert du quadri-moment a été mise en œuvre pour prendre en compte l'émission anisotrope dans le centre de masse de la collision proton proton. L'analyse à un pion a révélé que l'anisotropie de la distribution diminue avec l'augmentation de la masse de la résonance. Un tel comportement est attendu car la production de résonances plus lourdes nécessite un transfert plus important du quadri-moment. Un comportement similaire a été envisagé dans le cas de l'excitation de double résonances.

Une procédure d'ajustement a été développée en utilisant comme contrainte les informations obtenues dans la même expérience par la collaboration HADES pour l'excitation d'une seule résonance dans la production d'un pion et d'un kaon. Les résultats de notre analyse ont permis d'extraire la contribution de plusieurs résonances lourdes pour lesquelles seule une limite supérieure a été extraite de l'analyse à un pion ($\Delta(1620)$, $N(1675)$, $N(1680)$, $\Delta(1910)$) et de réduire l'incertitude sur l'excitation des résonances plus légères ($N(1440)$, $N(1520)$, ...). L'excitation de deux résonances a été extraite pour la première fois. Parmi toutes les contributions identifiées, les principales sont la double excitation de $\Delta(1232)$ et l'excitation de $N(1520)$. Une tentative d'extraction de la contribution du dibaryon D_{21} rapportée par la collaboration WASA a été effectuée, mais aucun signal n'est vu. Pour un dibaryon de masse $M = 2140$ MeV et de largeur $\Gamma = 110$ MeV, une limite supérieure de la section efficace de $0,3 \mu\text{b}$ est obtenue.

La contribution de la production exclusive de méson ρ a également été extraite après application des coupures cinématiques nécessaires. Pour déterminer la distribution angulaire de la production du ρ , la section efficace différentielle a été extraite dans chaque

bin d'angle polaire $\pi^+\pi^-$ au centre de masse. Cette distribution a été fittée avec les polynômes de Legendre et intégrée pour calculer la section efficace totale. La distribution angulaire est maximale vers l'avant/arrière, mais l'anisotropie est beaucoup plus faible que le résultat mesuré par la collaboration DISTO à une énergie de faisceau de 2,85 GeV. La contribution des résonances baryoniques à la production du meson ρ est aussi incluse dans notre cocktail de résonances baryoniques, dans lequel les rapports de branchement $N\rho$ sont extraits de l'analyse en ondes partielles de Bonn-Gatchina. Bien que les détails de cette contribution dépendent des rapports de branchement des résonances baryoniques dans le canal $N\rho$, il apparaît clairement que la fonction spectrale de Breit-Wigner utilisée pour extraire la production du méson ρ sous-estime fortement la production totale du ρ . Ceci est dû à la distorsion de la fonction spectrale du ρ par la production à partir de résonances baryoniques légères (i.e. $N(1520)$). La contribution du ρ "résonant" est discutée et comparée aux modèles existants. Ce travail souligne la nécessité pour les modèles de fitter directement la distribution de masse invariante $\pi^+\pi^-$ et pas seulement les mesures de section efficace de la production du ρ .

Nous avons également essayé d'extraire la contribution de $f_0(500)$ et $f_0(980)$ puisque leur canal de décroissance dominant est $\pi\pi$. Aucun signal n'est observé et les estimations approximatives pour les limites supérieures des sections efficaces sont 5 μb pour $f_0(500)$ et 1 μb pour $f_0(980)$.

Pour examiner notre analyse de la réaction $pp \rightarrow pp\pi^+\pi^-$ basée sur une somme incohérente de contributions dans une perspective plus théorique, nous avons développé avec Jacques Van De Wiele un modèle de Lagrangien effectif qui prend en compte les deux contributions principales, la double excitation de $\Delta(1232)$ et l'excitation de $N(1520)$. Il permet de comparer les résultats de notre modèle de résonance simple avec un modèle basé sur la théorie quantique des champs et de tester les effets d'interférences. Bien que certaines différences soient visibles, les caractéristiques principales sont très similaires. Globalement, notre modèle simple semble donner une meilleure description des données. Le modèle de Lagrangien prédit un effet négligeable des interférences.

Ensuite, nous avons comparé nos données expérimentales aux modèles existants dédiés à la réaction $NN \rightarrow NN\pi\pi$. Nous avons d'abord collaboré avec A. Jerusalemov pour comparer le modèle OPER à nos données. Le modèle ne fournit pas de section efficace absolue, mais il a été constaté qu'il surestime la contribution relative d'excitation de

double- Δ , $\Delta(1600)$ et d'autres résonances plus lourdes se trouvant autour de 1,8 GeV. Nous avons également collaboré avec Xu Cao pour confronter le modèle de Lagrangien effectif de Cao *et al.* à nos données. La comparaison a montré que l'excitation de double résonances est sous-estimée puisque seule l'excitation de double- $\Delta(1232)$ est incluse dans les calculs. Cela est dû au fait que le modèle a été développé pour décrire la réaction NN en dessous de 2,2 GeV. Il montre également que les contribution relatives d'excitations de $N(1440)$, $N(1710)$ et $N(1720)$ sont surestimées et que la contribution de la $N(1520)$ est manquante. Nous espérons que ce travail motivera d'autres travaux théoriques.

Les contributions de résonances extraites de l'analyse de données ont également été comparées aux résultats de calculs des modèles de transport (GiBUU, UrQMD et SMASH). Aucun modèle ne fournit des résultats totalement compatibles avec notre analyse. Parmi les contributions les plus importantes, le double- $\Delta(1232)$ est mieux reproduit par GiBUU et SMASH et les contributions de $N(1440)$, $N(1520)$ et $N(1675)$ sont mieux prédites par UrQMD. La confrontation des résultats expérimentaux avec les prédictions des modèles théoriques existants montre la nécessité de prendre en compte ces nouvelles données.

Les travaux présentés dans cette thèse démontrent que la réaction $pp \rightarrow pp\pi^+\pi^-$ à 3,5 GeV est un outil puissant pour contraindre les modèles utilisés pour décrire les collisions nucléon-nucléon et les collisions d'ions lourds. En particulier, ce canal est très sensible à l'excitation d'une ou deux résonances baryoniques, ainsi qu'à la production de mésons ρ , sources importantes de diélectrons. Ces données doivent donc servir de référence pour les modèles et sont très utiles pour décrire plus en détail les données HADES existantes pour la production de paires e^+e^- en réactions $p + p$ ou $p + Nb$ à 3,5 GeV ou encore fournir des prédictions réalistes pour les futures expériences en ions lourds à quelques GeV par nucléon avec HADES ou CBM à FAIR.

Resonance	σ_R [mb]	$BR_{N\pi\pi} \times I$	$\sigma_R^{p\pi^+\pi^-}$ [mb]
$N^+(1440)$	1.5 ± 0.4	0.17 ± 0.04	0.250 ± 0.017
$N^+(1520)$	1.8 ± 0.3	0.16 ± 0.03	0.29 ± 0.016
$N^+(1535)$	0.15 ± 0.03	0.023 ± 0.005	0.0030 ± 0.0002
$\Delta^+(1620)$	0.05 ± 0.01	0.44 ± 0.09	0.022 ± 0.002
$N^+(1650)$	0.027 ± 0.008	0.09 ± 0.02	0.002 ± 0.0001
$N^+(1675)$	1.05 ± 0.23	0.25 ± 0.05	0.26 ± 0.004
$N^+(1680)$	0.80 ± 0.08	0.016 ± 0.02	0.128 ± 0.011
$N^+(1700)$	0.10 ± 0.025	0.4 ± 0.1	0.04 ± 0.004
$\Delta^+(1700)$	0.45 ± 0.13	0.38 ± 0.10	0.17 ± 0.02
$N^+(1710)$	0.024 ± 0.008	0.09 ± 0.03	0.002 ± 0.0001
$N^+(1720)$	0.045 ± 0.005	0.33 ± 0.03	0.0148 ± 0.0003
$N^+(1875)$	0.027 ± 0.013	0.36 ± 0.17	0.0097 ± 0.0004
$N^+(1880)$	0.41 ± 0.20	0.16 ± 0.07	0.066 ± 0.003
$\Delta^+(1905)$	0.045 ± 0.005	0.56 ± 0.06	0.025 ± 0.003
$\Delta^{++}\Delta^0$	3.7 ± 0.15	0.33 ± 0.0	1.22 ± 0.05
$\Delta^{++}N^0(1440)$	0.81 ± 0.13	0.36 ± 0.05	0.54 ± 0.01
$\Delta^{++}N^0(1520)$	1.50 ± 0.10	0.46 ± 0.03	0.37 ± 0.02
$\Delta^{++}N^0(1535)$	0.46 ± 0.10	0.30 ± 0.06	0.138 ± 0.003
$\Delta^{++}N^0(1680)$	0.80 ± 0.07	0.43 ± 0.03	0.34 ± 0.01

TABLE (A.1) Les sections efficaces en unités de millibarns de la production de une et de doubles résonances dans les collisions pp extraites de l'analyse du canal $pp \rightarrow pp\pi^+\pi^-$. Les erreurs représentent la somme quadratique du fit et de l'erreur sur les rapports de branchement.

Titre : Etude de résonances baryoniques dans le canal $pp \rightarrow pp\pi^+\pi^-$ à une énergie de faisceau de 3.5 GeV avec le détecteur HADES.

Mots clés : Physique hadronique, simulation, résonances baryoniques, GSI, détecteur HADES.

Résumé : Le sujet de cette thèse est l'analyse de la réaction $pp \rightarrow pp\pi^+\pi^-$ mesurée à une énergie de faisceau de 3,5 GeV avec le spectromètre HADES à GSI. L'objectif est d'apporter des informations complémentaires à la production d'un pion et d'un kaon mesurés par HADES pour l'excitation d'une résonance ainsi que des résultats tout nouveaux pour la production de deux résonances et pour la production du méson ρ . Ces informations sont particulièrement importantes pour l'interprétation des spectres de di-électrons également mesurés par la collaboration HADES. L'extraction du signal pour la production de $pp \rightarrow pp\pi^+\pi^-$ est basée sur la détection d'un proton, un π^+ et un π^- dans le détecteur HADES et sur le calcul de la masse manquante. Les erreurs statistiques sont négligeables et les erreurs systématiques sont principalement dues aux corrections d'efficacité basées sur les simulations et à la normalisation. Un modèle simple basé sur le générateur d'évènements PLUTO a été construit pour l'interprétation des données en incluant trois types de contributions: la production d'une résonance décroissant en $p\pi^+\pi^-$ et l'exci-

tation de deux résonances décroissant respectivement en $p\pi^+$ et $p\pi^-$ et la production directe du méson ρ . Une procédure de fit est développée en utilisant comme contraintes pour l'excitation baryonique simple les résultats obtenus pour la production d'un pion et d'un kaon. La contribution du méson ρ a été également extraite après l'application des coupures cinématiques nécessaires et le rôle des résonances baryoniques dans cette production est discuté. Parmi toutes les contributions identifiées, les principales sont la double excitation de $\Delta(1232)$ et la simple excitation de $N(1520)$. Un modèle de Lagrangien a été mis au point pour ces deux contributions, les calculs donnent un résultat assez proche du modèle simple et prédisent un effet des interférences très faible. Finalement, la confrontation des résultats expérimentaux aux prédictions de modèles théoriques existants montre la nécessité de prendre en compte ces nouvelles données pour la description de la production de mésons et de di-électrons dans les collisions nucléaires au-delà de 1.5 GeV/nucléon.

Title : Study of baryonic resonances in the channel $pp \rightarrow pp\pi^+\pi^-$ at 3.5 GeV beam energy with the HADES detector.

Keywords : Hadronic physics, simulation, baryonic resonances, GSI, HADES detector.

Abstract : The subject of this thesis is the analysis of the $pp \rightarrow pp\pi^+\pi^-$ reaction measured at a beam energy of 3.5 GeV with the High Acceptance Di-Electron Spectrometer (HADES) at GSI. The aim is to provide additional information on the production of a pion and a kaon measured by HADES for the excitation of a resonance as well as new results for the production of two resonances and the ρ meson production. Such information is important, in particular, for the interpretation of the di-electron spectra measured by the HADES collaboration. The extraction of the signal for $pp \rightarrow pp\pi^+\pi^-$ production is based on the detection of one proton, one π^+ and one π^- in the HADES detector and the calculation of the missing mass. Statistical errors are negligible and systematic errors are mainly due to the efficiency corrections which are based on simulations and to normalization. A simple model based on PLUTO event generator was built for the interpretation of the data, by

including three main types of contributions: the production of one resonance decaying into $p\pi^+\pi^-$ and the excitation of two resonances, decaying respectively into $p\pi^+$ and $p\pi^-$ and the direct ρ production. A fitting procedure is developed, using as constraint the information obtained for the single resonance excitation from one pion and one kaon production data. The contribution of the ρ meson was also extracted after applying necessary kinematical cuts. Among all the identified contributions, the main ones are the double $\Delta(1232)$ excitation and the $N(1520)$ excitation. A Lagrangian model was developed for these two contributions, the calculations give a similar result to the simple model and predict a negligible interferences effect. Finally, the confrontation of the experimental results to the predictions of existing theoretical models shows the necessity to take into account these new data for the description of mesons and di-electron production in nuclear collisions above 1.5 GeV/nucleus